

Reliability assessment of lead- free solder joint, based on high cycle fatigue & creep studies on bulk specimen

vorgelegt von

M.Eng.

Joel Luther Thambi

geb.in Marthandam, India

von der Fakultät IV - Elektrotechnik und Informatik
der Technischen Universität Berlin
zur Erlangung des akademischen Grades

Doktor der Ingenieurwissenschaften

- Dr.-Ing. -

genehmigte Dissertation

Promotionsausschuss:

Vorsitzender: Prof. Dr.-Ing. Dietmar Kissinger

Gutachter: Prof. Dr.-Ing. Dr. sc. techn. Klaus-Dieter Lang

Gutachter: Prof. Dr.-Ing. Ulrich Tetzlaff

Gutachter: Prof. Dr.-Ing. Bernhard Wunderle

Tag der wissenschaftlichen Aussprache: 15.05.2017

Berlin 2018

ACKNOWLEDGMENTS

Firstly, I would like to express my deepest gratitude to my supervisors Prof. Dr.-Ing. Ulrich Tetzlaff and Prof. Dr.-Ing. Manuela Waltz (TH Ingolstadt, Germany) for their constant guidance, support, and motivation. It would have never been possible for me to complete the thesis without their illuminating instruction and inspiring encouragement.

At the same time, I am also grateful to Prof. Dr.-Ing. Klaus-Dieter Lang (TU Berlin, Germany) for providing me with valuable advice and access to related resources for my thesis.

My heartfelt thanks to Mr. Andreas Schiessl (Continental Automotive GmbH, Regensburg, Germany), for being a key motivator and inspiration to pursue my master and doctorate studies in Germany.

I would like to express my appreciation to Mr. U. Deml (EMZ Hanauer GmbH) and Dr. Alexander Sedlmeier (Continental Automotive GmbH, Regensburg, Germany) for many inspiring discussions.

I collectively would like to thank Prof. Dr. Andras Borbely (École de Mines, Saint-Etienne, France), Dr.-Ing. Mike Roellig, Mr. Rene Metasch (Fraunhofer IKTS-Dresden), Dr.-Ing Karsten Meier (TU Dresden, Germany), Mrs. Yvonne Hadinger (THI Ingolstadt), Mrs. Angelika Schingale, Mr. Marius Tarnovetchi, Mr. Frank Baur (Continental Automotive GmbH) in specific for their technical support.

Also my sincere thanks to Dr.-Ing. Olaf Wittler (IZM Fraunhofer, Berlin) and Prof. Dr.-Ing. Bernhard Wunderle (TU Chemnitz) for their expertise inputs and guidance.

Finally, I would like to thank my wife, parents, family, and friends for their continuous support during my doctoral study.

Yours faithfully,

Joel Luther Thambi

Rotterdam, August 2016

ABSTRACT (ENGLISH)

The advancement in the electronic technology, have produced smaller and smaller devices that handle ever increasing amounts of power and heat, the micro structural integrity of wire bonds, micro-terminals and solder joints become increasingly important. This is underscored by the fact that the majority of field failures of electronic modules are physical and structural in nature, mostly related to thermal stress and fatigue of solder joints resulting in failure. Within this framework, reliability assessment of lead-free solder joints is investigated by explicitly understanding the intrinsic material based creep and high cycle fatigue (HCF) properties.

First, this work establishes a modified creep model of a *SAC* alloy using a physical based mechanistic modelling technique. Through experimentation and reformulation steady-state creep behaviour is analysed with minimum strain rates ranging from (10^{-4} till 10^{-8} 1/s) for different temperatures 35, 80, and 125°C. The new modified physical creep model is proposed, by understanding the respective precipitate-strengthened deformation mechanism, seeing the dependency of the activation energy over the temperature along with stress and finally by integrating the subgrain size dependency λ_{SS} . The model is found to accurately modelling the creep behaviour of Lead (*Pb*) free solder alloy by combining the physical state variables. The features of the creep model can be explored further by changing the physical variable such as subgrain size to reduce the damage parameters for solder joints. Thereby a *structure-property* relationship is established for *Pb* free solder alloys, enabling design engineers or material experts to find the optimal solder life performance.

Second, the thesis gives deep insight into high cycle fatigue (HCF) behaviour of the *Pb*- free solder alloy in the region between 10^4 up to 10^8 cycles using fatigue specimen. This work uses a generalised local stress approach that can be translated into a solder joint fatigue evaluation in any microelectronic application. The effect of temperatures on the fatigue property of lead free solder alloy is considered in this work to understand the possible fracture mechanism and microstructural changes in a solder alloy at elevated temperature. Experiments were also performed for different interaction factors under mean stresses ($R = 0, -1, -3$), stress concentration (notched, un-notched) and surface roughness. SN (stress-life) diagrams presented in this work will compare the performance of *SAC* solder alloy for different conditions. Furthermore, mathematical fatigue model corrected based on FKM guideline is extracted out of the experiments under these external effects and the fatigue models can be exported later for evaluation purpose. The thesis thereby proposes the use of FKM guideline in the field of microelectronics for the first time.

The proposed generalised local stress methodology based on fatigue specimen is validated by performing vibration experiments on two different surface mount technology (SMT) components (chip capacitors and transformers) soldered on single strap PCB under a sine swept loading and elevated temperature. Local stresses from the frequency response, identified on the solder joints will be used as damage parameters in predicting the lifetime of the component. Influential fatigue factors such as temperature, stress gradient, *R*-ratio, roughness were also considered. Fatigue life of solder joints is determined and experimentally verified with that of the predicted fatigue life of solder joints results.

ABSTRACT (DEUTSCH)

Durch den Fortschritt in der elektronischen Technologie werden immer kleinere Komponenten produziert, welche stetig größerer Leistung und Erwärmung ausgesetzt sind. Die mikrostrukturelle Integrität von Wire-Bonds, Mikro-Anschlüssen und Lötverbindungen gewinnt rasant an Bedeutung. Dies wird durch die Tatsache begründet, dass die Mehrheit der Fehler in elektronischen Modulen, physikalisch oder strukturell bedingt sind. So führen thermisch induzierte Spannungen zur Ermüdung und dann zur Rissbildung in der Lötstelle. Im Rahmen dieser Arbeit wird eine Zuverlässigkeitsbewertung von bleifreien Lötstellen anhand des Kriechhaltens und des Schwingfestigkeitsverhaltens (HCF) des Lötwerkstoffes untersucht.

Im Rahmen dieser Arbeit wird zunächst ein modifiziertes Kriechmodell auf Basis der Legierung SAC erstellt. Es nutzt eine, auf physikalischen Grundlagen basierende, mikromechanische Modellierungstechnik. Anhand von Versuchen und einer Darstellung des Kriechverhaltens im stationären Zustand, wurden die minimalen Kriechraten (10^{-4} bis 10^{-8} 1/s) bei den Temperaturen 35, 80, und 125°C untersucht. Ein neues modifiziertes Kriechmodell wird vorgeschlagen, bei dem die Abhängigkeit der Aktivierungsenergie in Abhängigkeit von der Spannung und schließlich die Abhängigkeit von der Subkorngrößen λ_{SS} integriert wird. Das neue Modell beschreibt das Kriechverhalten des bleifreien Lots durch die Kombination verschiedener physikalischer Zustandsgrößen. Dadurch wird eine Struktur-Eigenschaftsbeziehung deutlich, die den Materialwissenschaftlern und Designingenieuren ermöglicht, eine Lotstellenlebensdauer zu ermitteln.

Des Weiteren gibt diese Arbeit, für eine Zykluszahl zwischen 10^4 und 10^8 , einen Einblick in das Schwingfestigkeitsverhalten des bleifreien Lots. Es wird ein verallgemeinerter lokaler Spannungsansatz benutzt, der in jeder Anwendung für die Beurteilung der Lötstellenermüdung eingesetzt werden kann. Außerdem wurden die Einflüsse der Temperatur (35, 85, und 125°C) auf die Ermüdungseigenschaft des bleifreien Lots untersucht, um die möglichen Rissmechanismen und mikrostrukturellen Veränderungen in der Lotverbindung zu verstehen. Es wurden auch Versuche mit den wichtigsten Einflussfaktoren durchgeführt. Dazu gehören der Mittelspannungseinfluss ($R=0, -1, -3$), die Spannungskonzentration sowie die Oberflächenrauheit. Unter Zuhilfenahme von *S-N*-Diagrammen wird die Performance von SAC -Lötlegierungen unter unterschiedlichen Bedingungen verglichen. Darüber hinaus wurde ein mathematisches Ermüdungsmodell, basierend auf der FKM-Richtlinie, erstellt. Die dafür notwendigen Daten wurden aus den Versuchen und den Umgebungsbedingungen ermittelt. Dieses Modell wurde für die Beurteilung des Ermüdungsverhaltens verwendet.

Die vorgeschlagene verallgemeinerte lokale Spannungsmethodik, basierend auf der uniaxialen Ermüdung der Proben, wurde mithilfe von Vibrationsversuchen validiert. Hierbei testete man zwei verschiedene Komponenten (Keramikkondensatoren und Transformatoren) auf einer Leiterplatte, unter einer Sinuswechsellast und erhöhter Temperatur, getestet. Lokale, während des Frequenzgangs auftretende Spannungen, die auf der Lötverbindung ermittelt wurden, dienen als Zerstörungsparameter für die Prognostizierung der Komponentenlebensdauer. Die Lebensdauer von Lotverbindungen wurde prognostiziert und experimentell verifiziert.

TABLE OF CONTENTS

TITLE PAGE
ACKNOWLEDGMENTS	I
ABSTRACT (ENGLISH)	II
ABSTRACT (DEUTSCH)	III
TABLE OF CONTENTS	IV
1 INTRODUCTION	1
1.1 INDUSTRIAL NEEDS	1
1.2 TECHNOLOGY	2
1.3 METHODOLOGY	3
1.4 OBJECTIVES	5
1.5 THESIS OUTLINE.....	6
2 FUNDAMENTALS AND STATE OF THE ART	7
2.1 THEORY	7
2.1.1 Surface mount technology (SMT).....	7
2.1.2 Metallurgy of Tin	8
2.1.3 SAC alloy types	8
2.1.4 Effects of solder joint microstructure.....	9
2.1.5 Causes of solder joint failures	12
2.1.5.1 Low cycle fatigue/thermo-mechanical fatigue	12
2.1.5.2 High cycle fatigue/vibrational fatigue	13
2.1.6 Fatigue theories and models.....	14
2.1.6.1 Stages of damage evolution in solder	15
2.1.6.2 Fatigue modelling	18
2.1.6.3 FKM guideline.....	18
2.1.7 Creep theories and models	22
2.1.7.1 Stages of creep	22
2.1.7.2 Creep mechanisms for particle strengthened solder alloy	24
2.1.7.3 Creep damage models.....	28
2.1.7.4 Implementation of creep models to FE problems.....	30
2.2 STATE OF THE ART	31
2.2.1 Phenomenological vs. mechanistic creep models	31
2.2.2 Low cycle fatigue/thermo- mechanical fatigue.....	34
2.2.3 High cycle fatigue/vibration fatigue	36
2.2.4 Local stress approach for HCF prediction	37
3 EXPERIMENTAL METHODS AND SETUPS.....	40
3.1 SOLDER ALLOY MATERIAL	40
3.2 SOLDER SPECIMEN DESCRIPTIONS	40
3.2.1 Solder specimen design for creep	40
3.2.2 Solder specimen design for fatigue	41
3.3 SOLDER SPECIMEN MANUFACTURING	42
3.3.1 Cast setup for specimen manufacturing	42

3.3.2	Post soldering treatments	44
3.4	EXPERIMENTAL SETUP FOR MECHANICAL CHARACTERIZATION	45
3.4.1	Fatigue characterization	45
3.4.2	Creep characterization.....	47
3.5	VIBRATION SETUP FOR APPLICATION VALIDATION.....	50
3.6	MATERIAL INVESTIGATIONS	52
4	CREEP INVESTIGATION OF SAC ALLOY	54
4.1	TIME INDEPENDENT STRAIN VS. STRAIN RATE CURVES.....	54
4.2	PHENOMENOLOGICAL MODELS	56
4.2.1	Norton power law.....	56
4.2.2	Garafalo – Arrhenius hyperbolic sine model	57
4.2.3	Double power law	58
4.2.4	Comparison of phenomenological creep models	59
4.3	DEVELOPMENT OF A MECHANISTIC CREEP MODEL	61
4.3.1	Implementing threshold stress using Orowan theory.....	61
4.3.2	Dependency of stress exponent (n) and activation energy (Q) on temperature	65
4.3.3	Incorporating the subgrain size dependency	70
4.3.4	Comparison of creep models.....	72
4.4	CREEP DAMAGE MODELS	75
4.5	RESULTS & DISCUSSION.....	77
4.5.1	Benchmarking proposed creep model.....	77
4.5.2	Limitations of phenomenological models.....	79
4.5.3	Subgrain dependency	80
4.6	CONCLUSIONS.....	82
5	HIGH CYCLE FATIGUE INVESTIGATION OF SAC ALLOY	84
5.1	FATIGUE BEHAVIOUR OF SAC ALLOYS	84
5.1.1	Fatigue property under temperature variant.....	85
5.1.2	Fatigue property under mean stress influence.....	87
5.1.3	Stress gradient effects	92
5.1.4	Effects of surface roughness	94
5.2	RESULTS & DISCUSSIONS	97
5.2.1	Effects of fatigue factors	97
5.2.2	Creep interactions at fatigue	99
5.3	CONCLUSIONS.....	99
6	MICROSTRUCTURE INVESTIGATIONS	101
6.1	QUALITATIVE COMPARISON OF CAST SOLDER AND SOLDER JOINT.....	101
6.2	CREEP MICROSTRUCTURE ANALYSIS	105
6.2.1	Primary grains and necking.....	106
6.2.2	Subgrains polygon formation.....	106
6.2.3	Influence of primary IMC phase particles	109
6.3	CREEP FRACTURE ANALYSIS	109
6.4	HIGH CYCLE FATIGUE MICROSTRUCTURE ANALYSIS	112
6.5	HIGH CYCLE FATIGUE FRACTURE SURFACE ANALYSIS	116
6.6	CONCLUSIONS.....	120

7	LIFE TIME PREDICTION UNDER VIBRATION AND THERMAL CONDITIONS	123
7.1	GENERALISED METHOD OVERVIEW FOR VIBRATION PREDICTION	123
7.1.1	Experiment summary	124
7.1.2	Finite element analysis - component level	124
7.1.3	Mesh dependence	126
7.1.4	Material damping properties of PCB	128
7.1.5	Correlating PCB deflections (simulation vs. experiment)	130
7.2	FATIGUE EVALUATION	131
7.3	RESULTS AND DISCUSSION	132
7.4	IMPLEMENTING NEW CREEP MODEL IN FEA	137
7.4.1	Mechanistic creep model into FE problems	137
7.4.2	Subroutine of the modified creep law in ANSYS	138
7.4.3	FEA with new subroutine using chip capacitors under TMC	139
7.5	CONCLUSION	142
8	SUMMARY & FURTHER RECOMMENDATIONS	144
8.1	CREEP INVESTIGATIONS	144
8.2	HCF INVESTIGATIONS	146
8.3	FURTHER RECOMMENDATIONS	147
	REFERENCES	149
	APPENDIX	159
	NOMENCLATURE	169
	LIST OF FIGURES	172
	LIST OF TABLES	177
	LIST OF PUBLICATIONS	178

1 INTRODUCTION

1.1 INDUSTRIAL NEEDS

Assessing the reliability of electronic products in the product development process is the need of an hour in electronic industries. Increased customer requirements and reduced time for development is necessary over the span of the product development. Solder joints in specific are the weakest link in electronic packages, with relatively lesser service intervals because of their poor mechanical properties compared to the metalized component or substrates to which they are attached. Most handheld electronic packages in a power train sector in automotive applications undergo thermo-mechanical cycling combined with vibration environments, which eventually results in thermomechanical fatigue (TMF) of solder joints, which is regarded as a failure superposed of creep and fatigue by many in the active research. This in turn produces tiny cracks sustained by a combination of tensile and shear loading on the solder joints resulting in the catastrophic failure of the solder joints or the failure of entire package [1].

When an electronic product fails in the field, the consequences to the manufacturers and OEM's can be quite significant. Warranty costs are a direct measurement of in-field failure, but there are many additional unseen costs. Customers become dissatisfied and consider moving to different competitor offerings, which leads to market share loss over time. In-field failures might also result in overdesign in subsequent offerings, reducing profitability. Today, single event static-only failure is rarely observed in surface mount technology (SMT) components during their life cycle. In-field solder joints failures are predominantly long term based due to TMF, creep and fatigue. Long-term prediction or performances of materials must be performed to understand the level implications of repeated, fluctuating, and rapidly applied loads. Thus, the need to resolve mechanical design problems for long-term performance has become a key driver for a growing number of companies to include fatigue and creep analysis as a standard protocol in their product development processes.

Nevertheless, qualification of such parts/products in industries nowadays are getting complicated as an equilibrium state between increased customer requirements (enlarged warranty, high temperature level, high complexity) and reduced development time/cost has to be figured out, as these conditions elongates the qualification time and shortening of qualification respectively.

Traditional electronic based manufacturers spend almost 73% of product development costs on the test-fail-fix methodology, according to Cunningham [2]. A summarised report of Cunningham [2] which was published 10 years back shows the cost split up during the product development phase (see *Figure 1-1*). Statistical reliability standards such as test-fail-fix methodology based on data tables are questionable because they do not tell the fundamental failure mechanism involved in the failure of the electronic product. The test strategies have become less feasible given the rapid advancements happening nowadays in the materials and technology and it is for the exact reason that the traditional approaches consumes more time to commercialize a long term performing product in the market.

For automotive applications, solder joints in SMT are often responsible for both electrical and mechanical connection failures. Solder joints typically do not have adequate ductility at lower temperatures to ensure repeated relative displacements of the SMT and the PCB substrate. The reliability of solder joints of electronics components plays a critical role in service lifetime of

SMT components [2]. Researchers [3, 4, 5, 6, 7, 1], investigated vibrational/thermal reliability of solder joints based on FEA and experiments on several types of SMT devices systematically and extensively. Although the research works are available for the SMT, it is primarily based on component level testing which needs further validation when a different component or material is chosen for the investigation [8]. The behaviour of *Pb*-free alloy on solder joint level is not often discussed with respect to HCF experiments and creep-fatigue interaction, especially in the automotive sector, where the SMT devices undergo vibration load simultaneously with thermal cycling.

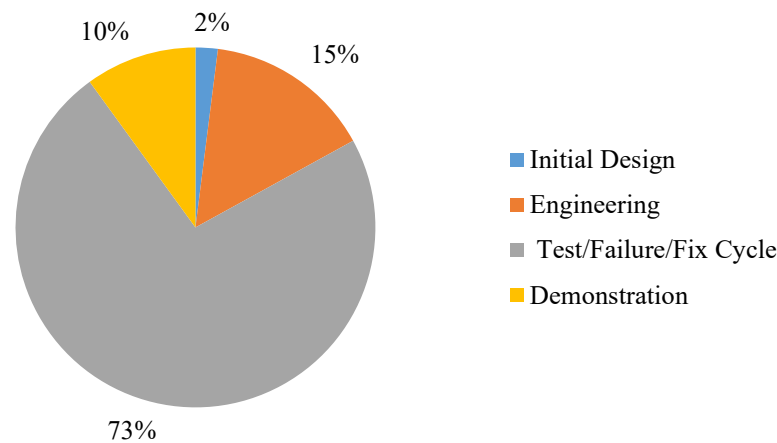


Figure 1-1: Product development cost split up for an electronic based OEM's [2]

In parallel, industries are consistently engaged in developing and improving solder alloys to meet the stringent loading requirements and harsh environments in which they operate. The requirements are mainly due to the operating temperature ranges (-20°C and 125°C) and even more for automotive sector. With the miniaturization and increasing power of power electronics, high temperature operation has also become an issue. The melting temperature of *SnAgCu* (SAC) ternary eutectic alloy is higher approximately 34°C than that of eutectic *Sn-Pb* binary alloy [9]. Accordingly the overall reflow temperatures are raised to about $40 - 50^{\circ}\text{C}$ more compared to *Pb* reflow soldering [9]. Even though the consideration of a proper melting range from phase equilibrium diagram of solder alloys gives a quick hint of designing a solder alloy for reflow condition, most of the automotive industries faces issues in designing solder joints for the stringent operating conditions (dynamic loading situations, for e.g. TMF along with vibration) during the lifetime of automotive electronics. The fluctuations in temperature and vibration accumulate the damage over the lifetime, eventually leading to component/sub-component failures.

1.2 TECHNOLOGY

Traditional technology for qualifying microelectronics products depends on the ability of products to withstand the industry standard test protocols. As a result, a design-built-test-fix methodology is developed to assure that the product/part/component would survive the qualification testing. Even though it is a common practise to conduct experiments on application level, it is an expensive process in terms of cost and time. Nevertheless, the whole cycle of application

testing has to be repeated, when components/materials are changed for any optimization of cost and performances.

Alternatively, numerical simulations are widely used in the development of microelectronic products over the past two decades. It is a technology, which started getting notice, for assessing and improving the durability of electronic equipment with validated mathematic models and simulation tools. However, the microelectronic industry has been slow to pick up and adopt the full potential of the methodology. Understanding the physical process of failure for the evaluation of the reliability from mechanistic perspective remains a challenge. Predicting electrical performance of electronic hardware is very common: however, simulation of failure behaviour of the hardware is less frequently encountered. Significant amount of time can be saved using *through process modelling* of lifecycle characterization, product modelling techniques, load transformation, and most importantly failure assessment, if studied with careful considerations. The current study addresses the above said problems and involves the application of prediction model using physical model to determine the desired long performance goals of solder joints. Using physical model allows design or material engineers in a microelectronic industry to work in tandem to develop an optimal solder joint design and solder alloy for long-term performance.

A generalised lifetime prediction tool or methodology is apparently a prerequisite in the industries to predict the fatigue life in product development phase for thermomechanical and vibration loads. One such kind of software tools are developed in the current research group (Continental Automotive GmbH) with various collaborators, which act as a front end for the user interface along with ANSYSTM, a finite element analysis (FEA) software that acts as the back end. For instance, two different types of tools are currently being developed one for performing analysis on thermal issues and other one for vibration problems. First, one is called ‘implementation of life time prediction’ (iLTP), which uses parameterized modelling to design the surface mount technology (SMT) for the optimal thermo-mechanical fatigue performances. The other one called ‘quick predict tool’ (QPT), which uses a drag and drop functionality of wide range of SMT components on the printed circuit board (PCB) for a quick vibration fatigue evaluation. Both the tools rely on the solder joint material characterisation, which will be a core discussion in the current thesis. The applied work supports the software development technology by providing generalised methodologies and further details at various levels of the software development and implementation [10].

1.3 METHODOLOGY

Successful prediction of solder joint fatigue failure during thermo-mechanical fatigue (TMF) will depend on the ability to model the solder joints accurately. Focusing specifically on the mechanical wear out mechanism, most failures can be attributed to thermomechanical induced stresses in the soldered joints, caused by differences in the coefficient of thermal expansion (CTE). Methodology to predict the TMC failure consists of four primary steps.

First, a theoretical or constitutive equation, which forms the basis for modelling is either defined or chosen. Appropriate assumptions need to be made in constructing the constitutive equation. Second, the constitutive equation is translated into a finite element analysis (FEA) program and a FE model is created. The FEA program calculates the predicted stress-strain values for the system under study and returns stress values for the simulated conditions. Third, the FEA results are used to create a model predicting the number of cycles to failure, N_f . Fourth, the model or

results must be verified using thermal cycling data. These four steps describe the general process by which failure modelling is developed, implemented, or verified.

Developing the constitutive equations for creep forms a crucial step in predicting the TMF failure, as TMF based failure is a superposition of creep and fatigue mechanisms. The current work focuses on the development of the constitutive equation for creep and hence the methodologies behind the creep models are discussed in detail here.

Most solders currently used in electronic systems have low-melting temperature and hence experience significant amount of creep deformation throughout their lifetime because typical operational and test conditions represent high homologous temperature. Both phenomenological and mechanistic based creep models are used in the literature for predicting the creep response of both bulk and grain scale solder joints [1, 11, 12, 13].

On one hand, empirically calibrated phenomenological models are compact, easy to use, and necessary for such applications as finite-element modelling. The phenomenological approach is very convenient for electronic packaging analysts and designers to predict the expected deformation and durability of soldered assemblies. Phenomenological approaches characterizes the mechanical behaviour of lead-free solder joints using homogeneous constitutive models containing empirically determined coefficients and exponents. However, it is clearly difficult to make the phenomenological models sufficiently detailed to include all the important microstructural and loading parameters in a complex material system like solder. It is also a challenge to run a sufficient number of tests to find all the model constants with sufficient accuracy, across a sufficiently wide range of stress conditions and microstructural variations.

On the other hand, the mechanistic models are intrinsically more capable of addressing the fundamental drivers of creep deformation [1, 11, 12, 13]. Using mechanistic models, interactions taking place in the solder joints that contribute to creep deformations including individual grain structures, sliding grain boundaries and the propagation of dislocations around over or through IMC particles of various compositions can be analysed. Mechanistic models (overall summary reviewed in [11]) provides a rich understanding of the creep behaviour of complex material systems like solders, but are complex and usually do not provide a single closed-form equation at the end that can be included in such tools like finite-element material libraries. Industry is moving toward a hybrid approach where the mechanistic studies are used to gain fundamental understanding of the underlying deformation mechanisms and to gain quantitative insights into the effect of various driving forces and various microstructural features on the overall creep response of new solders. This insight is invaluable to the developers of phenomenological models because it provides the information necessary to create a realistic compact material model that are easy to be used by designers and applied at the length-scale of the solder joints. Mechanistic modelling approaches can also serve as a virtual testing tools to supplement experimental studies, thus reducing the total experimental time needed for characterizing the creep response of new solders and can support in obtaining the model constants for improved phenomenological models.

Another section of this thesis focuses on the vibration related failure (HCF) issues in the micro-electronics industry. Most electronic systems used in vibration environments are subjected to random instead of harmonic excitations. As a result, quality assurance of electronic devices usually uses random vibration as the test specification for acceptance tests, screening tests, and

reliability qualification tests. Generally, this kind of test can be conducted only after the prototype is manufactured. This is generally feasible only after a period has passed, and is often seen as uneconomic in today's fast-paced electronic technology markets. Thus, the establishment of an accurate and effective methodology for estimating of the fatigue life of components under vibration loading has become an urgent demand.

A common methodology used by both researchers and industries is to conduct vibration experiments on application/component level to understand the failure modes or to create failure models. Even though it is a common methodology to conduct experiments on application level, it is an expensive process in terms of cost and time. Normally, the whole cycle of application testing has to be repeated, when components/materials are changed for any further optimizations and developments. In addition, the damping influence of the PCB or even the complex micro material assembly makes it sophisticated to measure the local physical quantities on solder interconnects. Another methodology, which is also followed in this thesis, is to investigate the high cycle fatigue behaviour in a laboratory on specimens (coupon level): based on local stresses under influential fatigue factors such as stress amplitude, mean stress, stress gradients, temperature, and surface toughness.

1.4 OBJECTIVES

The main objective of this thesis work is to develop a physical based mechanistic creep model alongside high cycle fatigue (HCF) investigations. Henceforth, creep and fatigue behaviour of SAC alloys along with the possible creep-fatigue interactions can be investigated and routed out simultaneously. The mechanistic model investigated in the current work can possibly establish the *structure-property* relationship of a standard SAC alloy. According to the current thesis the models can be potentially used in a broader perspective e.g. in material development, predictive engineering (FEA), lifetime optimization etc. In order to achieve an intrinsic material investigation on SAC alloys, a careful revision of flow rates, typically encountered in standard reflow process also needs to be considered.

From the industry perspective, with this understanding it would be possible to generalize the prediction works on SMT component solder joint experiments, under thermal fatigue and vibration loads. The generalisation is realised using bulk solder specimen instead of directly testing components/parts to analyse the HCF and creep properties. In other words, using the bulk specimen results, it would be possible to predict (using FE approaches) the performance of solder joints in an SMT. To prove this hypothesis, the results of the bulk solder specimens should be translated to predict with failure of solder joints of SMT components (ceramic component and transformers) soldered on PCB.

From the scientific perspective, most of the literatures in the field of solder reliability refers to performance under relatively LCF as discussed in the previous section (cycle to failure, $N_f < 10^4$ cycles) fatigue conditions, whether imposed thermally, mechanically or both [14, 15, 16]. HCF behaviour of *Pb*-free solder joints are important to be investigated, for applications that deals with vibration loading, which is also considered into the scope of the current work.

1.5 THESIS OUTLINE

Following section gives a flavour of what can be expected in each chapter of the thesis:

Chapter 2 introduces the theory on the fundamentals of creep and HCF studies along with the state of art methods and techniques in the corresponding field of study. Investigation on creep and HCF for *SnAgCu* solder alloys will be the primary focus of the chapter together with the basic understanding of SMTs and solder joint microstructures. The chapter also confer upon various literature research which is active in the field of *Pb*-free solder alloys.

Experimental setup and protocols along with various test capabilities are discussed in *Chapter 3*. The chapter also gives details to the custom-made manufacturing of the bulk solder specimens for creep and HCF investigations. Further on, test setup used for creep and HCF material characterization along with SMT component testing used for validation are discussed.

Chapter 4 explicitly proposes a modified mechanistic creep model for *SnAgCu* alloy based on physical based micro-mechanical modelling technique. As described in the objective section, the chapter discusses in detail both positive and negative sides of phenomenological and mechanistic modelling and its benefits for SAC alloy. Implementation of the proposed mechanistic creep model onto FEA (using ANSYS™ by FORTRAN coding subroutines) is covered later under *chapter 7*, which establishes a relationship between microstructure and part performance. The subroutine helps in establishing a relationship between microstructures and the predictions, by means of through-process-modelling (TPM).

Chapter 5 investigates the HCF behaviour of *SnAgCu* solder alloy in the region typically above 10^4 cycles using bulk fatigue specimens. Experiments were performed under factors such as temperature, mean stresses, notch factor, and surface roughness. S-N (stress-life) diagrams for different loading conditions are discussed in the same chapter along with the corrected fatigue models followed based on FKM guidelines. It is interesting to point out the usage of FKM guideline in the current work is tried out for the first time in microelectronics material research.

The fractographs and micrographs of all creep and fatigue investigations along with its possible mechanisms are captured in detail under *chapter 6*. The microstructural and fractography analysis for both creep and fatigue experiments respectively enlightens more details on the phenomenon behind static and dynamic behaviour of solder alloys. The chapter also discusses the possible creep fatigue interactions explicitly.

Fatigue evaluation of solder joints by means of using the solder fatigue model and finite element (FE) simulations for vibration loading is investigated in *chapter 7*. The proposed methodology is validated in this chapter using vibration experimental results from two different SMT components (capacitors and transformers). Second section of this chapter details the implementation of the new creep library subroutines to ANSYS.

2 FUNDAMENTALS AND STATE OF THE ART

In this chapter, the theory behind the solder joint reliability and state of the art technology used in the microelectronic reliability field is reviewed. A clear understanding of the application (predominantly SMT) failure along with the theory of HCF and creep modelling is focused and revised.

The content gives a primary insight to the state of the art and discusses the need for an accurate modelling of SAC solder alloys, when the application is subjected to harsh environmental testing like vibration, thermal cycling etc. Since the thesis uses generic uniaxial solder specimens to investigate the HCF and creep behaviour of a solder alloy, it is important to validate the methodology for lifetime evaluation onto applications. Therefore, a fundamental understanding of both application and material characterisation for SAC solder alloy will be revised in tandem.

2.1 THEORY

2.1.1 Surface mount technology (SMT)

SMT, a classification of electronic components uses an assembly process in which the components are soldered to land on the surface of the board, rather than inserted into holes running through the board or different methods. The heart of the SMT assembly is the machine that places the components onto the printed board land areas prior to soldering. Unlike through-hole (TH) insertion machines, some surface mount placements machines are very versatile, capable of placing many different components, while other SMT machines are dedicated to a few component types. This work focuses only on such a SMT component for the fatigue evaluation of solder joints. *Figure 2-1-a*, shows a transformer (EHP 16) with the ferrite core, polymer frame, coil, and most importantly the lead frame used between polymer frame and a PCB substrate. The legs of the lead-frame are joined to bond pads on a packaging circuit board using SAC solder joints. The component being exotic, heavy relatively compared to other component, the lead frame act as a mechanical support for the solder joints [9].

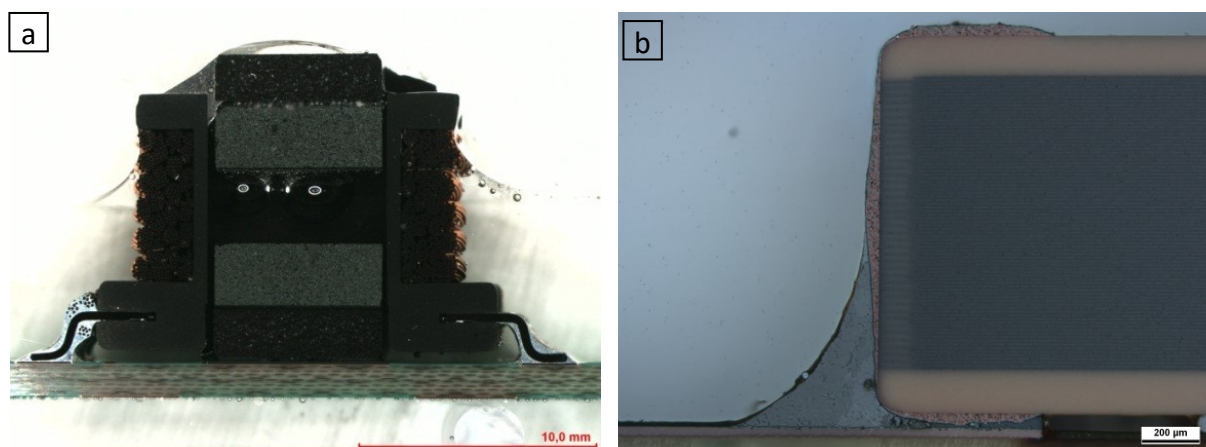


Figure 2-1: Cross section of SMT components showing (a) transformer EHP16-solder joints with lead frame (b) chip capacitor CC0805-without lead-frame – (Source: Engine control unit cross sections-Continental Automotive GmbH [17])

Another kind of SMT that is referred in this thesis for fatigue validation purpose is a chip capacitor, which has a leadless connection unlike the previous case. Chip capacitor consists of formulated ceramic dielectric materials, which is fabricated into a thin layer, interspersed with metal electrodes alternately exposed on opposite edges of the laminated structure. Conductive terminations are applied to opposite ends of the chip to make contact with the exposed electrode. Standard end terminations use a nickel barrier layer and a tin over-plate to provide excellent soldering property [9]. An example of an interconnection without leadless solder interconnect can be visualised in *Figure 2-1-b*.

2.1.2 Metallurgy of Tin

Tin forms a primary constituent and dominating phase in SAC alloys, which is predominantly used in SMT packaging for soldering. Tin has two allotropes, referred to ‘white tin’ (beta phase, written as β -Sn) and ‘grey tin’ (alpha phase, written as α -Sn). The common form is the beta phase (β -Sn), which is stable at temperature from 13°C to its liquidus at 231.9°C. Below 13°C, the alpha phase (α -Sn) is the one that is thermodynamically stable, but it is rarely encountered in real life. Henceforth all references to Sn will be to the β -Sn unless stated. The structure of β -Sn is body centred tetragonal with crystal lattice parameters of $a = b = 0.5820$ nm and $c = 0.3175$ nm [18]. The c/a ratio of 0.546 gives rise to a high anisotropic behaviour of β -Sn. Tests on single crystals of Sn was reported by Hedges [19] gives E -modulus values ranging from 26.3MPa in the direction one to 84.8 MPa in out of plane direction. Fine-grained Sn is reported to have a Young’s Modulus of 44.3 MPa [20].

Pure β -Sn also has very poor mechanical properties at room temperature for example a tensile strength of only 11 MPa [19] and hardness of 3.9 HB [20]. The creep resistance and tensile properties of β -Sn are very sensitive to alloying condition and particularly loading rates, therefore the discussion of these properties for pure β -Sn is of little importance. To enhance the creep and fatigue resistance properties, particle hardening is a key requirement, which is normally done through alloying elements. As SAC alloy is a multiphase alloy with particle hardening, details of single-phase tin alloy is out of scope in this work and will not be a part of discussion from here onwards.

2.1.3 SAC alloy types

Many researchers did the debate over the superiority of best SnAgCu composition, which is revised in this section. A clear standard cannot be set as it is clouded by many factors: the regime under which they are tested, whether the tests are on PCB assemblies or on bulk specimens and whether their performance metrics is the ultimate lifetime of solder joints or their success rate in mass production.

In the ternary phase eutectic system, the exact composition is still disputed and researchers have claimed it to be $Sn_{3.5}Ag_{0.9}Cu$ [21], $Sn_{4.7}Ag_{1.7}Cu$ [22], and $Sn_{3.9}Ag_{0.9}Cu$ [22]. From the early research to identify the eutectic composition of Sn-Ag-Cu, has now shifted the focus to more a hypoeutectic forms of the alloy such as $Sn_{3.0}Ag_{0.5}Cu$ (SAC305) in the industry. This is partially due to the reported tendency of $Sn_{3.8}Ag_{0.7}Cu$ to form large (>100 μ m) intermetallic plates which could affect joint integrity but mainly to a desire to save money due to the considerable cost of including silver in an alloy. The works of [23, 24, 25, 26, 27] discuss some of the summarized mechanical properties of common solder alloys.

Although the electronics industry has largely settled on the use of SAC alloy for the assembly of the majority of lead free products, debate among SAC alloys continue to exist over SAC305 ($Sn_{3.0}Ag_{0.5}Cu$) and SAC405 ($Sn_{3.8}Ag_{0.7}Cu$). Results of reliability testing of SAC 305 and SAC405 in three different cases on a test vehicle representative included a range of products from CBGA’s to discrete resistors were done by McCormick [28]. SAC405 generally outper-

formed the SAC 305 solder joints for the same failure mode. Even though no significant difference between SAC 305 and SAC 405 was observed at the harsh level environmental conditions, SAC 405 showed better long term creep and fatigue performance. An intermediate composition of standard alloy $Sn_{3.8}Ag_{0.7}Cu$ or referred as SAC 387 is selected in this present study, as it is an intermediate and commonly used solder alloy used in industries and development of any other further alloy in future can be benchmarked from this particular alloy. Whenever from here onwards the name SAC is specified refers to $Sn_{3.8}Ag_{0.7}Cu$ alloy.

2.1.4 Effects of solder joint microstructure

While there are many different processes used in soldering, they all involve four basic ingredients like base metals, solder, flux, and heat. Base metal reacts with the molten solder to form an intermetallic compounds (IMC), which establishes a bond between the two materials. While the intermetallic compound formation at the interfaces is required for metallic bonding, the interfacial intermetallic affects the properties and reliability of joints. The thickness of an interfacial IMC layer increases with increasing temperature and aging time. *Figure 2-2* shows the increase of the IMC thickness over time in a SMT component, analysed from an engine control unit (ECU) of a car.

Pb-free solder joints have a coarse-grained microstructure with only a few large anisotropic β -*Sn* grains throughout the solder joints after reflow. Within each grain, the proeutectic *Sn* is mostly in dendritic form, with the space between the dendritic lobes filled in with a eutectic *Sn–Ag* phase that consists of nanoscale Ag_3Sn intermetallic compounds (IMCs) present in a β -*Sn* matrix. In addition, there are microscale Cu_6Sn_5 IMC precipitates with either straight or branched rod like structures of hexagonal cross section, mostly present at *Sn* dendrite boundaries.

Even though interfacial IMC thickness grows with aging time, the layer contributed less to crack initiation mechanism, according to field results from Continental Automotive GmbH. There is a definite coarsening of the microstructure during the aging process, which contributed to the crack initiation mechanisms [17]. In addition, even though the stress localization is induced by the deformation mismatch between the solder and interfacial IMC, the layer did not induce an effective crack initiation mechanism, although it may affect the crack propagation rate.

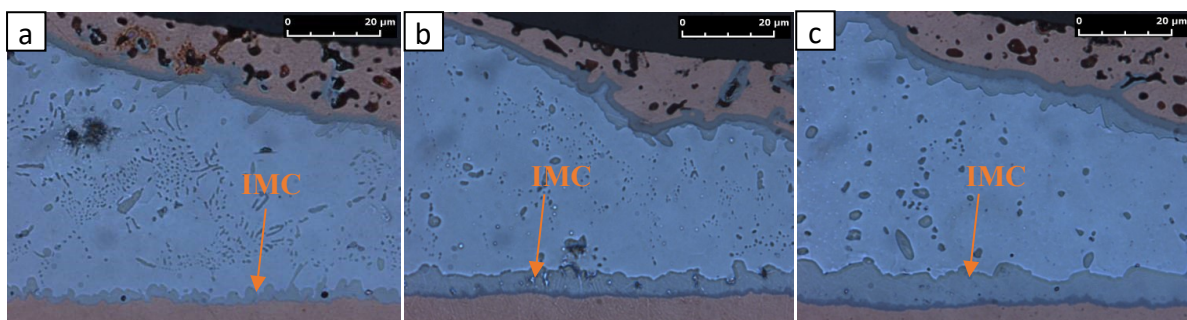


Figure 2-2: Changes in the IMC coarsening at automotive field temperature over aging time at a) 0hr b) 500hr c) 1000hr¹

¹ Source “Qualification testing- Continental Automotive GmbH, Regensburg, Germany”

Zhang [29] discussed a fatigue fracture test in which the solder joints were manufactured by reflow soldering, sandwiched between the *Cu* plates to analyse the IMC effects on the fatigue. Zhang observed the mechanical properties of solder play important roles in the fatigue lives by influencing the crack initiation mechanism, while the interfacial IMC microstructure determines the propagation cycles by dominating the fracture strength of solder joints.

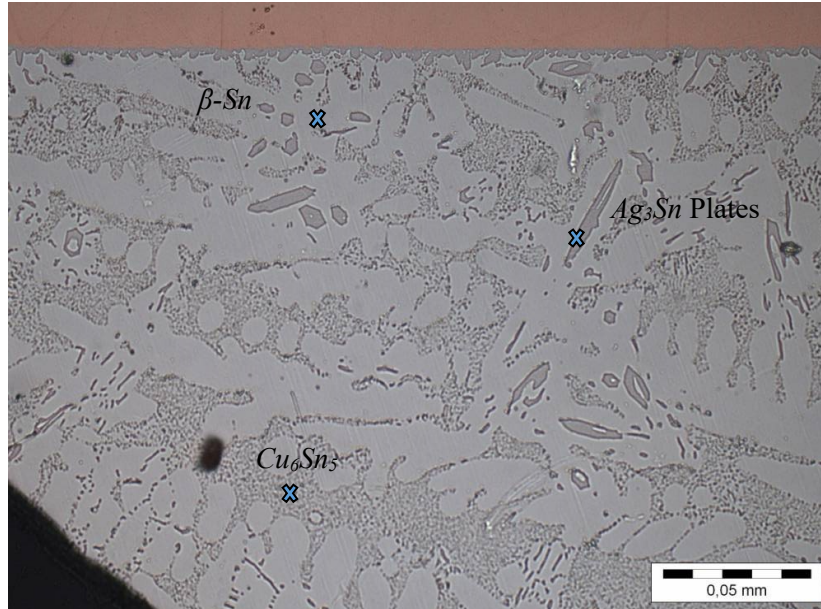


Figure 2-3: Microstructure of a typical SMT component solder joint depicting eutectic region consisting of second phase hardened particles in a β -Sn matrix

Apart from the formation of intermetallic on the interfaces, there is also dispersion of the second phase particles on the bulk material (β -Sn). When Ag_3Sn crystals are formed in a high stress area such as corner of the solder bump, this could potentially initiate cracks and propagate along the interface between Ag_3Sn and β -Sn leading to an earlier fracture life. The mixture of hardened second phase particles in β -Sn matrix plays an important role in determining the long-term performance of a solder joints.

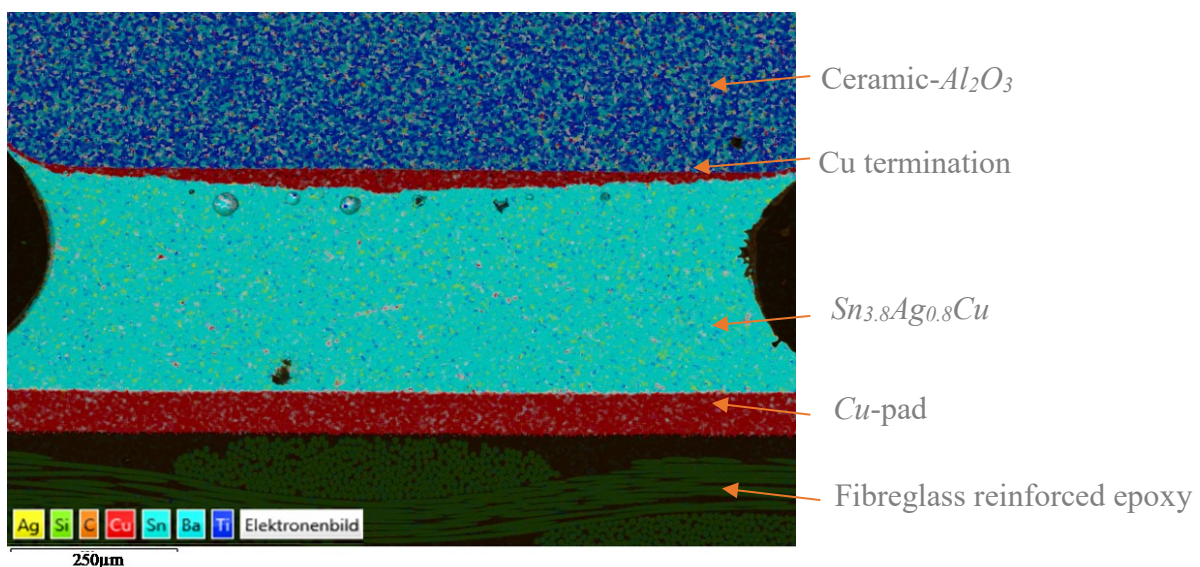


Figure 2-4: SEM-mapping of cross-section visualising different elements in SMT component (ceramic capacitors) used in this study

The dispersion of the second phase particles in β -Sn metallic phase will lead to the formation of the inhomogeneous microstructures, especially in the case of Ag_3Sn and Cu_6Sn_5 . The image of Ag_3Sn appears to be long needle like crystals in the eutectic $SnAg$ system. However, after the matrix of solder is removed by deep etching they turn into a plate-like on the cross section images, as seen in *Figure 2-3* .

The dispersion of the particles can be mapped to find the particle distribution of dendrite-like structures. An example of solder joint mapping and the various other elements in a chip capacitor component is seen in *Figure 2-4*. Along with the line scan of the particles, a special local region is selected on the line scan in the solder joint and is explained in detail with the graphics visualised in *Figure 2-5*, to confirm the local dispersion of all the hardened particles (Ag_3Sn & Cu_6Sn_5) in the higher volume fraction of β -Sn matrix.

A fundamental knowledge and understanding of the microstructure give an insight in understanding the particles dispersion, especially in the creep study, where the hardened particles are quantified for finding the localised dislocation motion of the vacancies around these Ag_3Sn and Cu_6Sn_5 particles in the β -Sn matrix. Investigating the microstructure of the solder joints also helps to compare qualitatively the material dispersion of the ternary eutectic phase between the bulk solder specimen and the solder joints. The variation in this particle dispersion along with the difference between the microstructures will be focused in this thesis. An extensive study on the microstructure for SAC alloy between bulk and interconnect is included in *chapter 6*.



Figure 2-5: SEM line scan of a SMT component (ceramic capacitor) solder joint used in this study

2.1.5 Causes of solder joint failures

As introduced in *section 1.1*, majority of field failures of electronic modules are physical and structural in nature, mostly related to items such as thermal over stress and fracture or fatigue of solder joints. The stresses and fatigue directly affects the microstructure leading to crack initiation with consequent crack growth mechanism. In this study, this two primary failure causing loads are studied in details which are classified under the low cycle fatigue (LCF) caused by thermal mechanical fatigue (TMF) and high cycle fatigue (HCF) caused by vibration. Other harmful conditions such as moisture absorption, electro- migration etc., are not in focus of the thesis.

2.1.5.1 Low cycle fatigue/thermo-mechanical fatigue

Solder joints should possess the reliability characteristics to survive thermal-mechanical effects that contribute to 65% of electronics failures [30]. The failures are caused by thermally induced stresses and strains, the root cause due to the coefficient of thermal expansion or CTE difference as schematically explained in *Figure 2-6*. The CTE mismatch between the substrate and metallic components could be generated from either global expansion mismatch, local expansion mismatch or internal expansion mismatch.

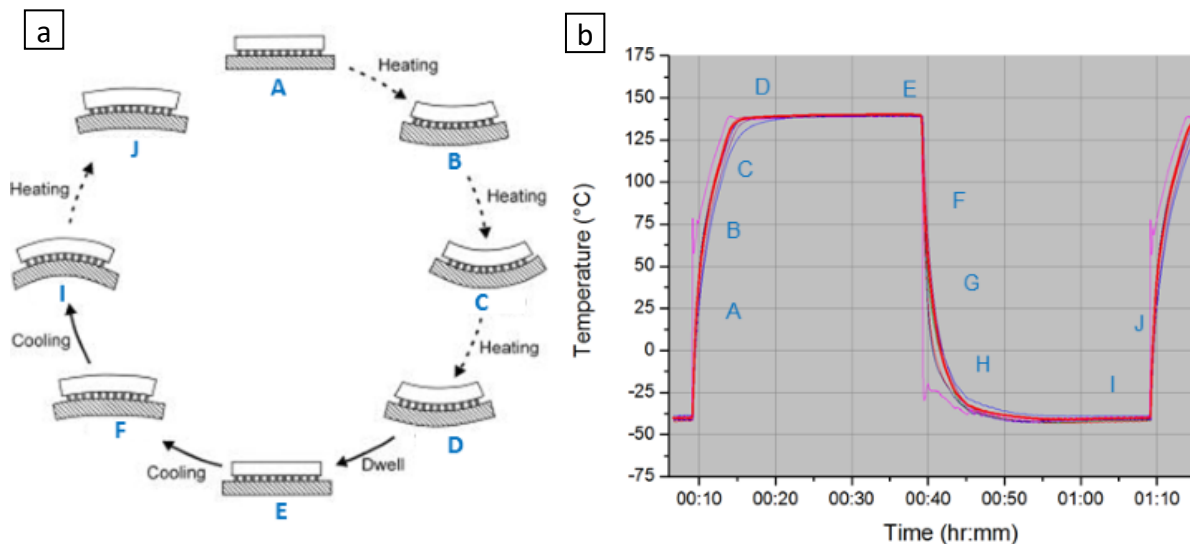


Figure 2-6: (a) Schematics of SMT showing various stages, marked in alphabets, encountered during thermomechanical cycling (b) corresponding stages of a TMC depicting temperature measured from various sample points in a SMT [17]²

TMF also termed as LCF failure, due to the thermal stress has long been a reliability problem. Due to the very large difference in the coefficients of expansion between, for e.g. *Si* ($\alpha_{CTE} = 2.6 \text{ ppm}/^\circ\text{C}$) and the organic FR4 board ($\alpha_{CTE} = 18 \text{ ppm}/^\circ\text{C}$), a very large shear strain develops in the solder joints during the temperature fluctuation. When the solder is in molten state, there is no thermal stress, but upon cooling, when the solder solidifies the thermal mismatch begins to interfere. This creates stages of flexural bending effects on the solder joints, and the solder joints deforms relatively lesser to PCB and components. Each stages of this changing phenomenon are explained in *Figure 2-6*, with the mechanical shrinking of the materials with the temperature ramping and dwelling.

² Source: Continental Automotive GmbH, qualification lab, process with 10s ramp, 30 minutes hold & 10s ramp down

2.1.5.2 High cycle fatigue/vibrational fatigue

For various applications involving vehicles such as automobiles, ships, and aircrafts, vibration induced stresses are still a critical component and may not be ignored. In the context of soldering research vibration loads are often referred to HCF, which is adopted in this study. As mentioned in *section 1.2*, one of the main limitation of component level vibration testing as practised by most soldering researchers is that, it involves the testing of PCB assemblies populated with component in order to determine their reliability under vibratory conditions. The precise conditions experienced by an individual solder joints vary hugely with the type of component and its position on the PCB along with vibration loading imposed on it. Each of these factors will be potentially responsible for a large variation in solder joint performance behaviour.

In general, long-term vibration loadings typically will cause integrated chip (IC) component failure, and will definitely influence the reliability of electronic systems. Root causes of failure has shown that the solder joints are probably the most stressed area and are the major failure locations in components under such dynamic loadings [31]. In BGA components with tens, hundreds, or even thousands of solder balls, a disastrous failure may occur even when only one of these solder joints fails. Assuring the reliability of these solder balls is thus a critical concern especially for electronic devices used in the dynamic environment.

As explained by Barry [8], the response of the components placed on the PCB to vibration depends on their size, stiffness, clamping conditions and critically test frequencies. A background to mechanical vibrations is given elsewhere [32]. In general, natural frequencies of a printed circuit board (PCB) system are those at which the undamped response of the system tends to infinity: that is, the output response (e.g. displacement) is magnified compared to the input. There is one natural, or resonant, peak for every degree of freedom in the PCB system. All PCB or any mechanical systems possess some degree of damping, which broadens and attenuates the resonant frequency peaks but does not appreciably alter their value in most situations with stiff materials, e.g. metals. For a simple, one-degree-of-freedom system such as a mass attached to a spring, the natural frequency, f_0 (in Hz) can be found analytically by an equation of the form:

$$f_0 = \frac{1}{2\pi} \sqrt{\frac{k}{m}}, \quad (2.1)$$

where k represents spring stiffness and m the mass. Natural frequencies of systems with more than two degrees of freedom are complex to determine analytically since they involve finding the eigenvalues of large stiffness matrices, a task more suited to computers.

Local bending stresses on solder joints are affected by the global response of the PCB it is attached to, according to *Eqn. (2.1)*. It is perhaps for reasons such as these that much vibration reliability testing is confined to the laboratories of companies whose electronic products are affected by vibration. Since the variation in stress condition for a given solder joint is higher than for an equivalent joint tested in thermo-mechanical fatigue, the results of such vibration tests are unlikely to be applicable to other PCB assemblies. In recent years, with the spread of electronics into increasing numbers of products and the introduction of *Pb*-free solders into mainstream research, the focus moves towards intrinsic solder material performance under vibratory conditions.

In addition, the vibrations of the solder connections are also often influenced by other factors such as number of joints, size-effects, and the type of solder material. Apart from that, temperature variation may cause large fluctuation in the deformation response of solder joint, bringing large difference in vibration loading [33, 34, 35].

2.1.6 Fatigue theories and models

Reliability of solder joints is not only defined by the tensile and shear properties, but also by the fatigue resistance. In other words, resistance to cyclic or repeating loads like vibration, thermal cycling etc. To investigate the reliability of solder joints facing the cyclic or repetitive conditions, a fundamental understanding of the damage mechanism driven by fatigue loads along with careful fatigue modelling needs to be considered. The procedures to study fatigue life of solder joints have evolved over years to deal with repeated loads in design. They can be studied under four main types [36]:

- The stress-life approach (SN)
- The strain-life approach (EN)
- The fatigue-crack propagation approach (part of a larger design activity that has become known as the damage-tolerant approach)
- The component test model approach.

Depending on the load level, i.e., the amount of plasticity in the solder joints, different methods can be used for fatigue assessment [37]. When there is a high level of plasticity in the solder joints (typically in LCF), strain based methods have proven to be more accurate compared to stress based methods. For lower load levels (for HCF), when there is less plasticity in the stress concentration regions (meniscus of solder joint), stress-based methods are more adequate. When the elastic limit is reached and strains have a significant plastic component the SN approach is no longer appropriate and a strain-based (EN) approach becomes necessary. The SN approach is selected instead of EN approach, as the number of cycle to failure is higher than 10^5 , that is typically encountered in vibration loading of components. In other words, the SN-approach on solder specimen level will be used to model a component test model [37].

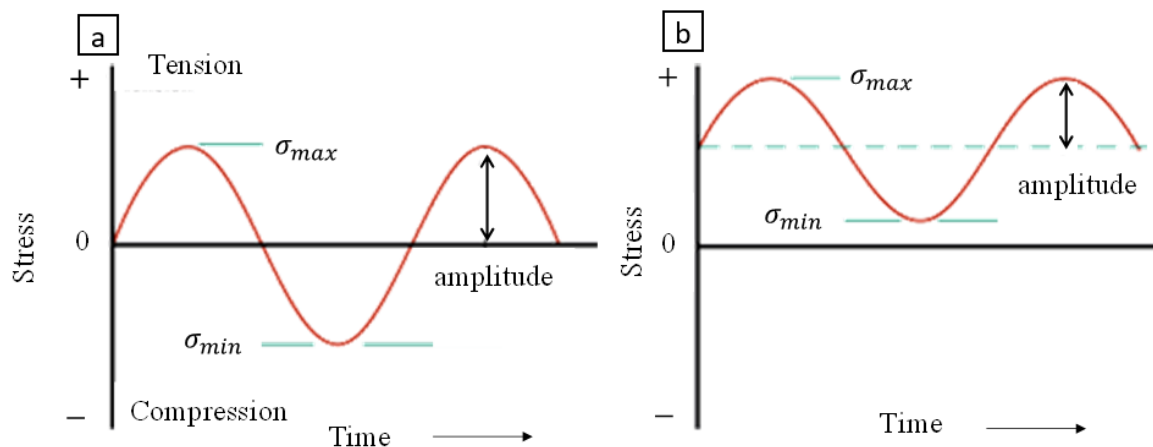


Figure 2-7: Characterizing maximum and minimum cycle with sinusoidal waveform, (a) compression/tension loading (b) tension/tension loading [38]

Figure 2-7, shows different types of loading and the common terminologies used in dynamic cyclic loading. The sinusoidal loading going from a tensile stress to a compressive stress is seen in Figure 2-7-a. For this type of stress cycles, the maximum and minimum stresses are equal. Figure 2-7-b visualises the sinusoidal loading with the minimum and maximum stresses both on the tensile stress regime.

The cyclic load seen in Figure 2-7 can be characterized by the minimum stress σ_{min} and the maximum stress σ_{max} along with mean stress σ_m and stress amplitude σ_a as follows:

$$\sigma_m = \frac{\sigma_{min} + \sigma_{max}}{2}, \quad (2.2)$$

and

$$\sigma_a = \frac{\sigma_{max} - \sigma_{min}}{2}. \quad (2.3)$$

To reach the number of cycles N , a time of $t = N \times T_p$ is needed, where T_p being the time period or the reciprocal of the frequency f_c . The stress ratio- R in parallel to mean stress σ_m can be also used to define the fluctuation of stresses between the tensile and compression regimes, which is quantified using R ratio:

$$R = \frac{\sigma_{min}}{\sigma_{max}}. \quad (2.4)$$

2.1.6.1 Stages of damage evolution in solder

Solder joints are anything but inhomogeneous structure on a microscale level. As investigated by Engelmeier [39] in his classical work on the solder joints reliability, grain structures of solder is inherently unstable. Studying the fatigue phenomenology, how damage initiates, progresses and accumulates it is of great importance to identify the fundamental steps that characterizes the overall process. Various stages of a solder alloy in a HCF study can be classified and investigated as follows:

1. Activation of cyclic hardening/softening process (see *Figure 2-8*, illustrated schematics with stress controlled cycle)
2. Crack initiation – intergranular crack from micro voids (see *Figure 2-10-a*) or transgranular crack initiation by means of PSB with mechanically small crack (see *Figure 2-10-b*)
3. Crack propagation under cyclic load- macro crack (see *Figure 2-10*)
4. Final fracture of the component growth with macro crack (see *Figure 2-10*).

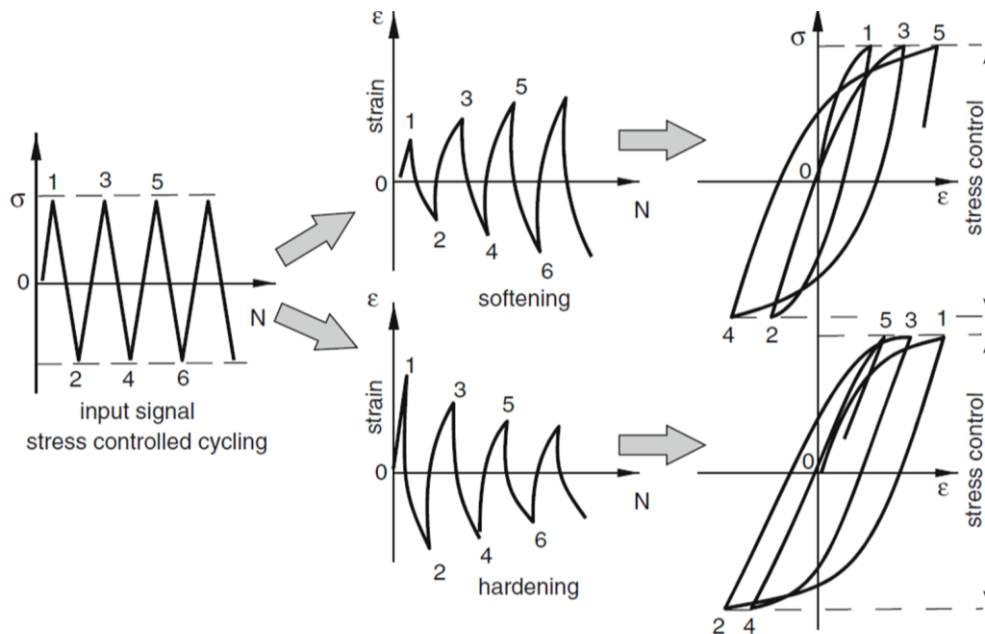


Figure 2-8: Stress controlled cycling resulting in softening and hardening, Millela [40]

The time scale of the above-mentioned four events is shown schematically in *Figure 2-9*. In the low cycle domain (during stress amplitude S_3 , *Figure 2-9*) the first phase of cyclic hardening or softening may end up in some hundreds of cycles ($N_{1,2}$) or even never ends. This is the case where the so-called saturation never occurs. In this case damage starts immediately after the first application of load and phase 2 of damage nucleation and mechanical small cracks (MSC) formation in practice coincides with phase 3 of MSC coalescence into a macro crack [40]. Normally, cyclic hardening occurs only when the stress amplitude exceeds the yield strength of the material.

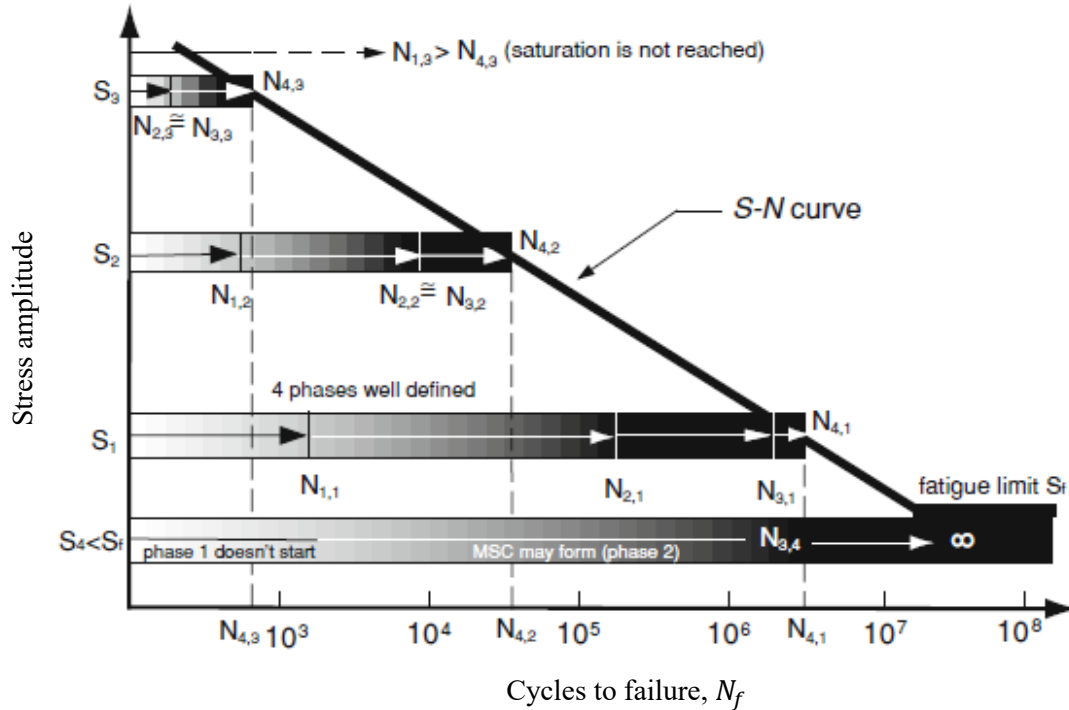


Figure 2-9: Time distribution in terms of cycles $N_{i,j}$ ($i = 1, 2, 3, 4$) of the four fatigue phases: (1) cyclic hardening or softening; (2) slips with mechanical small cracks, MSC formation (3) macro crack formation (4) growth of macro crack to failure, at four selected stress amplitude S_j , Millela [40]

The second stress region S_2 until S_1 as shown in above *Figure 2-9* is very typical to the solder joints undergoing vibration close to the room temperature. Here the material behaves elastically (minimal permanent deformation), at least on a macroscopic scales and the failure occurs under stress concentrations and microstructural changes. In high-cycle fatigue, close to fatigue limit, phase 3 may take even 90 or 95 % of the whole life [40]. This region is called the high cycle fatigue (HCF) region that extends in the range from 10^4 to 10^7 cycles. The specimens in this work will be tested within this range from 10^4 to 10^9 cycles. It will be also interesting to find any confined activities of the cyclic softening or the hardening in this test regime for the Pb-free alloy.

At S_4 , materials exhibit a true fatigue limit, sometimes also referred as endurance limit. In this case, there exist a limiting number of cycles N_E . Theoretically, a specimen that has survived N_E never fails. In many materials, there are no horizontal part of SN-curve [40]. Although the slope of the SN curve becomes smaller beyond certain number of cycles, failure can still occur in a solder joint interconnect as seen in the previous studies [3, 4, 41, 42]. If this is true, whether a SAC387 alloy on HCF testing will exhibit such endurance limit is subjected to investigation in this study.

The crack initiation can be analysed based on understanding the fracture pattern [40]. For the intergranular crack propagation phenomenon, the grain will grow in size over time as the grain

structure reduces the internal energy of a fine-grained structure. Typically, at elevated temperatures or the strain energy enhances this grain growth process during cyclic loading [39]. The schematics explaining the intergranular crack is seen in *Figure 2-10-a*, for a fine-grained microstructure. After reaching $\sim 25\%$ of the fatigue life, micro voids can be found at the grain boundary intersections: these micro-voids grow into micro cracks exceeding $\sim 40\%$ of the fatigue life [39]. Micro cracks in fact grow and coalesce into macro cracks leading to total fracture (see *Figure 2-10-a*).

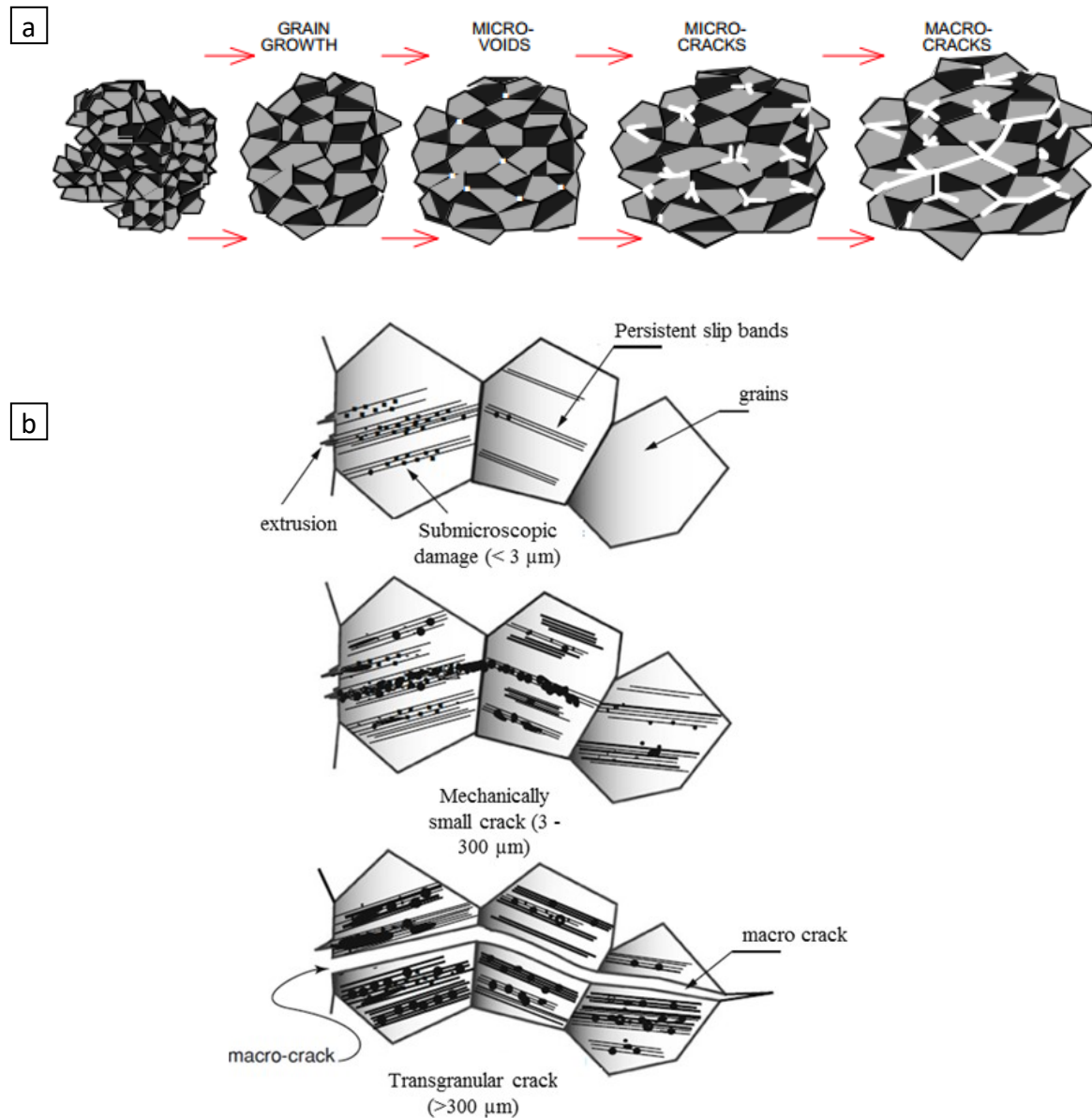


Figure 2-10: Schematics depicting the event progression after crack initiation by means (a) intergranular fracture from the micro voids [39]- for e.g. in fine grain alloys (b) transgranular crack from persistent slip bands (PSB) [40]

For transgranular crack to activate, one of key mechanism that has to be activated is a persistent slip band or PSB (assuming the surface roughness is polished). PSB normally starts on the surface preferably there where there is any kind of discontinuity. They may create an intrusion or extrusion [40], which itself is a discontinuity that favours the progression of slips into persistent bands, where the damage accumulates in the form of pores and micro cracks, *Figure*

2-10-b. Further cycling increases the damage that extends to the adjacent grains and grows to the grain boundaries or called as transgranular failure as seen in *Figure 2-10-b*. Finally, the micro cracks in each single grain coalesce to form the macro crack.

In this work there are two kinds of grains that is discussed, one being the primary grain which is formed during solidification and other one is referred as subgrain that are formed during the deformation. Both type of grains is analysed for the transgranular and intergranular fracture in this study to investigate the different phenomenon. Fracture mechanism for SAC alloy along with possible other mechanism will be investigated under *section 6.5*.

2.1.6.2 Fatigue modelling

For typical fatigue experiments, the number of cycles to failure is measured. If several fatigue experiments are performed and the number of cycles to failure N_f is plotted versus the stress amplitude σ_a or the stress range $\Delta\sigma$, the resulting diagram is called a stress-cycle or SN-diagram or Wöhler diagram. The number of cycles to failure are always plotted logarithmically in the SN-diagram: the stress can be plotted logarithmically or linearly as seen in *Figure 2-9-a*.

In a double logarithmic plot, the stress-cycles to failure (SN curve) of many materials are a straight line for a wide range of the number of cycles. For elastic behaviour (HCF), fatigue load and cycles to failure can be described by the Basquin equation [43, 44]:

$$\sigma_a = \sigma_f * (2N_f)^{-b}, \quad (2.5)$$

where σ_a is the stress amplitude [MPa], σ_f is the fatigue strength coefficient [MPa], N_f is the cycles to failure, and b is the fatigue strength exponent.

Investigating the strain based or stress controlled fatigue life property over LCF or HCF is an important step in establishing an effective fatigue model for SAC solder alloy.

2.1.6.3 FKM guideline

Apart from the stress amplitude on the impact on the fatigue strength, there are other external influential parameters related to metallurgical and physical factors that affect the fatigue resistance of solder. In addition, getting a realistic stress value (damage parameter) for a fatigue life evaluation on a structural part like solder joints is not straightforward and requires an adequate modelling [37].

For a fatigue evaluation/assessment, it is often left to own judgement of engineers or designers, to choose the right material properties [45]. The main questions that arises during the process of fatigue evaluation are,

- What kind of stresses must be used?
- Should the finite element hot spots be ignored?
- To include non-linear material properties?
- How to determine influence factors like surface roughness, stress gradient etc., and safety factor for mean stresses?

To deal with the questions especially on factors influencing fatigue life and with respect to fatigue evaluation on solder joints, a FKM guideline [37] is adapted in this work for the first time in microelectronics field. The German guideline “Fracture Mechanics Proof of Strength for Engineering Components” [37] has been released 2001 as a result of activities sponsored by the Research Committee on Mechanical Engineering (FKM), task group “Component Strength”. The guideline describes basics for the integrity assessment of cracked components subjected to static or cyclic loading and provides a systematic computational procedure, which

is considered in the practice of the current study. The guideline is normally used as a standard calculation procedure for mechanical and civil engineering problems.

Main reasons considering using the FKM guideline in this study are as follows. The guideline makes a double distinction between static and fatigue assessment on one hand, and between use of nominal stress (typically coming from analytical calculation) or local stress (usually given by FEA) on the other hand [37]. Especially in this study for fatigue assessment (in HCF), local stresses are used from linear elastic FEA results which is supported by the FKM guideline. Stress gradient around hot spots is considered and local peak stresses are smoothed out in fatigue calculation. The various possible definitions of the maximum allowable stress (i.e. the safety margin definition) are integrated in the mean stress factor calculation.

Different safety factor levels are set depending on failure criticality upon various factors and this is a key step in assessing the fatigue lifetime of solder joints. Some of the critical factors that influence the lifetime of solder joints in SMT are discussed as follows along with the FKM implications.

a) Surface finish

The surface finish of a solder joint may affect its fatigue life by introducing a notch factor resulting from surface roughness. Its importance to the fatigue life was well documented by Siebel *et al.* and Suhr [46, 47]. In other words, they cover the phenomena, which have an influence on the crack initiation mechanisms. Surface roughness implies that the free surface is no longer perfectly flat. Consequently, small sized notch factor will rapidly fade away from the surface; as it is significant for promoting cyclic slip and crack nucleation at the material surface. Since fatigue cracks generally initiate on the specimen surface, it is well known that the surface roughness of a specimen has a great effect on its fatigue strength [48].

According to FKM guideline, as the tensile strength and the surface roughness value increases, the correction factor also increases proportionally [37]. The roughness correction factor, $K_{R, \sigma}$ can be as written as:

$$K_{R, \sigma} = 1 - A \cdot \log R_z \cdot \log \frac{2\sigma_{uts}}{B}, \quad (2.6)$$

where A & B [MPa] are the solder material constant, R_z is the average roughness of the surface [μm] calculated according to German standard DIN 4768, σ_{uts} is ultimate tensile strength found from static experiments.

b) Specimen or component size

The dimension of the test piece may also affect the fatigue strength of materials. With the exclusion of surface finish, the fatigue failure depends on the metallurgical factors, being oriented either by a slip band mechanism (for e.g. persistent slip bands - PSB) or by inclusions or second-phase particles in the surface grain [40]. Normally there are high probabilities, these PSB are starting at the grain boundaries. With the volume of the materials under the highest stress state (also referred as process volume) increases the probability of finding the worst metallurgical conditions also increases [40]. In HCF, normally the initiation site is confined within a surface layer; therefore, the process volume actually becomes a process surface.

c) Load type

The stress amplitude is decisive in fatigue property of the solder material. As the mean stress increases, the fatigue cycles reach the critical values. Indeed, the literature indicates that the effect of an alternating stress of amplitude may be completely depending on whether or not a mean stress is acting on its amplitude [38, 49, 50]. In this study, three different mean stresses are investigated to the fatigue property of the solder alloy as seen in *Figure 2-11*.

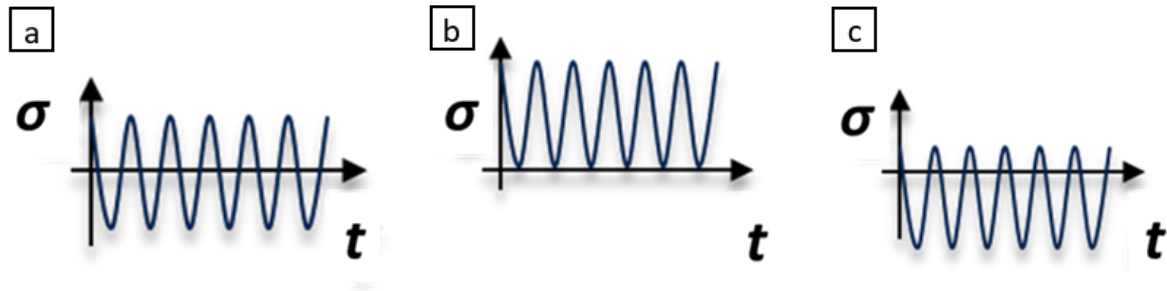


Figure 2-11: Different load types with varying mean stresses (a) fully reversed cycle the mean stress is zero and $R = -1$, (b) fluctuating symmetric load from origin to tension $R = 0$, (c) fluctuating load from tension to compression dominant $R = -3$

The dependence of SN diagrams on mean stress would apparently result in the need to experimentally derive not just one, but an entire family of curves each corresponding to a particular value of the mean stress σ_m . Such an approach is very lasting and expensive therefore not practical, has been excluded trying to take into consideration the mean stress effect by analytical procedures. At the turn of nineteenth century, several models were developed to take care of the mean stress. The most known are those proposed in 1874 by the German researcher Gerber [51], in 1899 by the British Goodman [52], in 1917 by the American Haigh [53] and in 1930 in the United States by Soderberg [54].

In this work, the fatigue strength diagrams after Haigh diagram modified based on FKM guideline is used to analyse the influence of the mean stresses on the fatigue life [44]. In Haigh fatigue strength diagram, stress amplitude σ_a is plotted versus the mean stress σ_m as seen schematically in Figure 2-12. The diagram can be quickly referred to determine the safe cyclic loading. If the coordinate determined from the stress amplitude and the mean stress lies under the curve, the part is expected to survive under dynamic fatigue loading.

The mean stress correction, which is the slope (M) in Figure 2-12 is analysed according to the FKM guidelines [37]. For mean stress ranges ($-1 \leq R < 0$) the mean stress correctivity factor (also called as Morrow factor) is indicated by letter M . Haigh diagram together with FKM guideline could explain better the lower mean stress regimes (M_3) compared to other model and also the model can cover the compressive cyclic regime (M_2). Another reason for the Haigh diagram is chosen over other model is the compatibility in the nCode Designlife™ (fatigue analysis) software, which is followed in this study.

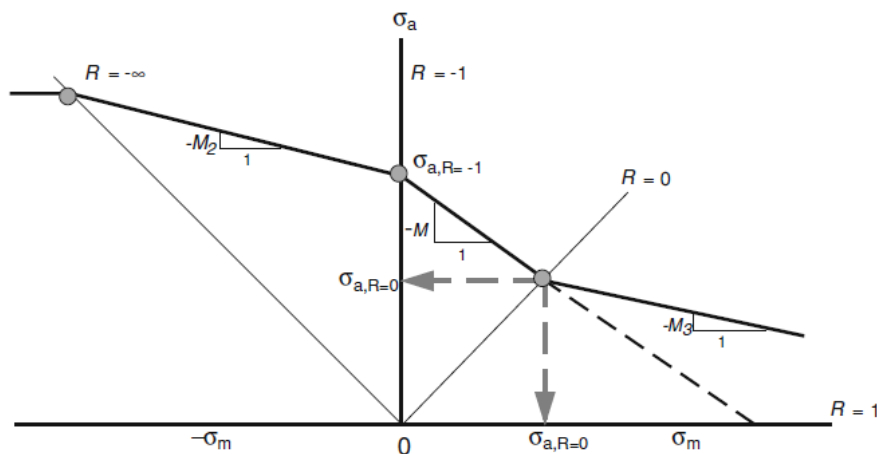


Figure 2-12: Haigh fatigue strength schematics used for mean stress corrections [40]

d) Temperature effects

Material property of solder is also depending highly on the temperature effects. The tensile strength, yield stress, and modulus of elasticity decreases with increasing temperature. Solder joints experiencing temperature fluctuations, bounded between -20°C to $+120^{\circ}\text{C}$, changes from stress to strain-driven solder responses [55]. The effect of temperature on the mechanical property of *Pb*-free solder alloy was observed in literature and is often associated with the microstructural transformations of the material, which may lead to effects such as cyclic softening, subgrain formation, intergranular cracking etc. [56, 57], which are reviewed and investigated in the current work.

e) Notch factor

Many low cycle fatigue and creep–fatigue studies [1, 58] have been reported on *Pb* and *Pb*-free solder alloys to obtain the low cycle fatigue and creep–fatigue characteristics of solders. However, the studies are often on unnotched specimens and did not discuss the notch effect on fatigue and creep–fatigue interaction of solder alloy. A few studies discussed the notch effect on low cycle fatigue lives using notched specimens are [59, 60] and discussed the propagation behaviour of cracks initiated from notch root, whereas the notch effect is actually essential for the quality assurance of the devices.

In a SMT assembly, the bulk of the solder comprising a solder joint must be externally supplied since the combined component and PCB solder volume is not sufficient to form a functionally adequate interconnection. The industry standard SMT's low-melting point interconnects melts during reflow process and collapses to an equilibrium state. This final equilibrium state creates convex solder joint surface shapes on SMT like ceramic capacitor, transformer as shown in *Figure 2-13*, depending upon the solder volume, pad dimension, package weight, and buoyant force provided by surface tension of the molten solder. In the SMT's like ball grid arrays (BGA), the solder ball will form a concave shape, where the neck of the solder ball is the most critical region for crack initiation. These solder balls have bump-like projection shape features enabling them to create local stress concentration regions. It is observed from the vibration experiments on SMT's from Metasch *et al.* [61], Steinberg [3] that the crack initiates from these local notch regions of the solder joints.

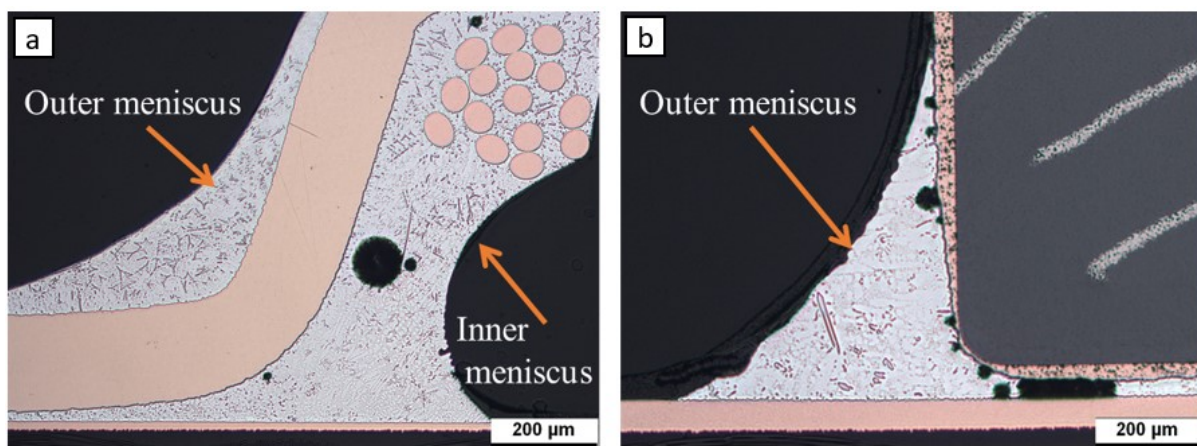


Figure 2-13: Stress concentration surfaces formed from the buoyant force provided by the molten solder surface tension on solder joint– (a) transformer, (b) ceramic capacitor [Source: Continental Automotive GmbH]

The solidification of solder joints leads to two major phenomena: the volumetric distribution of stresses (stress gradients) and so called the size effect, the former being the most important factor. The size effect is not the scope within this work. Literature sources show the influences

of these factors on the fatigue strength by using round and flat specimen with cross sectional areas and notch factors [40, 62].

Solder interconnects do not possess neither a homogenous shape nor a constant notch factor, for which a fatigue evaluation technique is possible to make. Therefore, the stress gradient G_σ effect on SAC alloy should be considered and has to be corrected based on the significant using the correction factor n_σ , for the fatigue evaluation.

The stress gradient is determined from the stresses in an FE analysis. If we define a local coordinate system $x'y'z'$ where z' is an outward surface normal, the stress gradient is denoted as:

$$\frac{\partial \sigma_{vm}}{\partial z'}, \quad (2.7)$$

where σ_{vm} being the Von Mises stress [MPa]. The correction factor for stress gradient n_σ can be formulated based on a range of normalised stress gradient G_σ according to FKM guideline [37].

The stress gradient is normalised with respect to the Von-Mises stress at the surface σ_{vm} , to arrive at the normalised Von-Mises stress gradient as seen in *Eqn. (2.8)*:

$$G_\sigma = \frac{\left(\frac{\partial \sigma_{vm}}{\partial z'}\right)}{\sigma_{vm}}. \quad (2.8)$$

The stress gradient G_σ in [mm^{-1}] from FE is then used to determine a correction factor, n_σ based on the type and ultimate tensile strength of the material as formulated in *Eqn. (2.9)*.

For $G_\sigma \leq 0$ the correction factor is not significant hence, $n_\sigma = 1$ and when the normalised stress gradient becomes significant which is $0 < G_\sigma < 10$ then:

$$n_\sigma = 1 + \sqrt{G_\sigma} \cdot 10^{-\left(a_g + \frac{\sigma_{uts}}{b_g}\right)}, \quad (2.9)$$

where G_σ is the normalised stress gradient [mm^{-1}], a_g [-] and b_g [MPa] are the solder material constants, σ_{uts} [MPa] is the ultimate tensile strength of the material. Material constants a_g [-] and b_g [MPa] can be found from the corresponding correction error between unnotched and notched (more details will be followed in *section 5.1.4*).

2.1.7 Creep theories and models

Creep resistance and thermal fatigue performance of soldered connections are critical reliability concerns for microelectronic and optoelectronic packaging system. As described in *section 1.3* the focus of the current work is to address this issue in the development of mechanistic constitutive model for SAC alloy. Hence, the review section of creep fundamentals is divided into two major sections; first is to introduce the stages of creep thereby understanding the basics of constitutive modelling of creep. Second section gives in the details of deformation mechanism that has to be incorporated for a mechanistic creep modelling.

2.1.7.1 Stages of creep

Creep is the time dependent, plastic deformation of a material. If a metallic component is stressed at elevated temperatures, that is at a homologous temperature T/T_m of at least 0.3 to 0.4, the strain of the component increases with time at constant load, where T_m being the absolute melting temperature in Kelvin scale. Initially the component reacts with a time independent

strain, which consists of an elastic and plastic part. The various stages (primary, secondary, tertiary) following the elastic and plastic part is described below *Figure 2-14*.

Creep test, in the general sense of deformation testing under stress or force controls are a simple but powerful and unique means of studying the work hardening and recovery kinetics of materials. However, insufficient understanding of particle hardening and most importantly, the dislocation processes involved in the dynamic recovery appears to be the limiting factors in modelling creep for SAC alloys [63]. The current work carefully addresses the issue in hand and the detail behaviour of a particle-strengthened alloy as SAC387 (details under *section 2.1.7.2*).

A constitutive model called as Norton power law based on Arrhenius form can express the relationship between steady state creep of materials and the applied stress in the form of [64]:

$$\dot{\epsilon}_s = A\sigma^n \exp\left(-\frac{Q}{RT}\right), \quad (2.10)$$

where $\dot{\epsilon}_s$ is the steady state strain rate [s^{-1}], A is a material constant, σ is the applied stress [MPa], n is the stress exponent, Q is the apparent activation energy [$J \text{ mol}^{-1}$], R is the universal gas constant [$J \text{ mol}^{-1} \text{ K}^{-1}$], T is the absolute temperature [K].

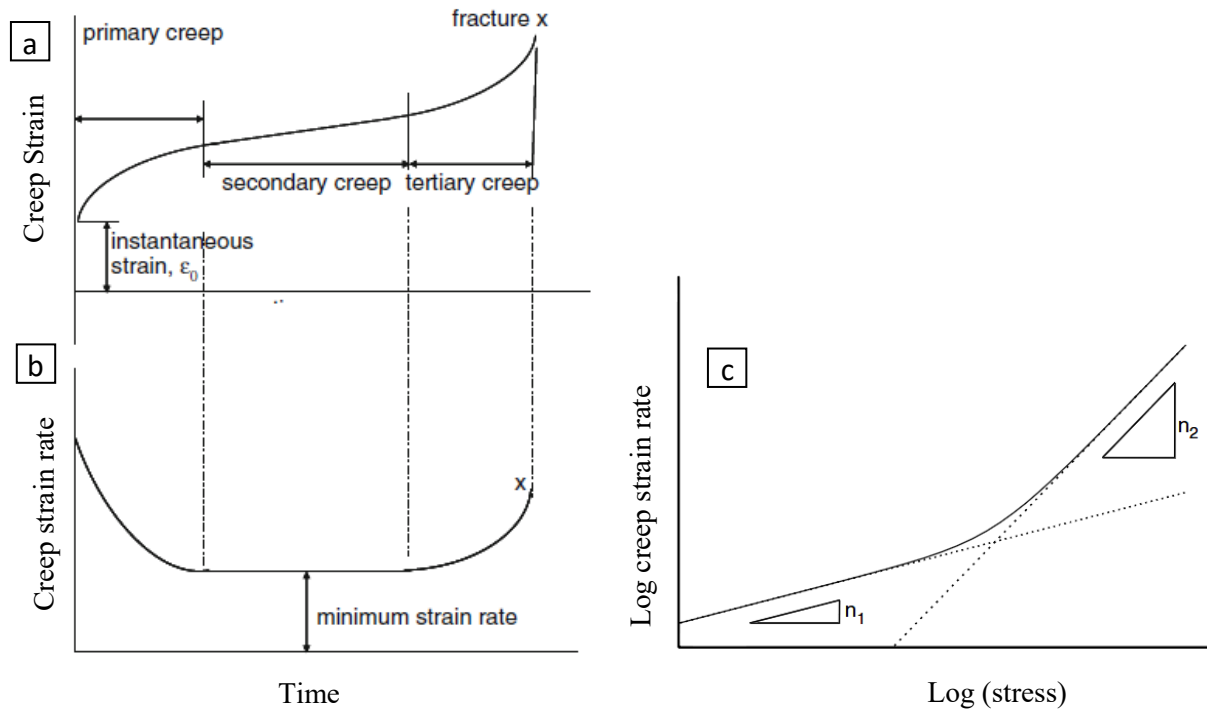


Figure 2-14: (a) Schematics of strain vs. time creep curve showing the typical three stages of creep and an instantaneous elongation on application of load (b) corresponding strain rate vs. time plot, Pelleg [65], (c) creep-rate vs. applied stress- Norton plot, showing change in stress exponents [66]

The activation energy Q is defined as the barrier to be overcome so that an atom might move from a higher energy location to a lower energy location. In crystalline materials, it is found that the activation energy Q is roughly equal to the self-diffusion activation energy of the material. High melting point materials have a large value of binding energy and require higher activation energy to create and move vacancies. The activation energy for creep Q can be formulated for a fixed stress σ as [67]:

$$Q = -R[\partial(\ln\dot{\epsilon}_s)/\partial(1/T)]. \quad (2.11)$$

The stress exponent n or the slope according to Eqn. (2.10) typically increases with the applied stress. In other words, the slope is no longer constant with the changes in the applied stress at higher stress as modelled with double stress exponents in Figure 2-14-c.

Many efforts were made by researchers to formulate the constitutive response of *Pb* solder and *Pb* free solder alloys during creep [1, 68, 69, 70]. Among the proposed constitutive equations, there are two widely accepted models for secondary creep that were compared in the electronics reliability work of Li and Wang [71], and Dudek *et al.* [72]. One is the hyperbolic sine law, which was used by Schubert [73] to represent the high stress region as a power law breakdown. The other double power law was studied extensively by Wiese and Wolter [70], Metasch *et al.* [58], and many others. The models describe the steady state creep of the solder by climb-controlled behaviour at lower stresses and the combined glide/climb behaviour at higher stresses [74]. However, these numerical based models cannot explain the deformation mechanism at different temperatures and stress levels. Most of all, above-mentioned models fail to explain the considerable stress exponents and activation energy value scatters under different studies [75]. These different parameters are the results of differences in microstructure and constraints from the assembly. In addition to it, the result of different microstructure is caused by factors such as cooling, rate, aspect ratio effect, and grain coarsening [76, 77, 78]. These above issues are discussable and concludes that some important physical quantity is missing in the above-mentioned creep semi-empirical models.

2.1.7.2 Creep mechanisms for particle strengthened solder alloy

Most multiphase creep resistant materials acquire excellent strength from hardening by other phases of various shapes, from spheres to lamellae, Blum [79]. Thus, quantification of such a particle hardening is given a primary importance in this thesis.

Microstructural effects in a particle strengthened SAC alloy can be investigated often using the following phenomenon:

- threshold stress for change in creep mechanism
- effect of volume fraction
- subgrain size effects
- coherent particles, semi-coherent, incoherent

Strengthening from coherent particles can occur in a variety of ways that usually involves particle cutting, also sometimes referred as Friedel cutting Kassner [67]. Since the volume fractions of second phase particles are small and the particles are incoherent with the β -Sn, coherent particles will not be in the scope of SAC alloy deformation behaviour. The rest of the phenomenon like threshold stress for change in creep mechanism, effect of volume fraction, and subgrain size effects is reviewed and analysed extensively in this thesis.

a) Threshold stress & Orowan theory

In a complex material system (ternary) such as SAC alloys form, various intermetallic phases contribute significantly to the hardening during secondary stage. Mobile dislocations are arrested or slowed down at these intermetallic precipitates [91]. It is well known that the second phase precipitates (Ag_3Sn and Cu_6Sn_5) provide enhanced strength at wide range of temperatures to the β -Sn matrix [70]. It should be mentioned that the strength by precipitates has been believed to be provided in two somewhat broad categories of strengthening, Friedel cutting or Orowan bypassing. Since Friedel cutting involves coherent particles and is excluded from this study the only other possibility is Orowan bowing or climb. At lower stresses, the dislocations contribute to the deformation by climbing over the precipitates and gliding in the β -Sn matrix as seen in Figure 2-15. With the increasing deformation, there will be more dislocations hin-

dered at inter-metallic precipitates. When the stresses reach the threshold, the dislocations between particle-matrix get enough energy to detach itself from the interface by bypassing the precipitate.

The Orowan bowing stress is approximated by the classical equation [67, 80, 81]:

$$\tau_{OR} = \frac{G \cdot b_v}{L} = \frac{2 \cdot T_d}{b \cdot L}, \quad (2.12)$$

where τ_{OR} is the threshold stress for Orowan bowing mechanism [MPa], G is the shear modulus [MPa], b_v is the magnitude of Burgers vector [mm], L is the average separation of the precipitates [mm], and T_d is the dislocation line tension [N]. This bowing leads to unpinning leaving behind dislocation loops around the precipitates. Separation of precipitates L can be schematically seen in the *Figure 2-15* along with the depiction of the Orowan bowing mechanism. The bowing leads to unpinning leaving behind dislocation loops around the particles.

Concerning the constitutive relationship for creep modelling, the precipitate strengthened alloys can be approximately described by a relationship that includes a threshold stress σ_{th} . The threshold stress can be incorporated into creep model *Eqn. (2.10)* by subtracting it from the applied stress. Hence, the creep strain rate during the steady-state regime can be expressed as [82]:

$$\dot{\epsilon}_s = C \left(\frac{\sigma - \sigma_{th}}{E} \right)^n \exp\left(-\frac{Q}{RT}\right). \quad (2.13)$$

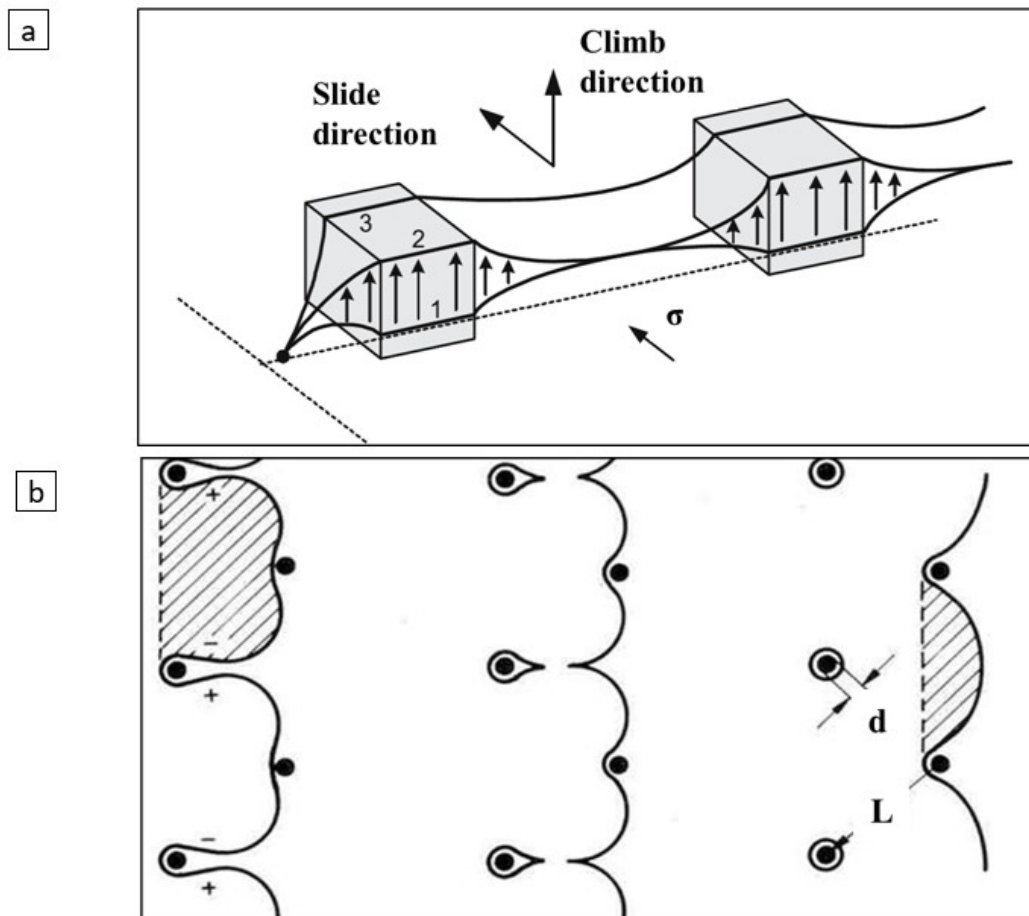


Figure 2-15: Dislocation motion under two-stress regimes (a) low stress region -glide assisted climb (b) high stress region -Orowan bowing mechanism [83]

Kassner [67] proposed that the activation energies should be determined using the usual equation but at constant $\sigma - \sigma_{th}/E$ rather than σ/E used in typical (especially power law for single-phase metals and alloys) creep activation energy calculations. These kinds of creep models gave unrealistic high values of the stress exponent in the high stress regime for SAC alloys [70]. Wiese *et al.* [70] studied the above said constitutional equations using threshold stresses for bulk, PCB, flip chips and found values around 18 for stress exponents (n). These higher values of the stress exponents were potentially from mathematical fits and could not establish proper physical quantities.

During the local climb mechanism, there is a sharp transition from the dislocation segment in the glide plane to surmount the precipitate, which will become unstable, as explained by Bergmann and Langenborg [84]. Therefore, the dislocation line requires a larger segment, which creates a back stress resisting the climb/glide sequence that is proportional to the applied stress. Nevertheless, at higher creep stresses, threshold stress σ_{th} is constant and defined by the stress to operate a particle-cutting mechanism or the Orowan mechanism [80, 84].

Figure 2-16, illustrates the threshold behaviour in low stress and high stress regime for precipitate hardened alloys in comparison. Blum and Reppich [85] also illustrated many of these features and parameters of a precipitate strengthening including the dynamic recovery process, which becomes the limiting factor for creep modelling. An apparent threshold behaviour is evident below the Orowan stress one for incoherent particles, and another for coherent behaviour. Figure 2-16 also visualises the kind of schematic linearity that can be expected only when the matrix β -Sn is present.

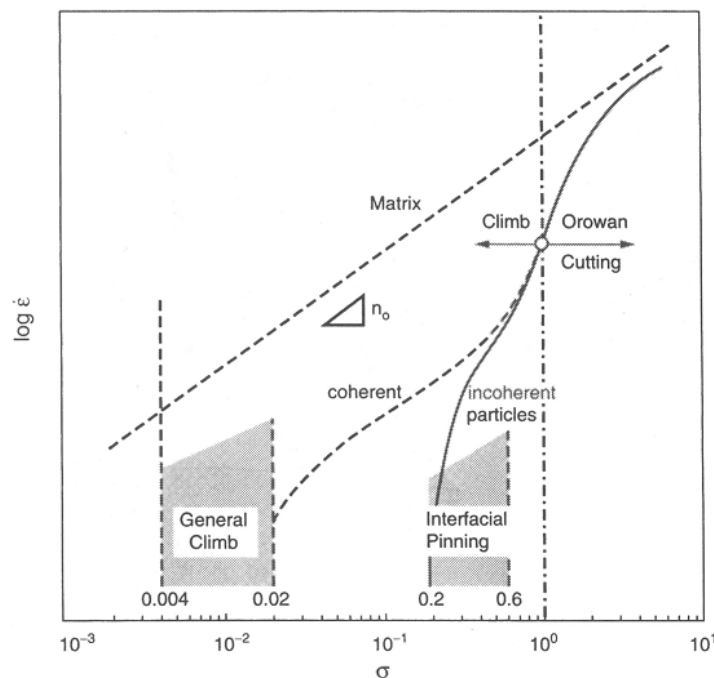


Figure 2-16: Creep behaviour of precipitate strengthened materials and pure matrix materials (only schematics), Kassner [67]

Apart from the lot of discrepancies between experimental data and theoretical models of above-mentioned studies, there are still major difficulties to detect the break between the high stress and low stress region. Kerr and Chawla, [80] worked with $Sn3.5-Ag$ alloys, concluded evidence of dislocation-particle interaction from the preliminary transmission electron microscopy (TEM) investigation. This also supports the Orowan bowing mechanisms encouraged for SAC alloys.

b) Effect of volume fraction

Miniaturized solder joints in microelectronics with a higher standoff height contains a large volume fraction of second phase-hardened particles. Higher volume fraction of particles results in a more dominant mechanical role, which is not very well known. As expected higher volume fractions for identical particle sizes, are associated with greater strengthening and threshold behaviour [86]. Peterseim *et al.* [87] have also suggested that the volume fraction of the second-phase particles can affect the value of the threshold stress.

The volume fraction can be calculated by $f = N_p/N_v$, where N_p is the volume of individual precipitates and N_v is the number of precipitates for one unit volume. For SAC alloys f can be calculated according to Agamennone *et al.*, assuming spherical precipitates as follows [63]:

$$f = \frac{\pi \frac{d^3}{6}}{N_v}, \quad (2.14)$$

where d is the average size [μm] of the second phase spherical intermetallic from the eutectic region.

c) Effects of subgrains

On the commencement of plastic deformation, the dislocation density increases, eventual leading to the formation of “subgrain” walls. This misorientation is defined as the minimum rotation required to bring two lattice separated by a boundary [67]. The individual grains are filled with subgrains along the β -Sn matrix during the primary hardening of creep stage as visualised in Figure 2-17. The individual grains in this study is referred as primary grains or termed also as general grains.

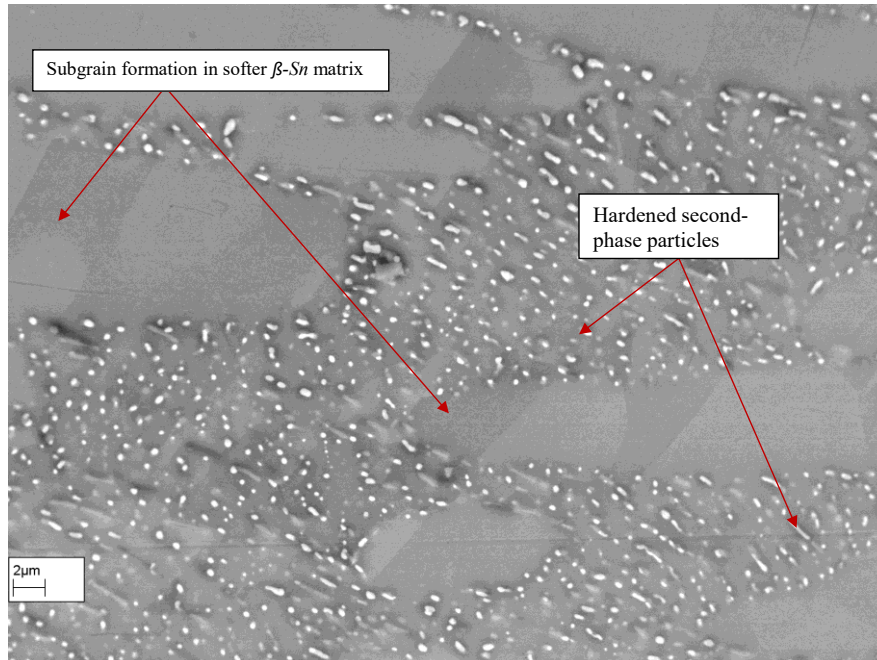


Figure 2-17: Subgrain detected from SEM, revealing subgrain formation along the β -Sn matrix in SAC 387 alloy

Subgrains are low-energy configurations of the dislocations generated from creep plasticity often arising from the primary stage [67]. At higher temperature this subgrain formation can be visualised more easily because of the higher misorientation angle, however at low temperatures this angle may fall down as low as 1° [67].

Once formed, subgrain boundaries reacts with the intruding dislocations. They act as sinks, collecting dislocations in the form of geometrically necessary ones and quickly annihilating dislocation of opposite sign, but they also act as obstacles as is evident from the decrease in the creep rate. Blum [79] explains the migration of boundaries under stress enables boundary recombination and annihilation necessary to keep the sub-grain structure equiaxed with a steady boundary spacing and thus completes recovery.

Phenomenologically, there is an approximate relationship between the subgrain size and the steady state flow stress:

$$\frac{\sigma}{E} = C_3 * (\lambda_{ss})^{-p} \quad (2.15)$$

where λ_{ss} is the intercept of subgrain structure [μm], σ/E the normalised stress [-], C_3 is the material constant [μm] and the exponent of p in literature found to be between 0.35 to 1 [67]. Analogous to this equation, there is a linear relationship between the density of dislocation ρ and the steady state stress with the value of p around 0.5 [67], which shows the indirect dependence of the subgrains with that of the dislocation density. The dislocations form a subgrain structure with subgrain boundaries, consisting predominantly of dislocation networks constituting low-angle grain boundaries, and free dislocations arranged in the subgrain interior. Each of the hardening contributions is necessary to reach the highest possible creep resistance. In another words, subgrains plays a key role in determining the creep resistance of the materials. At elevated temperatures neither the dislocation structure nor the precipitate structure are stable.

The subgrain formation translated to a SMT solder joint during TMC can be explained by two basic steps [88]: The first step is that a solder joint forms as general grains (also referred as primary grains) as seen in *Figure 2-18-a* just after the reflow process or solidification. However, upon thermal fatigue (TMC), a number of subgrains can be formed during the initial stages (see in *section 2.1.7.1*). The subgrain investigated in this work tends to grow near the strain concentrated regions as seen in *Figure 2-18-b*. In SMT solder joints; this can grow closer to the convex shape of solder joints as seen in *Figure 2-18-b*. On further thermal cycling (TMC) subgrain evolution process continues to micro cracks at and along the subgrain concentrated regions.

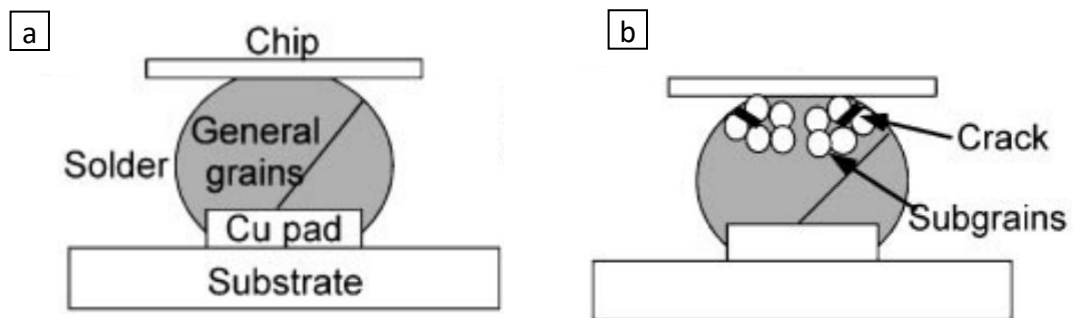


Figure 2-18: Schematic illustration to explain the subgrain and intergranular-crack behaviour in a SMT solder joint [88]

2.1.7.3 Creep damage models

Creep rupture behaviour under isothermal condition of *Sn-Ag-Cu* alloys is investigated in the thesis as an additional content together with the constitutive creep models. Methods of analysing creep rupture data emerged several decades ago [89]. One important purpose of the method is to extrapolate data, which have been collected in short-term experiments and at low temperatures, and thereby to estimate long term and high temperature properties which are difficult to

obtain for reasons of economics and experimental challenges. Since most available methods are empirical rather than based on physical principles, their usefulness is rather limited and should be checked for individual alloy systems. In this work, three methods of parametrization were considered to analyse the creep rupture of eutectic SAC alloys to determine their applicability in *Pb*-free solder alloys.

A basic verification of parametric approach to understand the relationship between creep rupture life with respect to the constant applied stresses is to make a straight isothermal relation (that is at different temperatures). This model is widely known as the Manson-Brown model [90].

In parametric approaches of analysing creep rupture life, Larson-Miller method [91], is often adopted because of its good agreement with experimental data, especially low temperatures. For SAC alloy Zhang *et al.* [92], showed a higher standard deviation from the scatter values for the high temperature experiments. Thus further well-established creep damage models like Manson and Haferd [93] and Monkman-Grant [94] are investigated.

Manson and Haferd [93], proposed creep damage model with a correlation parameter- P_{MH} as:

$$P_{MH} = \frac{(T - T_a)}{(\log t_R - \log t_a)}, \quad (2.16)$$

where P_{MH} is the Manson-Haferd parameter, T is the temperature [K], t_R is the time to rupture [h] and the subscript 'a' means the intercept points as visualised in *Figure 2-19*. In a plot of logarithmic rupture time (t_R) against the reciprocal of temperature ($1/T$), lines of constant stresses converged; meeting at a common point with coordinates $1/T_a$ and $\log(t_a)$. After fitting experimental data, normalised coordinate [183.6, 8.39] is chosen as common intersection point according to Manson and Haferd method [95, 96].

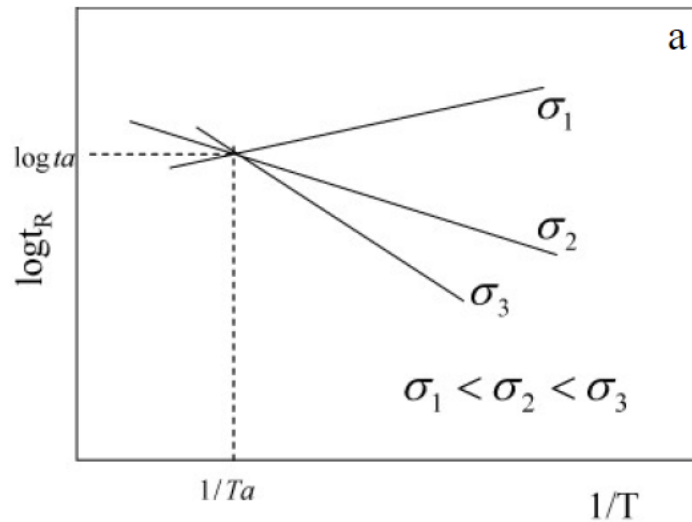


Figure 2-19: Schematic diagram of Manson-Haferd parameter

An alternative approach that is investigated in the current work is Monkman-Grant relationship [97], proposed 50 years back using the kinetics of deformation as seen in *Eqn. (2.17)*, that relates the time to failure t_f to the minimum (secondary) creep rate $\dot{\epsilon}_s$:

$$t_f \cdot \dot{\epsilon}_s^m = C. \quad (2.17)$$

t_f is the time to failure [h], $\dot{\epsilon}_s$ is the minimum creep rate [s^{-1}], m and C are the constants depending on the material investigated.

2.1.7.4 Implementation of creep models to FE problems

In the current work, the developed creep law is implemented to FE problems and this section introduces some of the background behind the implementation.

Introducing the creep law into the engineering problems, require the formulation and the solution of an initial-boundary value problem including the balance equation and the constitutive assumptions. The modelling of creep under multi-axial stress states is the key step in the adequate prediction of the long-term structural behaviour. Such a modelling requires the introduction of tensors of stress, strain, strain rate, and corresponding inelastic parts. In engineering mechanics, these concepts are often introduced based on intuitive assumptions, available experimental data, and applications. Some important assumptions being, the assumption of infinitesimal strains allows to neglect the difference between the true stresses and strains with the engineering stresses and strains. The linearized equations of the creep continuum mechanics can be used in the majority of the electronic applications because electronic components and materials are usually designed such that the displacement and strains arising because of the applied loading do not exceed the prescribed small values [98, 13].

In this study, the moment stress tensor and the anti-symmetric part of the stress tensor are not considered in the creep theory (*section 2.1.6.1*). The reason for this is the higher order complexity of the models and as a consequences increased effort for the identification of the material characteristics [13]. Finally, the assumption of the isothermal conditions makes it possible to decouple the thermal and the mechanical problem. Heat transfer problem are not considered. As we saw in the fundamental introduction *chapter 2.1.7*, the influence of the constant temperature is described by the Arrhenius function, which is incorporated already in the proposed new creep model.

The starting point for the implementation is the introduction of the inelastic strain, the creep potential, the flow rule, the equivalent stress and internal state variables [99]. We discuss here the secondary creep constitutive model along with the creep potential and flow rule for implementing the equation in FE analysis.

The programming of a creep law within the given framework deals with a scalar equation of the type, time hardening or strain hardening respectively as follows [99]:

$$\dot{\bar{\epsilon}} = f(\bar{\sigma}, t, T) \quad (2.18)$$

$$\dot{\bar{\epsilon}} = f(\bar{\sigma}, \bar{\epsilon}_{cr}, T) \quad (2.19)$$

where $\dot{\bar{\epsilon}}$ being the equivalent strain rate (1/s), $\bar{\epsilon}_{cr}$ is the equivalent creep strain, t is the creep time, T is the temperature [K], $\bar{\sigma}$ is the equivalent stress [MPa]. Equivalent stresses, $\bar{\sigma}$ as well as strains, $\bar{\epsilon}$ are used in conjunction with the von Mises yield surface, to define the von Mises equivalent stress as well as the incremental work per unit volume.

In the following implementation, we assume the creep law of the time hardening type according to *Eqn. (2.18)*. Principally, three steps have to be done to implement the new creep law on to FE software (ANSYS):

1. creep potential theory and assumptions
2. calculate the actual stresses at the time step $t + \Delta t$ with the given values at time t
3. calculate the algorithmic tangent modulus

Step 1, that is the basic of creep potential theory for subroutine development is covered in ANSYS™ documentation [99] and step 3, is calculated online during a typical numerical simulation. Therefore, only focus here in this content will be on the arrival of actual stresses for each integration point during time incremental Δt .

Using a creep potential, the creep strain rate can be derived by the derivate of the potential with respect to the stresses and finally taking the eukldean norm on both side, also applying the Newton-Raphson algorithm a final equation for stress calculation is designed. Only the final form of the equation is defined here, take from ANSYS documentation [99]³:

$$\gamma_{\bar{\sigma}(t+\Delta t_{\bar{\sigma}})} = \frac{\partial \gamma}{\partial \bar{\sigma}_{t+\Delta t}} = \frac{3}{2} \left[-\frac{\dot{\bar{\epsilon}}_{cr}}{\bar{\sigma}^2} + \frac{1}{\bar{\sigma}} \frac{\partial \dot{\bar{\epsilon}}_{cr}}{\partial \bar{\sigma}} \right], \quad (2.20)$$

where $\gamma_{\bar{\sigma}(t+\Delta t_{\bar{\sigma}})}$ is the proportionality factor for creep implementation at time $t + \Delta t$, $\dot{\bar{\epsilon}}_{cr}$ being the equivalent creep strain rate (1/s), $\bar{\sigma}$ is the equivalent stress. Unknown terms in Eqn. (2.20) are $\dot{\bar{\epsilon}}_{cr}$ and $\frac{\partial \dot{\bar{\epsilon}}_{cr}}{\partial \bar{\sigma}}$ that will be used from the new creep equation later in chapter 4.3.

2.2 STATE OF THE ART

2.2.1 Phenomenological vs. mechanistic creep models

Different phenomenological and mechanistic creep models are being investigated in the literature to capture the constitutive response of SAC solder alloys.

As introduced in section 2.1.7.1, two widely accepted and practical phenomenological models for eutectic *SnAgCu* alloys are Garafalo hyperbolic sinh formulation, Eqn. (2.21) and power law formulation [1, 69, 100, 101, 102], Eqn. (2.22). Both models describes the transition from high stress regime n_2 to low stress regime n_1 .

$$\dot{\epsilon}_s = A \sinh \left(\frac{\sigma}{\sigma_0} \right)^n \exp \left(-\frac{Q}{RT} \right) \quad (2.21)$$

$\dot{\epsilon}_s$ is the secondary creep rate [s^{-1}], A is the material constant [s^{-1}], σ is the applied stress [MPa], σ_0 prescribes the stress level at which the power law dependence breaks down, [MPa], n is the stress exponent [-], Q is the activation energy [J/mol], R is the universal gas constant [J/mol. K] and T is the absolute temperature [K].

$$\dot{\epsilon}_s = A_1 \left(\frac{\sigma}{\sigma_{n_1}} \right)^{n_1} \exp \left(-\frac{Q_1}{RT} \right) + A_2 \left(\frac{\sigma}{\sigma_{n_2}} \right)^{n_2} \exp \left(-\frac{Q_2}{RT} \right) \quad (2.22)$$

A_1, A_2 being the material constants [s^{-1}], Q_1, Q_2 are the activation energy for low and high stress regimes [J/mol], σ is the applied stress [MPa], σ_n prescribes the stress level for the creep mechanism, [MPa], n_1 and n_2 depicts the stress exponents for higher and lower stress regime (schematics in Figure 2-14-c). Generally, the subscript '1' in Eqn. (2.22) denotes the parameters for the creep behaviour at low stresses while the subscript '2' denotes the parameters for creep behaviour at high stresses.

Schubert *et al.* and Darveaux *et al.* [103, 104], extensively studied both phenomenological models in Eqn. (2.21) and (2.22) over past decades in the field of microelectronics reliability. It should be noted that these models are semi-empirical and understanding or introducing a physical meaning behind the equations, are still a challenge faced in the field of solder joint reliability prediction.

Although the creep behaviour of *Sn–Ag–Cu* based solders has been the subject of many recent studies, the impact of *Ag* and *Cu* content, and associated microstructural changes on the creep response of near-eutectic *Sn–Ag–Cu* ternary alloys has received relatively less attention. *Ag*

³ For complete derivation and further details in arriving at the final equation, kindly refer to ANSYS documentations [Source: CADFEM, GmbH, Germany]

and *Cu* related precipitates can have a huge effect on the creep behaviour of *Sn*-based *Pb*-free solder alloys due to the changing volume fraction of the eutectic phase and β -*Sn* dendrite with increasing alloy content in β -*Sn* matrix. In general, the steady-state creep rate decreases with increasing *Ag* content, and in particular with the increasing volume fraction of Ag_3Sn and Cu_6Sn_5 precipitates. The rate-limiting creep mechanism in solder alloys investigated was dislocation climb because of dislocation motion impediment from precipitates [11].

With phenomenological models as formulated in *Eqns. (2.21) and (2.22)*, significant scatter in creep constitutive properties of *Pb*-free solder joints discussed is observed depending on the size of the test specimens (polycrystalline bulk versus multi-crystalline joint size), specimen fabrication process, reflow profile for the solder, cooling rate during solidification, and different testing methods [11]. Even though the above factors are accurately controlled by a single investigator, significant piece-to piece scatter in constitutive properties is evident when testing small test specimens that are of the same length scale as functional solder joints [76]. This scale effect is attributed to the fact that there are only a few large highly anisotropic β -*Sn* grains in such joints [105], thus making every joint unique in terms of microstructure and the resulting mechanical response.

Alternatively, mechanistic or physical models used to capture the creep constitutive response of SAC solder available in literature are discussed here. In order to obtain insights into the physics of deformation induced by each of these microstructural features, mechanistic multiscale modelling framework that captures the dominant creep mechanisms in terms of key microstructural features is needed.

Dutta *et al.* [106] suggested that the creep response of *Sn–Ag* solders is controlled by the behaviour of the eutectic structure, which consists of Ag_3Sn IMC particles embedded in a β -*Sn* matrix. The total creep rate of *Sn–3.5Ag* solder is written as the sum of two simultaneous mechanisms: glide–climb mechanism (where either viscous glide or climb is the rate-controlling mechanism) and particle-limited climb mechanism. The authors proposed that glide–climb mechanism dominates the observed creep behaviour at low stresses, whereas the particle were limited to climb mechanism dominating at high stresses. The total creep rate $\dot{\epsilon}_T$ of *Sn–3.5Ag* solder may be written as the sum of two mechanisms, which occur simultaneously (i.e. in parallel with each other) [106]:

$$\dot{\epsilon}_T = \dot{\epsilon}_{gc} + \dot{\epsilon}_{pc}, \quad (2.23)$$

where $\dot{\epsilon}_{gc}$ is the strain rate due to glide-climb mechanism, where either viscous glide or climb is rate controlling, and $\dot{\epsilon}_{pc}$ is the strain rate due to particle-limited climb. The rate due to glide-climb is written as:

$$\dot{\epsilon}_{gc} = \frac{\dot{\epsilon}_g \dot{\epsilon}_c}{\dot{\epsilon}_g + \dot{\epsilon}_c}, \quad (2.24)$$

where $\dot{\epsilon}_g$ and $\dot{\epsilon}_c$ are the rates of the viscous and climb process respectively.

In addition to dislocations that cause deformation by the glide-climb process, which is passing through the β -*Sn* matrix regions between particles, many dislocations are also stuck at the Ag_3Sn particles. Because of the attractive nature of the interfaces, these dislocations are unable to participate in deformation of the β -*Sn* matrix via climb over particles at stresses lower than the detachment threshold. Nevertheless, once the Von–Mises equivalent stresses exceeds the threshold stress for dislocation detachment from particle–matrix interfaces (σ_{th}), the previously stuck dislocations lead to a parallel deformation mechanism, particle-limited climb with a strain rate of $\dot{\epsilon}_{pc}$, given by:

$$\dot{\varepsilon}_{pc} = A_{pc} \left(\frac{Gb}{kT} \right) \left(\frac{\sigma - \sigma_{th}}{G} \right) \exp \left(- \frac{Q_{Sn,Pipe}}{RT} \right), \quad (2.25)$$

where $Q_{Sn,Pipe} \approx 65$ kJ/mole is the activation energy for pipe diffusion in β -Sn, and the threshold stress σ_{th} is about $3 \times 10^{-4} G^5$ [11]. With increasing effective stress ($\sigma - \sigma_{th}$), the rate of this mechanism increases rapidly, ultimately exceeding the rate of creep via glide-climb.

Gong *et al.* [107] utilized the above micro scale dislocation climb models to capture the creep response of Sn–3.5Ag solder by considering the dispersion strengthening from nanoscale Ag_3Sn IMCs. To describe the microstructure of the Sn–Ag eutectic phase, three state variables are used by Gong *et al.* [107]: the volume fraction of Ag_3Sn particles, their diameter and inter-particle spacing.

Gong *et al.* [107] explained that the Orowan bowing process generally drives the effect of dispersion particles on the time-independent deformation of alloys. In this mechanism, the dislocation line cannot cut through a particle, but bows between particles under deformation. So an additional stress is required to overcome the energy increase arising from elongation of the dislocation line. This additional stress is the well-known Orowan stress, as discussed in *section 2.1.7.1*:

$$\sigma_{OR} = \frac{0.84MGb}{\lambda - 2r}, \quad (2.26)$$

where M is the Taylor factor [-], G is the temperature dependent shear modulus [MPa], b is the Burgers vector [μm], λ is the interparticle spacing [μm] and r is the median radius of precipitates [μm]. The model assumes that the behaviour is dictated only by the dispersion strengthening of nanoscale Ag_3Sn IMCs in the Sn–Ag eutectics. Only the eutectic Sn–Ag region is modelled, without any load sharing between Sn dendrites and Sn–Ag eutectics. This work of Gong *et al.* [107] is extensively referred in the current study to describe the microstructure of the Sn–Ag eutectic phase.

In another study, Chawla and Sidhu [108] reviewed the literature on analytical and numerical techniques available, to model the heterogeneous microstructure of multiphase solder materials. Models presented in their review in 2007, mostly simplifies the heterogeneous microstructure of multiphase solder materials. They addressed the critical link between microstructure and deformation behaviour, by using two-dimensional (2D) and three-dimensional (3D) virtual microstructures as the basis for a robust model to simulate damage caused by deformation. Their model was unable to capture all the dominant physical mechanisms during the deformation process because homogenized properties were considered for different phases in the solder during finite element analysis. These simplifications definitely make modelling and analysis more efficient and straightforward, but fail to predict the effective properties and local damage behaviour, which are dependent on the detailed microstructure of SAC, solder.

Cuddalorepatta and Dasgupta [105] proposed an isotropic mechanistic secondary creep model based on Rosler and Artz's dislocation detachment model [109] for SAC solders. The model captured the two lowest length scales in SAC solders: the smallest length scale modelled was that of nanoscale IMC via analytical dislocation creep models, and the next length scale was that of the micron-scale β -Sn dendritic colonies, via isotropic micromechanics homogenization theory. Since secondary creep measurements shows much sensitivity than the coarsening rained anisotropic β -Sn microstructure in the Sn3.0Ag0.5Cu specimens, geometric modelling of the β -Sn grains and grain boundaries was not necessary. Furthermore, isotropic modelling was considered adequate when developing analytical formulation of the secondary creep deformation at the two lowest length scales.

According to Cuddalorepatta and Dasgupta [105], the eutectic $Sn-Ag$ creep rate $\dot{\epsilon}_{eut-SnAg}$ is a combination of the $\beta-Sn$ matrix creep rate $\dot{\epsilon}_{mat}$ and the Ag_3Sn IMC dispersion-hardening shear creep rate, $\dot{\epsilon}_{disp-IMC}$ as given by Eqn. (2.27). The net shear creep rate of eutectic $Sn-Ag$ region $\dot{\epsilon}_{eut-SnAg}$ can be derived from the assumption that the time taken by a dislocation to traverse through a unit cell of the $Sn-Ag$ eutectic composite is the sum of the time it takes to travel over the $\beta-Sn$ matrix phase and the time to travel over the IMC phase:

$$\frac{1}{\dot{\epsilon}_{eut-SnAg}} = \frac{1}{\dot{\epsilon}_{mat}} + \frac{1}{\dot{\epsilon}_{disp-IMC}}, \quad (2.27)$$

where $\dot{\epsilon}_{disp-IMC}$ is given by:

$$\frac{\dot{\epsilon}_{disp-IMC}}{\dot{\epsilon}_0} = \exp\left(\frac{-G_{det}b^2r \left[(1-k) \left(1 - \frac{\sigma}{\sigma_d}\right)\right]^{3/2}}{kT}\right). \quad (2.28)$$

$\dot{\epsilon}_0$ is the reference strain rate, G_{det} is the shear modulus of tin and σ_d is the athermal detachment stress, found according to [105], r is the average radius of the nanometer dimension Ag_3Sn dispersoids, k is Boltzman's constant, T is the absolute temperature. σ_d , the athermal detachment stress refers to the stress required in the absence of thermal energy for the dislocation to overcome the obstacle in the post-climb regime and detach itself. Moreover, the creep of $\beta-Sn$ matrix is given by:

$$\dot{\epsilon}_{mat} = A_L \left(\frac{\sigma}{G_{Sn}(T)}\right)^{n_L} \exp\left(-\frac{Q_L}{RT}\right) + A_H(\sigma)^{n_H} \exp\left(-\frac{Q_H}{RT}\right), \quad (2.29)$$

where G_{Sn} is the shear modulus of tin, Q_H and Q_L refers to the activations energy at high and low stresses, n_H and n_L refers to the stress exponents at high and low stresses. This equation is similar to a two-term power-law secondary creep equation for Sn in tensile stress components. One of the shortcomings of Cuddalorepatta and Dasgupta [105] are the mechanistic prediction of steady-state creep properties of SAC solder as a function of Ag content and isothermal aging. Above-mentioned studies involving mechanistic modelling to capture the physics of the underlying viscoplastic creep mechanisms of SAC solder are very limited in the literature. Furthermore, studies that provide the influence of the Sn dendrites, micron-scale IMCs, and the eutectic $Sn-Ag$ region (Lower length scales) on the creep behaviour are required. This thesis thrives to provide more insight to the research gap in mechanistic modelling of SAC alloys.

2.2.2 Low cycle fatigue/thermo- mechanical fatigue

As seen in section 2.1.5.1, observing solder joint failures in field environments are not practical due to extensive amount of testing time it would take to reach effective failures. Instead, accelerated thermo-mechanical cycling (TMC) testing is state of the art technique in industries, which is performed on a component level at an accelerated rate and temperature extremes. Even though this is a common practise in industries, the danger of accelerated TMC tests is that a new or different failure mechanism unlike experienced in the real field could be introduced due to faster ramp rates and higher temperature extremes [110].

Thermal mismatch deformations in the package arise due to differences in the coefficient of thermal expansion (CTE) among the assembly materials, generating high solder joint stresses and strains. Because thermal cycling test is time-consuming and costly, finite element analysis (FEA) modelling is widely used methodology in the electronic packaging industry for modelling the physics of failure in solder joints subjected to thermal cycling test conditions. Stress-based, plastic/creep-based, energy-based, and damage accumulation-based methods have been used to model fatigue life [111]. In addition, the Darveaux method [104], which applies both

energy and damage accumulation-based theories, is a common approach used in fatigue modelling. In Darveaux method, the overall time to the failure time is obtained from crack initiation and fatigue life.

Early solder joint fatigue models were developed based on experimental thermal cycling tests. Most models that address fatigue require stress-strain data in order to predict service life. Early fatigue data was collected experimentally using strain gauges. However, with the decreasing size of the solder joints, experimental collection of stress-strain data is becoming increasingly difficult, and Finite Element Analysis (FEA) is becoming the more practical route for obtaining stress-strain relationships. Rapid thermal cycling of actual parts is still necessary for verifying the life predictions.

The most basic numerical model (FEA) is two-dimensional (2D), use linear elastic material properties and have a low computational time Pang *et al.* [41]. However, they are the most prone to be inaccuracy. The best models in literature, Syed [112], Pang [113] are 3D quarter models, include plasticity, and creep material properties, which may use a sub-modelling or sub-structuring approach for computational efficiency. Other well-documented models are the 3D strips or generalized plane deformation (GPD), which is a compromise between 2D and 3D. Irrespective of the type of modelling, the solder material property engaged still plays a vital role in determining the performance and deformation prediction of solder joint.

The state of the art is to choose a constitutive equation that is implemented within a FEA code. The constitutive relation describes the various factors involved and acts as the starting point in solder joint fatigue. The most frequently used constitutive relation is:

$$\dot{\varepsilon} = \dot{\varepsilon}_e + \dot{\varepsilon}_p + \dot{\varepsilon}_c. \quad (2.30)$$

where $\dot{\varepsilon}$ is the total shear strain, $\dot{\varepsilon}_e$ is the elastic shear strain component, $\dot{\varepsilon}_p$ is the plastic strain component, and $\dot{\varepsilon}_c$ is the creep strain component. Separating each of the components in actual life testing can be difficult and often leads to inconsistencies in the results. Recent research efforts have focused on constructing unified constitutive models and damage evolution for solder joint fatigue life prediction. A complete discussion of constitutive equations is beyond the scope of this paper, and the reader is encouraged to seek other sources for detail [114, 115, 116].

Assumptions need to be made in order to simplify the constitutive equations. For example, one simplification typically made was to neglect the creep strain component and assume contributions from only plastic and elastic strain [111]. This has simplified the solution, but assumed negligible creep, which invariably needs to be accounted for when analysing solder joints. Even with these simplifications, the equations can be complex, requiring numerical integration techniques to solve them. FEA simulation programs such as ABAQUS and ANSYS are some examples of commercially available FEA software programs that are capable of performing the analysis. The FEA models are used to determine the stress-strain relationship, which allows fatigue models to be constructed.

Research gap still exists in increasing the accuracy of TMC fatigue modelling, with newer and more accurate creep constitutive equations that will lead to more accurate fatigue life predictions. The work in this thesis proposes numerical methods in the form of finite element analysis (FEA) to capture the deformation behaviour of solder joints during TMC. However, the focus of the thesis will be more on the careful modelling of constitutive mechanistic creep models for SAC alloys. Investigation on creep modelling of SAC alloys will be extensively studied in *Chapter 4* and the corresponding implementation of the constitutive creep models in FEA for TMC prediction is discussed in *Chapter 7*. For a much broader review of fatigue modelling in TMC readers can refer to the work of Lee *et al.* [111] for an in depth review of fatigue models available of TMC.

2.2.3 High cycle fatigue/vibration fatigue

What follows is a review of state of research in *Pb*-free vibration performance of solder joints including the mechanistic understanding of various intrinsic SAC behaviours.

Possibly the most thorough study of fatigue in *Pb*-free solders conducted so far is that of Zhao *et al.* [117] in 2001. The work only relates to the *Sn-3.5Ag* binary alloy, but the results should be reasonably applicable to the *Sn-Ag-Cu* ternary system. The work is principally a fatigue crack propagation study; testing small-notched compact tension (CT) specimens machined from bulk solder (dimensions 39 x 50 x 6 mm). It was found that the results of the fatigue crack growth tests, conducted between 0.1 and 10 Hz could be separated into two groups which fits the two different fracture mechanics parameters: ΔJ (large plastic zone conditions)⁴ and C^* (creep-affected crack growth)⁵. At high frequencies and low R ratios, cyclic-dependent crack growth behaviour was observed to fit the ΔJ parameter and transgranular cracking was observed in the microstructure. At lower test frequencies and high R ratios, the data fitted the C^* parameter and the cracking behaviour were predominantly intergranular. These results demonstrate that the period of loading affects whether or not creep processes influence the cracking behaviour. Indications of recrystallization were also observed near cracks in the creep-dominated, slower tests.

Two pieces of research by Basaran *et al.* [118] and Zhao *et al.* [12], one a modelling exercise and one a real test, postulate that contrary to general belief strains in solder joints under vibration do not remain entirely elastic. In the former case, a damage mechanics model of *Sn-Pb* joints indicates a non-linear response of shear strain (with increased damage due to creep interaction) in joints at high acceleration and low frequency. It should be noted that the model used was based specifically on two-phase *Sn-Pb* microstructures. The study by Zhao *et al.* [12] attempts to verify this result by experiments on *Sn-Pb* BGA components, measuring strain fields optically with Moiré interferometry. The results appear to show that over 100 °C and for low (<1 kHz) frequencies, inelastic strains occurred. This seems to indicate that a longer period of loading (as in Basaran's results) can allow time-dependent processes (i.e. creep) to contribute to the damage process. However, in the author's view there is an oversight in the methodology employed in the tests related to the 'zeroing' method, which is meant to account for CTE mismatches at elevated temperatures: whether the plastic strain fields recorded were the result of vibration or not is in question. Kanchanomai *et al.* [119] conducted a detailed study of the tensile fatigue cracking behaviour of *Sn-Pb* solder with respect to its interface with *Cu* substrates. The (tetragonal) solder joint volume used was approximately 25 x 6 x 5 mm and tests were conducted at room temperature with $R = 0.1$ and a frequency of 10 Hz. Specimens were notched and fatigued to give a consistent pre-crack. The data fitted that of the cyclic-dependent regime identified by Zhao *et al.*, with transgranular crack growth and a similar ΔJ threshold value. As crack lengths approached half way through the section, the path of damage switched from the bulk solder to the IMC/solder interface. FE modelling of different a/W ratios (a = crack length and W = specimen width) showed that in the early stages of crack growth the plastic zone around the crack tip was small, but at $a/W = 0.46$ the plastic zone was much larger and debonded the interface with the *Cu* substrate. It was not reported exactly which interface was responsible for adhesive failure in the work.

A more detailed study is undertaken by Liu *et al.* [120] who characterise the crack growth due to vibration in (*Sn-Pb*) BGA solder joints by an optical method, although it should be noted

⁴In fracture mechanics; fatigue crack growth rates were correlated by parameters, ΔJ the parameter for large-scale yielding, and ΔK the parameter for small-scale yielding [119]

⁵In fracture mechanics; Due to high homologous test temperatures of solders, C^* is regarded as a crack-tip parameter to characterize the creep crack growth at elevated temperatures in ductile materials [119]

that as with some other studies, the joints themselves have to be cut in half initially before this method can be applied. The authors attempt to fit crack growth to the Paris Law (details of which are described elsewhere [121]) and predict life, with reasonable success. In that study the lifetimes spent in crack initiation and stable crack growth were 15 % and 60 % respectively. Stam and Davitt [122] have conducted vibration tests on a range of component and substrate coatings, comparing the reliability of *Sn-Pb* to that of *Sn-3.8Ag-0.7Cu*. They found that the difference between the solder types was less significant than the component type or substrate coating (e.g. *Cu* or *Ni*). This illustrates the disadvantages of testing complete PCB assemblies if the desire is to compare intrinsic solder performance.

The work to date on vibration of components with *Sn-Ag-Cu* ternary system solder joints in specific has been reviewed and found to be lacking in objectivity and scope. Other researchers [123, 124, 125] have concerned over the failure mechanisms and proposed analytical methods to estimate fatigue life under vibration loading for leaded solder joints. Most of the literature also focused on evaluating the failure under vibration loading using numerical simulations [120, 126, 31]. As seen from most of the review researchers [15, 120, 126] conducted HCF experiment as vibration or mechanical loading directly on SMT (e.g. BGA, chip capacitors etc.). It is often difficult to translate these application-oriented prediction solutions into widely applicable approach, when components or materials are changed or in case if further optimization is needed.

Most works has been done on the fatigue crack propagation of a limited selection of solder alloys such as *Sn-3.5Ag*, which was found to behave elastically in response to a 10 Hz fatigue test: decreasing frequency was shown to result in increasingly plastic behaviour. Other experimental work concentrates on particular components and does not isolate the intrinsic contribution of the solder to the fatigue results. Finally, modelling studies exist offering some insight into the degree of creep interaction in HCF but only for *Sn-Pb*.

Alternatively to understand the intrinsic solder behaviour of SAC alloys under HCF, coupon level testing can be performed. One of the few studies that is related to the HCF specimens on coupon level was a stress-controlled fatigue experiment at 2Hz but only up to 10^5 cycles on a bulk specimen with interface [56]. The second literature by Barry [8], was also done on a bulk specimen with interfaces, using the vibration shaker. But even though Barry [8] has explained the HCF of bulk specimen with a shaker, it still experience the material damping issues of the material itself and overall damping of the system, which could create a different local response on the cracking region.

2.2.4 Local stress approach for HCF prediction

There are two methodologies in stress life (S-N) modelling based on local and global stresses to assess the fatigue life of joints [127]. Since failure of a solder joint under vibration as seen in previous section review (*section 2.2.3*) mainly is determined by the local loading conditions and the stress induced in the concentrated regions cause failure initiation as seen in *section 2.1.6*, it is necessary to use local approaches. In addition, the local stress approach is more accurate compared to the global approaches [62]. This work presents a study of the ability for the local stress method to assess and predict the fatigue life of solder joints, where failure is expected from the meniscus side of the solder joints.

This method has proven to be quite successful: however, it is somewhat deficient in several aspects like accuracy of prediction of fatigue life. Therefore, it is often better to determine the local load-time function (local concept). In other words, the local stress curve is determined for the highest loaded conditions in a component, due to external loads from FE calculations. In case of vibration, this local stress at highest loaded conditions is associated with the frequency range of the dynamic system, which will be discussed in detail in the validation chapters later

under sections 7.2. The frequency response function (FRF) of the absolute stresses is used as damage parameter in this thesis, as seen in the schematics of *Figure 2-20*. Each cycle will induce a certain amount of fatigue damage on the component. The total damage caused by the time history can therefore be obtained by summing the damage caused by each cycle shown in the stress range histogram. This approach is commonly known as Palmgren–Miner damage rule after the two independent people who proposed it [62]. To understand more on the accumulated damage rule and fatigue life refer to Radaj *et al.* [62].

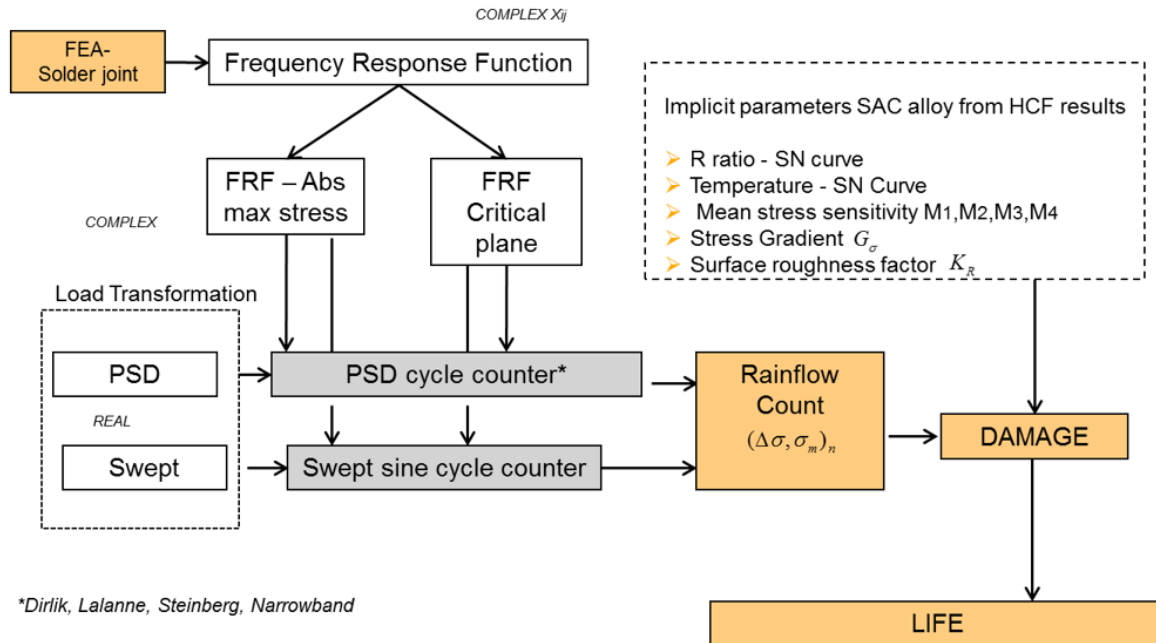


Figure 2-20: Summary of consolidating the fatigue analysis for vibration load using FRF local stresses with the implicit material parameters for fatigue models from the HCF experiments on SAC specimen, nCode⁶ [128]

The frequency response function (FRF) from FEA analysis of solder joints will be differentiated to an absolute stress method or critical plane method [128] as seen in *Figure 2-20*. A more theoretically correct method is used in this study (at the expense of being more computationally intensive) is to use a critical plane approach, where the FRF is resolved onto critical planes, which requires 2D stresses from FE calculations. The FRF is resolved onto multiple planes. The critical plane will be the plane with the most predicted fatigue damage. The planes on which the FRF is determined have normal that lie in the plane of the physical surface. For more details on critical plane method, refer to [128].

An appropriate rainflow-cycle-count method will be used based on power spectral density (PSD) load or swept vibration load as seen in *Figure 2-20*. The results from the rainflow count method will be used as a damage parameter to predict the lifetime performance of solder joints. The damage calculation will be based on then input from the implicit material parameters found from the SAC alloy HCF testing. In other words, the load transformation in this work is a complex vibration-load spectrum (frequency domain) which has to be determined with a counting method (rainflow count techniques) under the consideration of the mean stress influences. The rainflow-counting algorithm allows the application of the Miners rule, in order to assess

⁶ *Fatigue design software (nCode Designlife) will be coupled together with FE software (ANSYS) for the fatigue evaluation*

the fatigue life of a structure subject to complex loading, especially seen in the automotive power train sectors.

There are numbers of different theories for the prediction of the probability density function (PDF) of stress range [62]. All of these assume that the process (stress history) represented by the PSD of stress is stationary, random, Gaussian and ergodic. Current study uses Lalanne method probably as the best solution that is available for these SMT applications [128].

In a summary, with the knowledge of the load transformation (vibration spectrum) used in the application testing on SMT components and from the tolerable material load in the form of Wohler diagrams (SN curves) on solder specimen, a lifetime prediction of solder joints can be made for a mechanical element by means of damage accumulation hypothesis. Here it should be considered, that the prediction could only be made with certain probability, since amongst other things the load spectrum as well as the load capacity expressed in the form of a Wohler curve are random variables. It should be understood carefully that the local stress concept involves several uncertainties, due to the numerous influential parameters such as surface factors, size factors, stress gradient etc. These factors are incorporated in the damage accumulation models (written as *damage* in *Figure 2-20*) together with SAC material properties analysed according FKM guideline from Haibach [37]. Together with FKM guideline (introduced in *section 2.1.6.3*) it is possible to accomplish the complete fatigue evaluation process using nCode Designlife™ software (fatigue analysis software).

3 EXPERIMENTAL METHODS AND SETUPS

3.1 SOLDER ALLOY MATERIAL

Solder material investigated in the current work is a SAC387 standard alloy with a nominal composition of $Sn_{3.8}Ag_{0.7}Cu$. The detailed alloy composition from the supplier is tabulated in *Table 1*. Solder pellets for casting creep and fatigue specimens were purchased from Stannol GmbH (solder series selected is *Flowtin series TSC*).

Table 1: Alloy composition of the SAC alloy (all compositions in weight %) ⁷

<i>Sn</i>	<i>Ag</i>	<i>Cu</i>	<i>Co</i>	<i>Ni</i>	<i>Pb</i>	<i>Sb</i>
95.6	3.7	0.6	< 0.01	< 0.01	0.08	0.02

The melting point of the alloy is 217°C/220°C (solidus/liquidus) and is typically used for standard *Pb*-free reflow temperatures between 238-248°C. The alloy was supplied in the form of 6 mm diameter solid extruded blocks (pellets), which will be melted and casted to make bulk solder specimens. The extruded blocks were added to a “re-melting” process in a special designed aluminium die. Tensile bar specimens were casted under controlled temperatures, without macro-cracks and edges, which will be discussed in detail under *section 3.3.1*.

3.2 SOLDER SPECIMEN DESCRIPTIONS

3.2.1 Solder specimen design for creep

Dog-bone shaped creep test specimens were designed, fabricated, and validated based on the clamping, test equipment, extensometer according to the standard practices [129]. The specimen was designed with a shoulder-like structure in the measurement region of the creep specimen as seen in *Figure 3-1*. Since the creep specimens experiences tensile stresses with fairly lower strain rates in the region between $10^{-2} < 10^{-10}$ [1/s], the shoulder design prevents any potential minor slip of the extensometer from the gauge region [129].

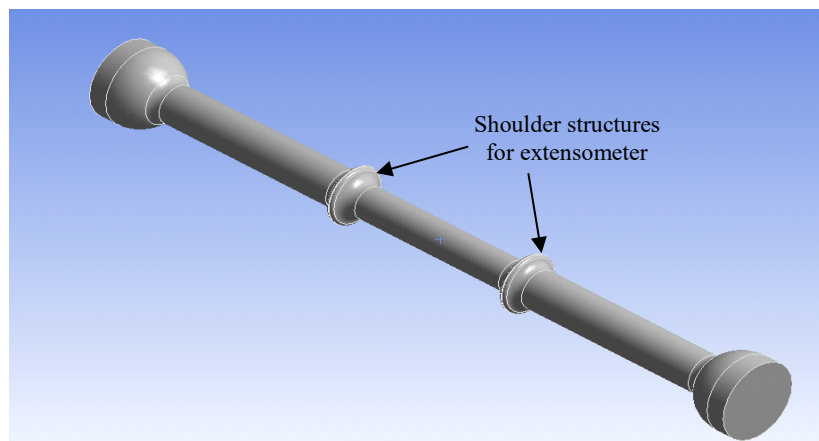


Figure 3-1: 3D- CAD model of the creep solder specimen with special shoulder design, detailed dimension in Appendix I

⁷ Data from supplier database

The extensometer was connected to the specimen using special adapters with the help of the shoulder design. The maximum static load that can be reached by the testing machine and the necessary static stress required for the experiment were considered during the design phase of the creep specimen. The length and cross section of the creep specimen was adapted to wide range of forces and strain values. Detailed dimension of the test specimen can be referred in *Appendix I*.

3.2.2 Solder specimen design for fatigue

Two different types of fatigue specimens were designed for the high cycle fatigue experiments. The design types were classified based on notch factors (stress concentration); notch and unnotched as seen in *Figure 3-2*. The notched specimen was considered to investigate stress concentration scenarios just as seen in solder joints as introduced earlier under *section 2.1.6.2*. The notched specimen was designed with a notch radius of 3.25mm that was calculated based on the stress concentration analysis (using FEA) in a SMT component solder joint. The notched specimen was designed in such a way that the crack initiation region (notches) is in the middle of the specimen, where the highest stress gradient is observed.

The specimen shape was designed to provide sufficient design space for higher stresses to be sufficiently removed from clamps and fillets calculated according to elementary Euler-Bernoulli theory. In other words, the specimen dimension was designed to be large enough to exceed any local stresses near the clamps according to the standard testing procedure [130]. This was done by varying the cross-sectional area gradually along the specimen length near the clamping region as per the standard practices [131]. The unnotched specimen does not include any stress concentration region, therefore the crack initiating regime can be expected anywhere in the gauge length (middle region).

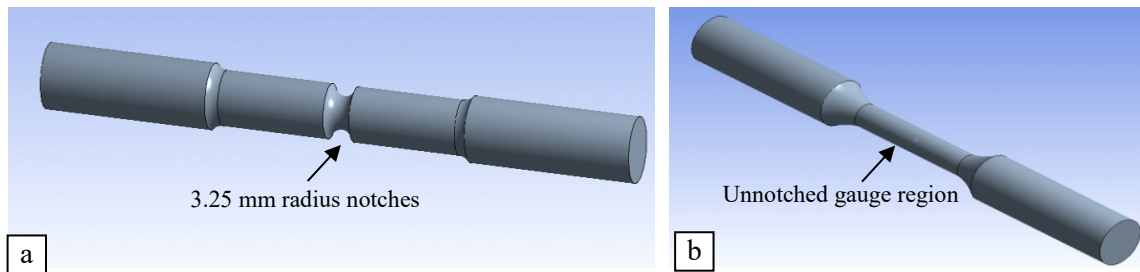


*Figure 3-2: 3D-CAD model of the fatigue specimens (a) notched specimen with higher stress concentration value $K_t > 1$ and (b) unnotched specimen with K_t value ~ 1 , detailed dimension in *Appendix I**

The stress concentration factor or a notch factor K_t , is the ratio between the peak stress at the root of the notch and the nominal stress. Notch factor, K_t was considered in the specimen design for notched and unnotched ones and is denoted as:

$$K_t = \frac{\sigma_{peak}}{\sigma_{nominal}}, \quad (3.1)$$

where σ_{peak} is the maximum stress and $\sigma_{nominal}$ is the nominal stress observed in the test specimen. Since the fatigue property of specimen has to be investigated for different stress ratios ($R = -1, 0, -3$): the specimen was designed to withstand any compressive dynamic loading. In other words, the specimens were designed to avoid any buckling under higher compressive loads at the different temperatures. The Eigen values of linear buckling analysis can predict the theoretical buckling strength (the bifurcation point) of the linear elastic solder specimen

[68]. The analysis was performed by designing for/against the critical buckling values of the solder specimen using finite element (FE) analysis. Firstly, the Eigen values for linear buckling was found for un-notched fatigue specimen at room and higher temperatures by FE-analysis using the linear buckling module in ANSYS™ 15.1. Then the critical buckling force was determined at room and higher temperatures. The critical buckling values were found to be ~ 3.61 times the applied load at 35°C temperature and about ~ 2.99 times the applied load at 125°C . Therefore the applied load during the HCF experiments with stress ratio $R = -3$ (compression dominant) should be below the critical load to reach the bifurcation point during buckling. A factor of safety, 3.61 and 2.99 of the applied load to reach first buckling mode was considered for room and high temperature experiments respectively. At higher temperatures, linear buckling analysis was performed considering the temperature dependent elastic property of the solder material. More details of the HCF specimen dimension is attached under *Appendix I*.

3.3 SOLDER SPECIMEN MANUFACTURING

3.3.1 Cast setup for specimen manufacturing

The cast setup enfold the development of a new cast and manufacturing setup for the fatigue and creep specimens. Special type of casting moulds (see *Figure 3-3*) were designed from aluminium die separately for all three types of specimen designs (notched, un-notched fatigue and creep).

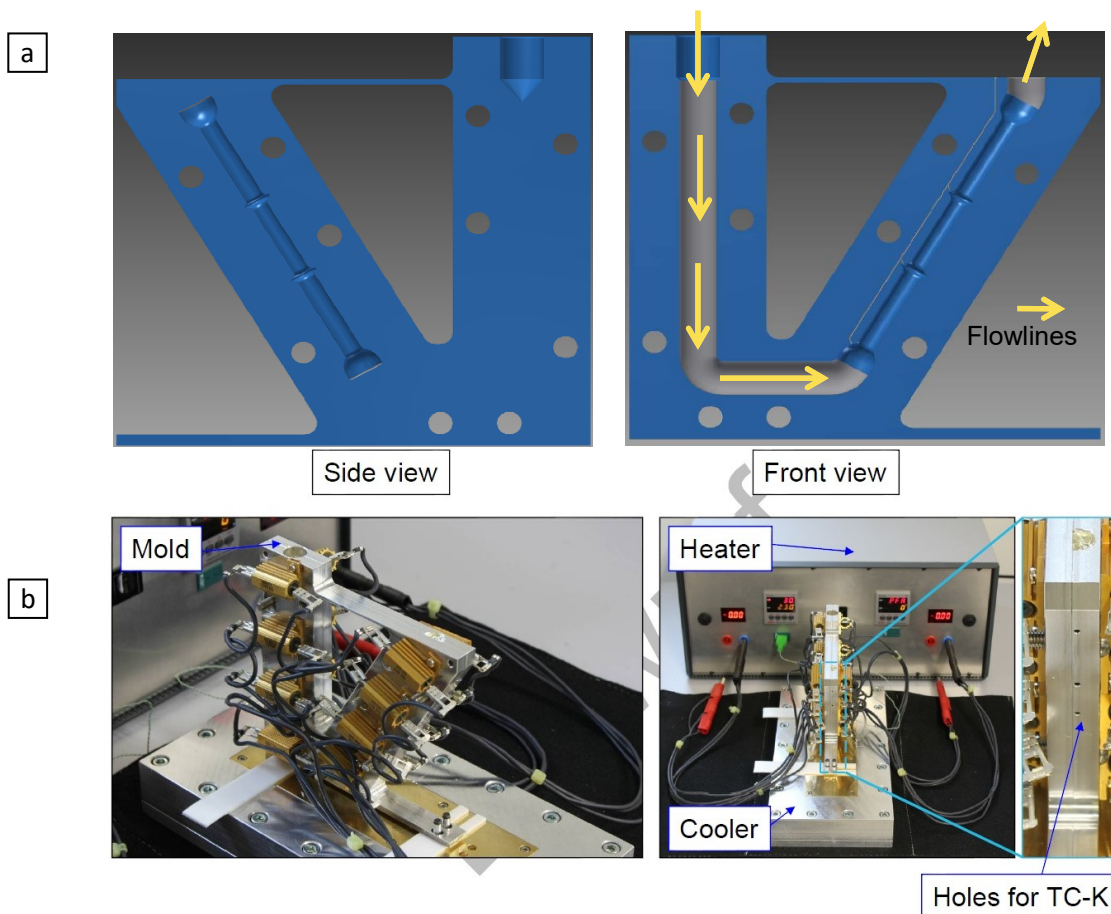


Figure 3-3: (a) CAD model of the die cast for the solder creep specimen (b) manufacturing mould cast setup showing resistors controlling the temperature in the aluminium die cast ⁸

⁸ Casting facility: Technische Universität Dresden/IZFP Dresden, Germany

Aluminium die cast was chosen over other materials due to its commendable surface roughness properties. The re-melting process is a standard process used in the current study for the fabrication of bulk solder specimens. Re-melting of the alloy with controlled temperature was achieved with special type of resistors around the aluminium die cast (*Figure 3-3-b*).

The round dog-bone like specimen design makes an easier extraction of the specimen out of the cast. Casted specimens had minimal rough edges and the changeovers regions from the measurement gauge area to the clamping area. The cast design was designed in such a way (see *Figure 3-3*), that the solidification rate occurs in a preferable direction to avoid any possible formation of shrinkage, blowholes, cracks or any inhomogeneous shapes of the specimen due to the volume contraction according to Roellig *et al.* [132]. *Figure 3-3-b* shows the developed cast with heating resistors where each resistors were separately controlled. The temperature sensor mounted at the four different measuring points controls the temperature state separately during the casting process.

The cooling phase starts immediately when the cast was filled with liquid solder and the temperature of the four temperature sensors, which were attached to the inside of the cast reaches the desired set point temperatures. Since the current work has to cater the requirements of the industrial reflow standards, the solidification rate used here is similar to the industrial standard practices (JEDEC standard). Ultimately, the aim is to maintain similar grain and microstructure qualitatively as compared to the solder joints in a SMT application. The cooling rate was held around 17K/min at 200°C to 160°C, which defines the orientation and structure of the required grain size. In addition, the temperature of the cast on the strain gauge measurement region and input region was also explicitly controlled.

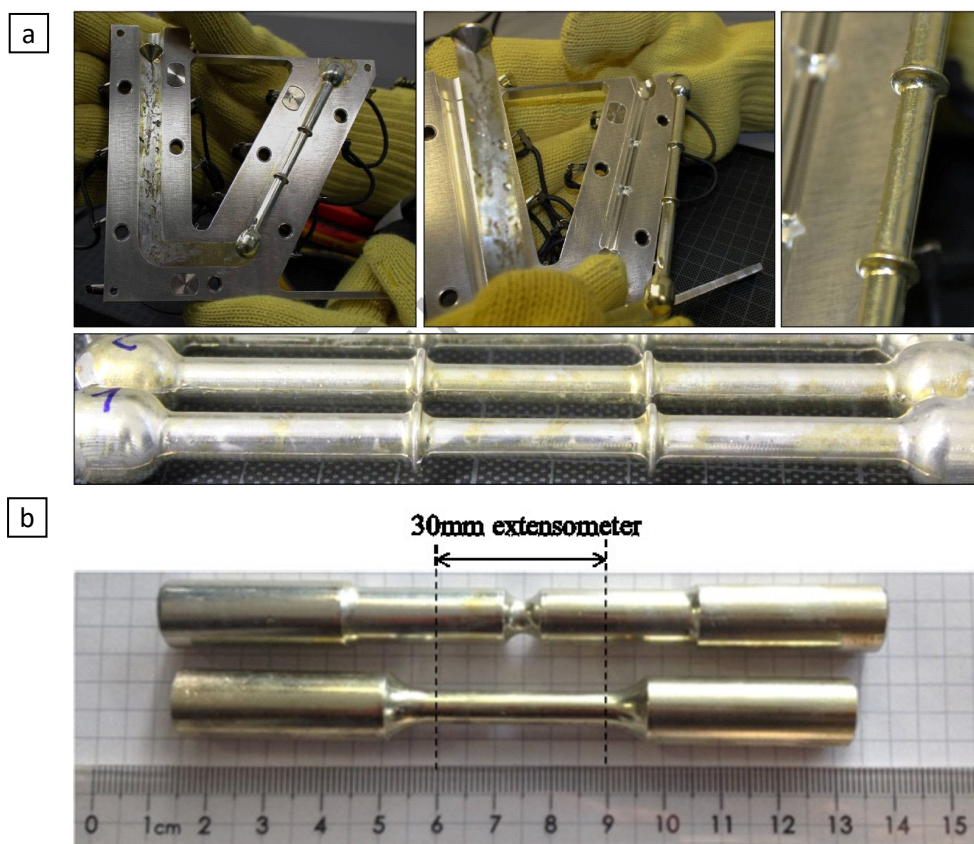


Figure 3-4: (a) Manufactured creep specimen taken out from the aluminium dies (b) notched and un-notched solder specimen for fatigue testing, detailed dimension, detailed dimension in Appendix I

The creep, notched and unnotched fatigue specimen taken out from the aluminium die cast are shown in *Figure 3-4*. The cross sections were compared to that of solder joints during the preliminary phases to replicate the microstructures (dendritic orientations and intermetallic particle sizes) as seen in *Figure 3-5*.

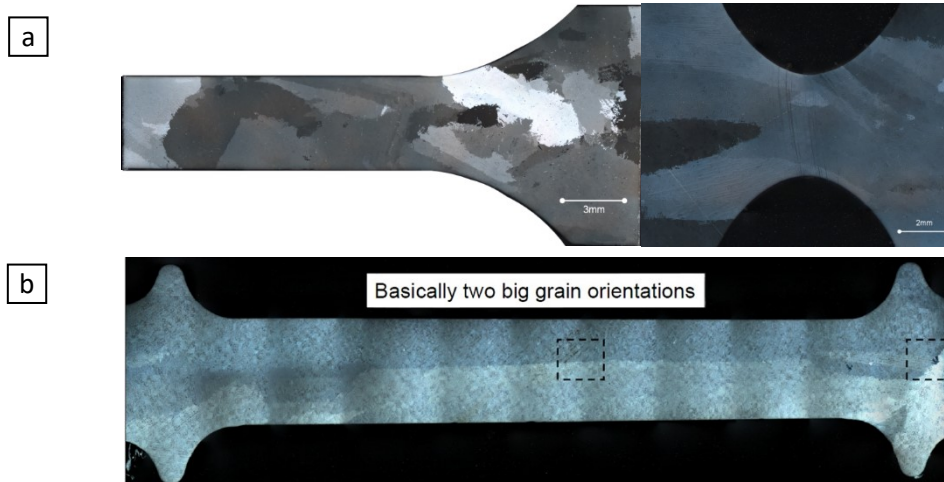


Figure 3-5: Cross-polarized optical micrograph of the cast solder specimens showing the primary grain orientations of (a) fatigue (b) creep specimens

Microstructure of the specimens were further analysed and compared under light microscopy between the cast bulk solder and solder joint. The process was iterated until the desired microstructure was achieved during the bulk solder casting. Special considerations were taken to get the dendrites positioning along the flow direction of the melt as an increasing cooling rate could potentially decrease the secondary dendrite size, as well as in the secondary dendritic arm spacing [82]. The comparison of the microstructures shows a resembled bulk solder cast and solder joint structures. Further details of the microstructure discussion will follow in *Chapter 6 (Figure 6-1)*.

3.3.2 Post soldering treatments

Casted specimens were annealed at 125°C for 24 hours to eliminate any potential residual stresses created during the extraction process. X-ray inspections were made on the fabricated specimens to verify quality issues. Ten specimens were randomly selected and quantified for qualitative analysis from different manufacturing lot. The X-ray analysis showed homogenous grey scale distribution, which is an indication of flawlessly casted specimens fabricated without any blowholes or voids as seen in *Figure 3-6*.

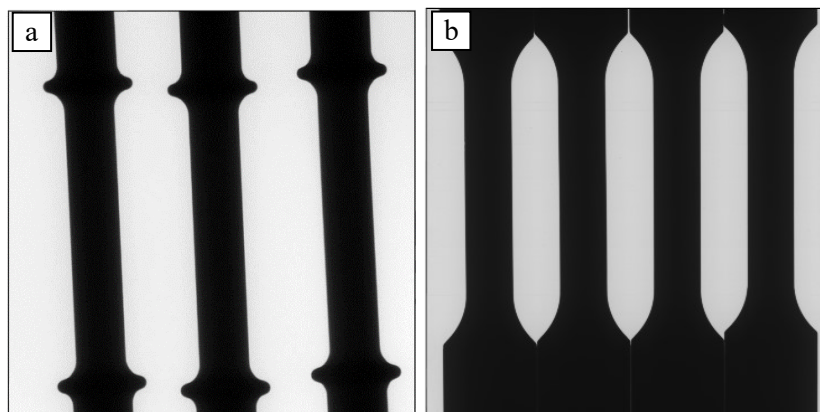


Figure 3-6: X-ray inspection for cast quality and void detection on random lots (a) creep (b) fatigue

Surface roughness on test specimens can create stress concentration regions (hotspots) and initiate cracks (see section *Surface finish*), which has to be avoided to get lesser-scattered results especially during HCF testing. After annihilation at 125°C, fatigue specimens were analysed for progressive surface scans to find any possible undesired surface roughness values. If any indentations were found on the surface, the regions were checked with μ -surface scans. The maximum average surface roughness (R_{max}) value of the indentation were close to ~ 8 -15 μm and an average surface roughness R_a value of ~ 0.68 μm were obtained. The high indentation values were mechanically reduced using plane grinding consumables *SiC* papers at first level with P360 (coarse paper) and finally with P2400 (fine paper), where an average R_{max} value of ~ 8 μm was obtained.

Special investigations were performed on fatigue specimens that were polished with high performance diamond liquid products DiaPro from StruersTM. Selection of premium grade diamonds in a stable suspension provided fine mirror polishing surface on the solder specimen with glossiness, edge retention, and retention of inclusions. With this polishing technique, surface roughness close to R_{max} of ~ 3 μm was obtained.

Most of the fatigue specimen experiments were conducted on the grinded specimens ($R_{max}=8$ μm). To understand the surface roughness influence on the fatigue property of the solder, specially treated specimens with the diamond liquid ($R_{max}=3$ μm) and also non-treated cast specimens directly from the manufacturing with ($R_{max}=11$ μm) were also used.

3.4 EXPERIMENTAL SETUP FOR MECHANICAL CHARACTERIZATION

3.4.1 Fatigue characterization

To characterize the HCF fatigue properties of $\text{Sn}_{3.8}\text{Ag}_{0.7}\text{Cu}$, specimens were loaded in a INSTRON E3000[®] dynamic testing machine that can apply the sinusoidal loads for various waveforms ($R = -1, -3, 0$) as seen in *Figure 3-7*. Equipment features a fatigue-rated load cell with maximum dynamic capacity of 3kN. The test was controlled by WaveMatrixTM dynamic test software that includes the needed features designed to assist various post processing of the data acquisition.

For all the experiments at elevated temperatures, a climate chamber was used that is integrated to the test equipment. The climate chamber can be operated in a wide range of temperatures from -100 to 350°C. The fatigue property of the samples were tested at constant stress amplitudes for different ranges of stresses, R -ratios, temperatures, notch factor, surface roughness etc. An average of three samples were tested at each of the stress amplitude (see test matrix in *Table 2*).

Extensometer was clipped on to the measurement region (see *Figure 3-4-b*) firmly for all the fatigue experiments to detect any local deformations of the material within the gauge length region as seen in *Figure 3-7*. True strain [-] is measured based on instantaneous length during fatigue experiments:

$$\varepsilon = \ln\left(\frac{l}{l_0}\right), \quad (3.2)$$

where l is the instantaneous length measured at multiple points during each cycles and l_0 is the initial reference point of the extensometer at zero force.

Since cyclic strain values is of interest in the current study, average strain amplitude ε_{mean} and true strain amplitude $\Delta\varepsilon$ are calculated as per equations:

$$\varepsilon_{mean} = \frac{\varepsilon_{max} + \varepsilon_{min}}{2}, \quad \frac{\Delta\varepsilon}{2} = \frac{\varepsilon_{max} - \varepsilon_{min}}{2}, \quad (3.3)$$

where ε_{max} [-] and ε_{min} [-] are the strains measured at maximum stress σ_{max} [MPa] and minimum stress σ_{min} [MPa] of each complete cycle.

Most of the experiments showed approximately similar displacement values on the local strain (from extensometer) and global strain measurement (relative displacement of test equipment), indicating relatively lesser displacements observed from the clamping regions. For all the experiments, a common frequency of 60 Hz was maintained. Detailed test matrix can be seen in *Table 2*. Fatigue test equipment at such a high frequency gains control the applied force values between 50 to 400 cycles. In the current study, this region is referred as machine control region, which are the minimum cycle needed to reach the desired set force values.

Table 2: Test matrix for the solder material mechanical characterization

	Creep test	High cycle fatigue test
Temperatures [°C]	35, 80, 125	35, 80, 125
Applied stress [MPa]	8 up to 31	7 up to 40 (stress amplitude)
<i>R</i> -ratio [-]	<i>n.a.</i>	0, -1, -3
Frequency [Hz]	<i>n.a.</i>	60
Surface roughness type	Grinded	Polished, Grinded, Casted
Specimen type	Unnotched	Unnotched, Notched

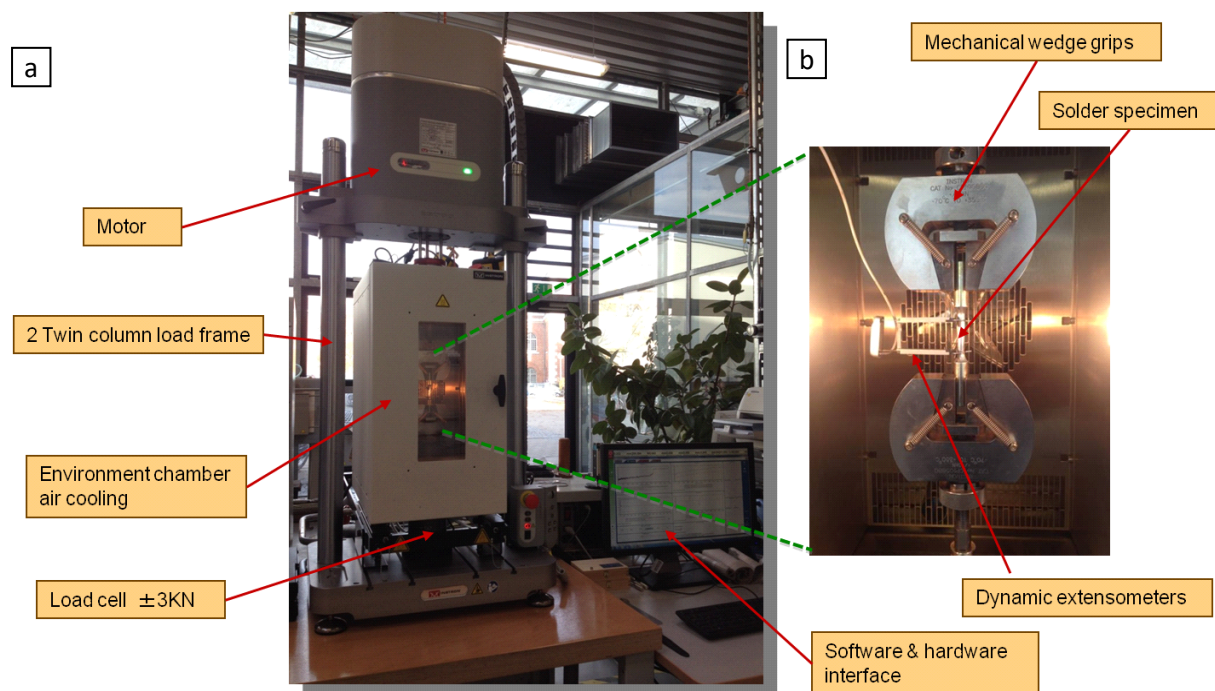


Figure 3-7 : (a) Universal test equipment for uniaxial creep and dynamic fatigue experiments (b) magnified view of the clamping wedges installed to the specimen and attached extensometer⁹

⁹ Testing facility: Technische Hochschule Ingolstadt, Germany

3.4.2 Creep characterization

The creep experiments were performed on the same test equipment as fatigue (see *Figure 3-7*). The test equipment applies the desired constant force along with the temperature control. The temperature chamber was used together with the test equipment for high temperature creep characterisation. The experimental parameters used for the creep test can be found in *Table 2*.

Tensile static creep tests were performed at different temperatures (35°C, 80°C, and 125°C) and stresses ranging from low stress (LS), medium stress (MS) to high stress (HS) depending on the set temperatures. The classification of stresses (LS, MS, or HS) were based on the creep mechanisms investigated in the current study. Detailed test matrix of the creep investigation can be referred in *Table 2*, where the application of constant force over the experiment is controlled throughout the experimental time.

Once the creep strain is calculated from the extensometer as per *Eqn.(3.2)*, the strain rates are analysed gradually and investigated further to arrive at the steady state creep rate as seen in *Figure 3-8*.

The systematic approach to calculate steady state minimum creep rate are as follows:

1. The creep strain rates were found out from the slope of creep strain ε vs. time (*Figure 3-8-a*), by calculating the slope values over five consecutive scatter points. The slope values over the five consecutive scatter points were calculated using the *SLOPE* function in Microsoft Excel 2016.
2. Secondly, the slope values, which are the calculated creep rate, $\dot{\varepsilon}$ are now plotted against both creep time (*Figure 3-8-b*) and creep strain (*Figure 3-8-c*). This intermediate step has two purpose: one is to help identify the steady state creep region and other is for an easy comparison of steady state curves of all experimental conditions.
3. Finally, the minimum creep rate $\dot{\varepsilon}_s$ can be found from steady state region *Figure 3-8-c*. In other words, the minimum creep rates on the steady state region is calculated by converting the strain dependency over time (*Figure 3-8-b*) to a time independent format (*Figure 3-8-c*). The systematic conversion of a creep strain ε vs. time, into a creep strain ε vs. creep strain rate $\dot{\varepsilon}$ is shown in detail in *Figure 3-8*.

Two different possible scenarios are typically encountered while calculating the creep strain rates based on the calculated scatter results of the creep rates, $\dot{\varepsilon}$.

1. For creep rates lesser than $\sim 10^{-5} [s^{-1}]$, the extensometer is expected to show high scatter values. Hence a prior smoothening function using *Cauchy weight function* and *mean local fit* (JMP software) is applied to the measured creep strain before finding the minimum creep strain rate values, as shown in green scatter points in
2. *Figure 3-9-a*.
3. For creep rates higher than $\sim 10^{-5} [s^{-1}]$, the quality of the creep strain measurement was found to have less scatter and no further smoothening was required. The minimum creep rate, $\dot{\varepsilon}_s$ found according to *Figure 3-8-c* will be used as a key input later in investigating the phenomenon based creep model, and mechanistic based creep models.

The minimum creep rate that is calculated for all experiments forms the base of characterizing the creep behaviour of solder alloys, based on both phenomenological model and mechanistic model in *Chapter 4*.

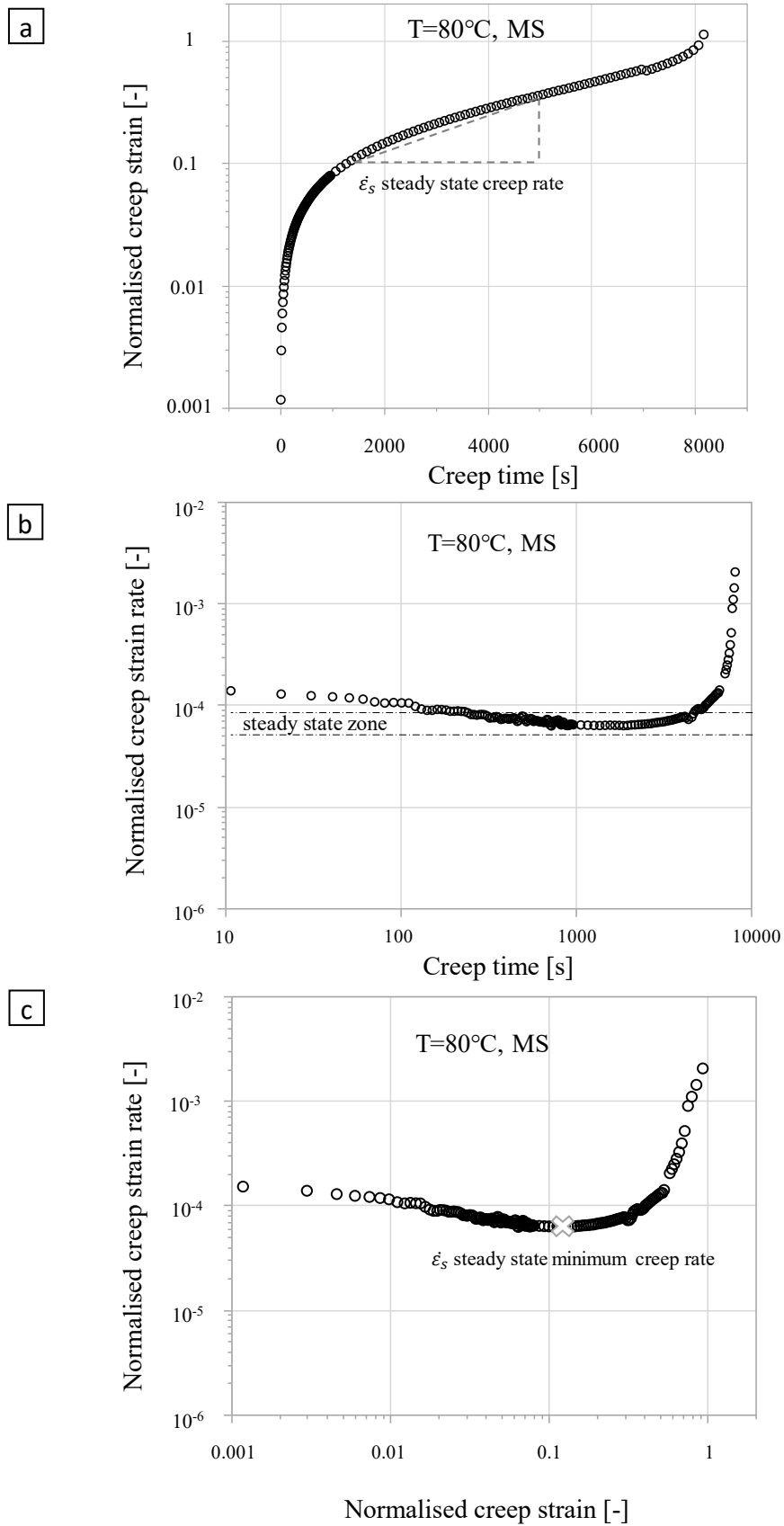


Figure 3-8: Time independent derivation steps at low medium stress (MS) showing (a) creep strain, ϵ vs. time (b) creep strain rate, $\dot{\epsilon}$ vs. time (c) time independent diagram, ϵ vs. $\dot{\epsilon}$

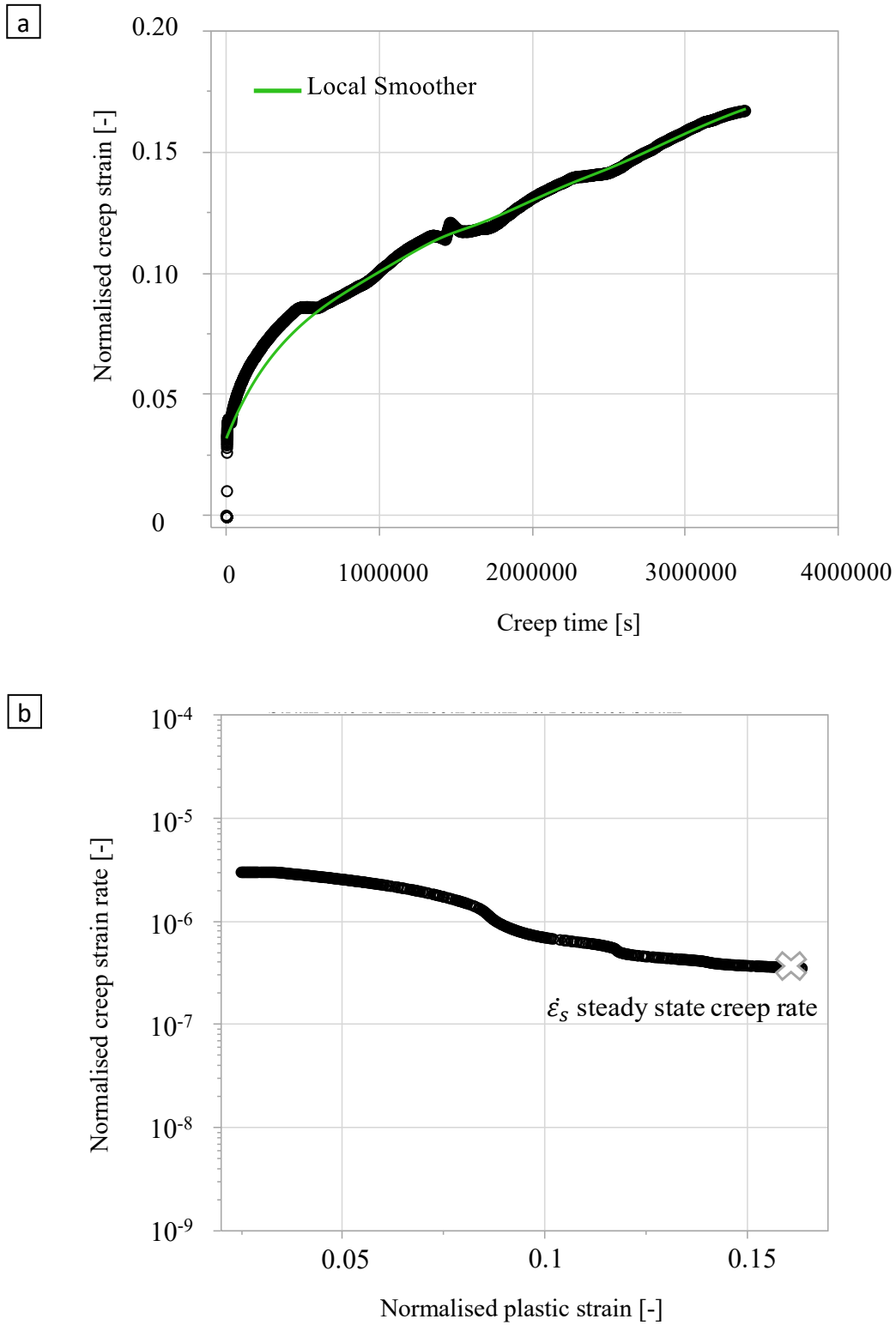


Figure 3-9: Time independent derivation steps at lower stresses (LS) showing (a) creep strain, ϵ vs. time with smoothening function (b) time independent diagram, ϵ vs. $\dot{\epsilon}$

3.5 VIBRATION SETUP FOR APPLICATION VALIDATION

The second set of experiments are the component level vibration testing performed on an application level (SMT parts). To prove the validity of the local stress approach introduced as in *section 2.2.4*, vibration loading experiments were done on SMT's soldered to the PCB's. Current work was done parallel to TU Dresden and IKTS Dresden with the study of Meier *et al.* [4, 61]. Meier and co-authors conducted experiments on application level to understand the vibrational fatigue behaviour of the solder joint.

In a first step, an adequate test vehicle was designed with the schematics and test setup as seen in *Figure 4.12*. A line clamping, instead of a simple board and a tapered strap cross section at the component mounting positions completes the design elements of the setup. The design enables the testing of multiple components simultaneously, with application of well-defined load during the experiments. Ceramic components (CC0805) and transformers (EHP16) were taken as primary SMT components for the validation of simulated results.

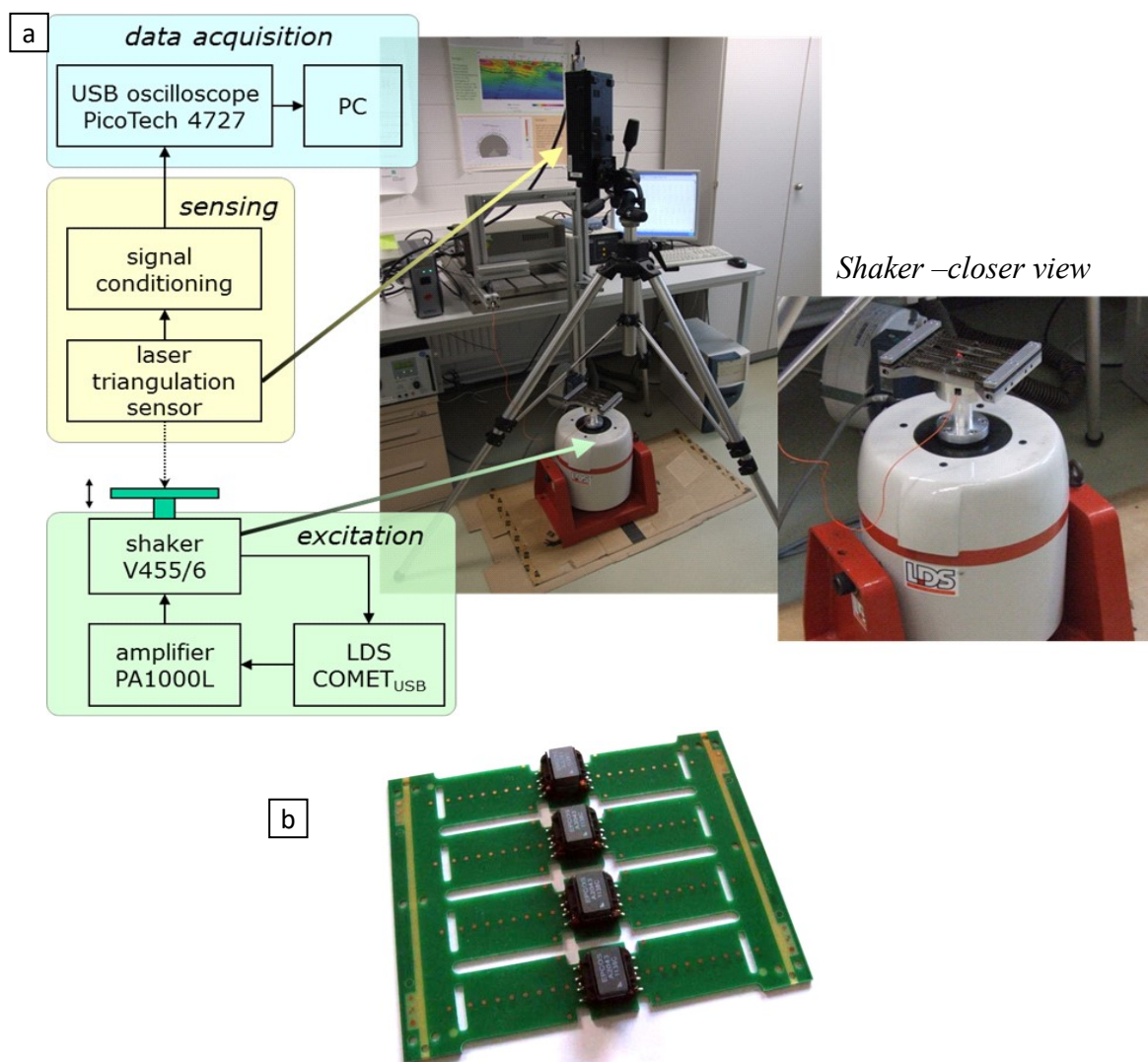


Figure 3-10: (a) Experimental setup and schematics of vibration experiment setup on the PCB strap with SMT, including vibration shaker and optical data-acquisition measurement systems ¹⁰ (b) closer view of component placed on the PCB straps

¹⁰ Testing facility: Technische Universität Dresden/IZFP Dresden, Germany

A sinusoidal vibration over a constant frequency was applied [61]. The excitation amplitude was kept constant during a single experiment; but varied between experiments to achieve different stress levels on the solder joints. PCB manufacturing, screen printing, component assembly and reflow was done under industrial conditions to assure adequate an industrial standard solder joint quality. Cross sectioning of the solder joints were later investigated which exposed solder grains, microstructures and crack occurrences.

The overall test setup was integrated by a permanent magnet shaker: LDS 455/6 a custom made specimen fixture and an optical measurement system that records the acceleration of the component under test as seen *Figure 3-10-b*. A closer view of the setup and the details of the SMT and solder joints are seen in *Figure 3-11*. To enable vibration experiments at elevated temperatures (HT), a strap heater element was developed. Meander shaped copper traces were used to heat the each strap near the component mounting position (see *Figure 3-11-b*). This prevents a considerable change in the PCB deformation shape during vibration and prevents the need for a heated chamber. Hence, optical measurement of the strap deflection based on laser triangulation was easy to apply. Since the heating of the component mounting position works very homogeneous, the heater traces act as sensors to measure the temperature of each strap.

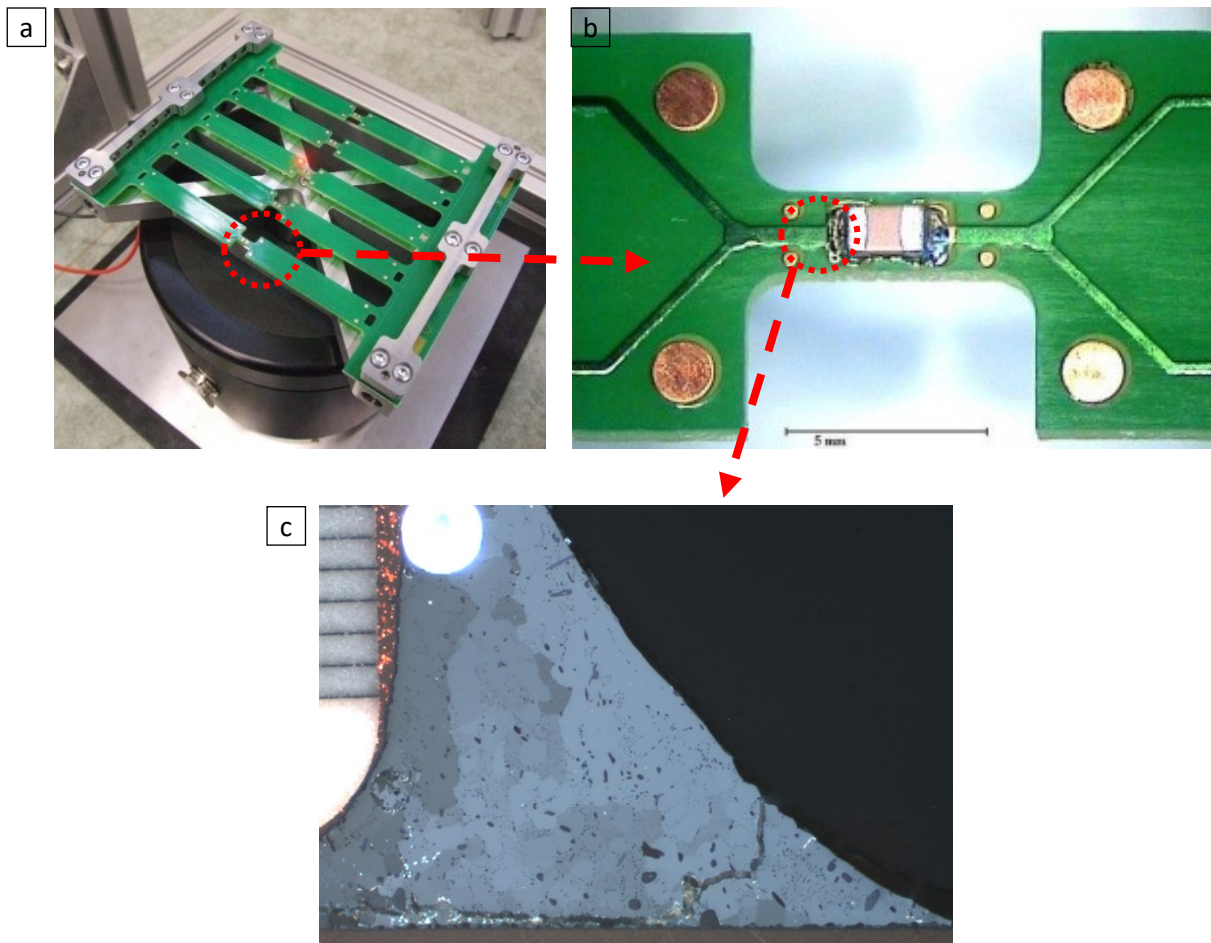


Figure 3-11: (a) PCB strap design for vibration experiments on SMT ceramic components integrated on a shaker table setup (b) top view of the ceramic capacitor placed on the middle of the straps for achieving highest deformation (c) cross section of failure observed ¹¹

¹¹ Setup: Fraunhofer IKTS, Dresden, Germany

All the components were tested for a specific period of cycles, after which the experiments were stopped to do analysis on the solder joint cross sections (see *Figure 3-11-c*). The failure criterion in the current study is any visually detectable cracks from the LM analysis. The observed crack length was quantified according to the length of each solder joint from cross section analysis (according to [61]). The maximum crack length per component will be detected and recorded. Since the cross sectioning of all solder joints of a transformer is extensive, only four out of eight joints were analysed. Solder joints, which did not show any evidence of cracks were marked “passed” and the ones that failed were marked as “failed”. The downside of the method is that the real cycles to crack initiation cannot be determined, as the experiments were not stopped for analysis at the exact crack initiation time.

The setup and experiments were designed in such a way, that the FR4 does not see any failure and the stresses generated from the applied dynamic loads were concentrated on to the solder joints. A detailed experimental setup of FR4 and the components are shown in *Figure 3-11*. The corresponding experimental parameters used are shown in test matrix *Table 3*.

Table 3: Parameters for vibration experiment testing on ceramic capacitors and transformer

	Chip capacitor	Transformer
Resonant frequency f_0 (average)	265 Hz	Not available
Vibration type	sine dwell at f_{exc} close to f_0	
PCB strap deflection [mm]	0.2...0.94	0.07...0.71
Cycles [10^6]	20...220	1...60
Number of tested components	105	90

3.6 MATERIAL INVESTIGATIONS

Solder joints and bulk solder specimens, cross-sectioned for metallographic analysis were prepared at Continental Automotive GmbH, Quality lab according to the following test protocol:

1. set up the cold-curing epoxy resin,
2. remove undesired material by grinding on rotating wheels with fresh grit papers in the order from coarse to fine polishing (80, 240, 320, 1200 at 150rpm),
3. polish on rotating wheels with cloths impregnated with $6\mu\text{m}$ and then with $1\mu\text{m}$ diamond paste at no more than 120 rpm,
4. final polish with a $0.02\mu\text{m}$ colloidal silica solution.

The resulted surface revealed a clear microstructural contrast under light and scanning electron microscopes (SEM). Light microscopy studies were conducted at Continental Automotive GmbH, Regensburg, Technische Hochschule Ingolstadt and Fraunhofer IZFP Dresden facilities using a typical compound microscope under polarised light. Cross-polarising filter was used to give the primary grain (sometime referred as individual grain) orientation contrast. DIC (differential interference contrast) prisms were occasionally used to enhance the contrast of microstructural features. For fractography investigations (HCF), cracked samples were washed in acetone prior to the dry blowing for further investigations.

Scanning electron microscope (SEM) was frequently used in the current work to perform qualitative analysis of microstructural behaviour caused by the temperatures and stresses during HCF and creep testing. SEM not only enables to capture the information on microscale level but also offers capabilities such as qualitative and quantitative elemental analysis, which will be used in the preliminary steps of the current study.

In addition, Electron backscatter channelling contrast (EBCC) and Electron back scattered diffraction (EBSD) analysis were carried out at Technische Hochschule Ingolstadt using the LEO 1430 SEM equipment. EBCC and EBSD were used in a specific way to analyse the substructure with lower misorientation angles (used in the creep investigations). For EBCC analysis, the table of the specimen holder was increased gradually in steps with minimum angle of 2° .

Cross sections from creep experiments were analysed for inverse pole figures using Electron backscatter diffraction (EBSD) at Ecole National Supérieure des Mines, Saint-Etienne, France. EBSD analysis projects the crystallographic directions present in the primary grains, which constitute the solder alloy. Subgrain structures from the bigger primary were mapped using such an EBSD technique.

Finally, X-ray diffraction (XRD) technique was used in the current study for phase identification of a crystalline material before and after experiments. The specimens were powdered homogeneously and finely to determine the phases of the materials below the surface. The intensity of diffracted X-ray beams were recorded more homogeneously with fine powders in comparison to analysing cross sections or bulk samples. As the incident and diffracted beam rotate through all-possible perspective angles of the powdered samples, a much more reliable phase information can be obtained. The facilities from Technische Hochschule, Ingolstadt with Panalytical™ Empyrean machine were used to perform the XRD studies.

4 CREEP INVESTIGATION OF SAC ALLOY

This chapter compares the creep test results based on phenomenological and mechanistic models. The phenomenological approach used here is based on a well-established Norton power law and other models that are used very often in SAC alloy applications such as the hyperbolic sine law and the double power law. A new mechanistic model is proposed later in this chapter based on a physical based micro-mechanical modelling technique. The reason for establishing a physical mechanistic model will be analysed and discussed in detail, also addressing the advantages and disadvantages of phenomenological creep models for *Pb*-free *Sn*-based alloys. The phenomenological models addressed in the work, will be used as benchmark in developing a modified physical based creep model.

A detailed review of available literature and state of art for *Pb*-free alloys for creep modelling using both phenomenological and mechanistic models is discussed earlier under *section 2.1.7* and *section 2.2.1*. As summarised from the literature reviews, phenomenological based models could not explain the creep deformation mechanism at different temperatures and stress levels. Literature reviews claims that the phenomenological models showed significant scatter in the stress exponents and activation energy values [1, 75, 133, 134], when the models are used across different studies.

To prove the validity of the literature claims in this research, it is needed to build a phenomenological model in the first place and then compare with the values in the literature (literature listed in *Table 7*). Also plausible reasons (microstructure, constraints from assembly etc.), behind the challenges of the phenomenological model being used for SAC alloys will be also discussed in the current chapter.

4.1 TIME INDEPENDENT STRAIN VS. STRAIN RATE CURVES

Time independent creep rate results (according to *Section 3.4.2*) of the creep experiments at different temperatures is plotted in *Figure 4-1*. The creep rate curves shows no particular deformation zones where the creep rate will be constant. In fact, there is a minimum creep rate region (at secondary creep stage) for a strain observed of approximately around 0.5 - 3% of creep strain as seen in *Figure 4-1*, depending upon the type of loading and temperature. As the test progresses, the strain increases after primary creep region and gradually slow down to a minimum steady strain rate (secondary region). After the secondary region in *Figure 4-1*, comes the tertiary region during which the strain rate increases until rupture. This occurs due to both necking, voids, and damage (macro cracking) occurring in the solder toward the tertiary stage. A detailed investigation on the microstructures is explained under *section 6.2*.

A finite amount of primary creep takes place prior to achieving a steady state wherein a minimum creep rate is observed for all temperatures as seen in *Figure 4-1*. For all tested temperatures, the minimum creep rate region is observed to dominate the creep time. Also, considering the application and thermal cycling (see *Figure 2-6*) used in this study which had a slower temperature ramp up rate and longer dwell times, primary creep is neglected for modelling the constitutive creep models in the current study. It should be also noted that the proportion of primary creep strain to total creep strain changes with different thermal profiles, therefore the unknown and variable error in neglecting primary creep is a function of thermal profile parameters. With the current research group of the thesis, using an accumulated creep strain energy density (damage metrics) based on secondary creep model showed higher accurate lifetime modelling; thereby it is decided to develop models based on the secondary-only creep constitutive models. Moreover, the secondary or the steady state creep is the dominant deformation experienced by solder alloys [135].

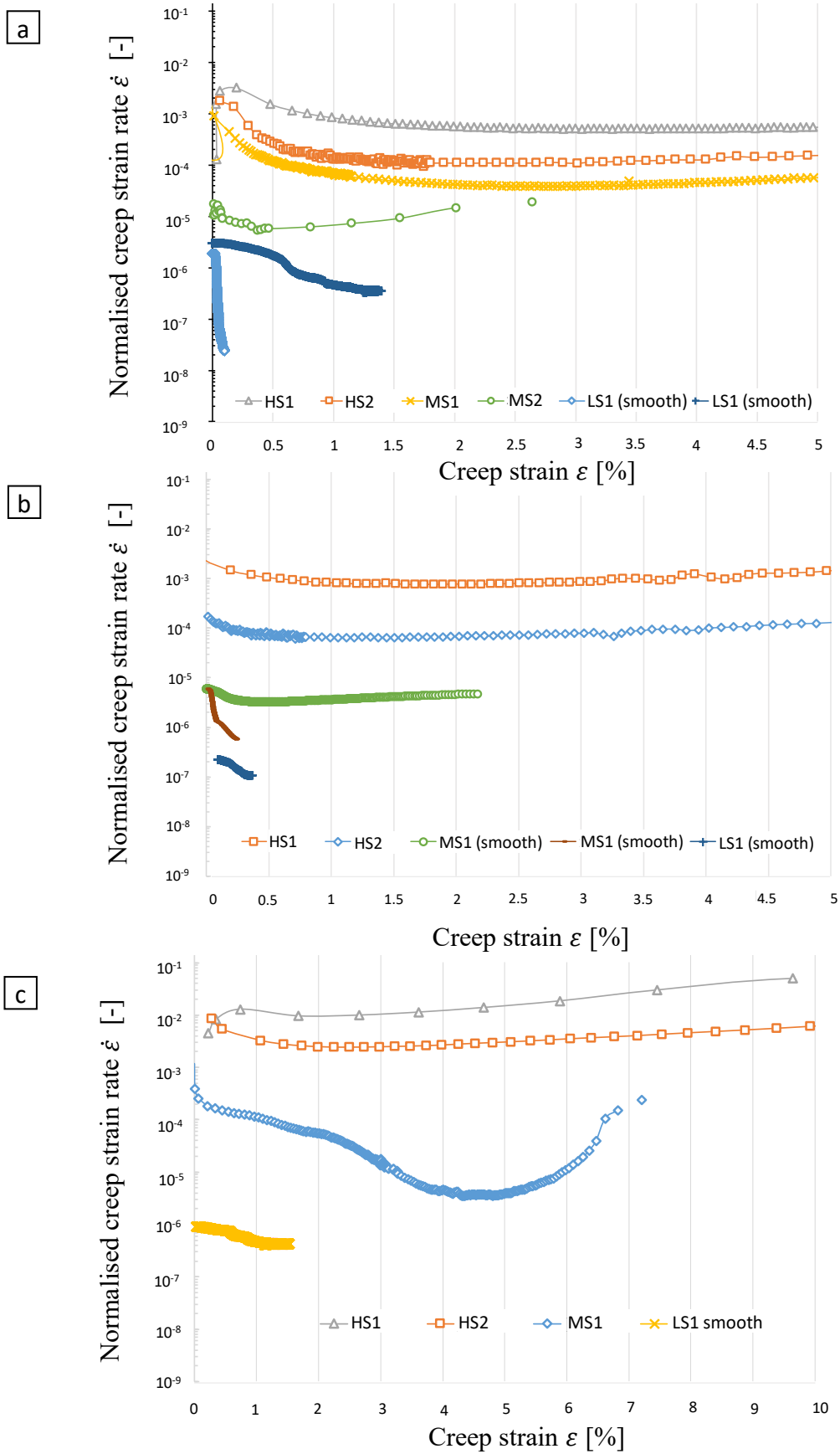


Figure 4-1: Strain ϵ vs. strain rate $\dot{\epsilon}$ plot at low stress (LS), medium stress (MS) up to high stress (HS) for some test parameters (a) 35°C (b) 80°C (c) 125°C

At the secondary stage, the strain rate is retarded by strain hardening which decreases the deformation speed, while the associated recovery mechanism tends to accelerate the creep rate. In addition, the minimum creep rate region (secondary stage) controlled by hardening effects due to presence of IMC which is of key importance is discussed in the creep model development in *section 4.3*. The minimum creep rate at the steady state region is found according to the creep characterization *section 3.4.2*. The minimum creep rate from *Figure 4-1* will be used as a primary factor in modelling the following phenomenological and mechanistic models.

4.2 PHENOMENOLOGICAL MODELS

The steady state creep rate is quantified by means of constitutive creep models, which are semi-empirical as described in *section 2.1.7.1*. Models as described in *Eqns. (2.10), (2.21), and (2.22)* based on the secondary creep rate are used here for characterization of solder alloys considering the diffusion controlled creep deformation mechanism [136]. The basic characterization based on Norton power law, Garafalo and double power law will give a primary reference for further creep model development and for comparing the phenomenological and mechanistic model approaches. Classical model such as the Norton power law and widely accepted models for SAC like Garafalo hyperbolic sine and power-law creep model is analysed here to compare the coefficients of the models with the available literatures (discussed later under *section 4.2.4*).

4.2.1 Norton power law

The most common expression to describe the stress, temperature and microstructure dependence of the steady-state creep is using Norton power law, *Eqn. (2.10)* based on Arrhenius rate equation as described earlier under *section 2.1.7.1*. The creep coefficients of Norton power law are obtained through a nonlinear modelling. Determination of the parameters are according to Darveaux *et al.* [104] using power law model as introduced in *section 2.1.7.1*.

The optimization of the constants in *Eqn. (2.10)* is done using the software JMP 13.0, where the iteration of analytic Gauss-Newton method is used [58]. The values of the creep constants in *Eqn. (2.21)* is optimized by minimizing the weighted square of the residues of experimental scatter points in *Figure 4-3*. An iterative approach followed here uses σ_0 (stress level for power law break down), which is gradually incremented from an initial value of $\sigma_0 = 1 \times 10^{10}$ [MPa] using a step size of $\sigma_{i+1} = \sigma + 1 \times 10^{12}$. At each step, a best-fit parameter (A, σ_0, n, Q) is found using a non-linear regression. This process is iterated until a local minimum is detected in the mean square error for a particular set of four parameters. The corresponding optimal σ_0 is then confirmed with a second iterative solution, where σ_0 is set just below the previously determined optimal value. A finer step size of 1×10^{-16} is used to find the minimum mean square error. The experimental points and the Norton power law fit after optimization is shown in *Figure 4-2* and the values of the each parameters is referred in *Table 4*. The optimization is completed with a R^2 (Goodness of fit) value of 0.966. The value of A represented in the *Table 4* is a normalised value; however the stress gradient n and the activation energy Q value represents the right optimised values for further discussions.

Since the R^2 for Norton power law is found to be lesser than the scientific approved values (>0.98), indicates relatively higher deviations from the experimental results. Stress exponent, n is found to be 9.47. The deviation of the experimental results from the model could indicate the possible different creep mechanism for SAC alloy. Therefore, other well known models used for SAC alloys of Garafalo hyperbolic sine law and double power law will be discussed.

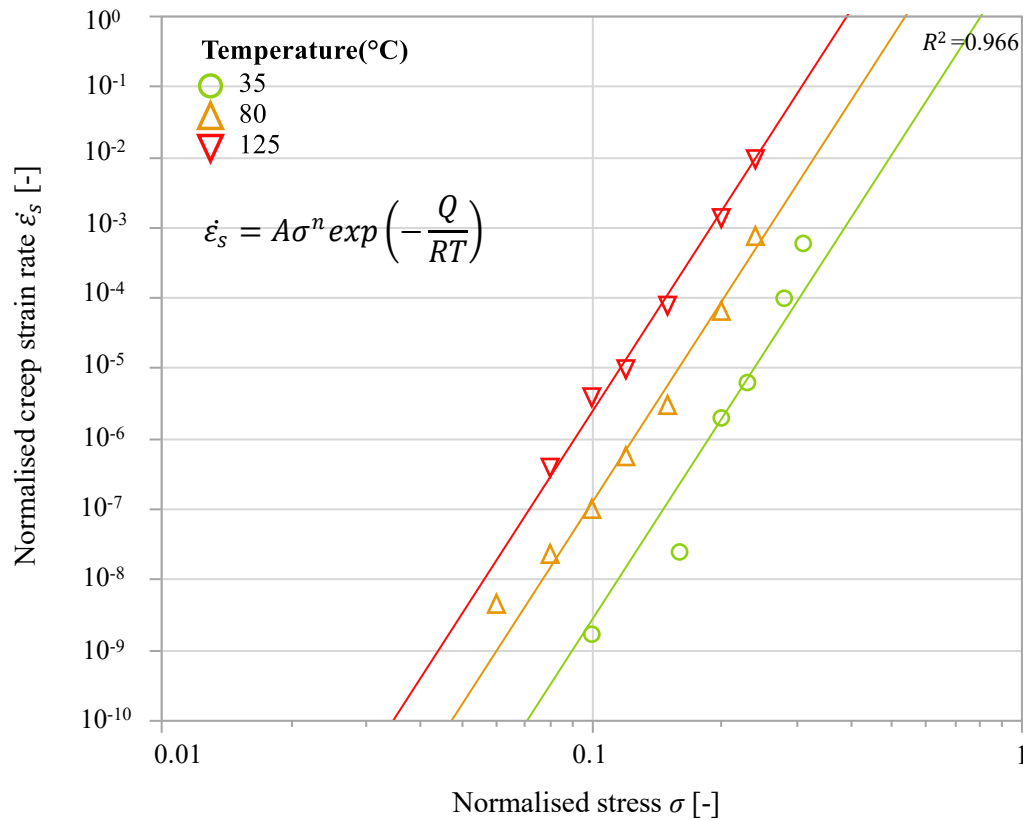


Figure 4-2: Norton power law fit over experimental creep strain results at different temperatures, with normalised fit parameters

Table 4 : Parameters of the Norton power law fit out of experimental optimization

Norm A [-]	n	Q [kJ/mol]
1E-7	9.47	76.97

4.2.2 Garafalo – Arrhenius hyperbolic sine model

The hyperbolic sine law as per Eqn. (2.21), for steady state region based on modified Arrhenius equation is elaborated with the secondary creep rate values. The creep coefficients for the Garafalo law are obtained through nonlinear modelling just as described for Norton plot in earlier section 4.2.1. The experimental fit after optimization and the values of the each parameters is shown in Table 5, which is modelled with a very high R^2 value of 0.990.

Figure 4-3 identifies evidence of high and low stress regions with stress exponent, n value of 6.1, which postulates not a significant power-law breakdown possibility. This is similar to Garafalo predicted model in Figure 4-3 which did not explicitly partition the low and high stress creep mechanisms but rather treats the steady state creep with an effective or apparent activation energy that may represent multiple creep mechanisms as introduced in section 2.1.7.

Table 5 : Parameters of the hyperbolic Garafalo law fit out of experimental optimization

Norm A [-]	Norm σ_0 [-]	n	Q [kJ/mol]
684.8	1.071	6.1	80.978

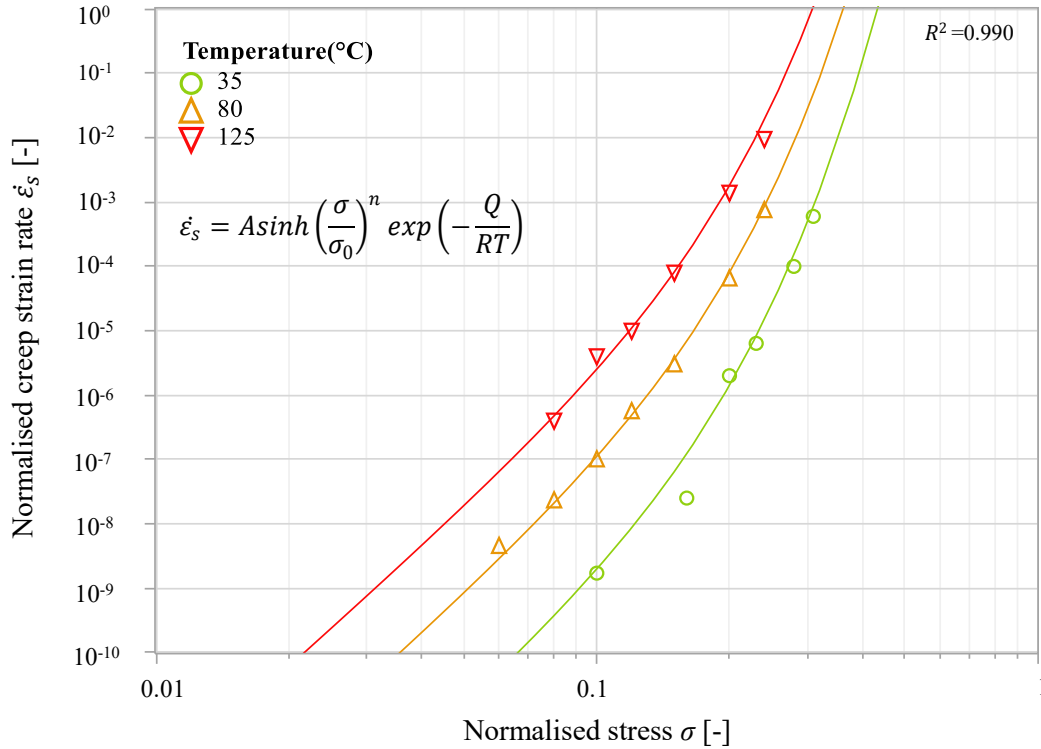


Figure 4-3: Hyperbolic sine fit over experimental creep strain results at different temperatures, with normalised fit parameters

4.2.3 Double power law

A two-regime power law, which assumes power law-dependency over lower and higher stress regimes, formulated according to Eqn. (2.22) is modelled with experimental creep results. The experimental fit after optimization and the values of the each parameters is calculated similar to the Garafalo sinh method as described in earlier section 4.2.1. The results of the double power law model is shown in Figure 4-4, which is modelled non-linear regression showing slightly lesser R^2 value of 0.988 compared to single exponent Garafalo law. A single parameter Garafalo law is found to be sufficient to explain the experimental creep rates in the current study. The experimental fit after double power law optimization and the values of the each parameters are shown in Table 5.

As seen in Figure 4-4, at lower stresses, stress exponent, n_2 of SAC387 alloy is 4.89, and activation energy resulted is 62.49 kJ/mol, which is close to that of lattice self-diffusion of Sn [1]. At higher stresses (HS), stress exponent n_1 equals to 12.62 and the activation energy of 80 kJ/mol is obtained which similar to that of dislocation-pipe diffusion [1]. Overall parameters for high stress regimes A_1, σ_1, n_1, Q_1 and for low stress regimes A_2, σ_2, n_2, Q_2 is tabulated as in Table 6.

Table 6 : Parameters of the double power law fit out of experimental optimization

Norm A_1 [-]	Norm σ_1 [-]	n_1	Q_1 [kJ/mol]	Norm A_2 [-]	Norm σ_2 [-]	n_2	Q_2 [kJ/mol]
140.18	1.021	12.62	80	1.14	0.93	4.89	62.49

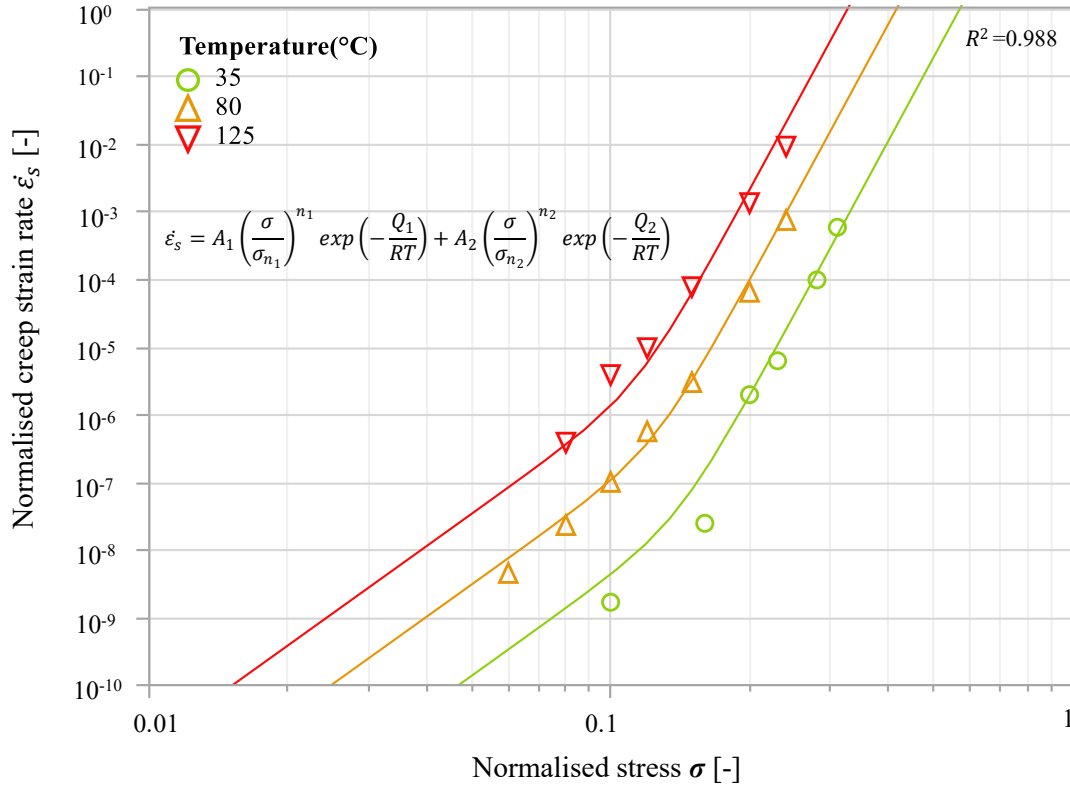


Figure 4-4: Power law fit over experimental creep strain rate results at different temperature, with normalised fit parameters

4.2.4 Comparison of phenomenological creep models

The material parameters of the Garafalo hyperbolic law Eqn. (2.21) is modified (for comparative reasons) to Eqn. (4.1) accommodating the material coefficients for different Pb-free solder investigated by many researchers (see Table 7).

$$\dot{\epsilon}_s = A[\sinh(\sigma_0 \times \sigma)^n] \exp\left(-\frac{Q}{RT}\right) \quad (4.1)$$

The comparisons from the literature of all the creep parameters is tabulated in Table 7. Only Garafalo law is compared with the current work to other literatures, as the double power law model will follow the same explanations and arguments as the Garafalo law.

As seen in Table 7, when compared the values of the Garafalo sine law with the other research works along with the current work (see final row in Table 7). Stress exponents, n values of SAC 387 of different literatures [134, 137, 138] are in the range of 4.2 to 5.1 is compared in the current work, where the stress exponents are found to be 6.1, which is slightly higher with less effect on power law dependency.

The values of the creep parameters from all the literature had a huge span of values especially for the standard Sn based alloy as follows:

1. A range (6.385E-6 - 1.5E9) 1/s
2. σ_0 range (5E-9 - 2) MPa
3. n range (0.2 – 6.65)
4. Q/R range (160 - 12267) K

The range differences mainly come from the different alloy compositions (e.g. *Au*, *Ni*, *Zn*, *Sb*). However, it is still interesting to note the range span changes for even specific alloys from Table 7.

Table 7: Values of the coefficients in Eqn. (4.1) for different Sn- based alloys from various research works

Solder alloys	A [1/s]	σ_0 [1/MPa]	n	Q/R [K]
<i>Sn</i> _{1.3} <i>Ag</i> _{0.2} <i>Cu</i> _{0.05} <i>Ni</i> [1]	8E +5	0.1	7	9020
<i>Sn</i> _{1.3} <i>Ag</i> _{0.5} <i>Cu</i> _{0.05} <i>Ni</i> [1]	6.00E+04	0.11	7	8419
<i>Sn</i> _{2.7} <i>Ag</i> _{0.4} <i>Cu</i> _{0.05} <i>Ni</i> [1]	2.00E+07	0.143	5	12026
<i>Sn</i> ₈₀ <i>Au</i> [139]	4.62E+15	2E-5	2.07	12267
<i>Sn</i> _{3.5} <i>Ag</i> _{0.7} <i>Cu</i> [133]	4.61E + 6	0.037	6.17	8400
<i>Sn</i> _{3.8} <i>Ag</i> _{0.7} <i>Cu</i> [140]	926(508-T)/T	(37.78 x 106- 744147T) ⁻¹	3	6360
<i>Sn</i> _{3.5} <i>Ag</i> [140]	98437	0.103	6.65	9561
<i>Sn</i> ₅ <i>Sb</i> [140]	42409	0.04	5	6542
<i>Sn</i> ₉ <i>Zn</i> [140]	81524	0.06	5	7841
<i>Sn</i> _{3.0} <i>Ag</i> _{0.5} <i>Cu</i> [133]	6.385 E-6	0.08638	5.84	160
<i>Sn</i> _{3.8} <i>Ag</i> _{0.7} <i>Cu</i> [134]	3.2 E4	0.037	5.1	6524
<i>Sn</i> _{3.8} <i>Ag</i> _{0.7} <i>Cu</i> [137]	441000	5E-9	4.2	5412
<i>Sn</i> _{3.8} <i>Ag</i> _{0.7} <i>Cu</i> [138]	8.09 E5	0.115	5.02	5466
<i>Sn</i> _{3.9} <i>Ag</i> _{0.6} <i>Cu</i> [141]	500000	0.01	5	5802
<i>Sn</i> _{3.5} <i>Ag</i> [142]	18(553-T)/T	145.0364x [1/(6386- 11.55T)]	5.5	5802
<i>Sn</i> _{3.9} <i>Ag</i> _{0.6} <i>Cu</i> [55]	441000	0.005	4.2	5412
<i>Sn</i> _{3.6} <i>Pb</i> ₂ <i>Ag</i> [55]	462(508-T)T	145.036 x [1/(5478- 10.79T)]	3	6360
<i>Sn</i> _{3.8} <i>Ag</i> _{0.7} <i>Cu</i>	325000	0.05217	5	5800
<i>SnAgCu</i> _{0.03} <i>Ce</i> [143]	284000	0.02432	6.1	6400
<i>Sn</i> _{3.5} <i>Ag</i> [143]	900000	0.0653	5	8690
<i>Sn</i> ₃₇ <i>Pb</i> [143]	10	2	0.2	5400
<i>Sn</i> _{3.8} <i>Ag</i> _{0.7} <i>Cu</i> [current work]	684.8 (normalised)	0.98 (normalised)	6.1	9739

One major reason for a higher span of material fit parameters being the fitting parameter values are often based on optimizations and it did not include any explicit physical models. Studies [76, 77, 78] concludes that the different mechanical properties are a result of differences in microstructures and constraints from the assembly/different phenomenon for e.g. cooling rate,

aspect ratio effect and grain size. The drawbacks of the phenomenological models are debatable and shows the challenges faced in modelling phenomenological creep models. Consequently, it also involves the potential risk of over/under performance prediction of SMT solder joints, which are eventually derived out of the creep models.

4.3 DEVELOPMENT OF A MECHANISTIC CREEP MODEL

As concluded from the literature reviews (*Section 2.2.1*) and also by addressing the phenomenological models in the current chapter (*Section 4.2*); describing the creep model with physical state variable is argued to be the missing factor. This also means incorporating physical state variables including microstructural parameters for the relevant creep mechanism is a need and remains a challenge for SAC alloy. The creep mechanisms for particle strengthened involved in SAC as described in *section 2.1.7.2* shows the complexity of implementing such a mechanistic creep model.

The following section will be an attempt to develop such a mechanistic model for SAC alloy. The mechanistic model is expected to address the corresponding creep mechanisms at different temperatures and stress including addressing the relevant physical state variables.

As adapted from *section 2.1.4*, a wide range of IMC morphologies (obtained through various compositions and processing techniques) and the presence of a few large anisotropic β -Sn grains in coarse-grained SAC solders contribute to heterogeneity and joint-to-joint variation in the creep behaviour and the kinetics for SAC alloys. In such a case of dispersion-hardened materials such as SAC solder, the intermetallic particles serve as obstacles to the path of dislocation glide and climb. This interaction between the particle and dislocation can be either attractive or repulsive. To capture this interaction effects in the hardened alloy, a mechanistic constitutive creep law is developed in this section based on the following steps:

- implementing threshold stress using Orowan theory,
- dependency of stress exponent (n) and activation energy (Q) on temperature ,
- incorporating subgrain size dependency.

4.3.1 Implementing threshold stress using Orowan theory

Before investigating the dependency of the stress exponent (n) and the activation energy (Q) on the temperature and stress, different stress regime that elaborates the two different mechanisms of creep has to be defined. However, to find the stress regimes, where the non-linearity starts (sometimes referred as power law break down), a threshold stress or back stress needs to be calculated theoretically using the Orowan theory (refer *section 2.1.7.2-a*). According to the theories, the effective creep rates are dictated by the differences between the applied stresses and the threshold stresses. Within the limits, the two stresses may reach comparable magnitudes, thus acting as a creep arresting mechanism; thereby distinguishing the stress regimes.

At low stress regime, it is assumed that the dislocations pass through by climb and glide in the eutectic region, which consists of β -Sn matrix over the Ag_3Sn and Cu_6Sn_5 intermetallic precipitates. While in high stress regime, dislocations are glide-controlled [67]. According to different creep mechanisms in both stress regimes, back stresses from the mechanistic model is calculated by analysing the corresponding microstructures. Once the back stress is theoretically and experimental determined, the n_1 (low stress regime exponent) and n_2 (high stress exponent), are calculated based on the threshold stresses. The correlations between the theoretical and experimental results based on the microstructure explains the evidence of Orowan based bowing mechanism.

To arrive at the threshold stress based on the Orowan theory, the works of Kerr [80] and Gong [107] is adapted in the current study based on following four steps:

- volume fraction,
- interparticle spacing,
- Orowan based bowing stress,
- threshold back stress.

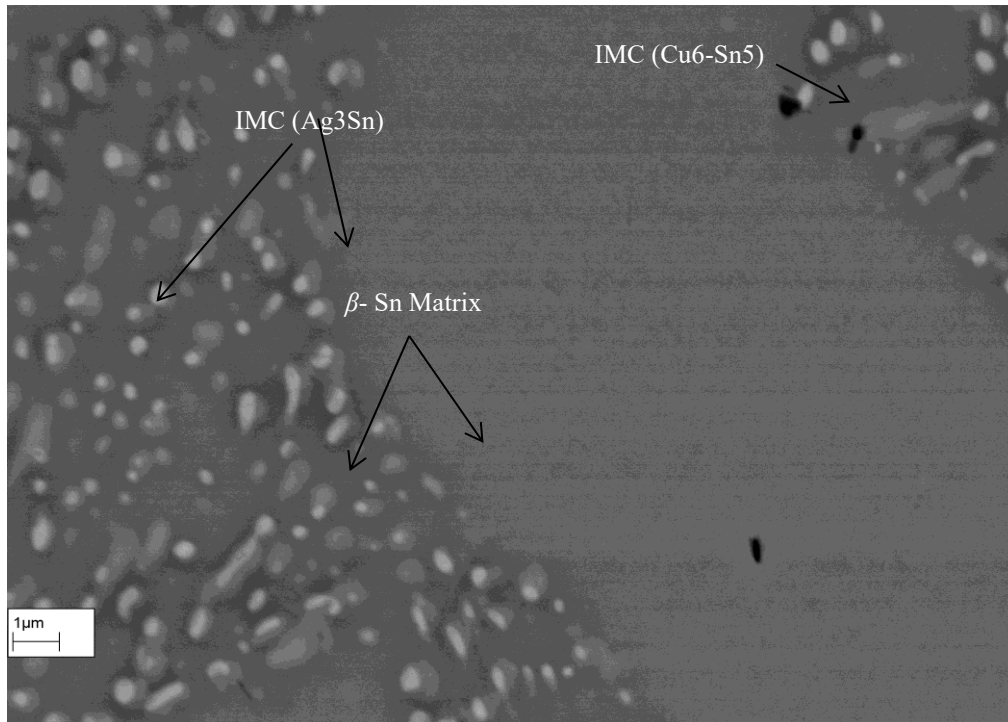


Figure 4-5: SEM micrographs showing microstructure of SAC alloy with the intermetallics (Ag_3Sn and Cu_6Sn_5) and the β -Sn matrix

As seen in section 2.1.4, microstructure of $SnAgCu$ alloys consists of β -Sn matrix, which is nearly pure Sn, distributed with the various amounts of eutectic micro constituent comprising a dispersion of intermetallics. The size distribution and the spacing of the intermetallic phase are analysed from SEM micrographs. Figure 4-5-a, shows the dispersion of intermetallic phases in the matrix. The Ag_3Sn sizes are assumed spherical in size for the current analysis and the Cu_6Sn_5 is not considered for further analysis, as their density in β -Sn matrix is relatively minimal compared to Ag_3Sn . The highest count distribution of local second phase precipitate size ' d ' is found to be $\sim 0.62\mu m$, observed for the volume fraction calculations over the eutectic IMC dominated regions. Samples are randomly chosen after specimen manufacturing for this analysis.

The volume fraction $f = N_p/N_v$ is calculated according to Eqn. (2.14) from the work of Agamenonne *et al.* [63]. The value of N_v is analysed to be around ~ 1 from the unit volume of the matrix through SEM. The value of volume fraction, f is found to be approximately ~ 0.138 .

At high stress regime, the back stress from particles for precipitation-hardened materials is derived based on Orowan stress σ_{OR} according to Eqn. (2.26), which is a modified form of Eqn. (2.12) [136]. The mean radius of precipitates [μm] r is determined from the global calculation (β -Sn and eutectic regions) and is found to be around $0.45\mu m$.

As introduced earlier under *section 2.2.1* in Eqn. (2.26), characteristic length of a lattice dislocation is defined by the magnitude, b of the Burgers vector. Burgers vector, b characterizes the strength of the lattice distortion caused by its presence. This technique is adapted from the similar works of Gong *et.al* [107], which in fact is originally investigated by Rosler & Arzt [109]. Taylor factor, M is used to express the flow stress, σ as measured in a polycrystals in terms of critical resolved shear stress, τ in constituent single crystals. It is an average orientation factor, which depends on the texture of the material and on the crystallographic nature of the assumed slip systems and the material values are adapted from the work of Gong *et al.* [107].

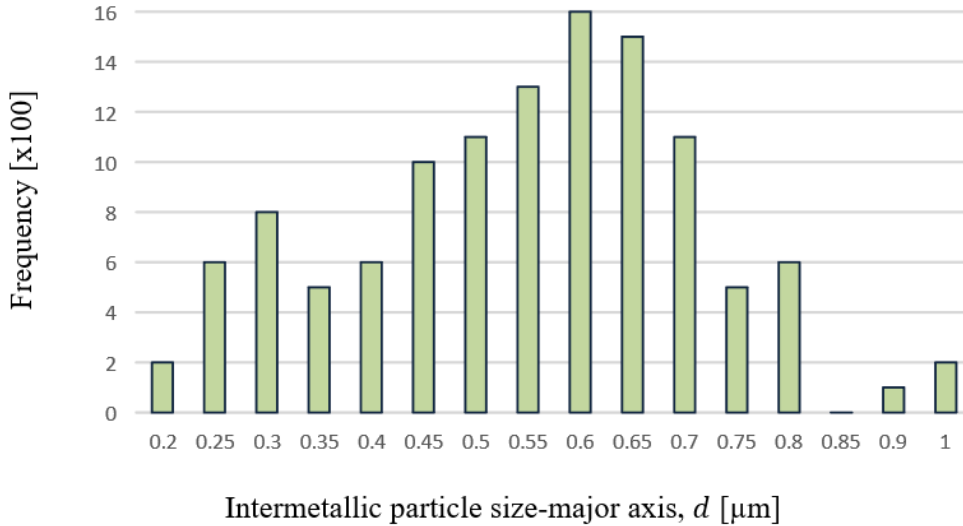


Figure 4-6: Distribution of Ag_3Sn intermetallic precipitates analysed from pre-experimental samples

The interparticle spacing λ is determined using the following relation [80, 136]:

$$\lambda = d \left(\frac{\pi}{6f} \right)^{1/2}, \quad (4.2)$$

where d is the average intermetallic precipitate diameter from Figure 4-6 and f is the volume fraction.

According to Rosler and Arzt [109], dislocations are attracted by particles since the dislocation energy at the particle/matrix interface is lower than that in the matrix. Therefore, the back stress arises from the energy increase when dislocations leave the particle rather due to the elongation of the dislocation line at the beginning of the climb. The intensity of attraction between the particles and dislocations can be characterized by the relaxation factor, K_r .

Now, the back stress σ_b is expressed from the Orowan stress σ_{OR} [136, 107]:

$$\sigma_b = \sigma_{OR} \sqrt{1 - K_r^2}. \quad (4.3)$$

When $K_r = 1$, the particle has no effect on the dislocation movement and if the relaxation factor $K_r = 0$ the threshold stress is equal to Orowan stress. The values for σ_b are tabulated for various temperatures in Table 9.

All parameters from Eqns. (2.14), (2.26), (4.2), and (4.3) is summarized in Table 8.

Table 8: Calculated parameters from the volume fraction Eqn. (2.14), inter-particle spacing Eqn. (4.2), and Orowan stress Eqn. (2.26)

K_r	M	b [nm]	d [μm]	f	λ [μm]
0.87 [107]	3 [107]	0.21 [107]	0.62	0.138	0.98

A trend of decreasing back stress with increasing testing temperature is observed from the calculated values as visualised based on a double power law model modified in *Figure 4-7*. This observation can be attributed to the different creep mechanisms at high stress regime. As the temperature increases, the temperature effect on creep becomes more prominent. It will result in easier slip for dislocation motion and more recovery due to thermal activation. When the back stresses are plotted on the Norton plot against the tested data for all the temperatures, the calculated values are found to be fitting with those of the experimental data as seen in *Figure 4-7*, proving the mechanisms as hypothesized. The absolute values calculated for back stress are shown with normalised value below in *Table 9*. In other words dotted threshold stress, which represents the back stress values in *Table 9* passes through the experimental knee region in *Figure 4-7*.

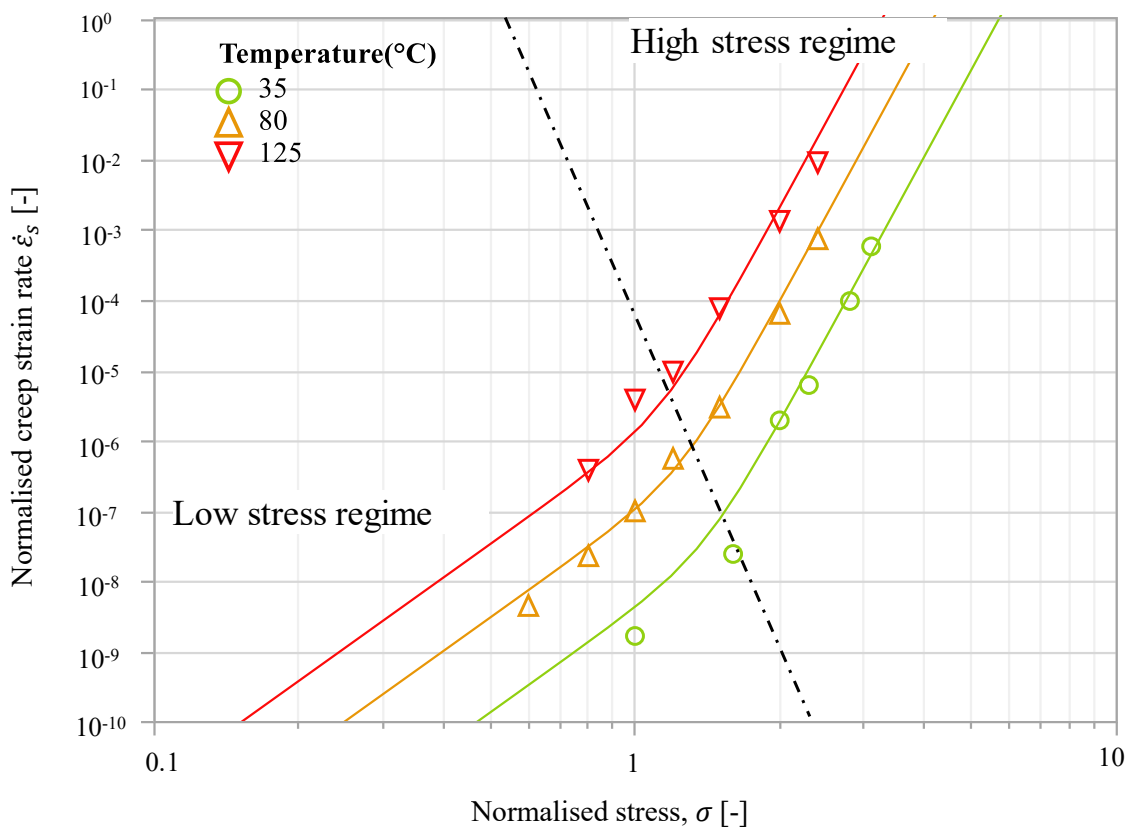


Figure 4-7: Threshold stress line (dotted) calculated as per Eqn. (4.3) - values from Table 9, plotted at various temperatures to differentiate the low stress (LS) and high stress (HS) regime

The temperature dependency of back stress is calculated from the Orowan stress *Eqn. (2.26)* by substituting in the shear modulus, G values. Note that the shear modulus G values cannot be found from the static experiments, hence Young's modulus E values are converted into G values based on the Poisson ratio of 0.4 [144]. The Young's modulus had a good correlation with temperature values with linear dependency, which is also observed in the works of Darveaux [145], Lau [146].

Table 9: Calculated back stress from the Eqn. (4.3)

Temperature T [K]	Normalised back stress σ_b [-]
308	1.63
353	1.40
398	1.23

It has to be noted that since the material is casted, the flow direction will acquire higher strength, hence a shear testing is encouraged to calculate the G values, compensating the anisotropic behaviour. Due to the assumption of temperature independent K_r and anisotropic effects, for the first approximation, the correlation is encouraged more for the room temperature experiments.

4.3.2 Dependency of stress exponent (n) and activation energy (Q) on temperature

From the calculated back stress line (see *Figure 4-7*), the regions can be easily identified to make a linear regression for determining the stress exponents at high stress regime (HSR) and low stress regime (LSR). The linearity of stress exponents between the LSR and HSR is determined with respect to the temperatures as shown in *Figure 4-8-a*. The analysed values are now plotted versus temperature to get a linear-relationship with respect to the temperature.

It is therefore visualised that the stress exponents at HSR and LSR decreases with increasing temperature. A classical Arrhenius equation in *Eqn. (2.21)* will not be linear as the stress exponents (n) are varied between 5.7 and 12.9 in *Figure 4-8-a*. In other words, the creep flow of the solder is no longer dominated by constant mechanism over the wide testing range of temperature from 35°C to 125°C and applied stress level from LS to HS. To get a steady state function out of the stress exponent, a term σ/RT is used and the stress exponents is collapsed onto a single linear fit in *Figure 4-8-b*.

The changing stress exponents in *Figure 4-8-a, b* over the stresses and temperatures could be potentially from the assumption of a constant activation energy value. In a creep model development, using both stress exponent and activation energy dependency over either stress or temperature will overcompensate the mathematical model. Because SAC alloys have a relatively lower melting point, the activation energy is considered in the current study for the temperature dependency. This is because relatively small temperature changes can causes relative large changes in the experimental creep data [75].

It should be also noted that for a given stable structure and applied stress as described in *Eqn. (2.21)*, a steady relationship is seen in logarithmic coordinates between the minimum creep strain rate and the reciprocal of temperature. The slope of the curve *Figure 4-9* represents the activation energy (Q). Apparently *Figure 4-9*, shows the experimental values displaying non-linearity characteristic at any given stress level, indicating that for any given stress level there are more than one process that controls the creep phenomenon throughout the temperature range examined. It is concluded, that an iso-stress method is not suitable to determine the activation energy of the solder alloy.

A new measurement method, called temperature differential creep test approach is proposed by [75, 136] to determine the activation energy dependencies. Under a given stress, the differences between the steady state minimum creep strain rates associated with T_1 and T_2 are recorded. T_1 is the initial temperature, and T_2 is the elevated temperature, which is greater than T_1 . The activation energy for small differential values between each consecutive temperature point on *Figure 4-9* is formulated as:

$$Q = R \left[\frac{\ln \left(\frac{\dot{\varepsilon}_1}{\dot{\varepsilon}_2} \right)}{\left(\frac{1}{T_1} - \frac{1}{T_2} \right)} \right], \quad (4.4)$$

where $\dot{\varepsilon}_1$ and $\dot{\varepsilon}_2$ and are the creep strain rate at the temperature T_1 and T_2 respectively.

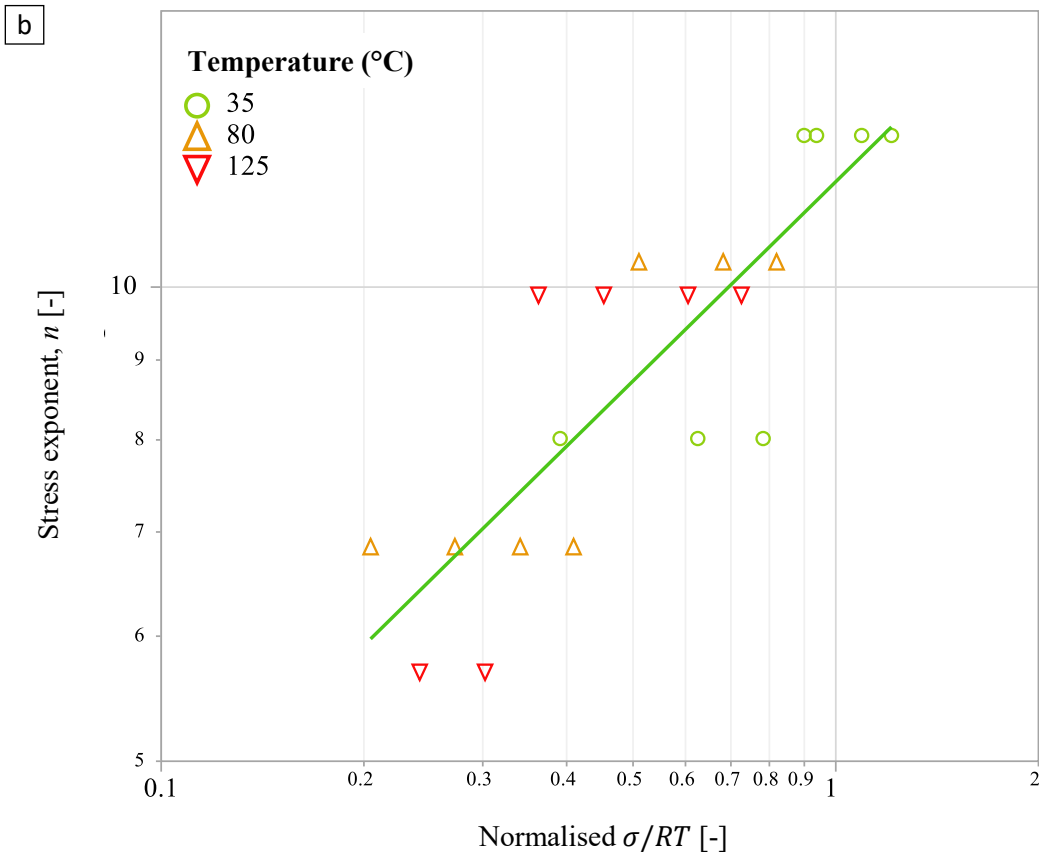
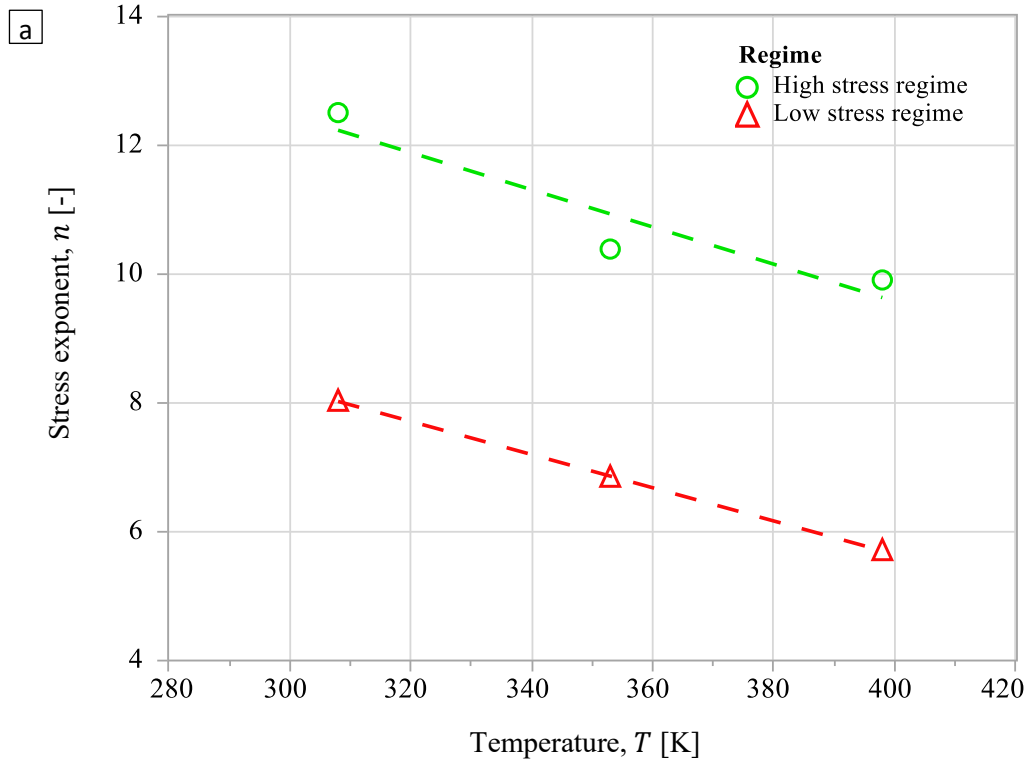


Figure 4-8: (a) Stress exponents of LSR and HSR showing steady relationship with temperature (b) stress exponents plotted versus σ/RT

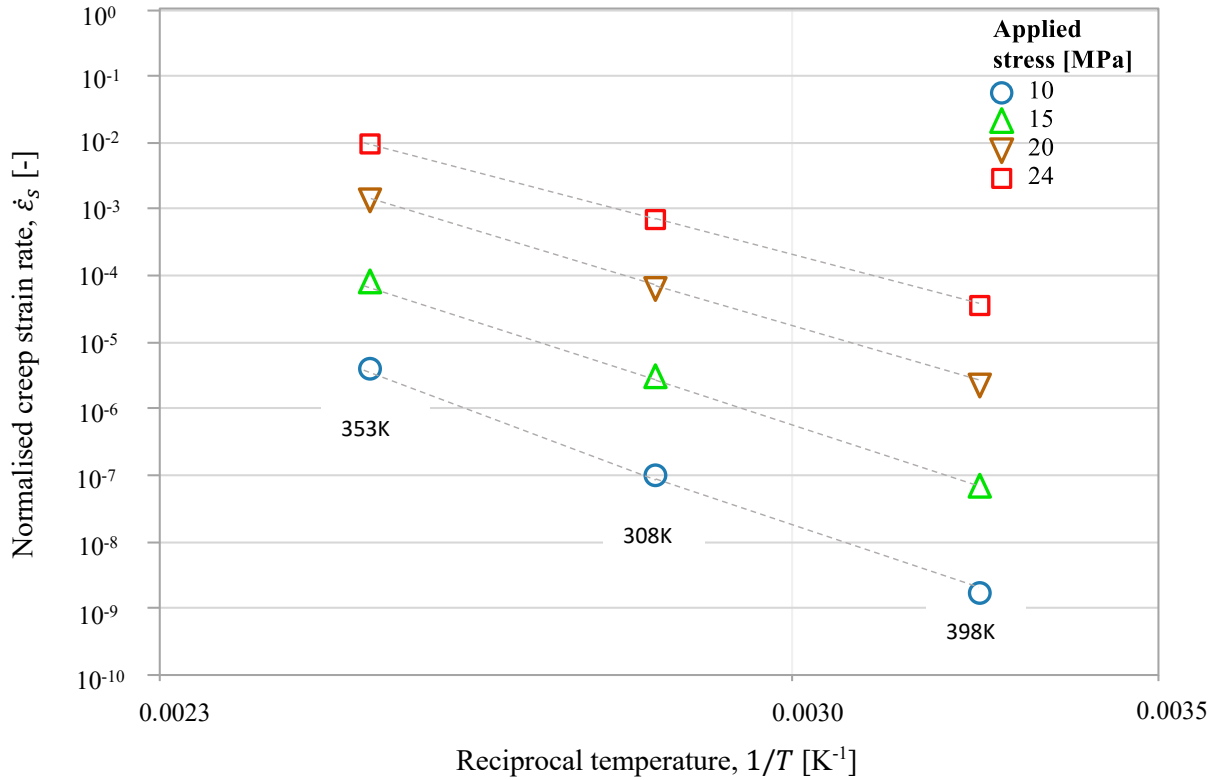


Figure 4-9: Iso-stress lines plotted for creep strain versus reciprocal of temperature to determine activation energy Q

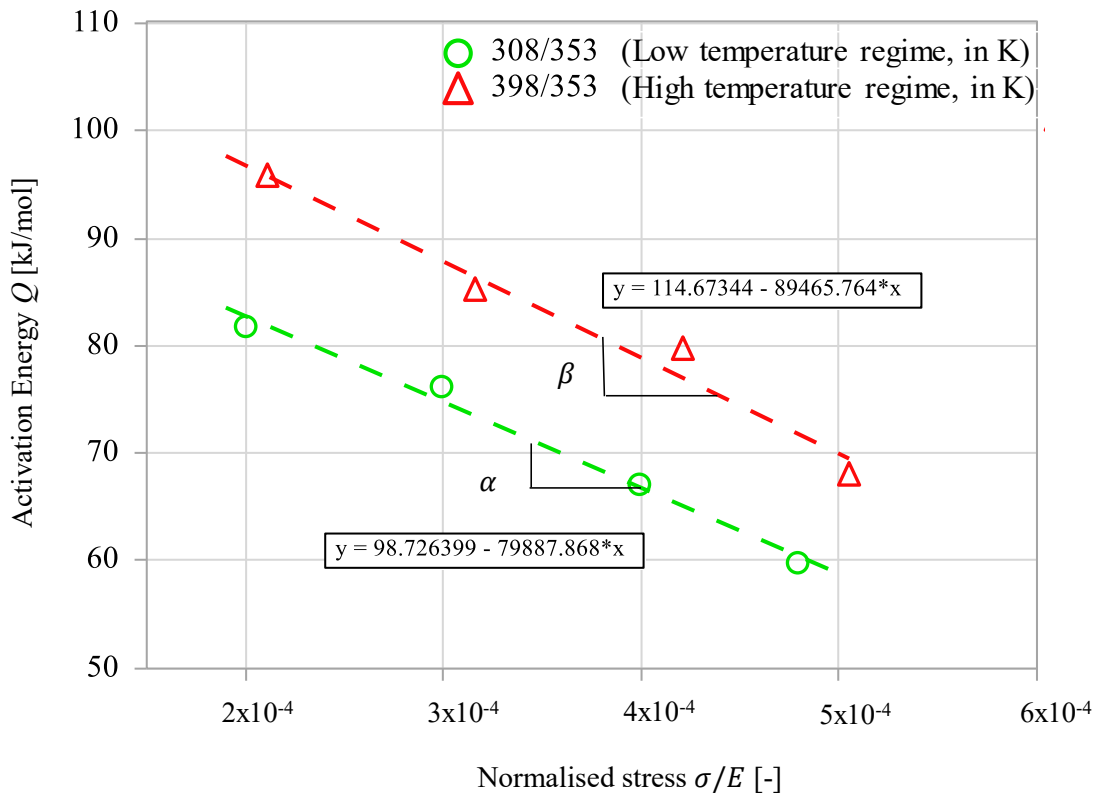


Figure 4-10: Activation energy, Q plotted against the normalised stress for high temperature range and low temperature range

From the trend observed of the results in *Figure 4-10*, it is interesting to note that the activation energy for SAC does not remain constant and decreases with increasing stress levels. It is clear that activation energy is a function of temperature and stresses. This means, at any given stress level there are more than one process that controls the creep at various temperatures. It is evident from the current study that creep activation energy of the solder alloy is a function of both temperature and stresses.

Based on the activation energy dependency observed over stresses and temperatures, the creep model is derived out in the following section. The experiments in the current work yielded activation energy value in the range of 60-82 kJ/mol at the low temperature regime (LTR, 35–80°C) and 68-96 kJ/mol values at the high temperature regime (HTR, 80–125°C). It is interesting to note that the values in the HTR are in agreement with activations energies for self-diffusion of pure *Sn* [147], where the activation energy for lattice diffusion (Q_l) is reported between 88 and 118 kJ/mol. At lower temperatures, Suh *et al.* [147] concluded that the activation energy of *Sn* (40 to 69 kJ) corresponded to diffusion along dislocation cores (Q_c).

In order to incorporate the analysed steady state dependencies of the activation energy values (Q_c and Q_l) over the stress and temperature to the creep model, a detailed work is done by Kocks *et al.* [148] and for *SnPb* alloys by Shi *et al.* [75]. Kocks *et al.* [148] explained the activation energy dependency based on Gibbs free energy theory. The activation energies required for cutting or bypassing a random obstacle for precipitation hardening alloys can be quantified by modifying Kocks original equations [148]. As seen in *Figure 4-10*, an activation energy has a linear relationship with applied stress level at any given temperature.

Therefore, for high temperature and low temperatures, activation energies are defined as follows:

$$Q_{c1} = Q_c - \alpha \left(\frac{\sigma}{E} \right) \text{ and} \quad (4.5)$$

$$Q_{l1} = Q_l - \beta \left(\frac{\sigma}{E} \right). \quad (4.6)$$

Table 10: Summarized value of activation energy related parameters (intercept and slope in Figure 4-10) with respect to the temperature

Q_c [kJ/mol]	Q_l [kJ/mol]	α [kJ/mol]	β [kJ/mol]
98.726	114.67	79887.87	89465.76

From a holistic point, creep equation written in *Eqn. (2.21)* is incapable of explaining all experimental facts, notably the changes in the activation energy as seen in *Figure 4-10*. Both, dislocation core diffusion and lattice diffusion is expected to contribute the overall diffusive transport of dislocations. One of these mechanisms becomes dominant under certain loading conditions. Hence, an effective diffusion coefficient D_{eff} is introduced to combine the two mechanisms according to Ashby and Frost [74]:

$$D_{eff} = D_l \left[1 + \frac{10a_c}{b^2} \left(\frac{\sigma}{E} \right)^2 \frac{D_c}{D_l} \right], \quad (4.7)$$

where a_c is the diffusive section of a dislocation core [μm^2], b is the burgers vector [μm]. The term $10a_c/b^2$ is treated as a SAC material constant. The power term of “2” in σ/E is an empirically determined value. Instead, the fixed stress exponent with the value of two in *Eqn. (4.7)*

in this work is treated as parameter n_2 . D_l is the lattice diffusive coefficient, D_c is the core diffusive coefficient, which can be written as follows:

$$D_l = D_{0l} \exp \left[-\frac{Q_{l1}}{RT} \right] \text{ and} \quad (4.8)$$

$$D_c = D_{0c} \exp \left[-\frac{Q_{c1}}{RT} \right]. \quad (4.9)$$

With further derivation and by combining the Arrhenius Eqn. (2.21) together with effective diffusive coefficients in Eqn. (4.7), (4.8), and (4.9), further equation is developed as follows:

$$\dot{\epsilon}_s = C_{11} \frac{E}{T} \left(\frac{\sigma}{E} \right)^{n_1} \left[1 + C_{22} \left(\frac{\sigma}{E} \right)^2 \exp \left(-\frac{Q_c - Q_l}{RT} \right) \right] \exp \left(-\frac{Q_l}{RT} \right). \quad (4.10)$$

By replacing the activation energy with the stress dependent activation energy in (4.5) and (4.6), (4.10) can be rewritten to a final form as follow:

$$\dot{\epsilon}_s = C_{10} \left(\frac{\sigma}{E} \right)^{n_1} \left[1 + C_{20} \left(\frac{\sigma}{E} \right)^{n_2} \exp \left(-\frac{(Q_c - Q_l) - (\alpha - \beta) \left(\frac{\sigma}{E} \right)}{RT} \right) \right] \exp \left(-\frac{Q_l - \beta \left(\frac{\sigma}{E} \right)}{RT} \right), \quad (4.11)$$

where E is a temperature dependent E - modulus [MPa]¹².

In this equation ($n_1 + n_2$) and n_1 are the stress exponents for the low temperature and high temperature regime, respectively, with constants C_{10} and C_{20} . The values, α and β are the slope and Q_c and Q_l , are the intercept at zero stress, analysed from Figure 4-10. E is the temperature dependent E -Modulus [MPa] analysed from the static tensile measurements, σ/E is the normalised stress and R is the universal gas constant 0.008314 (kJ/mol.K).

The activation energy Q_c and Q_l refers to the activation energies of the different creep phenomenon and the Youngs modulus, E is used to normalise the tensile stresses. In the current work, the effect on E/T [75] is investigated with and without its presence in Eqn. (4.11). The effect of $1/T$ is also used as global coefficient to take in to account of the temperature, according to Ashby *et al.* [74].

$$\dot{\epsilon}_s = C_1 \frac{E}{T} \left(\frac{\sigma}{E} \right)^{n_1} \left[1 + C_2 \left(\frac{\sigma}{E} \right)^{n_2} \exp \left(-\frac{(Q_c - Q_l) - (\alpha - \beta) \left(\frac{\sigma}{E} \right)}{RT} \right) \right] \exp \left(-\frac{Q_l - \beta \left(\frac{\sigma}{E} \right)}{RT} \right) \quad (4.12)$$

The proposed creep model in the current work is compared to the similar work of Shi *et al.* [75]. The proposed work avoids the optimization techniques (assumption of n_2 as zero) used by Shi *et al.* [75], instead introduces a subgrain-size power exponent, which will be discussed in upcoming section 4.3.3. Orowan stresses analysed in previous section (see section 4.3.1) helps in differentiating the non-linearity regime, which is used later in the creep model development in the current section. Shi *et al.* [75] who investigated similar creep equation on *SnPb* alloy is translated in the work to *SAC* alloys for the first time. The other feature of the creep equation is the possibility of using the uniaxial tensile stress σ and E -Modulus instead of shear values.

¹² Used as a normalizing factor in the current creep investigations

4.3.3 Incorporating the subgrain size dependency

One notable difference between the microstructure of specimen before and after creep is the appearance of substructure (sometimes referred to subgrain) development in individual big primary grains. At higher temperature or deformation, this subgrain formation can be visualised from the disorientation angles. More detailed fundamental explanations and its impact on creep phenomenon is explained for reference earlier in *section 2.1.7.2*. The results and discussion of selecting subgrain as a modelling parameter and the relevant justifications is briefly explained later under *Section 6.2.2*.

From microstructure study, in addition to the average subgrain size calculations, the substructure of the deformed material is frequently characterized, by averaging the subgrain structure size λ_{ss} (measured as intercept). Investigations are made on necking and non-necking regions separately. The misorientation angle of the subgrain boundaries is generally investigated as seen in *Figure 4-11*, using an EBSD (Electron backscatter diffraction). The contour plot in *Figure 4-11* represents the orientation of the grains in the bulk.

To cross-confirm random samples of different of HSR and LSR from various temperatures are analysed using Electron Backscatter Channelling Contrast as seen in *Figure 4-12 (a)*. Statistical analyses are then performed with the inverse pole figures from EBSD. The distribution of the sample direction with respect to the crystal lattice reference gives a hint of the orientation of the subgrains, which is identified, mapped, and studied further.

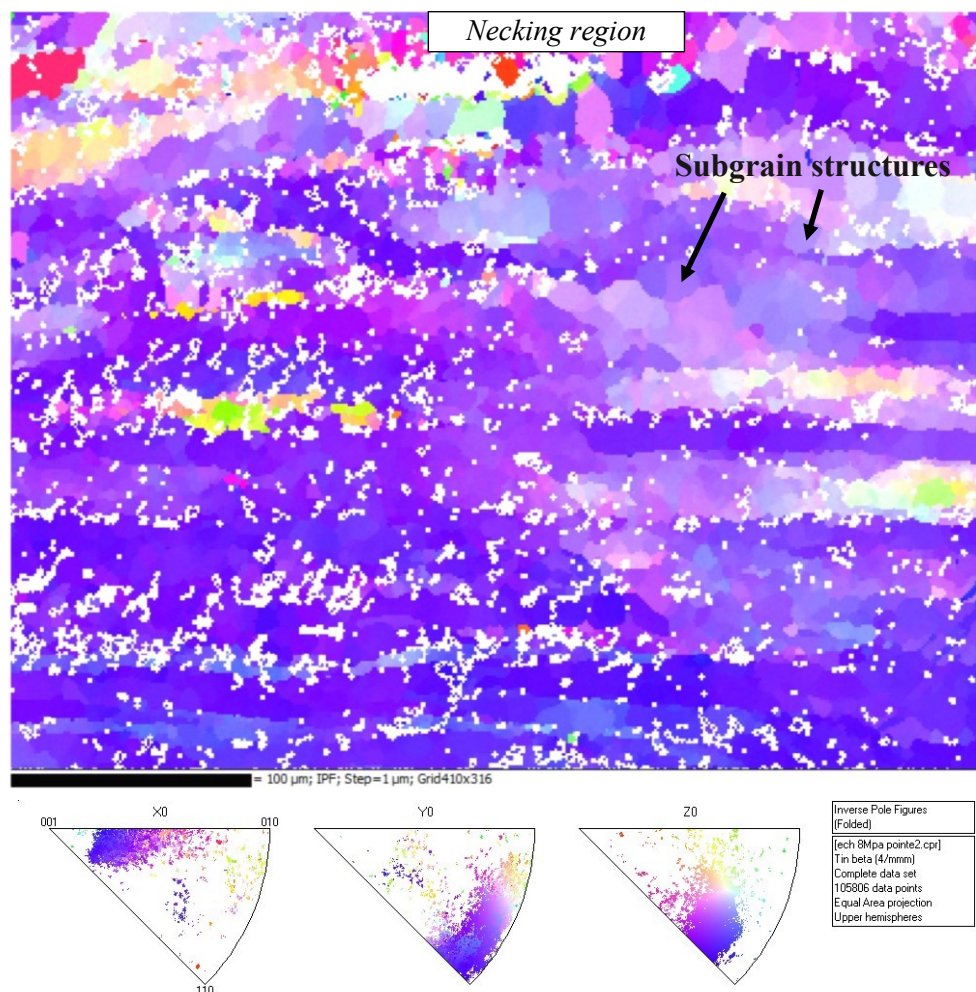


Figure 4-11: EBSD investigations of the substructure formation on a creep specimen from the necking region revealing subgrain orientations

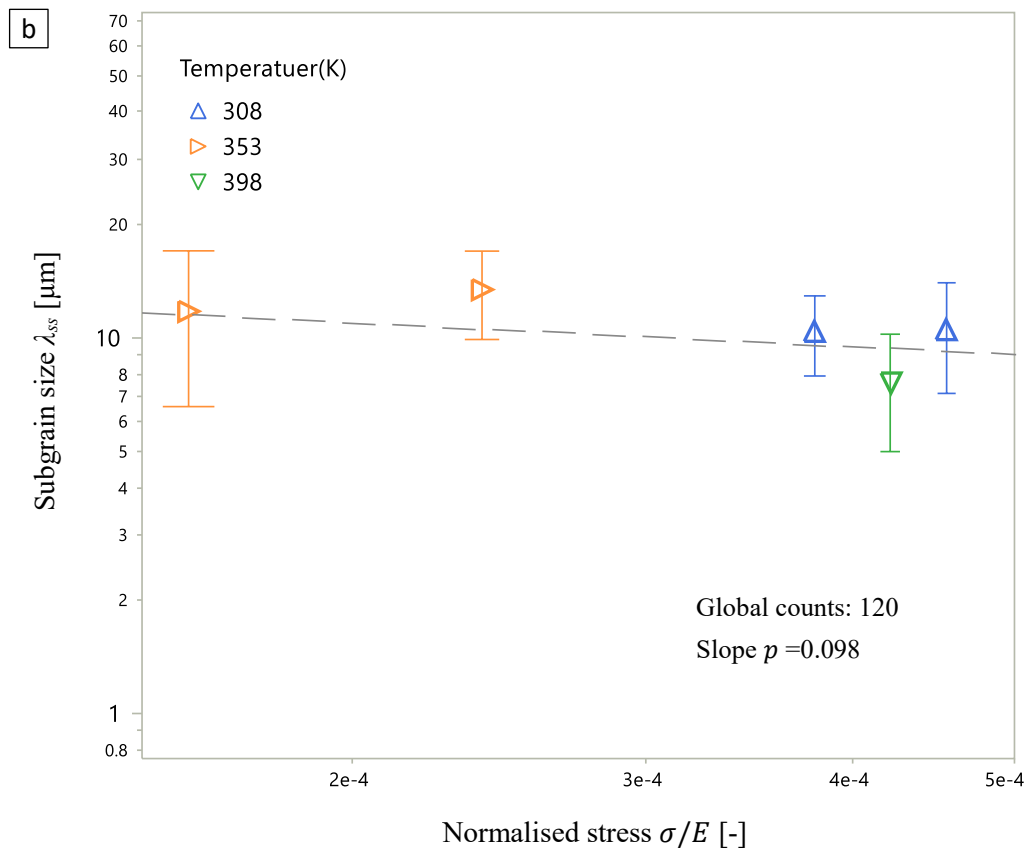
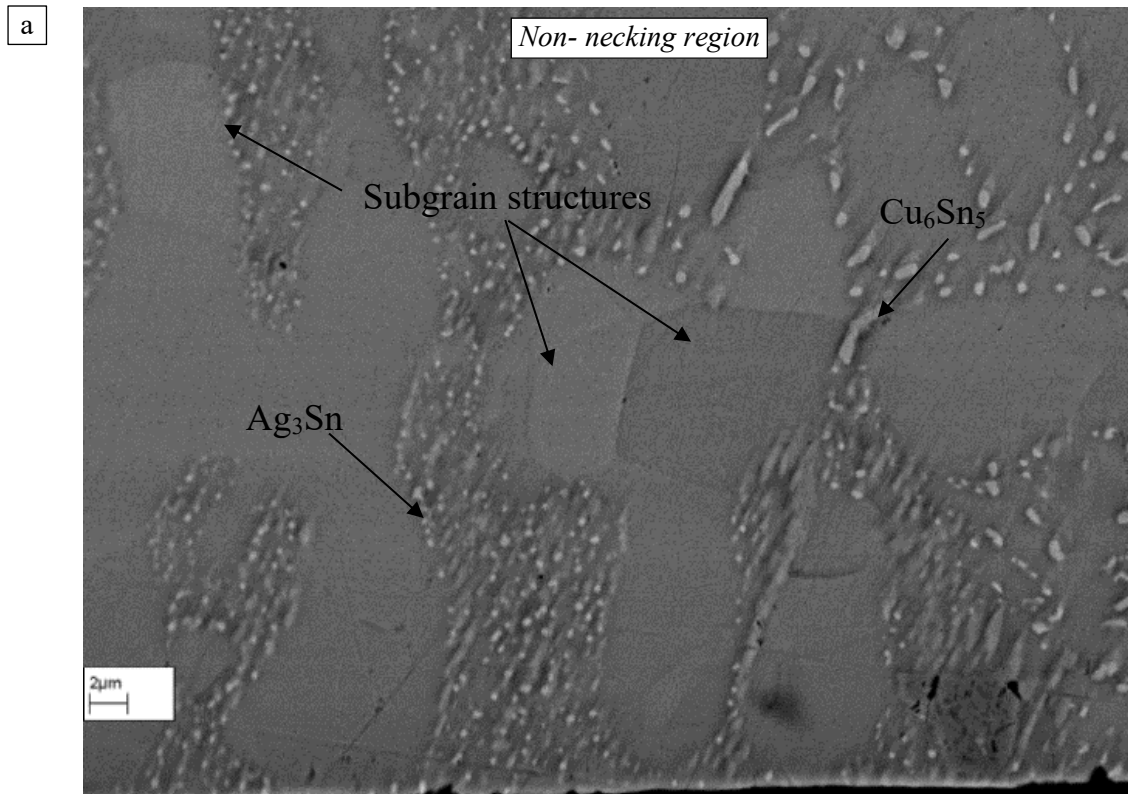


Figure 4-12: (a) EBCC image showing subgrain between dendrites on the non-necking region (b) EBCC, EBSD measurements of subgrain size measured from random samples

A maximum intercept of the polygon is used for the statistical subgrain size calculations. The EBSD statistics for both HSR and LSR shows a normal distribution with median values reaching $\sim 12.2 \mu\text{m}$. This is confirmed with a manual image analysis of Electron Backscatter Channelling contrast (EBCC). EBCC revealed a shallow slope of 0.098; almost a straight line explaining the low dependency of normalised stress against the subgrain size as shown in *Figure 4-12-b*. Statistical errors are determined as the 95% confidence intervals of mean values obtained from different samples prepared for investigation. A detailed study on the effects of creep deformation and subgrain investigations for non-necking region is investigated later under *section 6.2.2*.

The relationship between the subgrain size and the applied stress is explained in *Eqn. (2.15)* according to Kassner [67]. Subgrain exponent, p in *Eqn. (2.15)* from literatures is found to be between 0.35 to 1 [67]. However, it should be emphasized that the classical literature works are done on one-phase materials and the substructure formation for precipitate-hardened alloy like the one SAC solder, will have very less ‘ p ’ values. In other words, the subgrain size are investigated to be showing almost constant relationship over stress, for SAC solder alloy as explained from Electron Backscatter Channelling Contrast and also from the EBSD analysis, irrespective of performed experiments (temperature and stress independent). As postulated by Pharr [149], subgrain are stable even when the stress regime changes and does not involve any catastrophic break-up or elongation of cells.

To summarize, for the SAC alloy the dependency of the subgrains with stress is nearly temperature independent and is found to be minimal with stresses. The flow stress relationship with the substructure λ_{ss} (μm) is assumed constant in this investigation at any applied stress or temperature and this can be now incorporated onto the global terms (outside bracket) in the creep equation of *Eqn. (4.12)*, combining with *Eqn. (2.15)*, as a one generalised term.

As stress exponent is not a global term and being substituted by subgrain dependency, the creep model shows finite creep even at zero stress. In other words, the model shows very low finite creep (less than, $\dot{\epsilon}_s \sim 10^{-10} \text{ s}^{-1}$) because of the subgrain dependency. The model is potentially capturing a finite creep resistance due to the presence of the activated subgrain boundaries at zero stress. Moreover, this lower creep resistance values are to be neglected when the stress becomes zero.

A final equation is derived as follows:

$$\dot{\epsilon}_s = C_4 \frac{E}{T} (\lambda_{ss})^{-n_1 p} \left[1 + C_2 \left(\frac{\sigma}{E} \right)^{n_2} \exp \left(- \frac{(Q_c - Q_l) - (\alpha - \beta) \left(\frac{\sigma}{E} \right)}{RT} \right) \right] \exp \left(- \frac{Q_l - \beta \left(\frac{\sigma}{E} \right)}{RT} \right). \quad (4.13)$$

4.3.4 Comparison of creep models

The creep model for lead free alloys now can be categorised as seen in *Eqns. (4.12)* and *(4.13)* in two ways; without and with subgrain size dependency respectively.

A stepwise optimisation is done here, by splitting the *Eqns. (4.12)* and *(4.13)* into two sections, by just multiplying the global terms in with the terms inside the brackets. This allows, calculating the terms C_4 , n_1 , and C_2 , n_2 separately from *Eqn. (4.13)*. Both models are optimised with experimental actual strain rates, using similar methods to calculate the unknown parameters. Once the constants are initialised, it is possible to calculate the values C_4 , C_2 , n_1 , n_2 optimizing with the experimental values. The boundary range of stress exponent values n_1 and n_2 for optimization can be found in *Figure 4-8*.

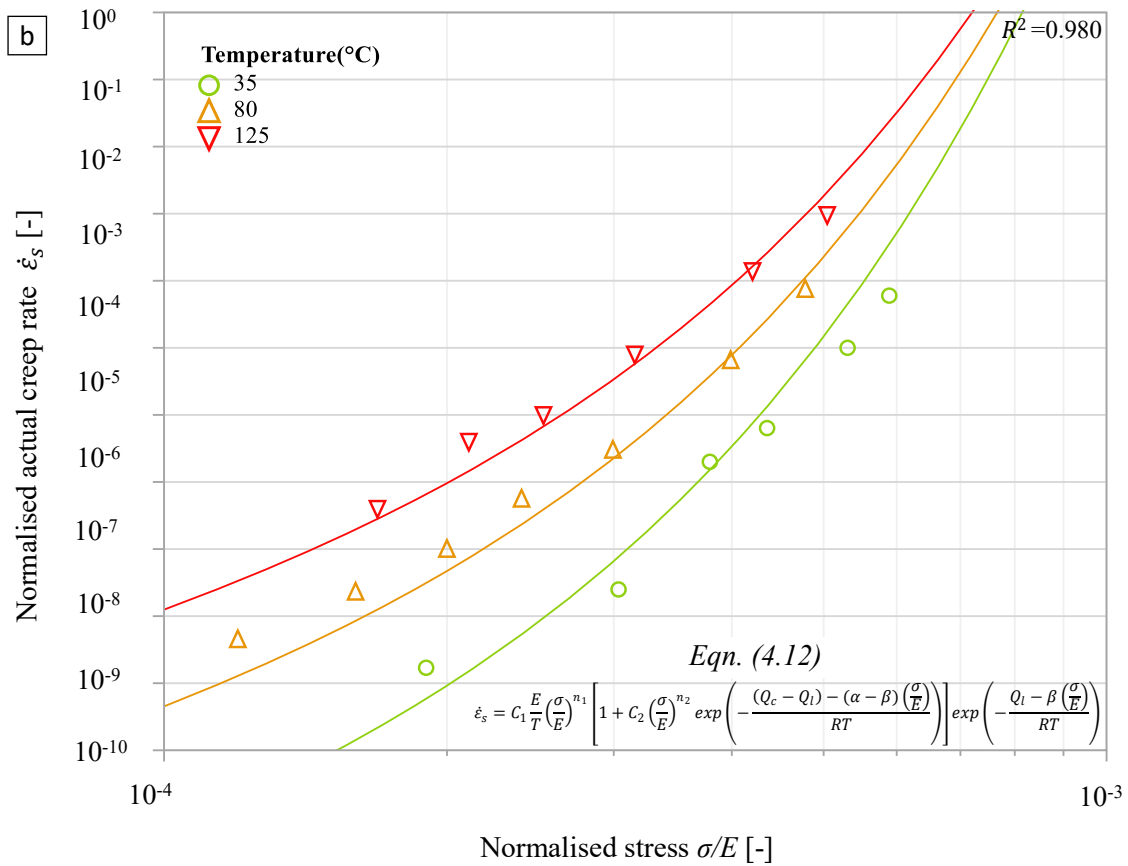
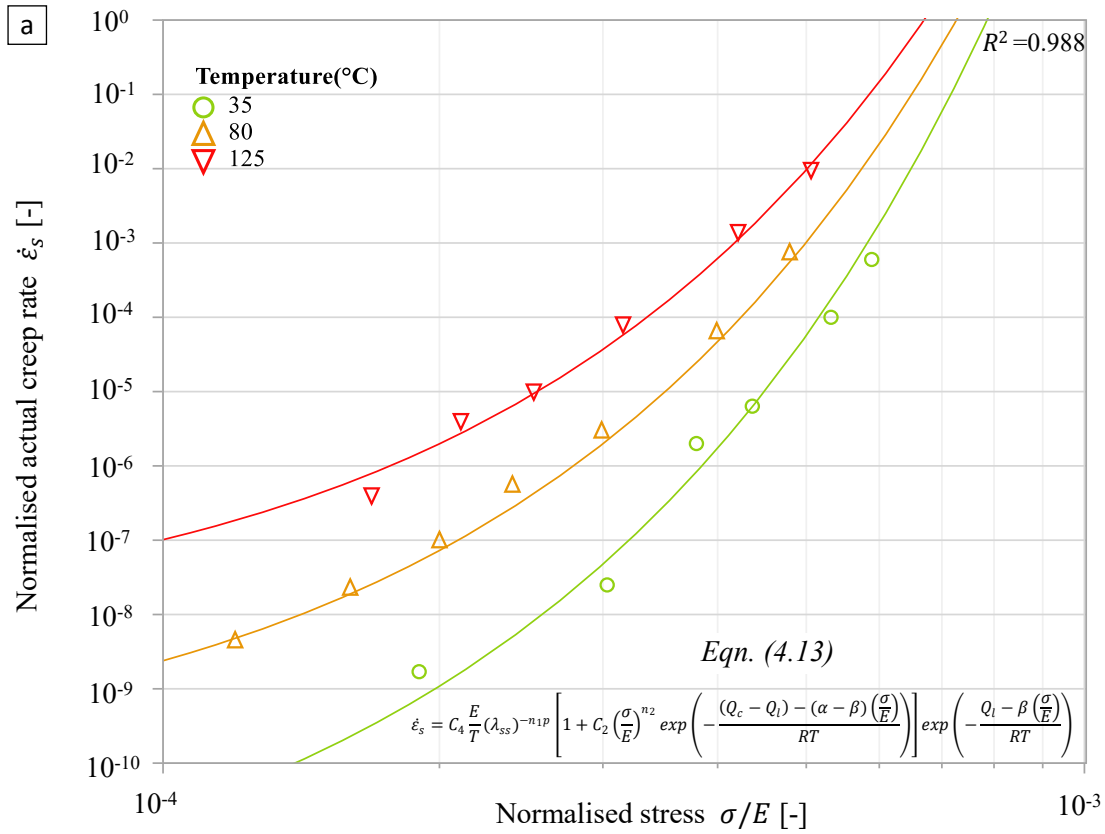


Figure 4-13: Creep strain- rate obtained from the experimental results (a) with new modified creep model incorporated subgrain size as in Eqn. (4.13), (b) without subgrain dependency as in Eqn. (4.12)

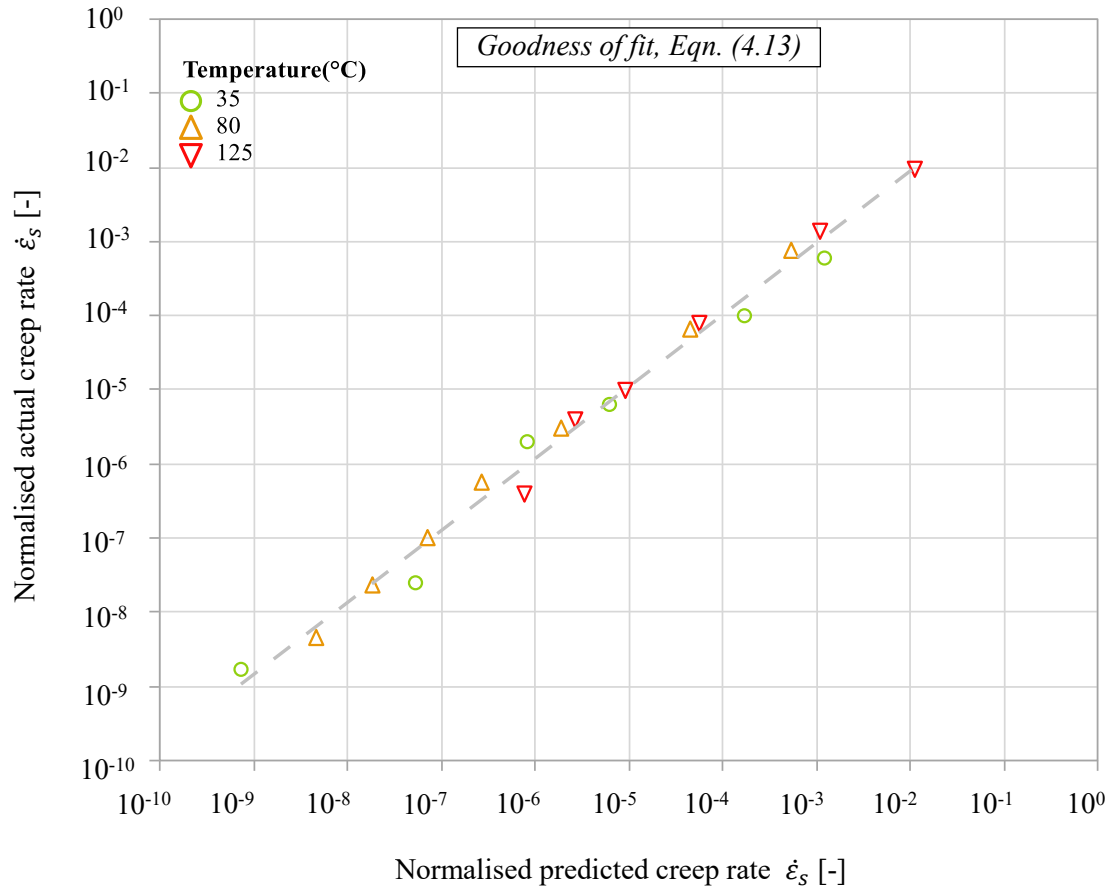


Figure 4-14: Predicted vs. actual creep strain rate for the best-fit creep model that has subgrain dependency on applied stress as in Eqn. (4.13)

Another elegance of the proposed mechanistic model is its capability to use Q value dependency as a constant value rather than as a fitting value in phenomenological models. It is emphasized that the Q value dependency factors (α , β , Q_c , Q_l) are directly determined from Figure 4-10 and incorporated in the mechanistic model. From Figure 4-13, which shows the overall optimized fits of both models, shows that the Q value dependency is well in agreement with the actual measured creep strain rates. The overall summary of the comparison between subgrain and original model is tabulated in Table 11.

The subgrain exponent, p is calculated from the relationship shown in Figure 4-12-b. The subgrain size, λ_{ss} is evaluated to have median value of $\sim 12.2 \mu\text{m}$ for SAC alloy. The nonlinear modelling with experimental values, after optimization for the modified model with subgrain size physical state variable is seen in Figure 4-13-a and without subgrain dependency in Figure 4-13-b. The corresponding actual and predicted values is plotted to estimate the R^2 values as seen in Figure 4-14. R -squared (R^2) is a statistical measure of standard deviation of data when fitting regression line as seen in Figure 4-13-a, b.

The stress exponent, n values in Table 11 are compared to the Norton and other phenomenological models. It should be noted that a direct comparison is not possible as the n values in mechanistic models are different from the Norton plot because the n_1 value in Eqn. (4.13) is used as a subgrain exponent and not as a stress exponent. On the other hand interesting to note that the stress exponents, $n_1 + n_2$ follows and establishes an approximate greater values than a “five power creep law” [67] and becomes the average value of the linear relation between stress exponent n and σ/RT in Figure 4-8-b. The same trend ($n > 5$) is also found on the Norton plot, where n values are close to be 9.5 and for Garafalo hyperbolic sine law where

the n values is found to be 6.1. These are evidences again concreting lesser significance of the powerlaw break down irrespective of the phenomenological and mechanistic models being studied in the thesis. The R^2 value of 0.988 with subgrain size parameter of the new modified creep equation is also analysed to be more accurate compared to the R^2 value 0.980 of the original model excluded with subgrain-size parameter as visualised in *Figure 4-13-a, b*. The exponent, n_1 according to model without subgrain in *Eqn. (4.12)* according to the work of Shi *et al.* [75], reported values around 2.5 for *SnPb* solder and in this work for SAC is found to be 1.4.

Table 11: Summarized values of creep model with and without subgrain size dependency

Parameters	With subgrain size, <i>Eqn. (4.13)</i> (R^2 - value = 0.988)	Without subgrain size, <i>Eqn. (4.12)</i> (R^2 - value = 0.980)
α [kJ/mol]	79887	79887
β [kJ/mol]	89465	89465
Q_c [kJ/mol]	98.73	98.73
Q_l [kJ/mol]	114.67	114.67
Norm C_1/C_4 [-]	1.2E3	3E3
Norm C_2 [-]	4.5E3	4.4E6
n_1	3.51	1.4
n_2	1.8	1.3
R [kJ/mol.K]	0.008314	0.008314
λ_{ss} [μm]	12.2	-
p	0.098	-

4.4 CREEP DAMAGE MODELS

The sole purpose of this section is to find the optimal creep rupture model for SAC alloy. The scientific importance of these methods is that, it is an important guide to investigate creep-rupture mechanisms. In the current work, three different methods are considered to analyse the creep rupture property of the SAC alloy.

Simplest of model is a Manson-Brown model [90], which correlates the relationship between the creep rupture time (t_R) and applied stresses for different temperature as shown in the graph *Figure 4-15*. Between creep rupture time and constant applied stresses at different temperatures, the results shows different slope and slight kink on each isothermal curve. The method is good only for comparing experiments tested under same temperature. At different temperatures, the results shown in *Figure 4-15* shows that the Manson-Brown model will result in interpolation and extrapolation errors.

As introduced in *section 2.1.7.3*, another parametric approach for analysing creep rupture is to use the Manson and Haferd [93] approach. This approach uses a correlation parameter according to P_{MH} denoted in *Eqn. (2.16)*. Manson- Haferd model predicted on experimental results is seen in *Figure 4-16*. The predicted model compared to experimental values shows better fit compared to Manson-brown model. However, the model is observed to show slight deviations for elevated temperature tests. Especially, the experiments at 80°C and 125°C at higher applied stress levels showed deviations from the predicted Manson- Haferd model. This can be debated to explicitly revealing different possible creep mechanism at higher temperatures and higher stresses for SAC alloys. Details of the possible creep mechanism leading to different rupture mechanism can be also understood by analysing fracture surface at higher temperatures and higher stresses. The results of creep fractography are discussed under *section 6.3*.

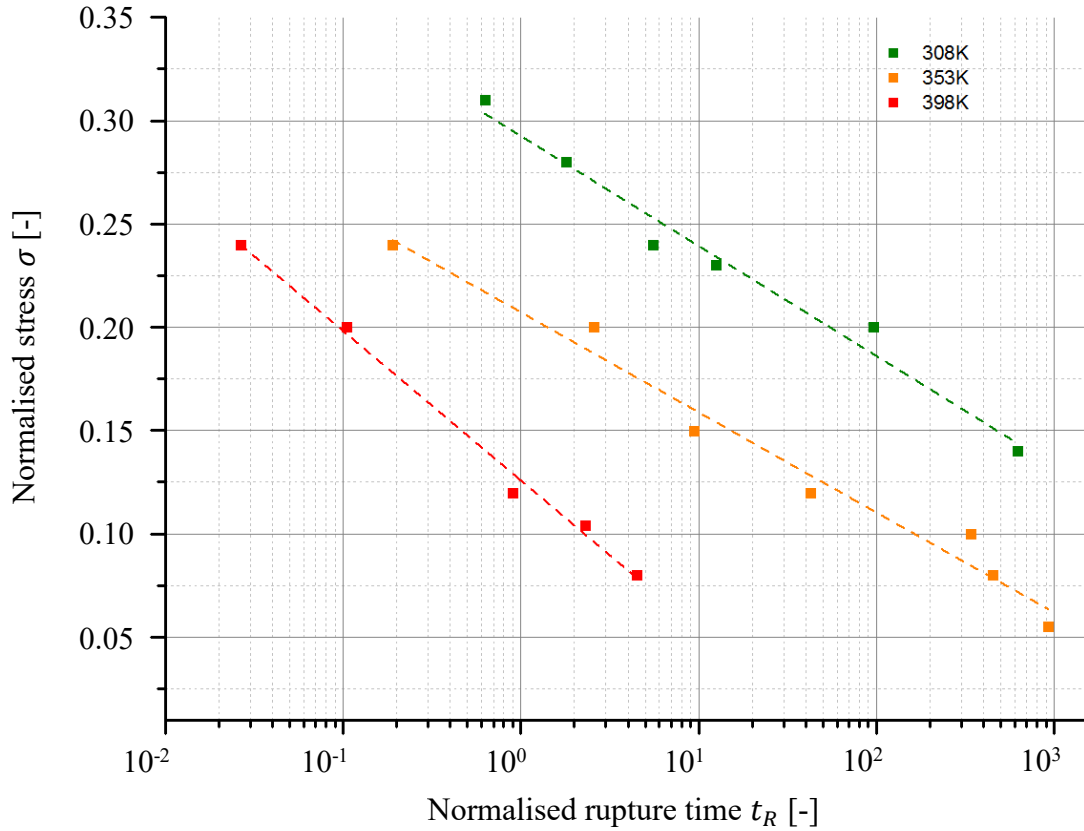


Figure 4-15: Manson-Brown model correlating creep rupture life versus different temperatures and stresses

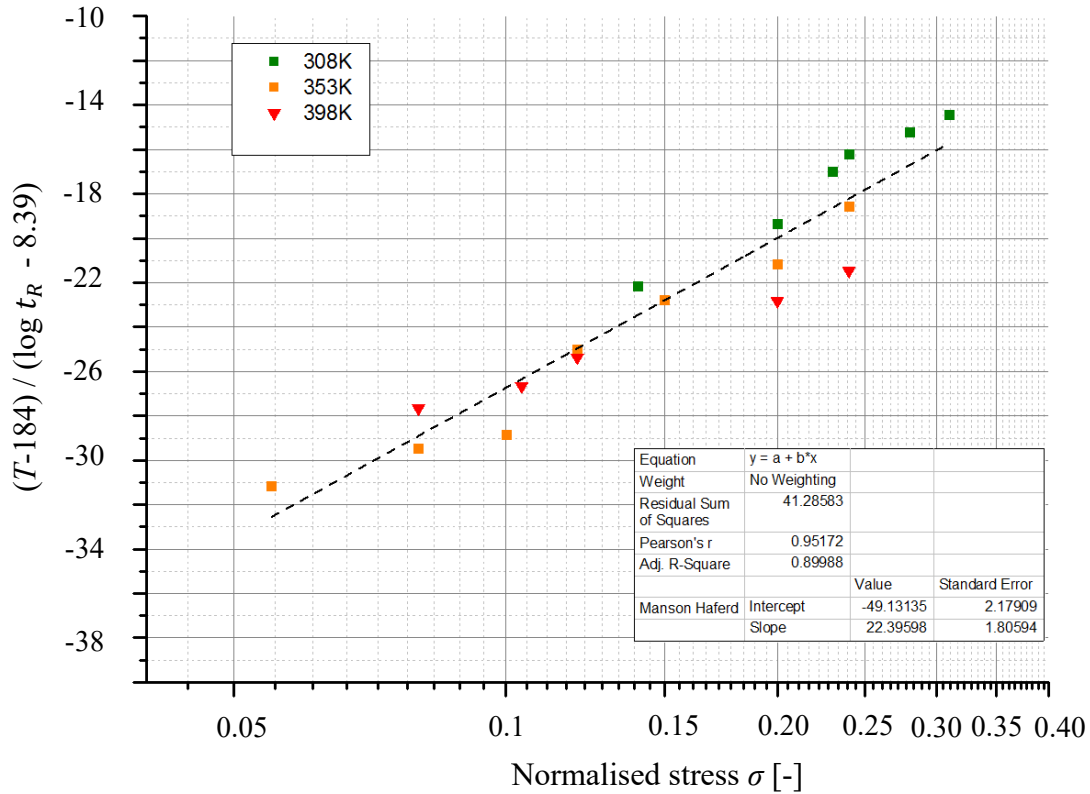


Figure 4-16: Manson-Haferd plot of $\log \sigma$ versus P_{MH} (normalised coordinates) for SAC alloy, dotted line represents the predicted model Eqn. (2.16)

Third approach of Monkman-Grant relationship [97] according to Eqn.(2.17) correlates the time to failure, t_f to the minimum creep rate, $\dot{\epsilon}_s$. The Monkman-Grant relationship is found to be the relatively better fitting method for the SAC alloy as seen in Figure 4-17. For metal and alloys originally evaluated by Monkman and Grant, the exponent, m had values between 0.8 and 0.95 [94], while the constant C varied between 3 and 20. It is interesting to note that the slope value m is found to be around 1.04, which is quite higher comparing the solder to other alloys [94]. This clearly shows that the Monkman- Grant relationship with $m = 1.04$ reflects the failure time, linearly relating to the minimum creep rate $\dot{\epsilon}_s$. Material constant C for solder alloy is found to be 1.3.

From the above comparison of all three-creep rupture models, the relationship of applied stresses and creep rupture life, seamlessly explained by the Monkman-Grant relationship have a better agreement of the experimental data. Correlation coefficient R -square value of about 0.958 is obtained from the Monkman-Grant predicted model, in comparison to the stress based relationship technique of Manson- Haferd with R -square value reaching only 0.89.

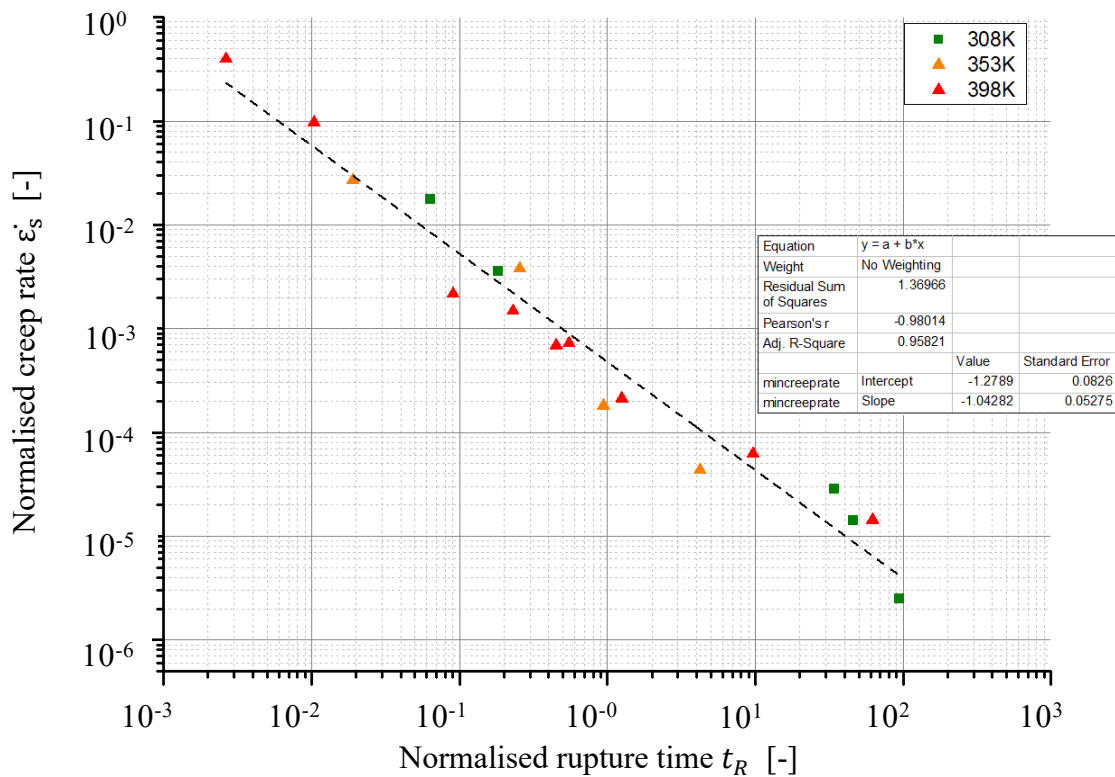


Figure 4-17: Monkman – Grant model for SnAgCu alloy correlating creep rupture against minimum strain rate: dotted line represents predicted model in Eqn. (2.17)

4.5 RESULTS & DISCUSSION

4.5.1 Benchmarking proposed creep model

Benchmarking the creep model against available creep models in literature is a first key in the validation of the proposed creep model. A classical phenomenological model such as Norton power law and well-established model in microelectronic industry such as Garafalo hyperbolic sine and double power law model is investigated in the current study. A single parameter hyperbolic model is found to correlate with experimental values much better compared to other phenomenological models investigated in the current study.

Since the hyperbolic sine model in *Eqn. (2.21)* shows a better correlation to experimental results, it is used as a reference model to compare with the proposed mechanistic model. *Figure 4-18* illustrates the comparison of the new mechanistic and Norton power law for SAC solder alloy with the Garafalo models proposed by other researches. *Figure 4-18* uses the same testing temperature (125°C) and stress levels of a SAC alloy for comparison purpose. *Figure 4-18* shows that the proposed model appears to lie in the middle of all available models for SAC alloys. Also interesting to see the current model also agrees quite well with the Garafalo hyperbolic sine model used by Xia *et al.* [150].

Once the available Garafalo model is validated with literatures, it is possible to translate the validation onto the proposed model subgrain based mechanistic model. Mechanistic model based on one parameter (single stress exponent) as per *Eqn. (4.13)*, is found to have a better fit than the two parameter (double stress dependency) creep model *Eqn. (4.12)*. As observed from the *Figure 4-13*, the two-parameter model shows deviation from the predicted model for the low temperature, low stress experiments. A similar behaviour is also observed when comparing the phenomenological based models of Garafalo and double power law under *section 4.2*. This concludes that the power law break down is less significant for the SAC alloy under investigation, from both investigations on phenomenological model and proposed mechanistic model. In addition, the one parameter creep equation is expected to predict the SAC creep behaviour more accurately especially at low temperatures and lower stresses, when compared to two parameter models. Similar finding is also made by Ma [68], where he compared a standard hyperbolic sine law to a two-parameter power-law model. Overall, one parameter subgrain based mechanistic model in *Eqn. (4.13)* is a better model to fit the current experimental data for SAC alloy with physical terms and also is benchmarked with the literature works from other researchers.

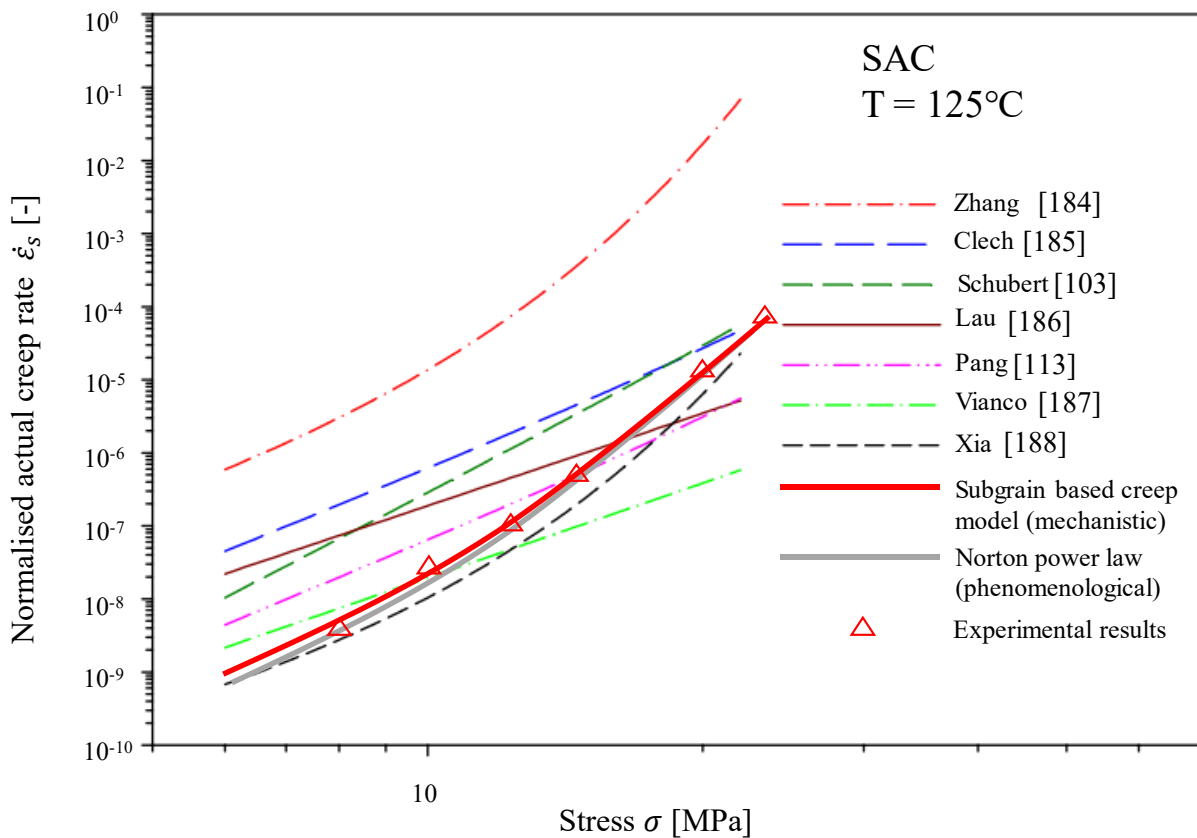


Figure 4-18: Comparison of proposed subgrain based model with other phenomenological models for SAC solder alloys at 125°C

4.5.2 Limitations of phenomenological models

Constitutive properties of selected lead-free solders are reported with literature values and current studied in *Table 7*. High discrepancies are reported in both studies for secondary creep strain rate data of a similar SAC solders reviewed from different authors. The discrepancy is mainly caused by differences in specimen geometry, testing methodology, and test conditions (varying temperature and stress levels). It is encouraged to see the references in *Table 7* for more details on test conditions and test methodology for each SAC model constant. Therefore, semi-empirical models used for capturing the constitutive behaviour from the creep data available needs further careful examination.

For phenomenological creep models, creep deformation mechanisms at different temperatures and stress levels are not describable. Even though semi-empirically calibrated phenomenological models are compact, easy to use, and necessary for applications such as finite-element modelling, it does not explain explicitly the spread of the stress exponent and activation energy values. Stress exponents (n terms) varied from 4.2 to 10.9, which is also observed in the current research study 4.89 to 12.62. The activation energy differed considerably from 43.5 to 96.5 in literature (seen in *Table 7*) and in current study from 62.5 kJ/mol to 80 kJ/mol. There are various theories postulated to explain this scatter.

Mei and Morris [76] studied the effects of cooling rate during solidification on the shear creep behaviour of eutectic *SnPb* solder joints and on the bulk specimen tensile properties. It is shown that for quenched air-cooled and furnace cooled solder joints very similar stress versus strain behaviour is observed above a strain rate of 10^{-4} s^{-1} , but below this strain rate there is a marked divergence between the different thermal treatments. The microstructure of the quenched samples is finer than the air-cooled and furnace cooled specimens.

Ranieri [77] investigated the relationship between different aspect ratios (length/thickness) and the fracture behaviour of *SnPb* solder joints. As the joint thickness decreases the aspect ratio increases and the constrained thin layer of solder can develop a hydrostatic stress component orders of magnitude greater than the yield stress of the bulk solder material. This aspect ratio effect is referred to as Friction Hill model [151].

Frear [78] studied the microstructure mechanisms of lead to eutectic *SnPb* solder joint failures in thermal fatigue for a shear configuration. The fundamental study of microstructure evolution in an actual solder joint is very complex, thus a simplified solder joint is designed that experiences simple shear upon thermal cycling. It is observed that the development of an accurate creep response for solder material under multi-axial stress is enhanced by cataloguing the grain size coarsening effect in relation to stress, strain rate, temperature, and joint thickness parameters.

Even though various theories are postulated about the scatter of physical state variable of phenomenological creep models, there are no substantiate ones to explain the cause. The drawbacks of the phenomenological models are discussable. Evidences from *section 4.2.4* and literature reviews reveals a missing physical quantity (state variable). From the application perspective, it involves the risk of over/under performance prediction of SMT solder joints, which is eventually coming from such a creep characterization.

Mechanistic models in the work is an attempt to address the above issue. Mechanistic creep models as developed in the current work explicitly addresses the fundamental drivers (e.g. subgrains) of creep deformation. The attempted mechanistic approaches models the interactions taking place in the solder joint that contribute to creep deformation, including subgrain structures, and the propagation of dislocations around, over, or through IMC particles of various compositions. For SAC alloys, the implementation of precipitate hardening and most importantly the interaction of dislocation with the obstacles appear to be the limiting factors in

modelling creep laws as introduced in *section 2.1.7.2*. This work explicitly considers the creep behaviour in case of these precipitate strengthened alloy like SAC387 ($Sn_{3.8}Ag_{0.7}Cu$), with two hardened phases of Ag_3Sn and Cu_6Sn_5 . Subgrain formation that acted as resistive element in a creep deformation are considered as a key highlight, in specific in the creep model development during later stages.

Another elegance of the proposed creep model is its ability to use the Q value dependency as a constant value rather than as a fitting value in phenomenological models. *Figure 4-13* shows the overall optimized fits of both models, revealing the Q value dependency is well in agreement with the actual measured creep strain rates.

4.5.3 Subgrain dependency

In the creep characterization, subgrain size dependency is found to be a key parameter (driver) that is decided to be implemented in the new modified constitutive model in *Eqn. (4.13)*. Evidences of the subgrains are shown in *Figure 4-11 and Figure 4-12*, which is compared with the microstructure of the specimen before creep tests *Figure 3-5*, where subgrains are not found. These new small grains could have been formed due to recovery of dislocation substructure during testing. Further analysis of the microstructure behaviour of SAC alloy during creep loading, along with the fractographs are discussed in *sections 6.3 and 6.2*. Hardwick *et al.* [152] indicated that subgrains usually form in metals and alloys, which have high stacking-fault energies, e.g. tin. The subgrains in Sn and Sn -rich phase are also observed for the creep tests on pure tin [153], and LCF tests on $SnAgCu$ [154]. Therefore, small grains observed in the current study probably should have resulted from the polygonization rather than recrystallization.

It is a critical discussion to be made on how the subgrain effect can be translated to a solder joint in an SMT application. Since no solder joint cross section analysis is done in the current study for crystal orientation and SEM works, other literatures [88, 155, 154] are used to confirm the hypothesis of subgrain driven mechanism for solder joint failure in SMT during thermal cycling (TMC).

Several literatures [88, 155, 154] are discussed in the thesis, which supported the hypothesis of a similar subgrain and recrystallization based failure mechanism in SMT component solder joint during a multiaxial state as seen in *Figure 4-19*. The present work on solder specimen at coupon level is tested under uniaxial state propels the discussion one-step ahead, where subgrain formation and intergranular cracking is observed to be a key driving creep mechanism in SAC materials.

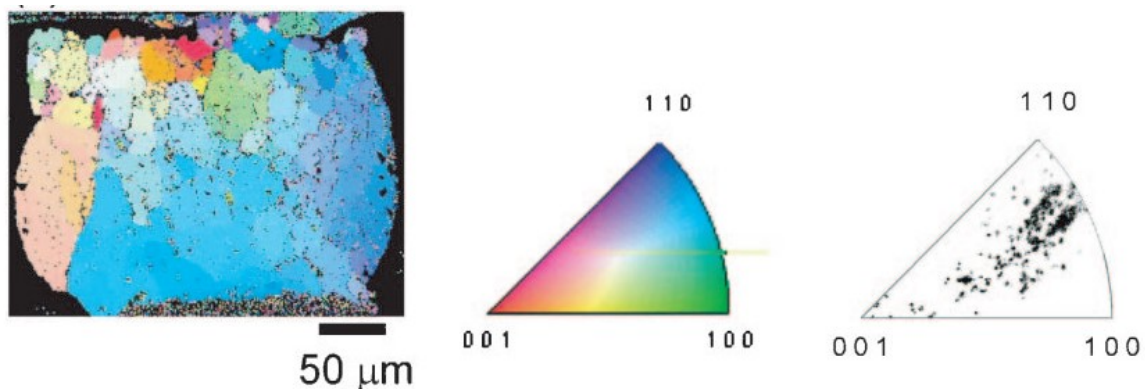


Figure 4-19: Inverse pole figure of BGA solder joint cross section after thermal cycling revealing subgrain formation during a multiaxial stress state on the stress concentration region and intergranular crack along the grain, Terashima [88]

Subgrain formation behaviour is likely to happen in a SMT solder joint according to the study of Chen *et al.* [155], and Kanchanomai *et al.* [154]. Both authors discussed the same behaviour of subgrain formation for a solder specimen in a SMT solder joint [156, 154]. As seen in the current work, the initiation of the cracks and the propagation of cracks inside the specimen occurred both transgranularly through *Sn-Ag* eutectic phases, and intergranularly along *Sn*-dendrite boundaries and/or subgrain boundaries [154]. In the SMT works of Tereshima *et al.* [88], many small angle subgrains are observed during the initial thermal cycling (TMC), which suggests that thermal strain induced these subgrains. Additionally, several primary grains are also observed where the cracks initiated.

During initial thermal cycling, cracks occurred from the edge of the solder near the solder/chip bonded interface (in this case a stress concentration). Tereshima *et al.* [88] confirmed by SEM analysis, that cracks propagated through the solder after several thermal cycling. Similar to the current work, one large general grain almost covered the solder and several small subgrains are formed near the strain concentrated locations, as seen from *Figure 4-19*. The subgrain development on the solder balls are also emphasised by Wiese *et al.* [157], based on various cooling effects and specimen sizes along with various alloys. He found that phenomenon had an abrupt change in the microstructure investigated which is in agreement with the current work.

From the SMT works of Chen *et al.* [155], the cross-polarized image and EBSD orientation map of the cross-section of the solder interconnect during initial thermal cycles are shown in *Figure 4-20-a and b*, respectively. In a localized region, many small grains are observed with varied colours (each colour represents an individual orientation). The sizes of the small equiaxed grains with various orientations range from 5 μm to 30 μm , indicating that localized recrystallization has taken place in the *Pb*-free solder interconnect.

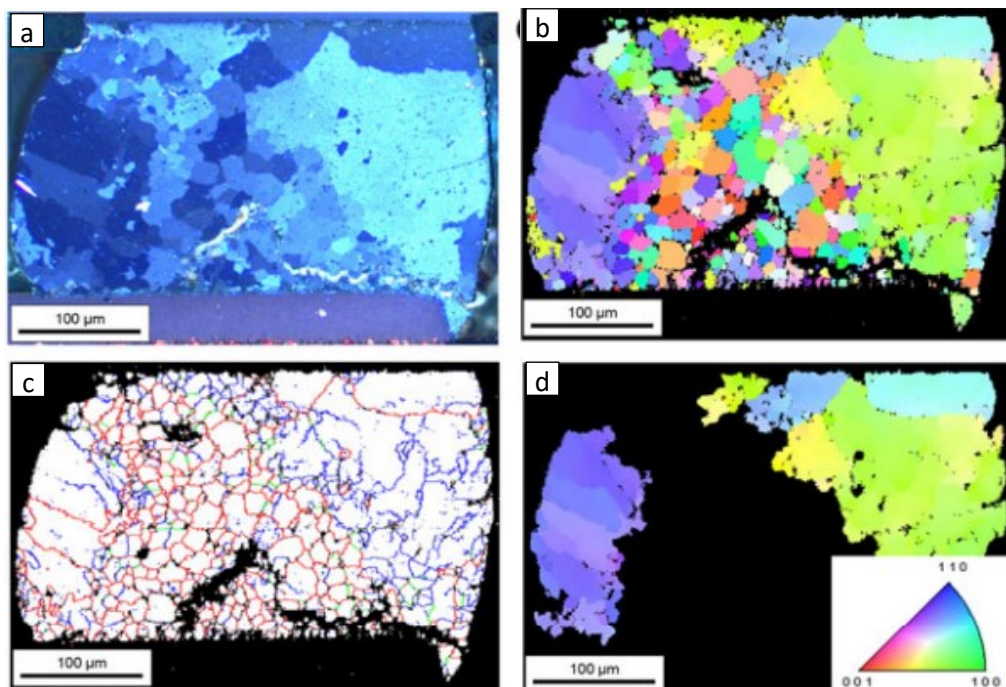


Figure 4-20: SMT subgrain formation after thermal cycling visualised by (a) cross polarized image (b) EBSD orientation map (c) grain boundary map, and (d) non-recrystallized region of SAC solder interconnects after thermal cycling [155]

In addition to the recrystallization grains as observed in *Figure 4-20-c*, many smaller grains with low-angle grain boundaries ($\sim 5^\circ$) and boundaries with disorientations between 10° and 15° are located around the recrystallized microstructures. From *Figure 4-20-b* and *d*, three predominant orientations of non-recrystallized grains are observed. It is highly likely that the original grains formed during reflow could have spread from the few predominant orientations to the random orientations in the localized recrystallized region, in which subgrain rotation plays an important role in the deformation behaviours of the solder interconnects.

Most of the above mentioned works [88, 154], revealed the smaller subgrain formations along the surface, and on stress concentrated regions. Chen *et al.* [155] being exception to report out both recrystallized grains and subgrains from a single interconnect. The sizes of the small equiaxed subgrains, λ_{ss} with various orientations, confirms the initial hypothesis for Pb-free solder interconnect. These results agree well with those obtained in this study of λ_{ss} of $\sim 12 \mu\text{m}$ from *Figure 4-12* also with previous studies [158, 159].

The proposed way of incorporating subgrain dependency and the dominant deformation mechanism with the help of micro modelling, helps in obtaining the relationship between the damage parameter for the creep model and micro-structural features. Later under *section 7.4*, a method to implement the subgrain dependency and to validate the new creep model calculation into the SMT solder joints (under thermo-mechanical cycling) that can capture the creep strain and relaxation effects on solder interconnects is discussed. The proposed mechanistic creep model will be translated into a high-level language in the form of FORTRAN codes in order to enable ANSYSTM to perform the user subroutine with new creep model will be continued in *section 7.4.2*.

4.6 CONCLUSIONS

- Phenomenological creep models reviewed in the current chapter have no explicit mechanistic dependence on microstructural features and the creep data has discrepancies across the various literatures. Therefore, the constitutive relations derived using the above models are difficult to extrapolate beyond the test conditions. The chapter reviews, discusses and attempts to show how some of the limitations can be possibly mitigated by using mechanistic or microstructurally motivated models.
- Mechanistic model based on one parameter (single stress exponent) as per *Eqn. (4.13)*, is found to have a better fit than the two parameter (double stress exponents) creep model *Eqn. (4.12)*. A similar behaviour is also observed on the phenomenological models where a Garafalo law (single stress exponent) is found to have higher correlation with experimental results when compared to double power law (double stress exponent)
- A mechanistic model on other hand based on microstructure changes is proposed in this chapter for Sn-Ag solder by incorporating the substructure size dependency in the β -Sn matrix. From a holistic perspective, in *Section 4.3*, a mechanistic model for creep proposes a micro modelling methodology to connect the microstructure explicitly to the creep response of solder, using fundamental mechanics principles. Such models not only provide physical insights into the creep deformation process but also provide understanding of the sources of variabilities in the creep deformation study. The obtained results demonstrate:
 - At low stress regimes, dislocation pass through the matrix by climbing over the second phase particles.

-
- The back stresses are found to be inversely proportional to the applied stresses. However, at the high stress regimes, dislocation are glide controlled. Orowan bowing of dislocations is expected to be the most likely mechanism.
 - The back stress or threshold stress calculated in the current study have a close relationship with precipitate particle size and volume fraction. The calculated back stress is in a good agreement with the experimental values as seen in *Figure 4-7*.
 - Systematic correlation are made between dominant creep mechanism and the parameters, activation energy (Q) and stress exponent (n) for SAC alloys, along with direct observations of microstructure at high homologous temperature under stress. Due to low melting point of SAC alloys, the thermally induced activation energy is considered primary dependency factor for creep. Therefore, in this thesis, activation energy dependency on stress is found have correlation as seen in *Figure 4-10*, which is considered in the creep model development.
 - Subgrain size is found to have exhibited approximately the same polygon size level irrespective of the temperature and stresses for the SAC solder alloy tested.
 - Implementing the subgrain size in the model *Eqn. (4.13)* in comparison to the phenomenological *Eqn. (4.12)* is found to accurately predicting the creep strain rates. The summarized parameters of both models are tabulated and compared in *Table 11*.
 - Creep damage models for SAC alloys are proposed based on best-fit models. From the investigations between the two methods based on stress and minimum strain rate as damage parameter with the experimental fit, it is apparent that the semi-empirical Monkman-Grant relationship [97] based on creep kinetics formulation have a better correlation fit with experimental data compared to other investigated models. The Monkman-Grant model exhibited relatively better regression fit as visualised in *Figure 4-17* with experimental results, when compared to other models like Manson-Haferd [93], Larson-Miller [91].

5 HIGH CYCLE FATIGUE INVESTIGATION OF SAC ALLOY

This chapter describes the HCF behaviour of *Pb*- free solder alloy studied on bulk specimens. The chapter attempts to implement a local stress approach, which can be later translated for solder joint fatigue evaluation (using FE approaches) in an application. Fatigue experiments were performed for different interaction factors under temperature, mean stress, notch factor, and surface roughness. S-N diagrams presented in the chapter will analyse the performance of $Sn_{3.8}Ag_{0.7}Cu$ solder alloy for different conditions mentioned above. Furthermore, mathematical fatigue model (SN based) modified based on FKM guideline is extracted out under all interaction factors.

Ultimately, the chapter aims to develop HCF fatigue models for SAC alloy based on FKM guidelines (see introduction *section 2.1.6.3*). Another objective of the chapter is to investigate the effects of external factors on the high cycle fatigue behaviour of SAC alloy and analyse the possible creep-fatigue interactions.

5.1 FATIGUE BEHAVIOUR OF SAC ALLOYS

The HCF results of SAC alloys are discussed throughout the contents of the chapter in three major steps as follows:

Firstly, fatigue parameters were determined from uniaxial experimental results for various load cases. The S-N (stress life) relationship was determined for various mean stresses, temperatures, surface roughness, stress gradient as introduced in *section 2.1.6.2*. The experiments were carried out in the range between 10^4 up to 10^8 cycles to failure, with a frequency of 60 Hz for all the experiments (more details in *section 3.4*). The stresses in the chapter will be referred based on low stress (LS), medium stress (MS) or high stress (HS). The classification of stresses (LS, MS, or HS) is based on the fatigue mechanisms; as fatigue dominated or fatigue with superimposed cyclic creep (see *Figure 5-1*).

Secondly, the mean strain progressions as explained in the experimental setup *section 3.4.1* based on *Eqns. (3.2) and (3.3)* were investigated throughout the course of fatigue testing. For a 60Hz fatigue cycling, machine control region were found between 100 and 400 cycles where the test equipment will control the applied cyclic waveform to the desired force level. The strain diagrams shown in the chapter only starts from the controlled regimes (~100 cycles) where the machine reaches the desired loading condition. For complete diagrams including machine control region refer to *Appendix IV*. As seen in the *Figure 5-1*, $R = -1$ (fully reversed cycle) had a macroscopic type failure when compared to the solder behaviour under R -ratio of 0 (tensile dominant cycle) and -3 (compression dominant cycle), where a gradual increase in the plastic strain is observed before the complete failure. Experiments other than at $R = -1$ showed a clear plastic strain development and related failure from plasticity. The strain tracking during fatigue experiments from the samples show indications of the possible different failure modes. Therefore, measured local strain during fatigue cycles were studied with variants of mean stress, temperatures and stress amplitudes to observe any possible cyclic softening or hardening effects (introduction in *section 2.1.5*). The results of cyclic softening/hardening will be discussed together with the micrographs and strain amplitude observations in this chapter.

Finally, fatigue models with the influence of the external factors will be modified based on Basquin equations *Eqn. (2.5)* for the purpose of local stress based lifetime prediction. As mentioned in *section 2.1.6.3*, guidelines from FKM version 2003 [37] were used to perform various modifications and corrections, as the SAC alloy material constants have to be determined for roughness, stress gradient, and mean stress. FKM guidelines based on 2003 version [37] were

used in the current study, as the software (used in this investigation- nCode Designlife™) is still based on 2003 version.

Since fatigue failure results from complex loading conditions involves a series of complex processes, the results and discussions are divided into four major sections, each dealing with one of the fatigue damage processes, namely, cyclic deformation, cyclic softening, fatigue crack initiation, fatigue crack growth, and fatigue lifetime.

The results and discussions are contained within the four sections based on external factors that determines the fatigue life for SAC alloy:

- fatigue property under temperature variants,
- fatigue property under mean stress influence,
- stress gradient effects,
- effect of surface roughness.

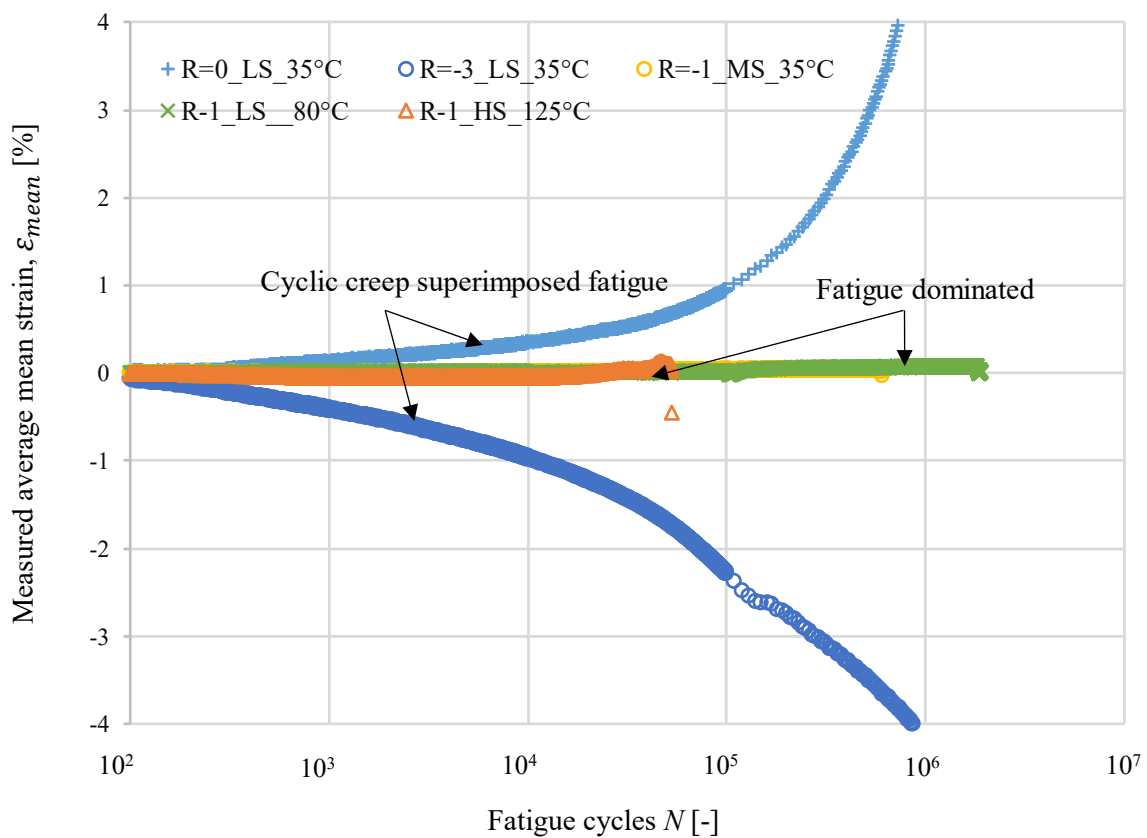


Figure 5-1: Average mean strain progression- Eqn. (3.3) of the solder specimen over lifetime for different load cases, temperatures and stresses- high stress (HS), medium stress (MS), low stress (LS)

5.1.1 Fatigue property under temperature variant

This section discusses the results of fatigue property during various temperatures. Figure 5-2 shows the relationship between the stress amplitude and fatigue life of the bulk solder $Sn_{3.8}Ag_{0.75}Cu$ alloy at different temperatures (35°C, 80°C, and 125°C). Each measured data point represents the final cycle to failure.

The effect of temperature on the mechanical property of *Pb*-free solder alloy is observed in literature and is discussed to be associated with the microstructural transformations of the material, which may lead to cyclic softening, subgrain formation, intergranular cracking etc., [55,

63]. The correlation between the cycles to failure, N_f and stress amplitude $\Delta\sigma$ for various temperatures can be quantified with the fatigue constant (b or slope) and the fatigue strength coefficient σ_f according to Basquin's equation, Eqn. (2.5) [43, 44]. The equation of the linear bivariate regression fit is obtained and plotted in a log-log space as seen in Figure 5-2. Fatigue strength coefficient, σ_f and fatigue constant, b from the S-N diagram for different temperatures are summarized in Table 12.

Higher fatigue resistance of the solder alloy is observed with the decrease in the nominal stress amplitude and temperatures (see Figure 5-2). This can be explained by the different slope value, b of the Basquin equation, with fatigue resistance being less sensitive at room temperatures. The different slope values of Basquin equation in Figure 5-2 also gives a clear evidence of the possible fatigue mechanisms for SAC alloys [8]. The differences in the slope behaviour in Figure 5-2 is further investigated by understanding the microstructures and observing the measured strain in Figure 5-3. A detailed discussion on further microstructure studies and the slope change behaviour of alloy is continued in next chapter under section 6.4.

Table 12: Tabulated fatigue parameters of the Basquin Eqn. (2.5) for different temperatures (log-log scaling)

Temperature [°C]	b	Normalised σ_f [-]
35	0.113	0.30
80	0.085	0.47
125	0.066	0.94

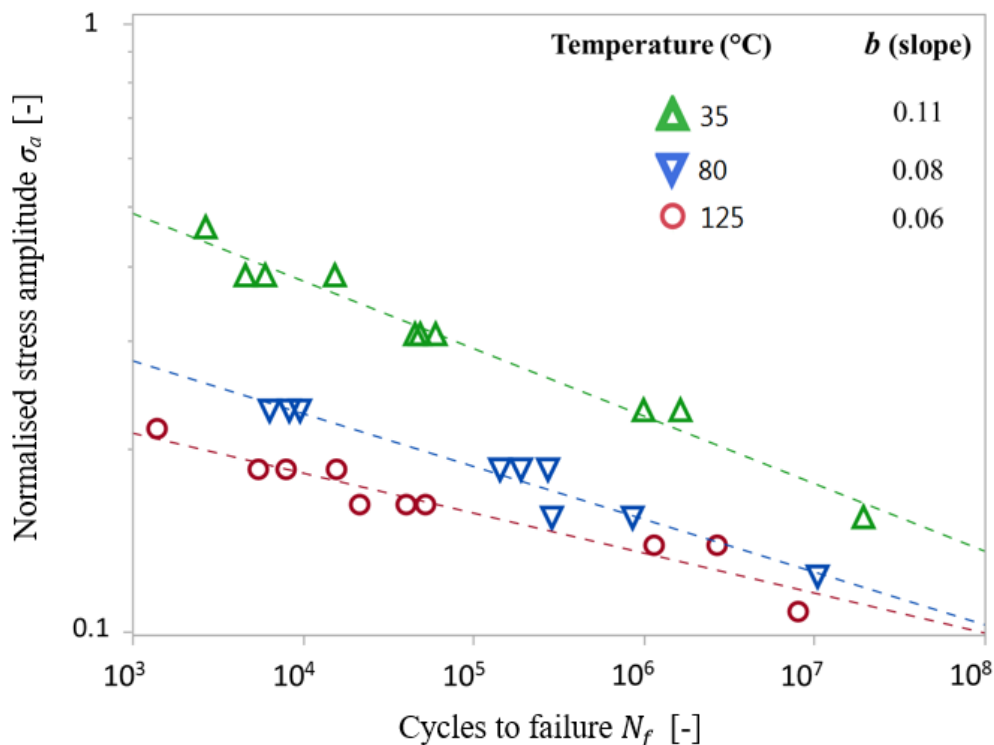


Figure 5-2: Normalised nominal stress amplitude vs. fatigue life (S-N) for different temperatures at 60 Hz, $R=-1$: symbols represent measured points and dotted line shows the fit based on Basquin Eqn. (2.5)

Development of cyclic softening at elevated temperatures can be also confirmed from the strain measurement, as per strain amplitude Eqns. (3.2) and (3.3), plotted in Figure 5-3 for various temperatures. As visualised in Figure 5-3, all experiments at temperatures, 80°C, and 125°C shows the effects of cyclic creep. At room temperature 35°C, phenomena of cyclic saturation is observed and not so significant pronounced cyclic creep is seen. This is because the applied temperature is less for a higher rate of recovery to get the effects of cyclic creep. When observed at 80°C and 125°C, there is significant development of cyclic creep behaviour superimposed as the thermal activation for the recovery phenomenon is higher compared to the tests at 35°C. At 125°C, the thermal activation for diffusion-based recovery becomes higher compared to the 80°C, thereby the cyclic creep behaviour becomes more pronounced.

SEM analyses on fracture surfaces are used to confirm the fracture mechanisms between higher-lower stresses and higher-lower temperature matrix. All fracture surface specimens are investigated qualitatively for crack initiation and propagation region until higher stress regions. The thread of this discussion can be followed in next chapter under section 6.5.

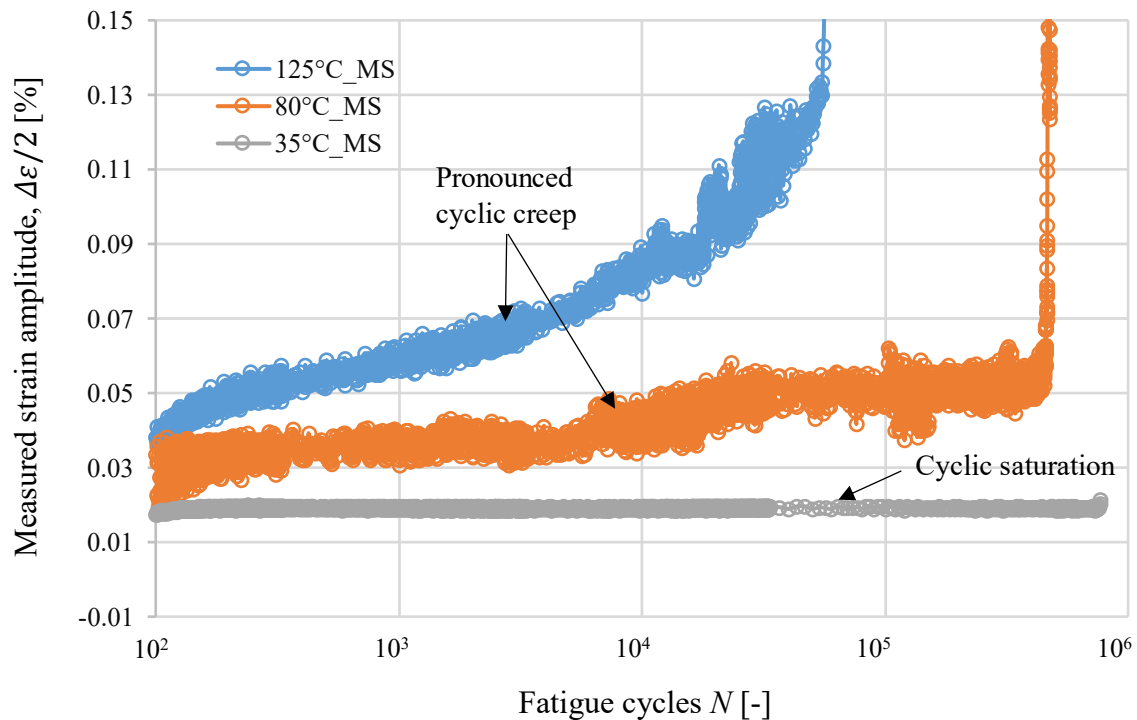


Figure 5-3: Cyclic true strain amplitude measured, $\Delta\epsilon/2$ as per Eqn.(3.3) vs. cycles for solder alloys subjected to completely reversed load at $R = -1$ for different temperatures, at medium stress (MS)

5.1.2 Fatigue property under mean stress influence

In this section, the fatigue behaviour of the solder alloy for different R - ratios (mean stresses) are investigated as seen in Figure 5-4. Fully reversed ($R = -1$), pure tension ($R = 0$), and compression-dominated load ($R = -3$) are considered in the current study. The fatigue lives at the three different scenarios of mean stresses are found to be decreasing, as the tensile fatigue load dominates. The values of the fatigue strength exponent b are calculated and investigated. It is interesting to observe that the R - ratio experiments tend to show approximately the same value of fatigue strength exponent, b of ~ 0.1 that is common for all of the three different stress ratios. The fatigue strength exponents for all R -ratio are tabulated in Table 13.

To understand the behaviour of mean stress the slope values of Basquin equation are used again for discussion. For mean stress fatigue results, the slope values, b seen in *Figure 5-4* and *Table 13* are not significantly different (~ 0.1) under tensile and compression dominance cycling. This could be due to a similar failure mechanism by means of local tensile residual stresses [127]. In case of $R = -1$, it is assumed that the micro cracks are closed under a compression load, but due to plasticity in the wake of the crack, failure occurs on tensile stresses. Whenever, the solder specimen is subjected to a higher compressive load ($R = -3$), there can be a significant plastic strain in the compression with local tensile residual stresses at the root of the crack tip as a result. In other words, compressive stresses will not cause crack initiation or propagation, compressive loads may result in local tensile stresses [127]. Also, if the cycle is compression dominant ($R = -3$), the possible formations of intrusions/extrusions from persistent slip bands (PSB) and the crack initiation is slowed down or at least substantially delayed. Thus, even though the cycle is under compressive stress, crack initiation and crack growth could be due to the presence of residual tensile stress field near stress concentration [127, 160] and eventually leading to same slope as seen in the *Figure 5-4*.

Table 13: Tabulated fatigue parameters of the Basquin equation Eqn. (2.5) for different R-ratios (log-log scaling)

R-ratio	b	Normalised σ_f [-]
0	0.101	0.17
-1	0.112	0.34
-3	0.111	0.57

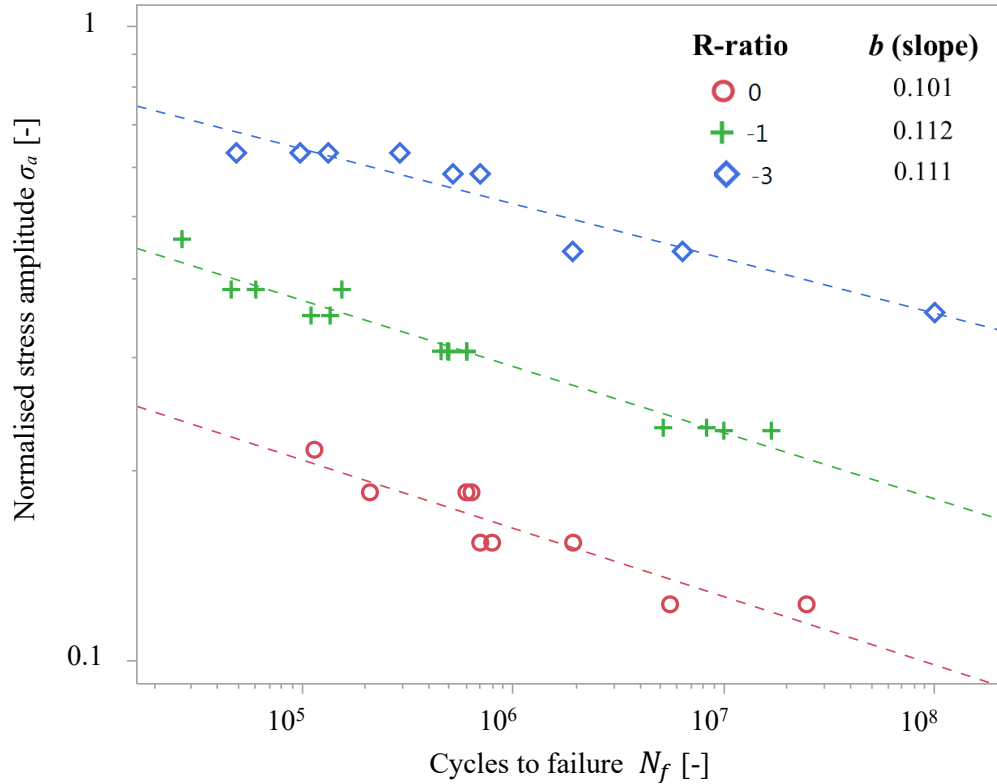


Figure 5-4: Normalised nominal stress amplitude vs. fatigue life (S-N), for different stress ratios subjected to fatigue loading at 35°C and 60 Hz: symbols represent measured points and dotted line corresponds to the fit based on Basquin Eqn. (2.5)

On the other hand, when the solder specimen is subjected to a tensile load ($R=0$), there can be a significant tensile plastic strain reaching the maximum tensile load, resulting in higher local tensile residual stresses at the root of the crack tip. This reduces the fatigue easily for SAC alloys compared to the other R ratios.

The pronounced cyclic creep effects are not highly significant on the mean stresses at room temperature, but certainly associated with the cyclic saturation for most of the lifetime as seen in *Figure 5-5*. However, at higher stresses, a minimal non-linear strain evolution is observed around 70% of N_f as depicted in *Figure 5-5*. The cycle-dependent softening has also been observed in ferrous and aluminium alloys for different mean stress experiments [161]. However, the behaviour in those alloys is typically transient, that it appears during the initial stages (a few hundred cycles) after which the peak stress becomes stable. In contrast, cycle-dependent softening (cyclic saturation) in SAC alloys persisted constant over most of the fatigue life until the final fracture. In other words, for room temperature, SAC alloys demonstrated cyclic saturation for most of the fatigue test time. The mean stress effect investigations at elevated temperatures ($> 80^\circ\text{C}$) is out of scope of this work. The strain progression measurements in *Figure 5-5* is similar to creep strain when a constant static load is applied as seen in *Figure 3-8*. In other words, a cycle dependent softening is comparable to the time dependent creep deformation under constant stress as discussed in *section. 4.1*.

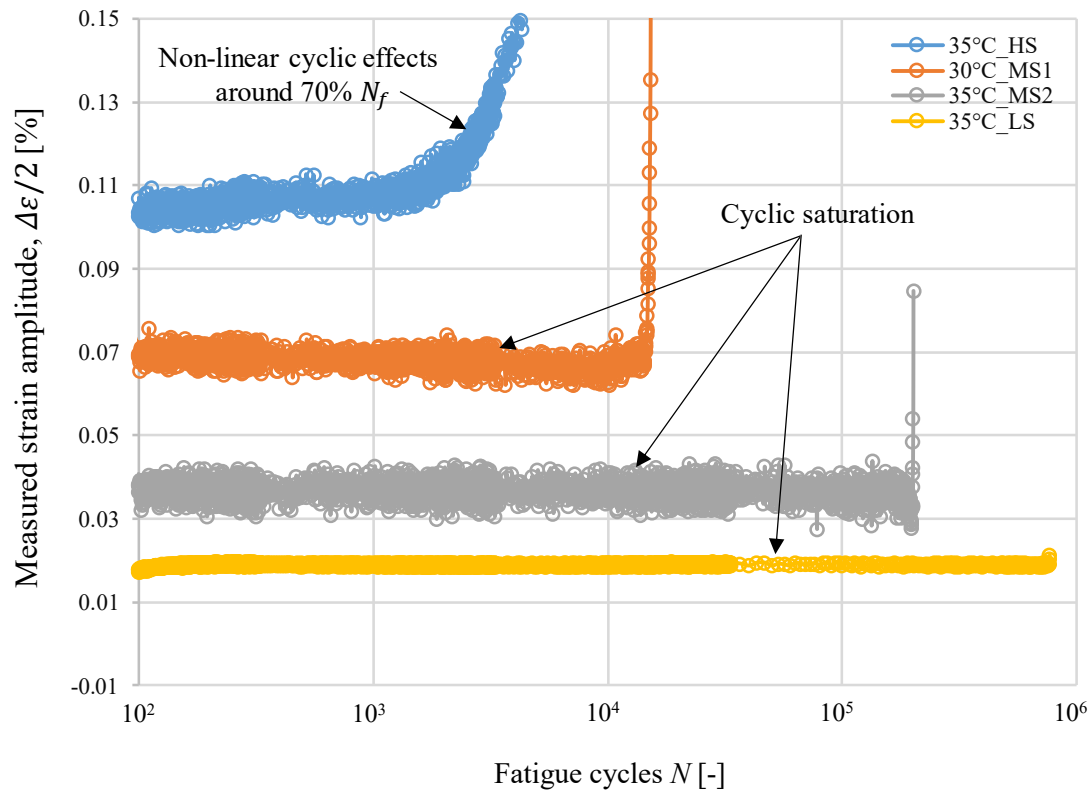


Figure 5-5: Strain amplitude measured $\Delta\epsilon/2$, as per Eqn.(3.3) vs. cycles subjected to $R=-1$ at 35°C , Low stress- LS, Medium stress-MS and High stress HS

At smaller strain amplitudes, $\Delta\epsilon/2$ of ~ 0.025 to 0.075 % (irrespective of stress amplitude), no remarkable cyclic softening is observed. Fatigue lifetime may be divided into extremely slow damage accumulation steps and a faster crack growth process at the end of lifetime close to $\sim 98\%$ of N_f . However, when the strain amplitude $\Delta\epsilon/2$ reaches a steady-state level of $\sim 0.1\%$ as seen in *Figure 5-5*, small in-fluctuation point changes in the strain pattern is observed at approximately 70% of the lifetime.

Figure 5-6 is extracted from Figure 5-4, to form a 3D graph with scatter matrix along with points that are missing by interpolation of input data limits. The four corners of the 3D-graph can be visualized to see the extrapolated influential parameters from the mean stress and stress amplitude on to the fatigue life of the SAC387 solder alloy under investigation.

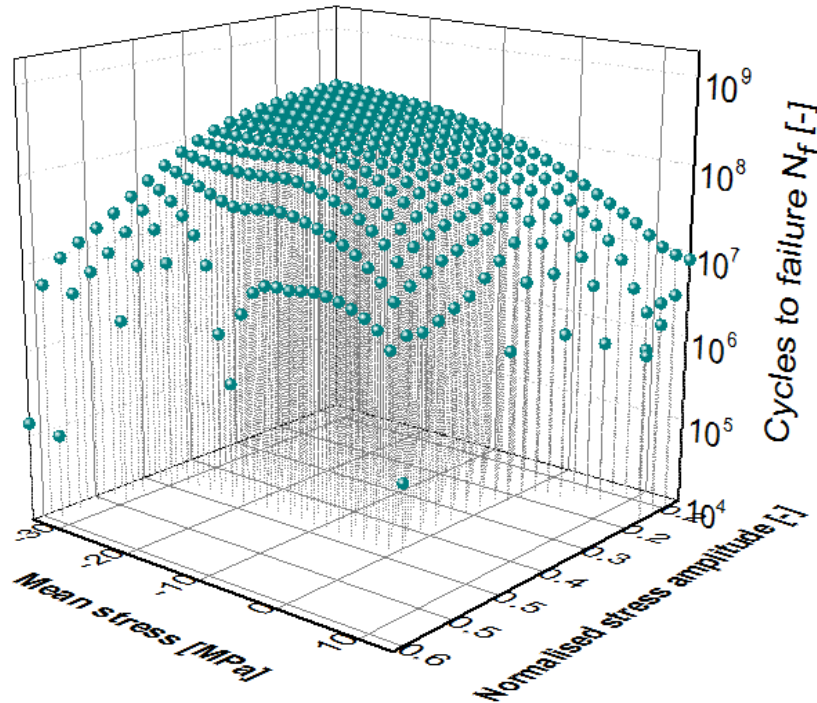


Figure 5-6: 3D- matrix scatter of the two parametric damage property of SAC387 solder under mean stress and normalised stress amplitude

To quantify the influence of the mean stress over a whole range of cycles to failure from LCF regime to the HCF, an extensive number of experiments are required. This can be incorporated by considering Haigh fatigue strength diagram as introduced in the *section 2.1.6.2*. Since no definite fatigue limit (endurance limit) is found for SAC solder alloy, a constant life Haigh diagram is used at $N_f = 10^8$ [40, 44]. A Haigh diagram plots the mean stress (σ_m), along the x -axis and the oscillatory stress amplitude (σ_a) along the y -axis. Lines of constant life are drawn through the data points. In order to compare the fatigue strength under a dynamic cyclic and static load, the static tensile load experimental results are compared with the fatigue strength diagram.

The construction of Haigh diagram (Figure 5-7) is detailed as follows: Firstly for the highest number of cycles to failure ($N_f = 10^8$) tested, corresponding stress amplitude σ_a and mean stress σ_m is identified and correlated. For e.g. from Figure 5-4, in a fully reversed load ($R = -1$) scenario, normalised stress amplitude to reach a failure of $N_f = 10^8$ cycles is 0.19 [-]. The same procedure is followed for other R - ratios measurements.

A safe¹³ dynamic region of designing SAC material can be visualised using such methodology seen in Figure 5-7. As per FKM guidelines, orange solid line visualised in Figure 5-7 is a safe threshold line, where the effective safe stress values are decided based on the available mean

¹³ For a material that has endurance limit, this indicates the region of finite and infinite cycles. In the current study for SAC alloy this denotes at least 10^8 failure cycles

stress. In other words, inside the safe boundary line (orange), the material is expected to reach a minimum of 10^8 failure cycles.

This technique of mean stress corrective measures are followed according to FKM guideline [37] that can be used in the FE- based fatigue evaluation as introduced in *section 2.1.6.3*. If there are no experimental data available for materials or if the R -ratio is beyond the experimental range, FKM guidelines with mean stress corrective factor (M) can be used.

For region ($-3 < R < 0$), experimental results are used which is seen with the orange dotted-solid line (from linear regression) as seen in *Figure 5-7*, to evaluate the effect of mean stress. Rest of the regions ($R > 0$, $R < -3$) are estimated according to FKM guideline and the overall results are tabulated in *Table 14*. Since no particular experiments were performed under the extreme compression loads ($-3 < R < -\infty$), mean stress effect is extrapolated until $R = -\infty$. If the stresses are observed structurally in compression and tensile mode in microelectronics applications, the mean stress considerations as explained above need to be made cautiously. The values of the mean stress sensitivity based on FKM guideline is tabulated in *Table 14* for different R -ratio ranges.

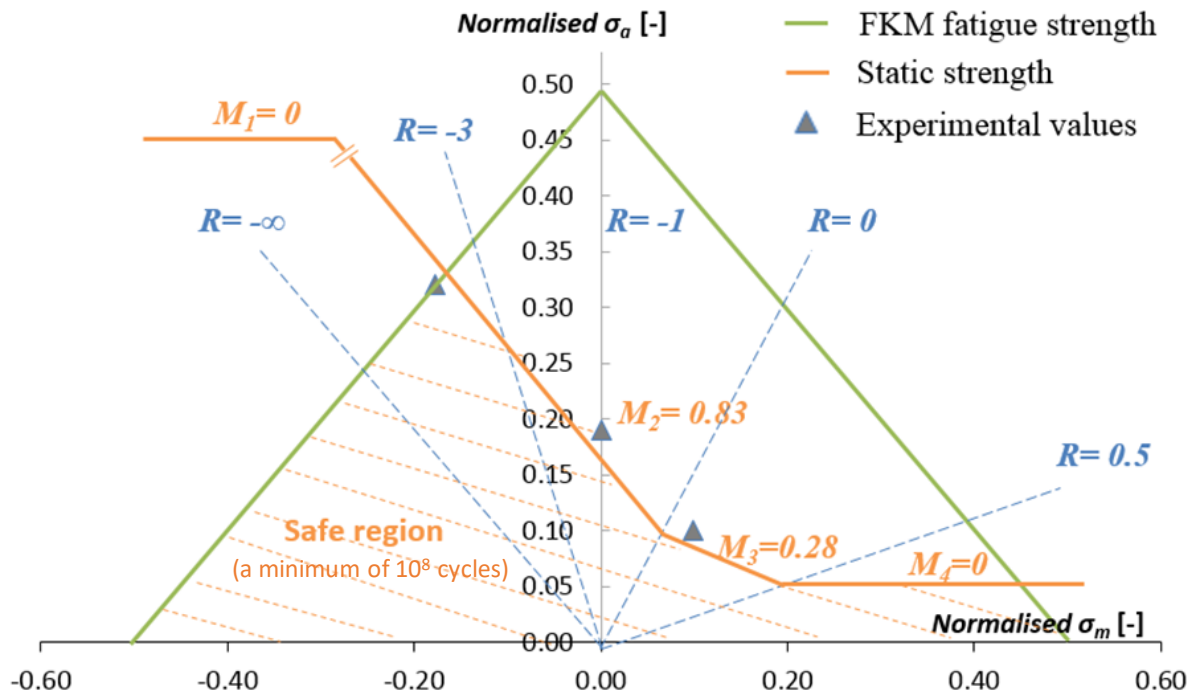


Figure 5-7: Haigh fatigue diagram of SAC 387 alloy at $1E8$ cycles to failure designed based on FKM guideline at 35°C

Table 14: Mean stress corrective description and their corresponding values for SAC387 alloy

Parameter name	Values	Mean stress sensitivity (slope of orange dot line in Figure 5-7)
M_1	0	when $R < -\infty$ for FKM mean stress
M_2	0.83	when $-\infty \leq R < 0$ from experiments
M_3	0.28	when $0 \leq R < 0.5$ for FKM mean stress
M_4	0	when $0.5 \leq R < 1$ for FKM mean stress

5.1.3 Stress gradient effects

The importance of stress gradient studies resulting in potential early failure of solder joints in a SMT is described in *section 2.1.6.3* under the sub-section “Notch factor”. For FE-based calculations on solder joints, where loadings and geometries may be quite complex, the stress gradient approach based on the FKM guideline [37] is considered in the current work. As seen earlier under *section 2.1.6.3*, the FKM method can effectively describe the fatigue strength of the SAC material that can be increased/decreased by a certain factor depending on the normal surface stress gradient. In any general case of a FE-based fatigue calculation, there are six stress gradients (corresponding to the six components of the stresses) and these can vary from moment to moment. In this work, author has adapted a method according to FKM guidelines [37], so that rather than adjusting the fatigue strength, the stresses before the fatigue calculation are adjusted accordingly [128].

Systematic procedures to correct the stress gradient are as follows:

- In addition to the stresses being extracted from FEA calculations, the gradient of the stress components in the direction of the surface normal (see *Figure 5-8*) are also determined. In other words, the stress gradient is determined from the stresses in the layer of elements adjacent to the surface averaged to the node as per *Eqn. (2.7)*.

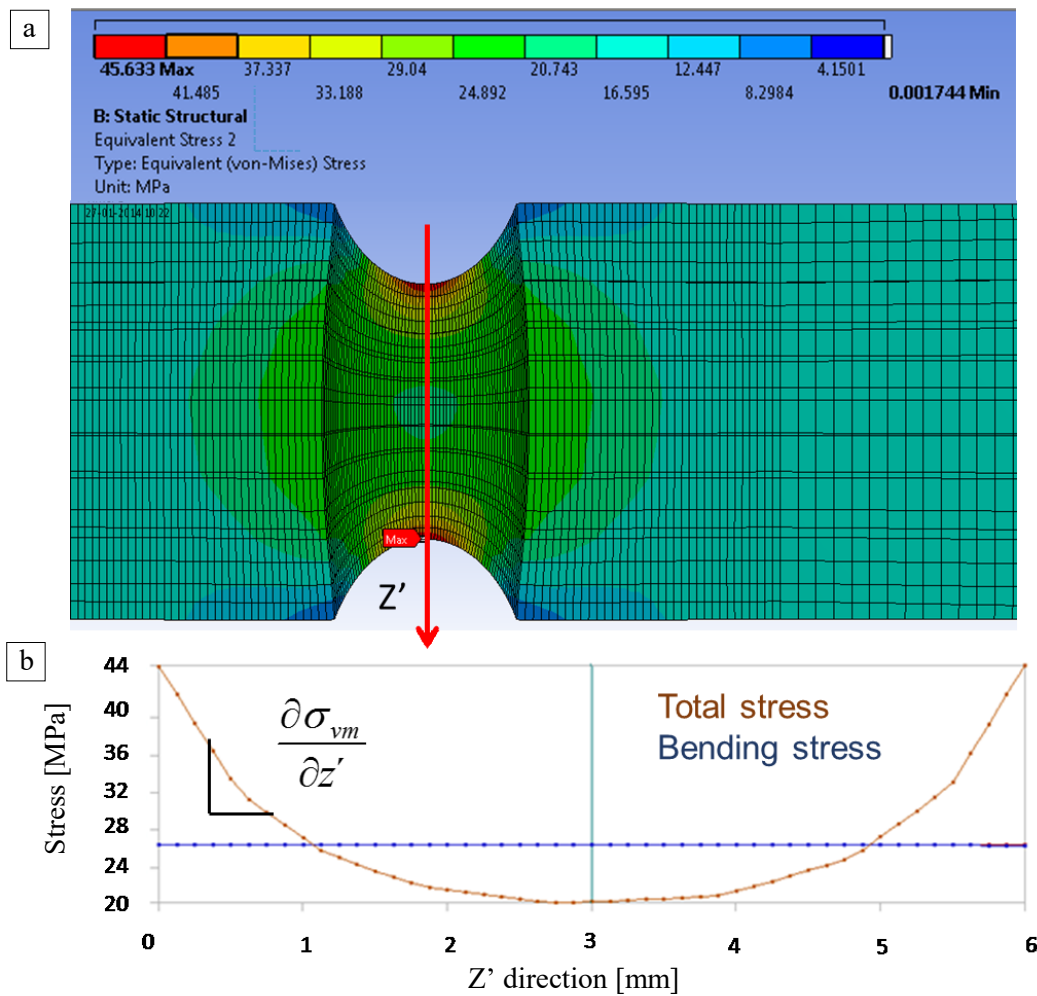


Figure 5-8: Determination of the normalised stress gradient, (a) stress-contour plot of the cross section from the notched solder specimen (b) corresponding linearized values of the von-Mises stresses

- Von Mises stress along the surface normal direction is determined [128] as seen in *Figure 5-8*. Surface normal direction in this context means along the thickness of the specimen, from where the von Mises stresses are calculated.
- The stress gradient is normalised with respect to the von Mises stress at the surface σ_{vm} , to arrive at the normalised von-Mises stress gradient [128], according to *Eqn. (2.8)*.
- The stress gradient G_σ in $[\text{mm}^{-1}]$ from FE calculations is finally used to determine a correction factor, n_σ based on the type and ultimate tensile strength of the material as formulated in *Eqn. (2.9)*.

The SAC material constants a_g [-] and b_g [MPa], in *Eqn. (2.9)* are found as follows:

- Certain set of experiments were done on unnotched and notched specimens at $R = -1$, 35°C with the same nominal stress amplitudes between LS and HS. The local maximum stress and nominal stresses for an unnotched specimen will be the same, as seen in *Figure 5-9*.
- Due to higher stress concentrations from the notch factor, the maximum stresses and stress gradients in a notched specimen will create a stress concentration region leads to an earlier crack initiation compared to the unnotched specimen as shown in the *Figure 5-9*, marked as notched nominal stress.

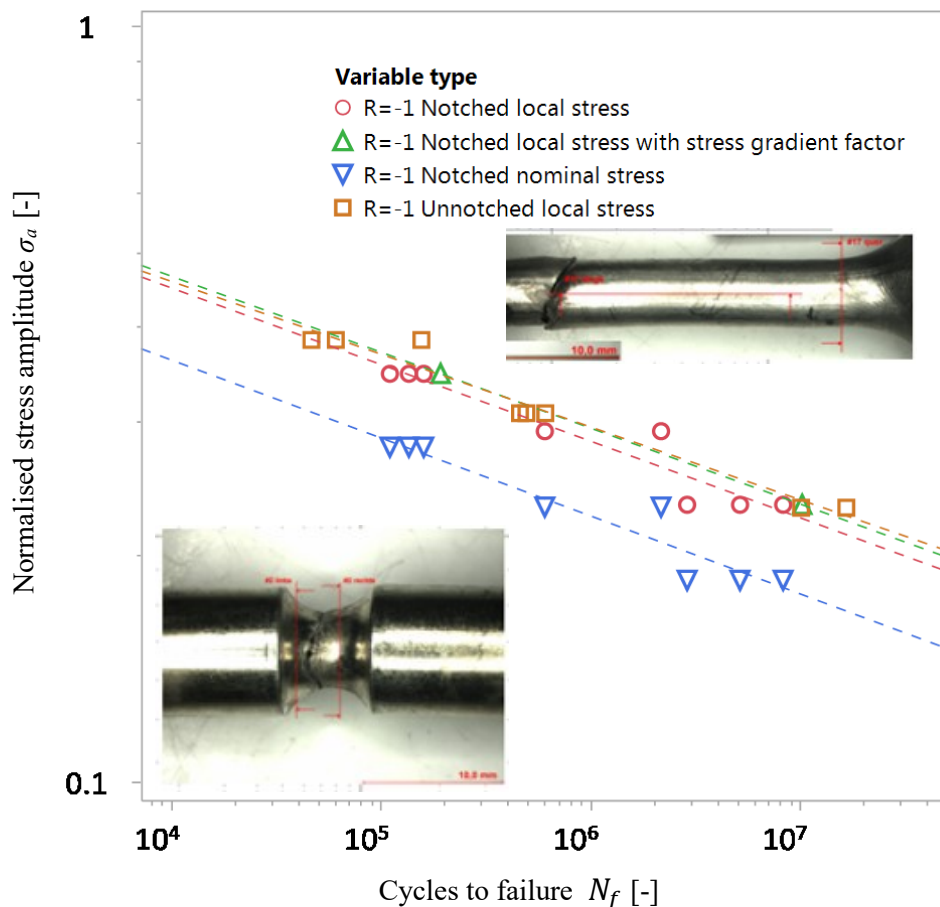


Figure 5-9: S-N curve for notched and unnotched specimens to investigate stress gradient effects: symbols represent measured points and dotted line corresponds to the fit based on Basquin Eqn. (2.5)

- Now the local stresses of the notched versus unnotched specimen is compared in the S-N curve and checked for any possible shifts, as seen in the linear regression fits of *Figure 5-9*. There will be a shift in values between the notched local stress and unnotched local/nominal stress. This is due to the stress gradient error that will eventually occur over predicting the fatigue life evaluation.
- The effective stress factor can be found from the above routines [37]:

$$\sigma_{eff} = \frac{\sigma_{vM}}{n_{\sigma}}. \quad (5.1)$$

From the correction error between the local stress of unnotched and notched specimens in *Figure 5-9*, the material constants a_g [-] and b_g [MPa] are found out and tabulated in *Table 15*.

Table 15: Values of the normalised stress gradient in Eqn. (2.9) and their corresponding correction factors

G_{σ} [mm^{-1}]	a_g [-]	Normalised b_g [-]
0.407	0.05	1.69

5.1.4 Effects of surface roughness

The importance of surface roughness on fatigue is described in detail in *section 2.1.6.3* under “*Surface finish*”. During the HCF experiments, the crack initiation can also be associated with the surface roughness, which in fact is a result of quality from the production of solder joints. The solder joints create its own characteristic surface finish on the solder finish as shown with an example shown in *Figure 5-10*. At meniscus side, surface roughness close to 14 μm is observed from random lots. This is apparently from the reaction of the flux and the influence of the surface tension acting on the surface during the Pb-free reflow oven process [9]. The intrusions on the surface will create a micro notch effect resulting in a local stress intensity promoted in this region as seen with the roughness measurement on the bulk sample in *Figure 5-11*.

In the current study, three different types of surface roughness are investigated. The first case, which is a casted one, is obtained directly after the casting manufacturing, which had $R_{z,max}$ value of $\sim 15 \mu m$. The second one is rolled carefully with a grinded paper without creating any surface imperfections ($R_{z,max}$ of $\sim 11 \mu m$) seen in *Figure 5-11* and the final one with the least surface value of $R_{z,max}$ as $\sim 3 \mu m$ which is made from diamond polish liquids. In addition, the average values of maximum surface roughness $R_{z,max}$ are taken from qualitative statistical data of three different random specimens for each roughness cases.

The maximum values of surface roughness $R_{z,max}$ had a minor impact on the fatigue property of the solder material at cycles ($N_f < 10^5$), as illustrated in *Figure 5-12*. Two different stress amplitudes are selected for this study one at normalised stress amplitude, 0.23 [-] and the other one at 0.38. As observed from the influence of normalised stress amplitude at 0.38 [-], the surface roughness seems to affect the fatigue property at a very minimal level.

However, as the nominal stress amplitude is reduced to normalised stress amplitude, 0.23 [-], it is quite evident that the roughness of the casted specimen diverged from the slope of the polished specimen compared to normalised stress amplitude, 0.38 [-] test. This proves the fact that even though for a lesser hardened material like solder, surface roughness plays a role in determining the fatigue property, especially with the decrease in the stress amplitude (HCF region). Surface roughness impact on the fatigue strength is quantified following the FKM guideline using *Eqn. (2.6)*. This equation develops a relationship between the surface roughness and its impact on the solder surface values along with the tensile property of the material.

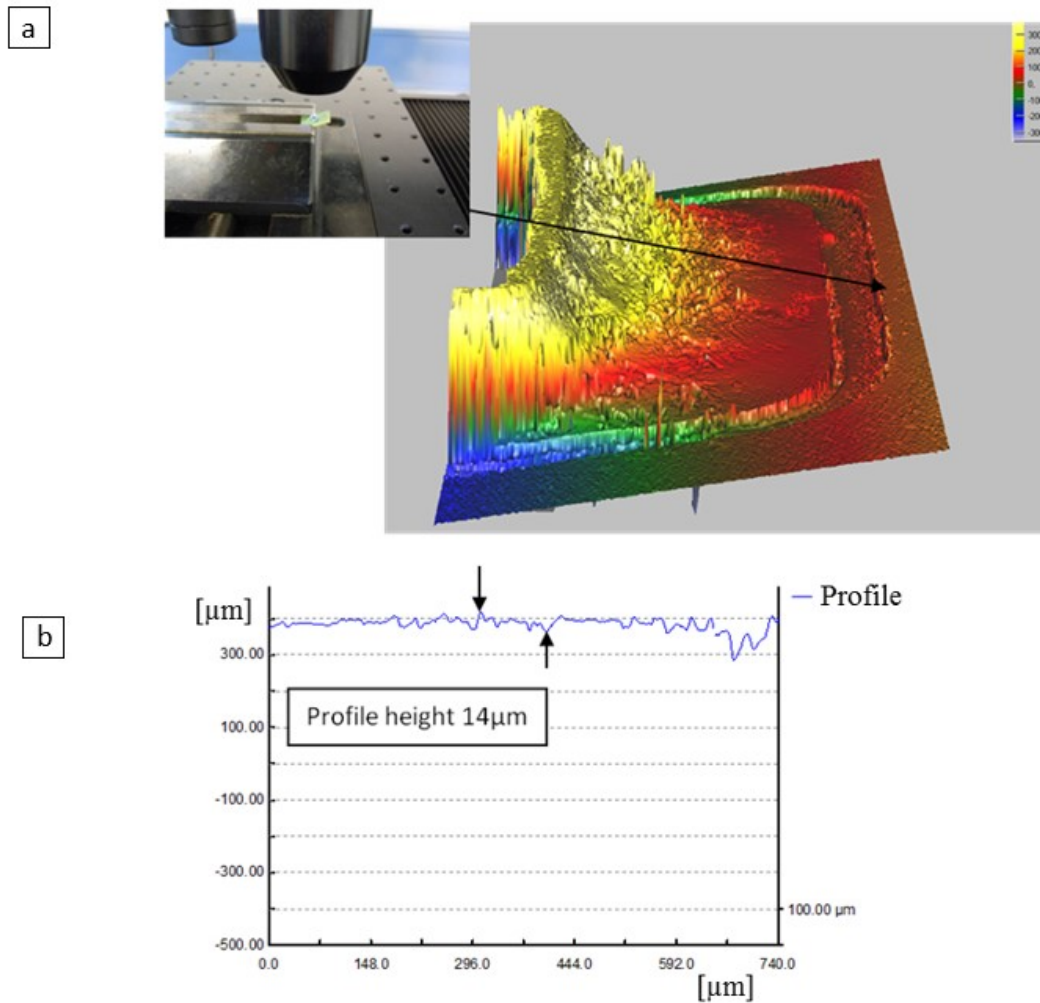


Figure 5-10: (a) Laser scan contour plot of the surface roughness on a ceramic component solder joint, (b) line map of the corresponding measurement of the R_z measured over the profile of the solder joint

The observations on the surface roughness suggests the need for mirror-polished specimens with an average surface roughness $R_z \leq 3 \mu\text{m}$ to derive the reference S-N curves. Intrusions and extrusions are surface defects in the order of some micron (see section 6.4). If surface finish is rather rough leaving material plicas higher than these few microns, then it will be not necessary to wait for extrusions formation or any surface slip process to get the initiation event. In such a condition, there is already surface damages and it is clear that fatigue life will be enormously reduced since most of cycles are spent just to initiate micro damage.

The surface roughness influence on fatigue can be quantified according to Eqn. (2.6). The optimized solder material constants in Eqn. (2.6) are found to be $A = 24.34 [-]$ and $B = 127.34 [\text{MPa}]$.

The material constant values of A and B in Eqn. (2.6) are calculated by comparing the effect of roughness on fatigue life of cast ($R_z = 12 \mu\text{m}$) and the polished ($R_z = 3 \mu\text{m}$) specimens during HCF (at LS) as seen in Figure 5-12. With the material constants A and B , the S-N curve is corrected according to Eqn. (2.6). This means that the value of applied stress will be corrected according to the roughness effects on cycles to failure. With the value of the tensile strength of the SAC alloy along with the average surface roughness values measured from the surface scan, the effect of roughness can be corrected. The boundary limits of A and B for optimization can be set according to FKM guideline.

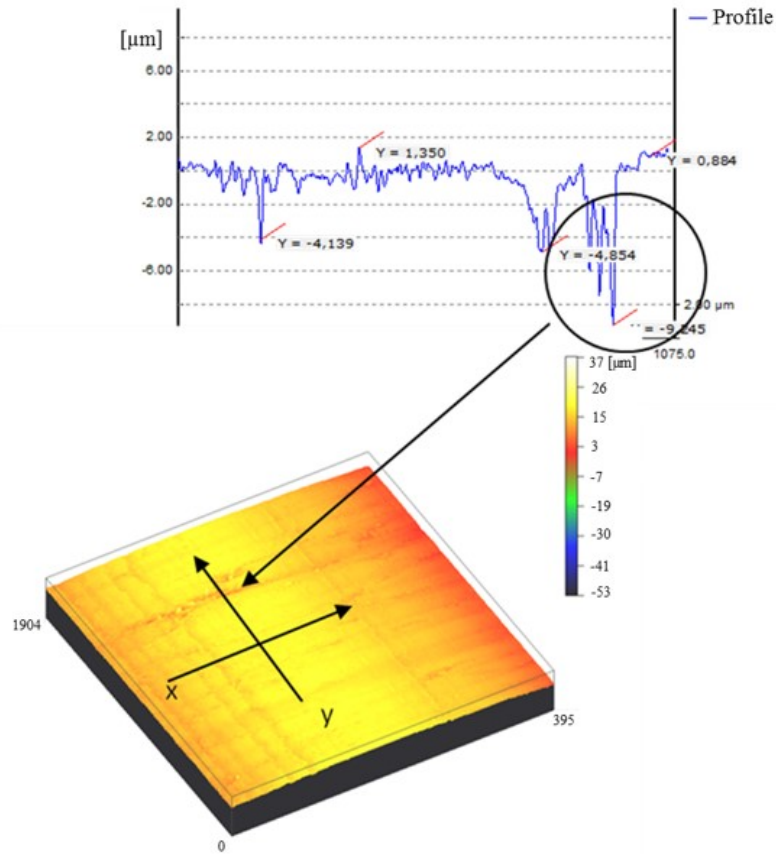


Figure 5-11: R_z measured over the profile of the solder specimen (as grinded) performed using laser scan showing peak profile values

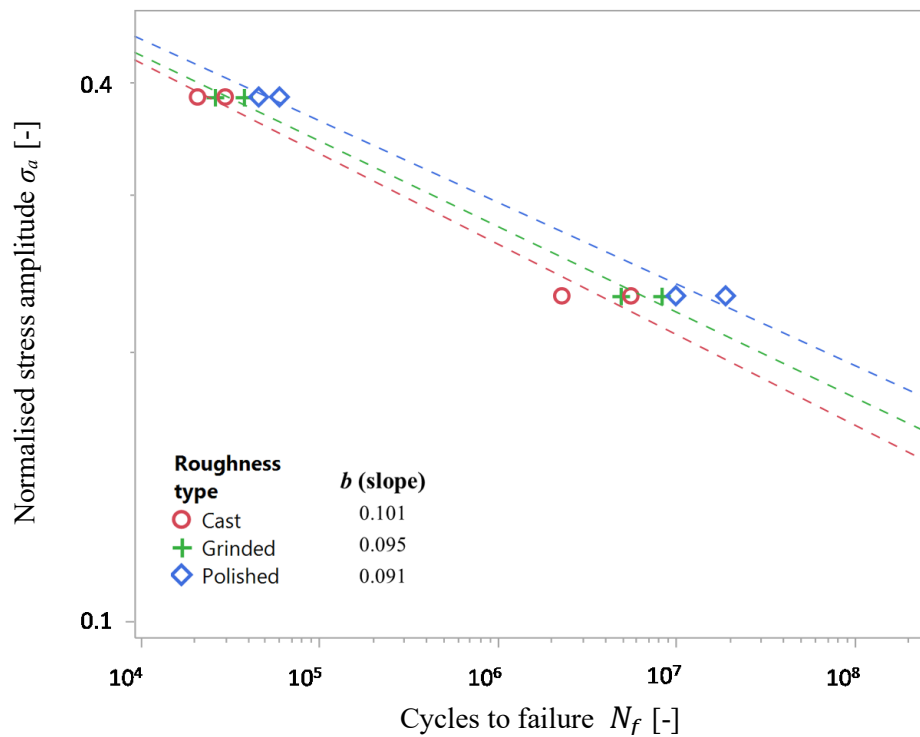


Figure 5-12: $S-N$ curve, impact of surface roughness on the fatigue property of the solder alloy at 35°C , $R = -1$, 60 Hz: symbols represent measured points and dotted line corresponds to the fit based on Basquin Eqn. (2.5)

Table 16: Tabulated fatigue parameters of the Basquin equation Eqn. (2.5) for different roughness cases (log-log scaling)

Roughness type	b	Normalised σ_f [-]
Cast	0.101	0.063
Grinded	0.095	0.032
Polished	0.091	0.033

5.2 RESULTS & DISCUSSIONS

5.2.1 Effects of fatigue factors

S-N curves for different parameters are investigated individually and analysed according to stress-life theories [43, 162]. The results of the effects on all the influential fatigue parameters is summarized in *Figure 5-13*. Some judgment is always required when assessing derivation of design S-N curves. Theoretically, a regression analysis is performed that provides a design S-N defined as 97.5 % probability of survival as function of number of test data that are available [127]. However, as seen in *Figure 5-13* the most critical probability of failure depends in fact on the external parameters such as correspondence between stress amplitude for stress gradient, mean stress, temperature, roughness etc.

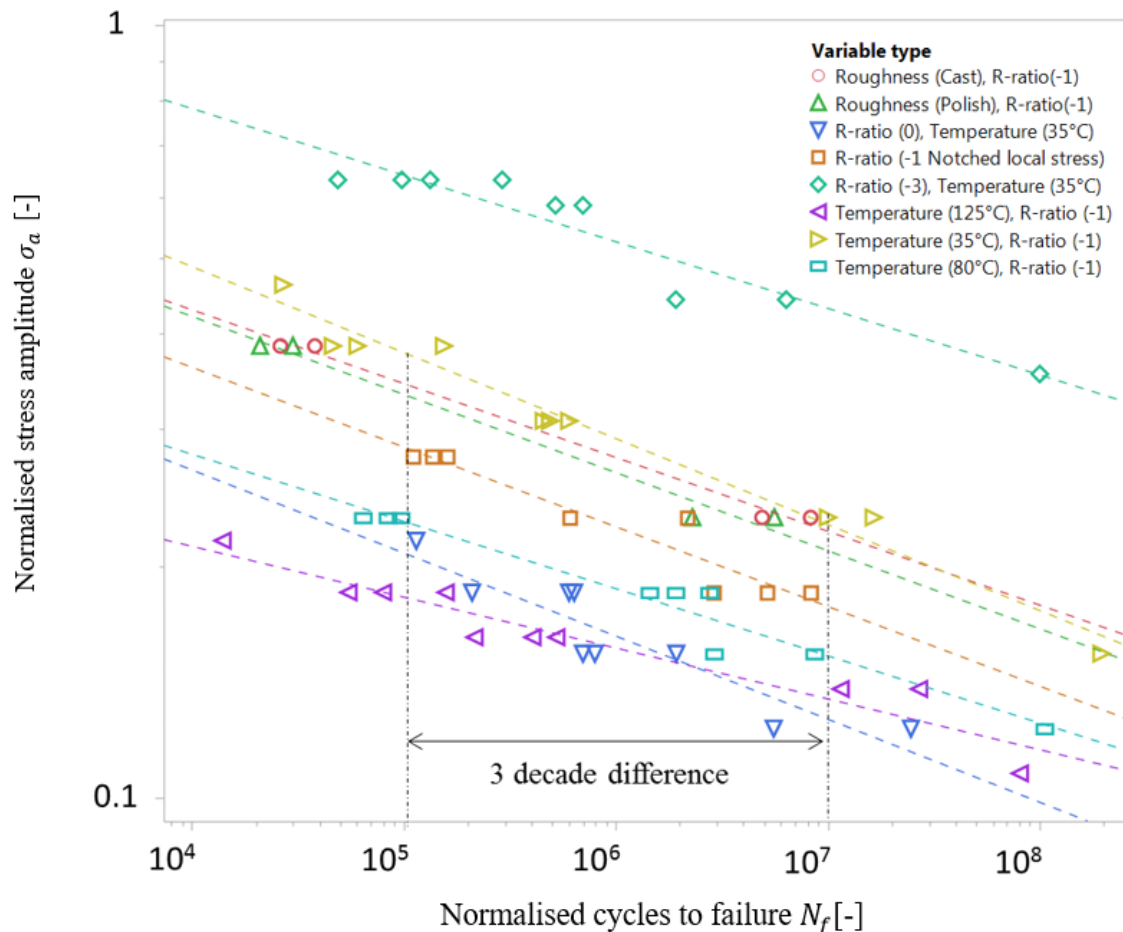


Figure 5-13: Summarized S-N diagram of SAC387 for various fatigue factors: symbols represent measured points and dotted line corresponds to the fit based on Basquin Eqn. (2.5)

It is inferred from *Figure 5-13* that the differences between the fatigue behaviour of solder specimen for various influential fatigue factors are significant when looked from LCF to HCF region. At a constant stress amplitude as seen in *Figure 5-13*, a factor of three to four decades of fatigue life differences is observed for a single solder alloy tested depending on the influential factors. This indicates that for a single solder alloy like SAC 387 a careful design for lifetime should be considered. It is recommended to incorporate influential fatigue factors, when performing a FE analysis to predict the lifetime. In other words, depending upon the actual loading condition of a SMT component solder joints, the right influential fatigue factors should be integrated during the lifetime prediction calculations (phenomenological approach combined with FE approach). A spin out of this discussion is continued in *section 7.1*, which proposes an approach to use the phenomenological equations combined with FE analysis to predict the lifetime of solder joints.

Effects of mean stresses investigated on the fatigue property reflected no change in statistical significance of the slope (steep gradient, b value ~ 0.1 , seen in *Figure 5-4*) on the fatigue curve and contributed lesser to cyclic creep/softening effects. For the room temperature test specimens on mean stress effects, cyclic saturations are observed, which dominated most of the specimen lifetime. The solder material proved good to perform during compressive loads ($R = -3$) as seen in *Figure 5-13*, which had the least impact on the fatigue life. The strain ratio of $R = 0$ is the most damaging one in this study (see *Figure 5-4*). Strain amplitudes tested with this stress ratio are below the endurance limit for the fully reversed condition, yet the fatigue life decreased significantly because of the mean stresses. When the solder specimen is subjected to a tensile load ($R = 0$), there is a significant tensile plastic strain when reaching the maximum tensile load with higher local tensile residual stresses at the root of the crack tip as a result. The whole range of mean stress is characterized for SAC solder alloy proposing a Haigh diagram based on FKM guideline, and the corresponding safe design region is depicted using Haigh diagram for the solder alloy in *Figure 5-7*.

Notch factor effect is found to have a significant influence on the crack initiation mechanism as seen in *section 5.1.3*. With a fundamental comparison of notched to unnotched specimen, the influence of notch effect on fatigue life are determined and the local stresses are compared in the S-N curve in *Figure 5-9*. The stress gradient error (that needs to be corrected) is detected from the shift of the S-N curve (intercept shift) between the notched and unnotched samples.

FKM method is referred again and implemented in the current study to describe the fatigue strength of the SAC material, which can be increased/decreased by a factor depending on the normal surface stress gradient. In addition, other effect of surface roughness is analysed here to see the significance on the fatigue property of the $Sn-3.8Ag-0.7Cu$ alloy. A clear distinction is observed in the S-N curve (*Figure 5-12*) when the specimen of various surface roughness are analysed. Casted specimens showed the least fatigue performance compared to the grinded and polished specimens. Mathematical models are found for stress gradient and surface roughness corrections with corresponding material constant for SAC alloy. The concept of FKM guideline is successfully followed to incorporate the external factor like the R -ratio, notch factor, roughness etc.

Fatigue models as summarized in *Figure 5-13* along with the discussed correction factors *Eqns. (2.6), (2.9) and Table 12 till Table 16*, is used and validated for standalone fatigue evaluation software such as nCode Designlife™, FE-safe™ etc., (discussed with an example HBM nCode under *section 7.2*). The software can import the SAC alloy results and support the fatigue models discussed in the current chapter. Eventually coupled together with FE software, it is possible to predict the lifetime of a real solder-joint in SMT component applications using the proposed local- stress approach.

5.2.2 Creep interactions at fatigue

Figure 5-2, which is an S-N curve under different temperatures indicated a clear slope change leading to the discussion of possible exclusive fatigue mechanism for *SnAgCu* alloys. Further down in the *section 5.1.1* it is discussed why the effect of high temperature on the mechanical property of lead free solder alloy is observed to have the critical impact on the fatigue life with slope gradients, b observed to be around 0.66 (see *Figure 5-4*). This is due to the temperature effects that are seen to be associated with microstructural transformations of material such as cyclic softening (dislocation restructuring) and subgrains formation. Such a kind of subgrain formation and micro-void formation is associated with creep mechanism of solder alloys, which is discussed earlier in *chapter 4.3.3* (see also *Figure 4-11* and *Figure 4-12*). This is an indication of possible cyclic creep during HCF at elevated temperatures, supported along with evidences from the local strain measurements (*Figure 5-3*) of the specimens. Further discussion in specific with respect to the corresponding fracture behaviour and microstructure analysis is in *section 6.4 & 6.5*.

Similar observations are also observed in the works of Barry [8] for SAC 305 alloys, tested under controlled vibration experiment on uniaxial fatigue solder specimen, the fatigue strength exponent, b showing different slopes. The same behaviour of varying fatigue strength exponent b is observed also for the SAC 387 alloys in the current work. As seen in the *Table 12*, the solder specimen tested at elevated temperature of 125°C showed the fatigue gradient b of 0.066, meaning it has the highest sensitivity to the applied dynamic stresses. In contrast, the room temperature specimen at 35°C had steep slope gradient b of 0.113, which is less sensitive to the applied stresses.

Concrete conclusions can be drawn that there is a possibility of a plausible superimposed phenomenon of creep during HCF testing. Even though literature *e.g.* [163] discusses the interactions between creep and low-cycle fatigue results in failure of solder joints, from the current study the interaction seems to also translatable also for HCF (tested more than 10,000 cycles) even at 60Hz. The effects of creep play a vital role in defining the high cycle failure behaviour and mode at high temperature. One has to consider the creep effects while investigating the solder joint performance under high cycle fatigue loads, as creep is found to be the dominant factor in driving the failure. In the current study, the behaviour is captured in intrinsic material property (S-N curve) however; this needs further investigations if one has to combine the creep and HCF in predicting the lifetime values.

5.3 CONCLUSIONS

A short summary of important finding from high cycle fatigue experiments highlighted in this section. HCF property of SAC alloy is investigated using different Wohler curves corresponding to the main four influential fatigue factors. The obtained results conclude:

- S-N fatigue model based on local stress approach is found to explain better the fatigue behaviour of SAC alloy over a range of various temperatures, stress amplitudes, R -ratios, surface roughness and stress gradients.
- The effects of high temperature on the mechanical property of lead free solder alloy is observed to be associated with microstructural transformations of material such as cyclic softening and subgrains formation. At low temperatures after cyclic softening, a cyclic saturation is observed. At elevated temperatures, a clear indication of a plausible cyclic creep effect is found, as the slope of the Wohler curve is observed to change. Along with temperature change, E -modulus of the SAC material is considered to be changed.

- The effects of mean stresses reflected no change (statistical significance) in the slope value of the Wohler curve and contributed lesser to the cyclic softening effects. Other effects such as notch-effect stress intensity and surface roughness showed slightly significant influences on the fatigue property. Mathematical models are found for stress gradient and surface roughness corrections with corresponding material constant for SAC alloy based on FKM guideline.
- The inclusion of FKM guideline (first time in microelectronics field) to explain the dependency of various factor on the fatigue life in the current chapter is validated in the current chapter and proved to be a systematic guideline for designing the lifetime of SAC alloy.
- From overall S-N curves, the differences between the fatigue behaviour of solder specimen for various influential fatigue factors are significant. At a constant stress amplitude, a factor of three to four decades of fatigue life difference is observed. This indicates that, a systematic consideration of influential factors should be considered for lifetime evaluation of solder joint applications.
- The fatigue models along with the discussed correction factors can be imported to a standalone fatigue evaluation software such as nCode Designlife™, FE-safe™ etc. Coupled together with FE software, it is possible to predict the lifetime of a real solder-joint in SMT component applications. Follow up of the prediction work possibilities and validations for SMT component solder interconnects will be discussed under *section 7.1*.

6 MICROSTRUCTURE INVESTIGATIONS

The correlation between the microstructures and their corresponding models for the creep and fatigue properties is very important, as the failure behaviours are dependent on the microstructures, which is in turn affected by different alloy compositions and cooling rate [24, 164]. Microstructural investigation of the current *Pb*-free solder will be the primary focus of this chapter, providing the fundamental information of material investigations in electronic package applications, and the consequent solder joint reliability issues encountered. The study will be classified based on creep failure (relevant to *chapter 4*) and HCF failure (relevant to *chapter 5*). Additionally, a right systematic protocol investigation for a fracture surface of HCF and microstructure analysis of creep is explained here.

The composition of the solder alloy (SAC387) is fixed in the study, thus the dynamic microstructural changes can be investigated separately for fatigue and creep. Once the SAC alloy is solidified after manufacturing, as discussed in *section 3.3*, the microstructure is still prone to dynamic changes under fatigue and creep loadings [1, 8]. The cooling rate from manufacturing along with the dynamic microstructural behaviour during course of the testing (fatigue and creep) will define the morphology of the Ag_3Sn and Cu_6Sn_5 intermetallics.

In a summary, the primary focus of this chapter will be towards understanding the dynamic microstructural changes during the course of the testing as explained and discussed in *Chapter 4* (creep) and *5* (fatigue). This chapter will support with understanding the deformation mechanisms and phenomenon discussed in earlier chapter, mostly with qualitative comparison using the techniques of LM, EBSD, EBCC, SEM, and XRD.

6.1 QUALITATIVE COMPARISON OF CAST SOLDER AND SOLDER JOINT

The microstructure of both types of solder preparation typically consists of dispersed intermetallic components (IMC) Ag_3Sn and Cu_6Sn_5 in a β -*Sn* matrix as seen in the LM images, *Figure 6-1* (introduced in *section 2.1.4*). The dispersed IMC's are studied and optimized during various phases of the casting process works extensively by Metasch *et al.* [58], by changing the mould temperatures, flow rates and mould pressures. This extends the work of Metasch *et al.* [58], investigating further on the optimized solder specimen after cast comparing using LM, SEM/EDX, and XRD.

LM investigations are performed initially to confirm the microstructures between the cast solder alloys and SMT component solder joints as visualised in *Figure 6-1-a*. To find out the composition of the dispersed elements in β -*Sn* matrix, energy dispersive X-ray spectroscopy (EDX) technique is used as visualised in *Figure 6-2* and *Figure 6-3*. Finally, to confirm the various phases like Ag_3Sn , Cu_6Sn_5 , and β -*Sn*, X-Ray diffraction (XRD) technique is used as visualised in *Figure 6-1-b*.

As the solder alloy is casted from a conditioned/controlled temperature, the processing and moulding conditions might change the microstructures. Hence, the analysis using the LM, EDX, and X-ray diffraction (XRD) is a prerequisite to cross confirm the microstructures of bulk solder and solder joint specimens. *Figure 6-1*, *Figure 6-2*, and *Figure 6-3* is one such example of comparing various steps and protocols followed in the thesis. In other words, such an analysis cross confirms and compares the microstructures of a solder joint in a reflow-solidified scenario to the coupon level solder specimens manufactured from casting.

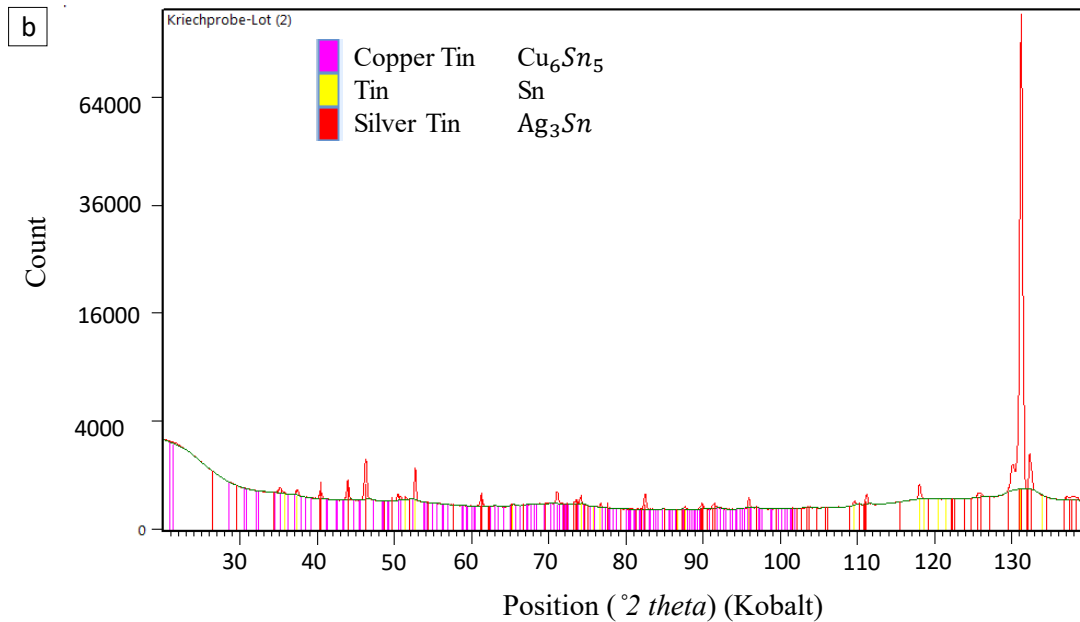
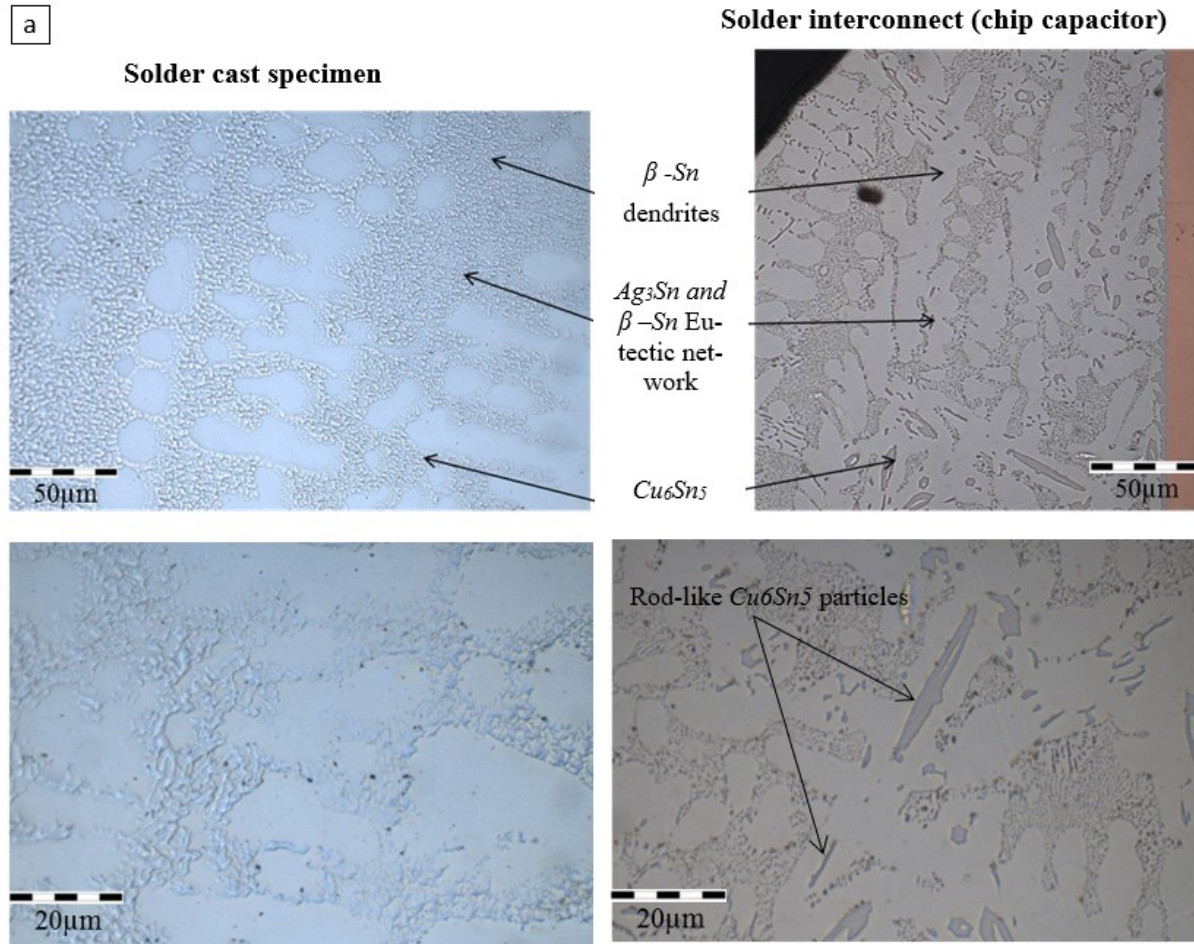


Figure 6-1: (a) Qualitative comparisons of a cast solder specimen and a non-aged solder joint at two different magnifications (b) XRD analysis on cast solder to confirm the phase constituents

The SEM/EDX analysis performed, (see *Figure 6-2* and *Figure 6-3*) shows spots/mappings, where alloying element and phase constituent like Ag_3Sn , Cu_6Sn_5 , and $\beta-Sn$ phases of the solder joint/cast specimen is determined qualitatively. In *Figure 6-1-a*, LM analysis shows few differences that comes from needle like Cu_6Sn_5 at certain location of the solder joint that is finer and dispersed together with the Ag_3Sn intermetallic. When the solder joint specimens where compared to the solder cast specimen, casted ones had spherical like particles [70]. Otherwise, similar peaks are detected on the EDX spectrum with the direct image comparison as seen in *Figure 6-2*.

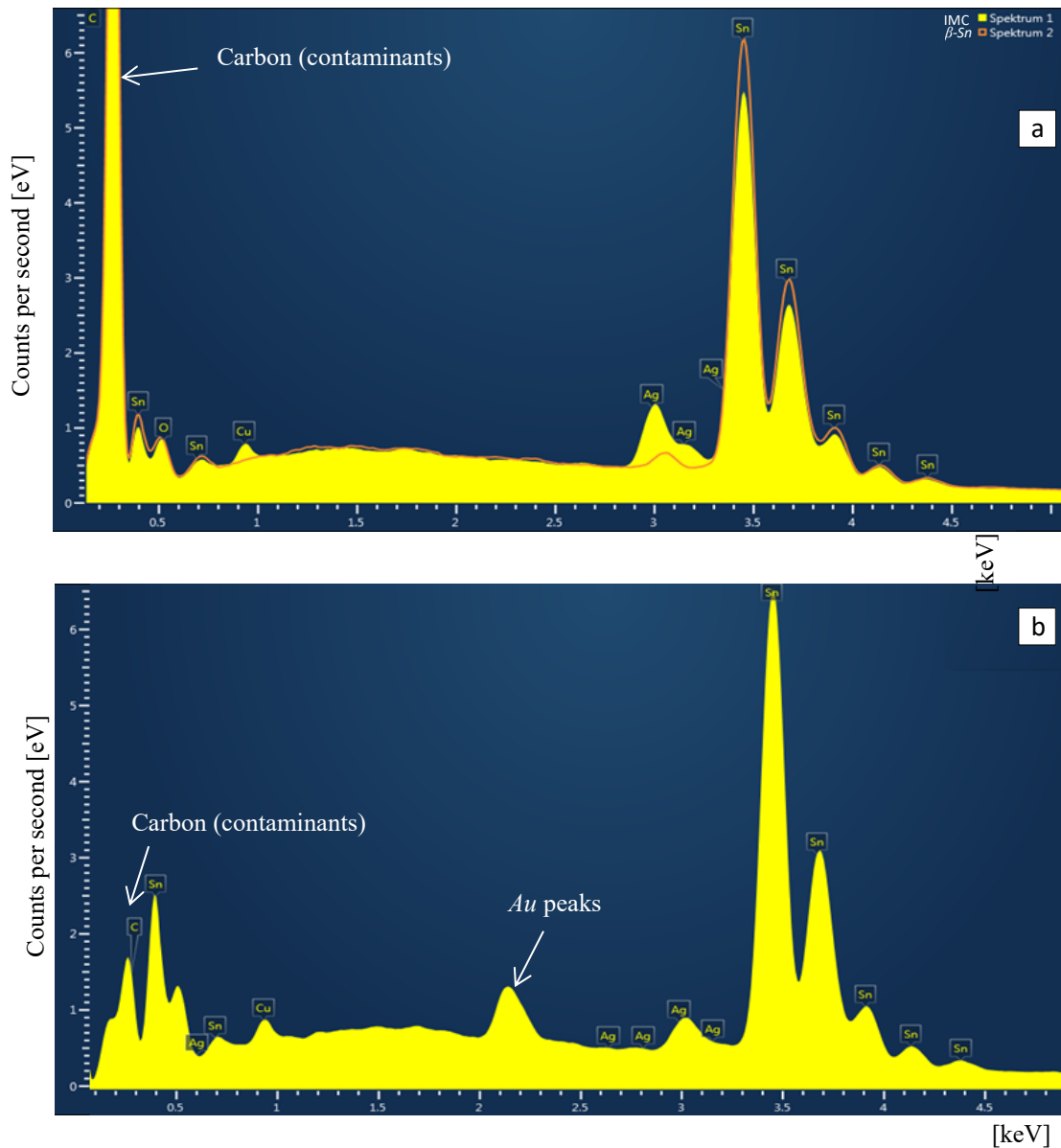


Figure 6-2: EDX- spot analysis on the $\beta-Sn$ -rich region to identifying alloying elements for (a) casted solder, (b) solder joint

EDX/SEM mapping in *Figure 6-3* shows an overview of the distribution of alloying elements in the final optimised cast specimen. The distribution of $\beta-Sn$ and IMC distribution in dendrites is differentiated. The Cu distribution is predominantly occupied and spread across dendrites, and on the $\beta-Sn$ matrix and whereas the Ag distribution is only along the dendritic networks.

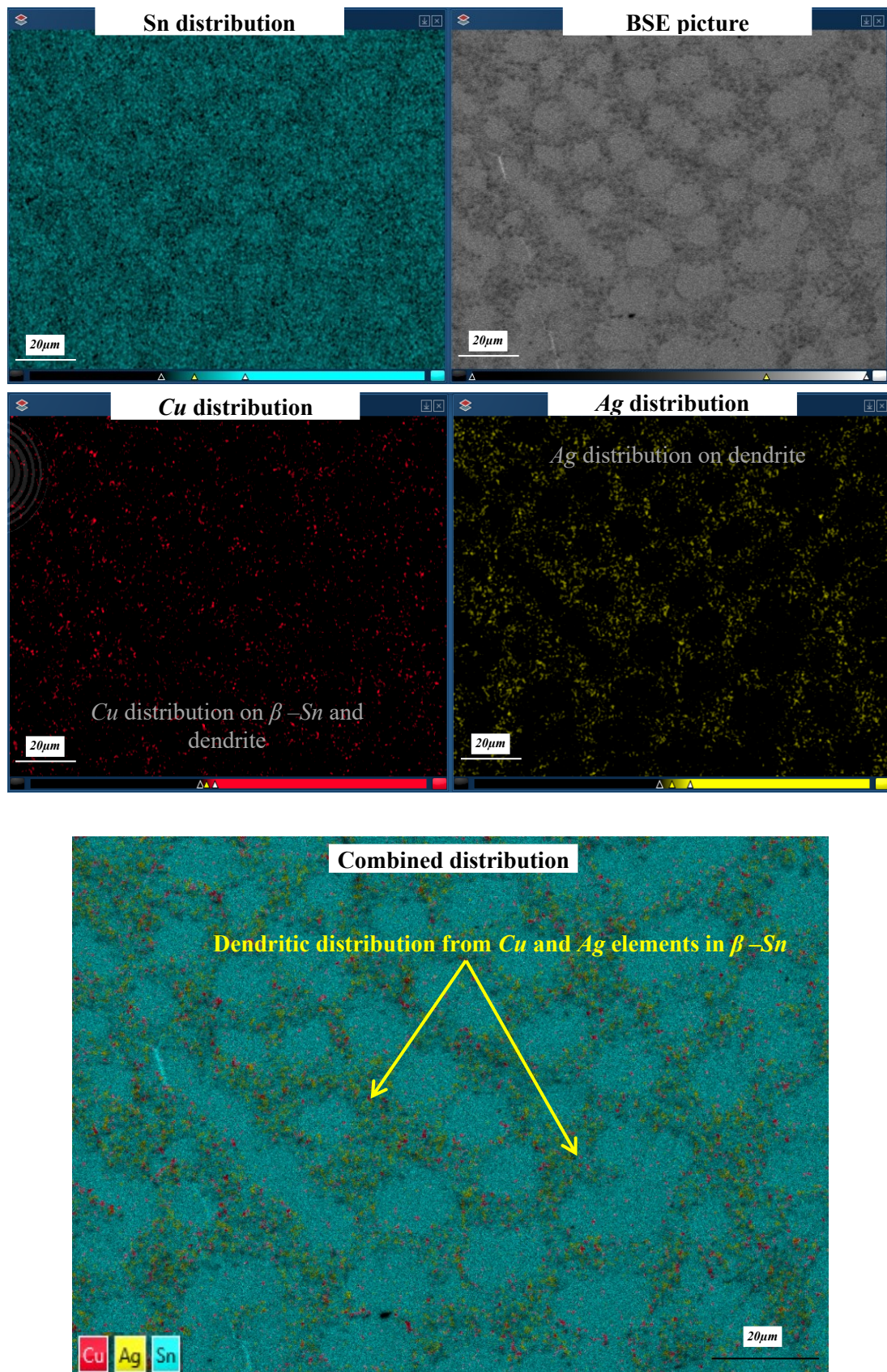
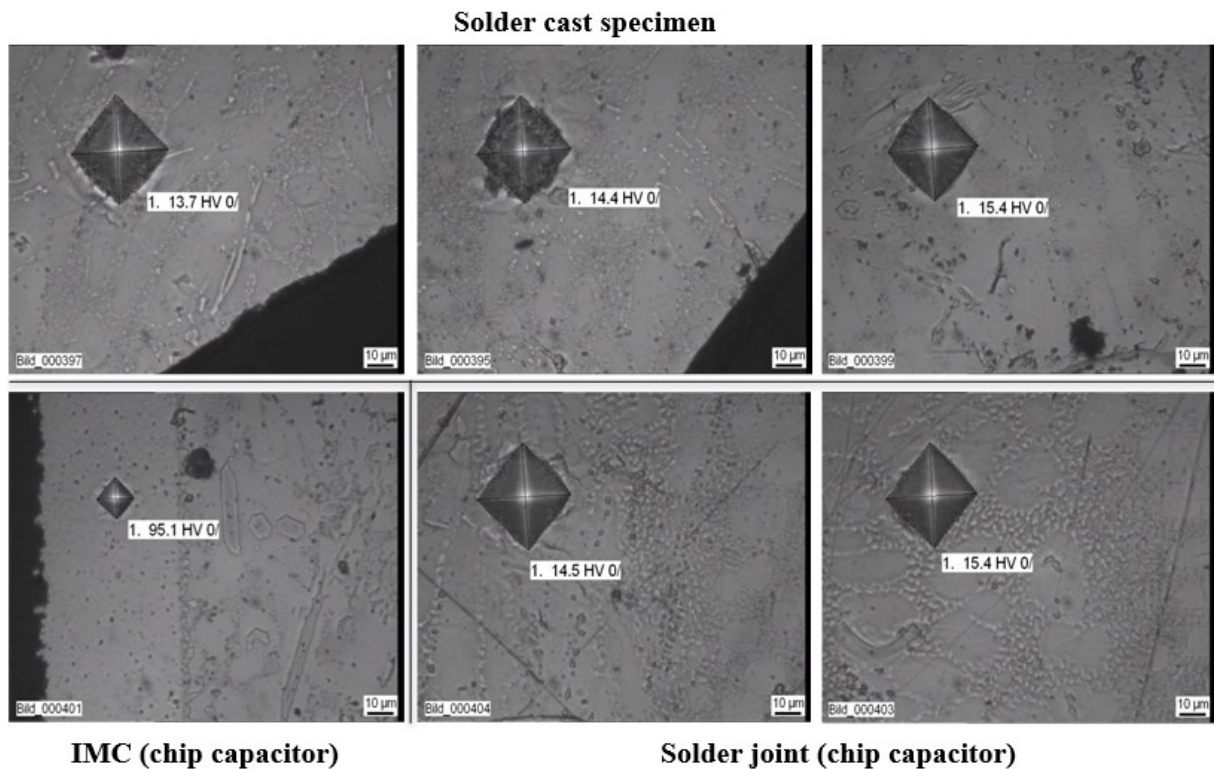


Figure 6-3: EDX/SEM mapping of the element distribution in a cast solder specimen, visualising the distributions alloying constituents in β -Sn matrix and dendrites.

Apart from the qualitative and phase comparison studies, the cross section of the cast solder and the solder joint are investigated using Vickers micro hardness measurement with a constant load (10 g). As seen in *Figure 6-4*, the value of hardness measurement is compared on some of the cast solder and solder joint. Different primary grains are chosen to study the local hardness on the cast specimen [165]. The cast solder had different values at the three sample grains as 13.7 HV, 14.4 HV, and 15.4 HV and for the solder joint, the value ranged between 15.4 HV and 14.5 HV. The surface hardness of cast specimen is correlated to the solder joints. It is interesting to be noted that the intermetallic phase (see in *Figure 2-2*) between the solder joint and the *Cu* pad had hard surface when investigated with the Vickers micro hardness value of 95.1 HV. Phillipi *et al.* [166], performed more extensive study on IMC and their corresponding impact on fracture toughness for any further reference.



*Figure 6-4: Hardness measurement, HV 0.01 (10g) on cast solder, solder joint and the IMC phases that is developed between the *Cu* pad and solder joint*

6.2 CREEP MICROSTRUCTURE ANALYSIS

Fracture surface of the creep specimens from the matrix of the tests are selected and cut along longitudinal and latitudinal axis as shown in *Figure 6-5-a*. The primary focus in this section is to investigate the microstructure and macrostructure after the experiments to correlate with the creep models investigated earlier in *section 4.3*. Another purpose of these investigations is to cross confirm any presence of subgrain formation on necking and non-necking regions. A nomenclature of ‘LS’ for low stress ‘MS’ for medium stress and ‘HS’ for high stress will be followed from here onwards to describe the stress regimes. The classification of stress (LS, MS, or HS) is based on the creep mechanism investigated in *chapter 4* (see *Figure 4-7*).

6.2.1 Primary grains and necking

Most of the LM investigation with optical filters illustrated the presence of big primary grains (about 2 to 4), orientated along the longitudinal axis of casting flow, *Figure 6-5-b*. This is also observed on the specimen investigated before the experiments, which showed primary grain remaining stable during the complete creep deformations with almost no evidence of grain boundary sliding. The primary grains did not contribute significantly to any such intergranular macro cracks.

After the creep tests at 35, 80, and 125°C, microstructures becomes different and complex. From *Figure 4-1*, sufficient time is elapsed by the microstructure to reflect a saturation of transient creep and a complete transition to steady state creep rate. First notable difference between these temperatures of creep experiments is the percentage of necking on a macroscopic scale being decreased ~ 82% - 56%, as the temperature increases seen in *Figure 6-5*. Percentage of necking in the context means the lateral cross-section diameter ratio between the post mould and post fracture. This reveals the amount of ductility affecting the creep properties during elevated temperature at later tertiary stages [1, 8]. Also interesting observations is the detection of a shear fracture at an angle (45°) in the initial cavity break area along the fracture direction, for all the LM investigations performed at different temperature and stress levels.

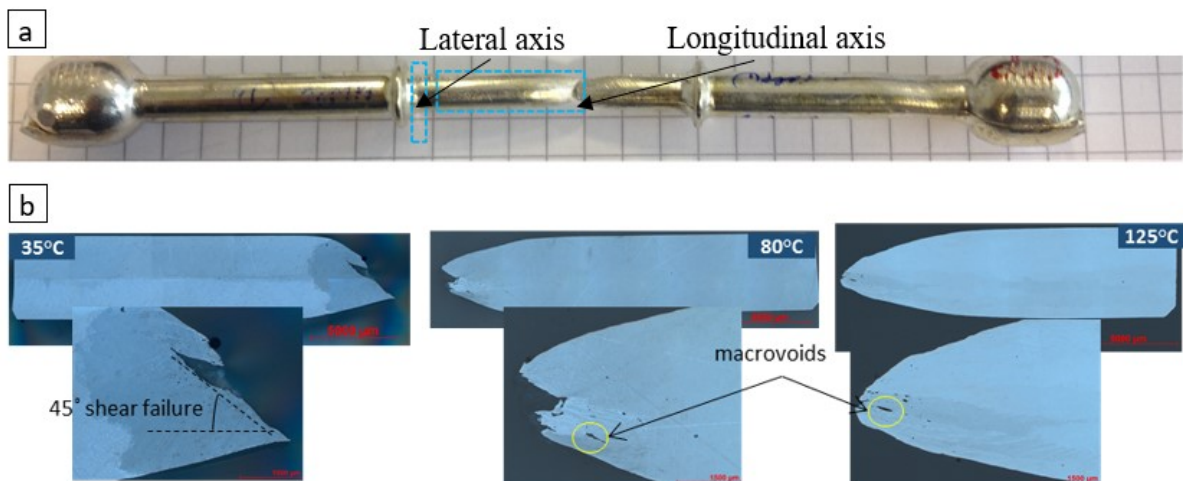


Figure 6-5: (a) Fractured creep specimens showing interesting regions analysed for cross section studies (b) optical LM of the creep specimens at 35°C, 80°C, and 125°C tested at lower stress

6.2.2 Subgrains polygon formation

One notable difference between the microstructure changes of creep specimens before and after experiments is the appearance of substructures (referred as subgrain) development in individual big primary grains (*Figure 6-6* and *Figure 6-7*). This investigation based on the statistical data is used in the creep equation development under *chapter 4.3.3*.

Subgrain formations are also detected on non-necking regions (see *Figure 6-6*), which could be a proof of subgrains enhancing strain hardening which is caused due to the dislocation interaction regions on the subgrain boundaries during the primary creep stage. This polygonization process is prominent in high stacking fault energy materials like *Sn* and *Sn*-rich *Pb* free solders when the temperature and extent of deformation are low enough to prevent the spontaneous formation of new grains according to the literatures [151, 167].

Subgrain formation and recrystallization are two competitive processes where the occurrence of the former reduces the tendency of the later [168]. Literatures [88, 155] shows recrystallization occurs if specimens are thermally fatigued (TMC) along with subgrains. This combination

of subgrain formation and recrystallization is a special case, which prevails when the critical dislocation density and thermal activation energy are lesser. In the current work, recrystallization is also evident along with the subgrain formations. An example of dynamic recrystallization resulting in higher orientation angle and dynamic recovery resulting in lower orientation angle subgrains from inverse pole figures is shown in *Figure 6-7*. In the current work, the subgrains and recrystallized grains are differentiated by the misorientation angles and size. Typically, subgrains have lesser misorientation angle ($< 15^\circ$) and bigger sizes compared to recrystallized grains which had relatively higher angles ($>15^\circ$) and smaller sizes. When the subgrains interact with the dislocations, they can possibly transform slowly into macro-voids near the necking region during final stages of creep as seen in *Figure 6-5* [67]. In the necking region because of the high stresses, the recrystallization could have occurred as determined by EBSD seen in *Figure 6-7*.

From the LM investigations in *Figure 6-5*, subgrain formations are not clearly detected for a proper statistical measurement (more counts), so that the data can be used in the creep development module in the previous *section 4.3*. Therefore, specimens are investigated further with higher magnification using Electron backscatter channelling contrast (EBCC) seen in *Figure 6-6* and with EBSD as seen in *Figure 6-7* and *Figure 4-11*.

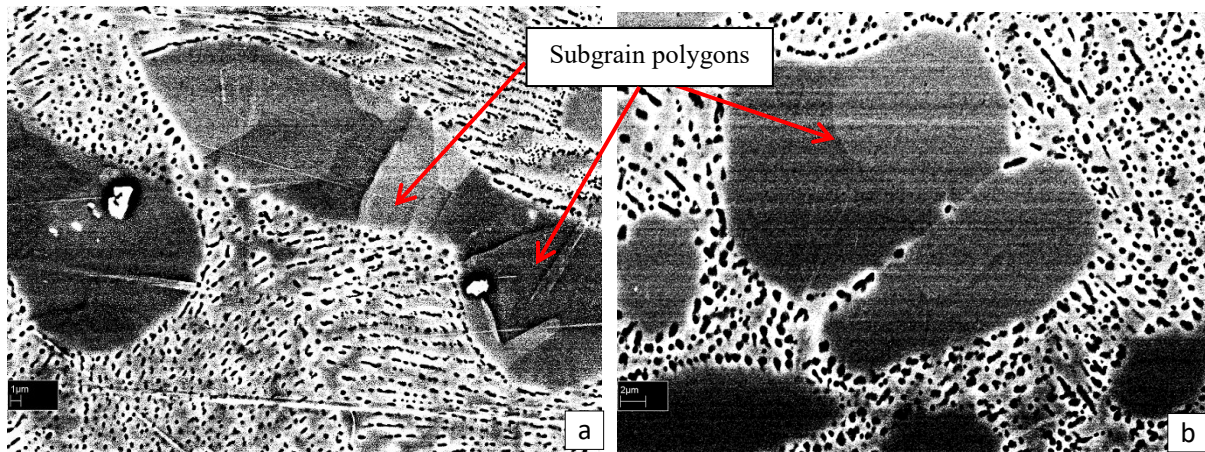


Figure 6-6: EBCC pictures showing subgrain polygon formation in β -Sn crystal during primary creep stage, non-necking regions for (a) medium stress, 35°C, (b) medium stress, 125°C

From the inverse pole figures, the distribution of the sample direction (rolling direction RD = X=[110], transverse direction TD=Y=[010], normal direction ND=Z=[001]) with respect to the crystal lattice reference gives a hint of the orientation of the subgrains which can be identified and mapped as shown in *Figure 4-11* and *Figure 6-7*. At higher temperatures, these subgrain formations can be visualised more easily because of the higher misorientation angle (2° - 15°): However, at low temperatures this angle may fall down as low as 1° [67, 155]. Recrystallized grains formed on higher angle boundaries (see *Figure 6-7*) detected are observed to on bulk regions on the microstructures (also supported by Chen *et al.* [155]). However, further EBSD works are encouraged to distinguish the recrystallization and subgrain formations, as it is not the focus of this thesis.

The microstructure analysis is performed for both low and high stress test specimens along with the various temperature variants. Both the necking and non-necking regions are investigated to find subgrain formations on the gauge length region of the creep specimen. In either case, subgrain formation is evident which could indicate the substructure formation during the primary stage of the creep when the strain hardening has happened. The intercept subgrain size,

λ_{ss} measurement of the polygon on the necking and non-necking are found from all the experiment around $\sim 10 - 15 \mu\text{m}$ (see *Figure 4-11* and *Figure 4-12*). Additionally, several general grains about $< 5 \mu\text{m}$ in intercept length can be also seen where cracks are initiated (see *Figure 4-12*).

With respect to the primary grain when compared to the subgrains (see in *section c*), primary grains and the polygon subgrain structures are determined when orientations of neighbouring measured points are different more than $\sim 15^\circ$ and under $\sim 5^\circ$, respectively.

The analysis can give different approximate orientation angles of crystals locally within the substructure, and consequent mapping can precisely plot the substructure and their corresponding crystal orientation with reference to the transverse, normal or reference directions. Each colour in *Figure 6-7* represents the crystallographic orientation. The quantification of the polygon substructure is studied in the creep development, *chapter 4.3*. This is done by setting threshold limits of the contrast and turning it into a grey scale picture as seen in *Figure 6-6*. This reading is also in agreement with the EBSD and EBCC micrographs, which would indicate the comparable sizes for 35°C and at elevated temperature test specimens.

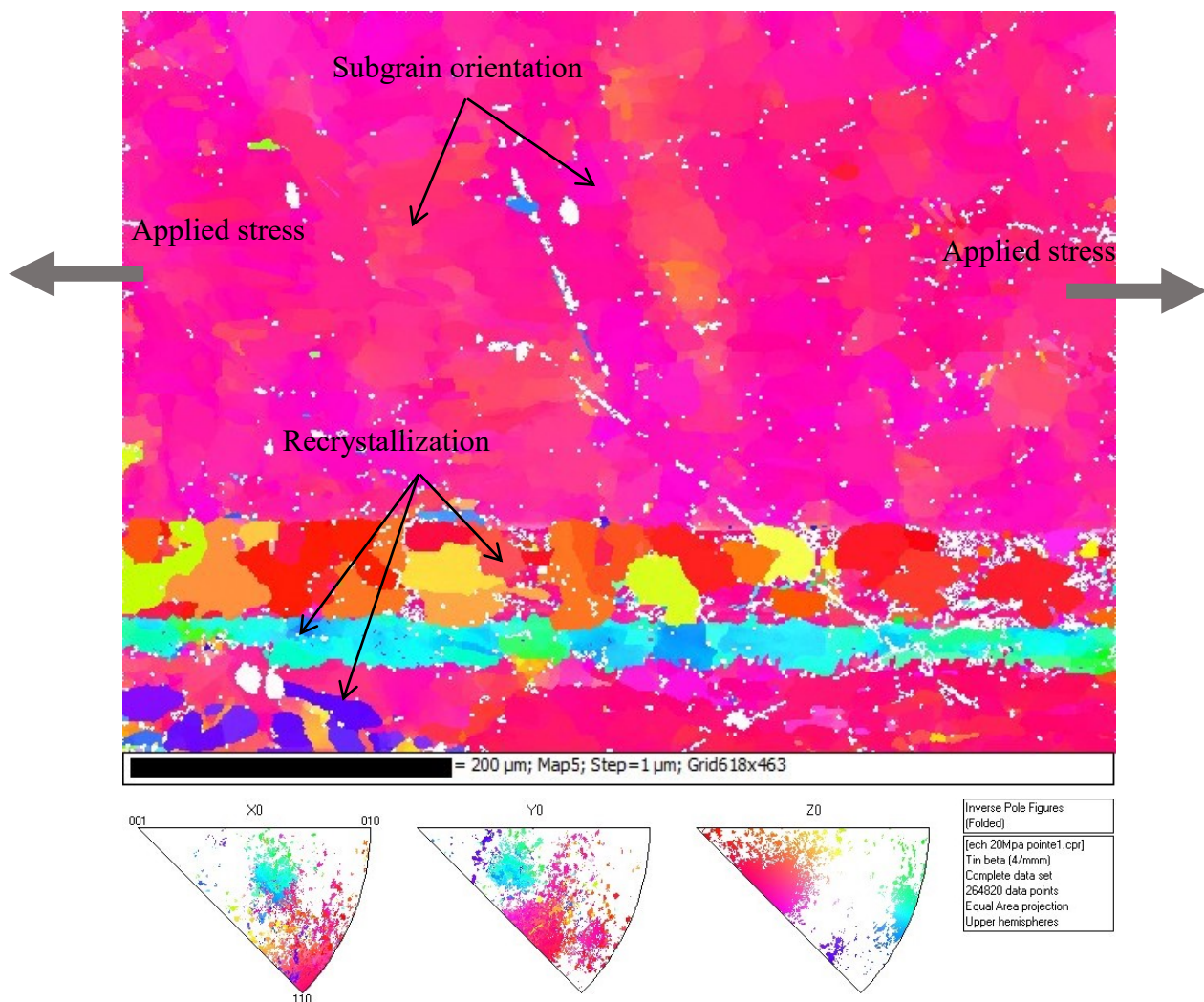


Figure 6-7: Inverse pole figures revealing substructure formations and recrystallized grains with low angle orientation detected from necking region at MS and 80°C

6.2.3 Influence of primary IMC phase particles

In this section, the influence of the primary hardened particles and its distribution with respect to the subgrain formation during creep experiment is discussed. The impact of the particles distributions, volume fraction and the density of particles are not to just contribute the creep resistance or from reliability point of view as explained in *sections 2.1.7.2 and 4.3.1* but also to the subgrain density. Even though it is known that the subgrain size are decided by the E -modulus and the stresses, the subgrain density are found to be dependent on the primary IMC particles [67].

The subgrains are mostly formed on β -Sn and surrounded with distribution of hardened particles (Cu_6Sn_5 , Ag_3Sn) as seen in *Figure 6-6, Figure 6-7, and Figure 6-9-d*. In few instances, the hardened particles appeared to be discontinuous at the boundary, but each portion of the particle remained aligned across the β -Sn boundary indicating that grain boundary sliding is absent. More commonly, the hardened particles that spanned the smaller subgrain boundary remained continuous (see *Figure 4-11, Figure 4-12, Figure 6-6, and Figure 6-9*) which confirms the distribution/density of hardened particles are playing a major role in developing the subgrain distributions. The presence of primary phase Cu_6Sn_5 and Ag_3Sn particles serves to resist defect movement [87], especially when located along the subgrain boundary as explained in the fundamental, *section 2.1.7.2*. Apart from improving the creep resistance, Ag_3Sn , and Cu_6Sn_5 primary phases is limited for diffusion-based mechanisms. However, the primary phases play a very important role in the local climb and Orowan mechanism for SAC alloys as proved in the *section 4.3.1*.

6.3 CREEP FRACTURE ANALYSIS

An understanding of plastic deformation and relationship between deformation and applied stresses from the *chapter 4* is discussed in the current section on how these effects influences the reliability related to the intrinsic solder properties. In order to enhance the knowledge and investigations discussed in the previous section on qualitative microstructure comparisons, fracture surfaces are analysed in this section. Analysis of the fracture surfaces are conducted to provide a basic post understanding of the creep deformation at different test temperatures and applied static stresses.

Significant dimple growths are observed in almost all the cases due to de-cohesion of β -Sn-rich dendrites from the eutectic region as seen in the *Figure 6-8-a* also seen in the works of [1, 8]. The fine morphology of the Ag_3Sn and Cu_6Sn_5 particles is pulled out from the β -Sn matrix and it is highly likely that the dimple formation is caused by the precipitates [24]. This behaviour is proven by the fact that the flow stresses in β -Sn rich regions are much lower than the flow stress in the eutectic region, so the fracture will preferentially occur at the β -Sn rich regions, also investigated by Ochoa *et al.* [82].

From the SEM investigation on the fracture surfaces, different behaviours are compared qualitatively for experiments between constant stresses and different temperatures. It is observed that the ductile rupture with dimples as a common rupture mode. However, the surface morphology near the vicinity of the fracture plane shows differences between the low and high temperature specimens. The comparison on the fracture surfaces from SEM in *Figure 6-9* revealed that the dimple morphology is a common phenomenon at all temperatures. However, the densities of the dimple formations of 125°C test specimens are compared relatively higher to that of the 80°C test specimens. When the grain boundaries (subgrains grains) are investigated at higher magnification, the observation showed that the 125°C specimens had clear three-point cleavage (sharp split) that evolved from their respective disoriented grains, indicating the possible dislocation interaction along with subgrains. Subgrains interacted also along with the dimple voids toward the final stages of the creep testing.

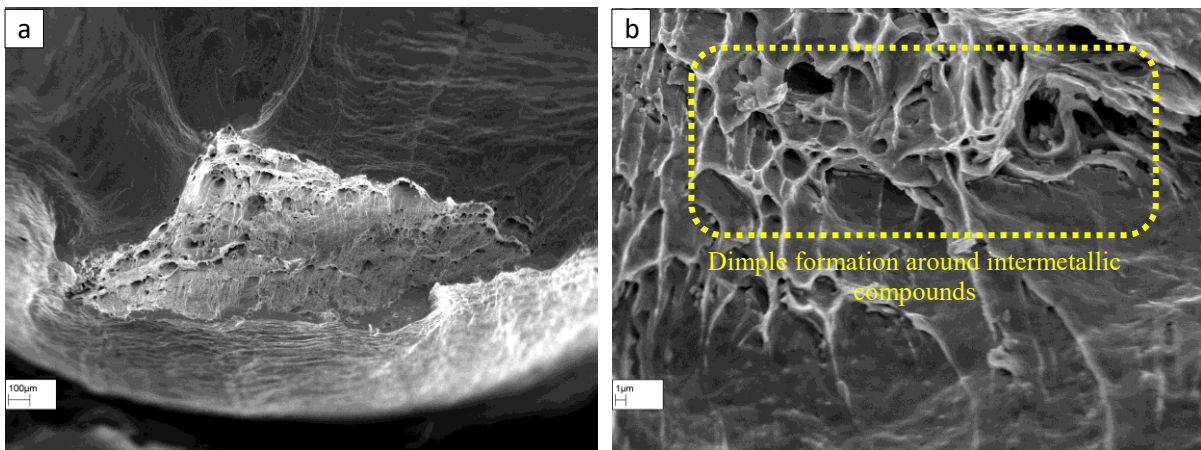


Figure 6-8: SEM picture of the fracture surface at LS and 80°C (a) showing the overview of the fracture surface with high necking (b) at higher magnification with view of the dimple formation

For the LS specimen at 80°C case (see Figure 6-9-c), the cleavage is not clearly visible (lower disorientation angle of substructures) as compared to the high temperature test creep specimens. This is assumed as a proof of commencement of plastic deformation, with increasing dislocation density and eventually resulting in the formation of low-disorientation subgrain walls, as hypothesised and assumed in section 4.3.3. The subgrains indications from some of the zones detected from the SEM should not be confused with the primary grains (discussed in section 6.2.1) that is formed during the solidification/recrystallization process. The newly disoriented grains reaches slightly higher disorientation angle and are more pronounced for the elevated temperatures [67]. Even though the presence of subgrain is an assumption based on the SEM investigation, the results are well in agreement with the inverse pole figures discussed under section 6.2.2. Further studies are encouraged to understand the crystallographic orientation and to analyse subgrain visibility over temperatures, as this is not the primary focus of this thesis.

The elevated temperature specimens ($\geq 80^\circ\text{C}$) had more porous void like formations, leading to the accumulation of the voids and eventual failure superimposed with the sharp cleavage like boundaries. For the low temperature specimens, the porous voids detected are relatively smaller (see Figure 6-9), and less densely packed eventually leading to the lesser void accumulations [165]. The same behaviour are also observed irrespective of the applied stress levels. It is assumed for most test cases, higher disoriented subgrains of smaller size are formed at the strain concentrated location [88]. The strain concentration in tensile creep specimens can be identified on the final fracture region during tertiary stage.

With all observations, it is quite evident that the subgrains are more pronounced on the strain concentration regions. This is cross-confirmed together with the microstructure analysis performed on both necking and non-necking regions as discussed in the earlier section 6.2.

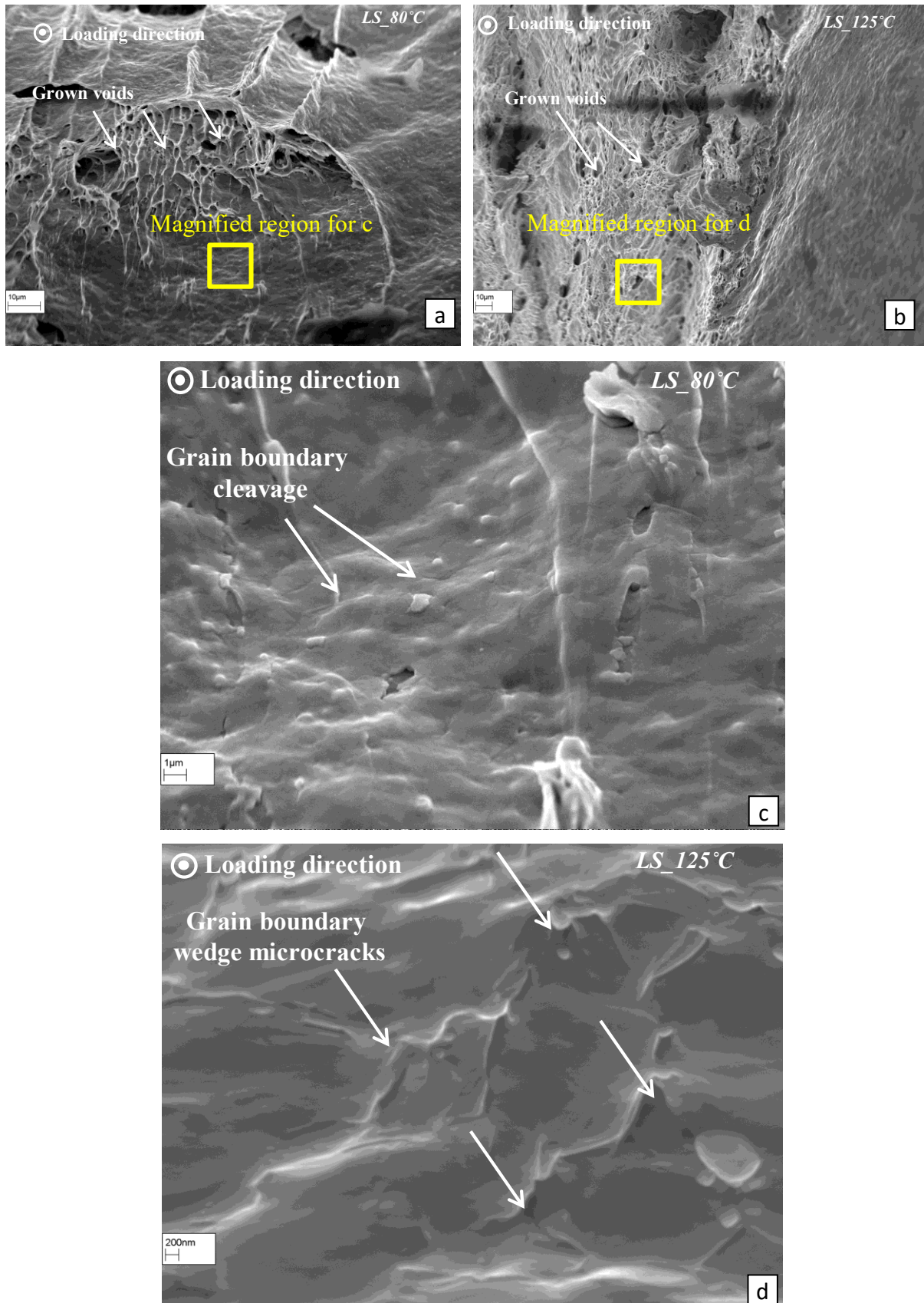


Figure 6-9: SEM micrograph at constant lower stresses (LS) at (a) $80^{\circ}C$ (b) $125^{\circ}C$ showing the dimple like formations (c) (d) corresponding higher magnification around the strain concentrations regions illustrating the different grain boundary wedges with cleavage (subgrain formation)

6.4 HIGH CYCLE FATIGUE MICROSTRUCTURE ANALYSIS

Microstructural analysis for HCF investigations are performed using a light microscopy (LM) on the cross sections for selected HCF specimens with the aim to explain the different fatigue mechanisms qualitatively at lower and higher temperatures. Initially the specimens are investigated under cross-polarized light to see the effect of the bigger primary grains on the fracture mechanism (see *Figure 6-10*). Primary grain deflections of cracks are observed closer towards the end of fatigue cycles. From *Figure 6-10*, contribution of primary grain boundary to the domination of fatigue is minimal, as a transgranular crack (though the grains) is observed.

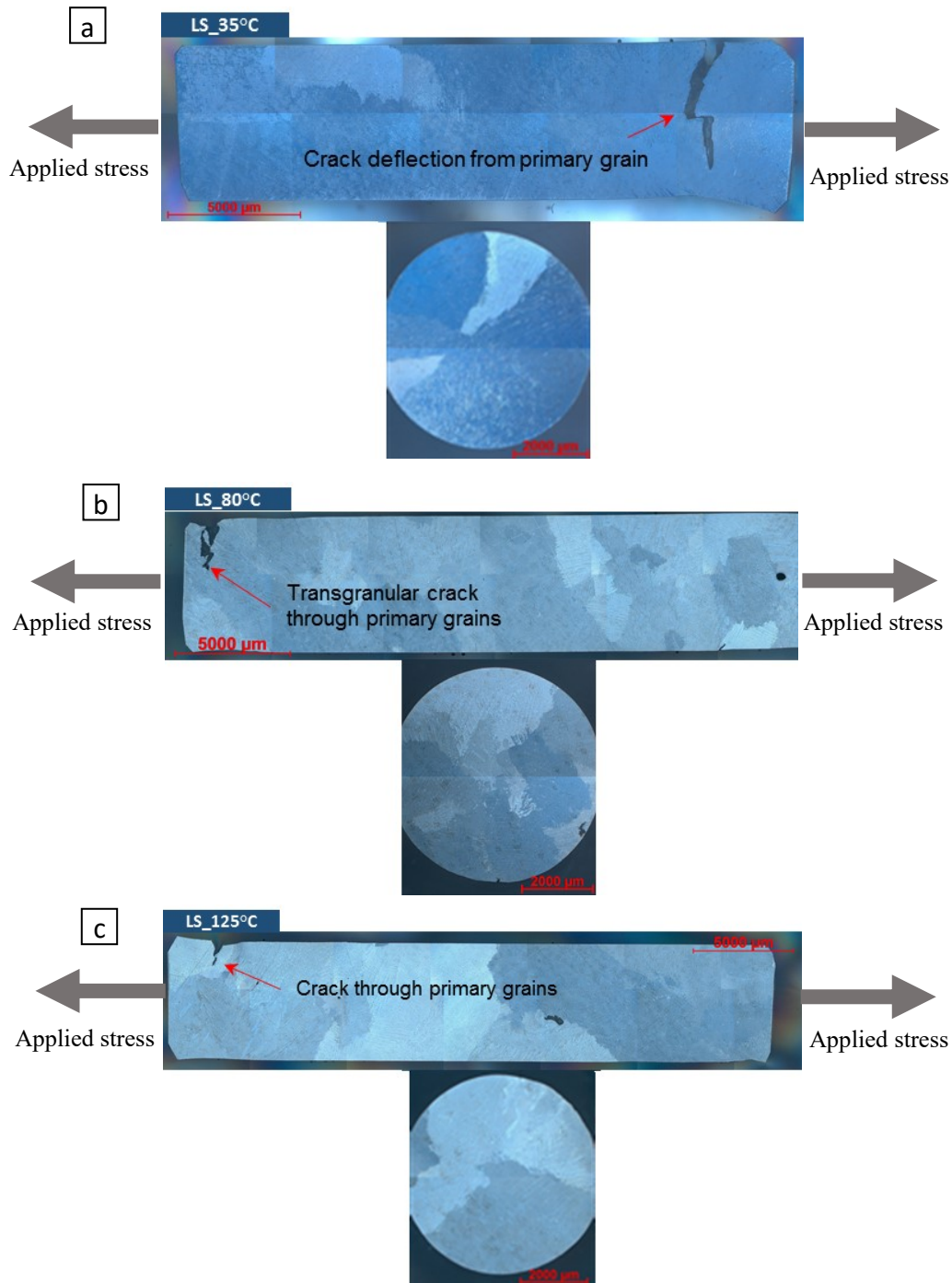


Figure 6-10: Cross polarized LM pictures of cross section showing the transgranular cracks on the primary grain at LS for (a) 35°C (b) 80°C (c) 125°C

Just as observed on the creep specimens, difference between the microstructure of specimen before and after fatigue experiments at higher temperature ($>80^{\circ}\text{C}$) is the appearance of substructure (for qualitative comparison see *Figure 6-6*, *Figure 4-5*, and *Figure 6-9* for creep subgrains and *Figure 6-11* for HCF subgrains). The subgrain develops in a primary grains just like the ones observed in the creep specimens inducing the possible phenomenon of cyclic creep, which is assumed to be the case under HCF chapter *section 5.2.2*. Development of creep can be also observed from the strain measurement discussed and seen in the *Figure 5-3*. To confirm, if the fatigue damage at higher temperatures is due to the formation of smaller subgrain boundaries, SEM investigation will be discussed in the successive sessions along with other possible fatigue mechanisms.

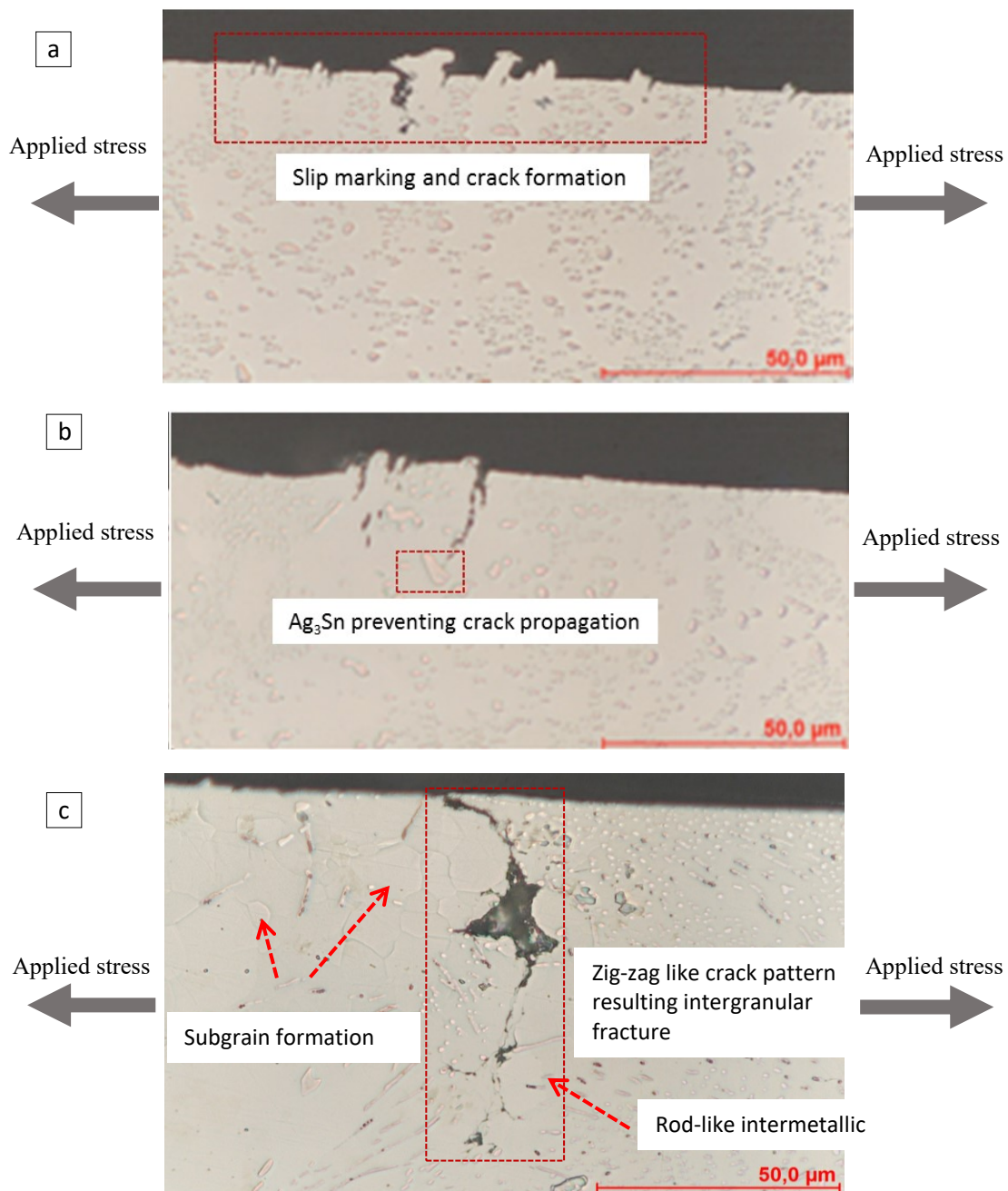


Figure 6-11: Microstructure of a non-necking region, LS and 125°C tested specimen showing (a) development of short parallel slip markings at an angle of 45° (b) nucleation hindered by the Ag₃Sn precipitate (c) subgrain formations and crack growth in a zigzag pattern along subgrain boundaries

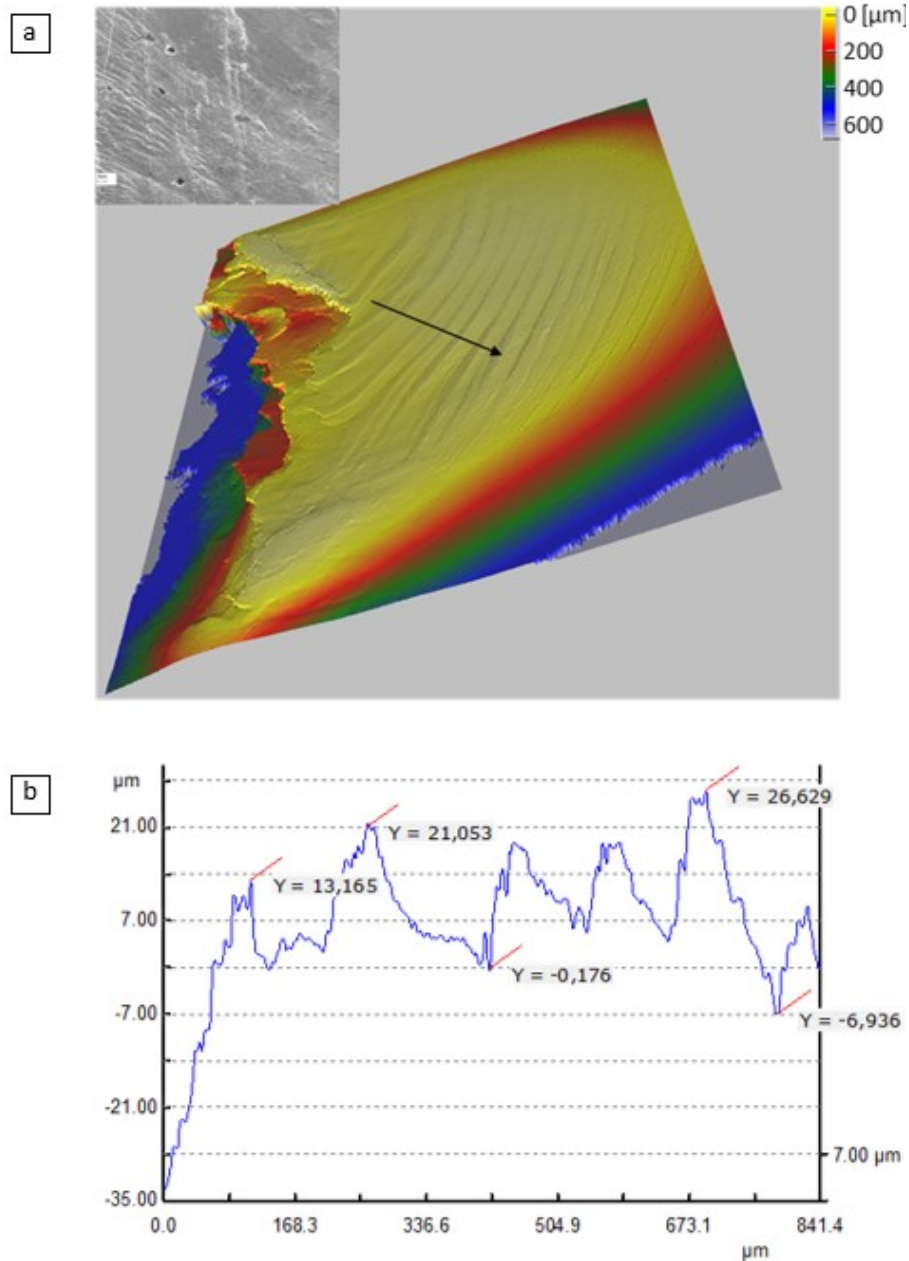


Figure 6-12: Surface scan of the specimen tested at LS and 125°C showing the wavy slip markings (PSB) (b) corresponding intrusion values over line scan

Along with the subgrain formation mechanisms, HCF regime at higher temperature ($>80^\circ\text{C}$) are investigated for any presence of persistent slip bands (PSB) [56, 169, 170], using surface scans is seen for example in Figure 6-12. More fundamentals of PSB and their relevant mechanism is introduced in section 2.1.6.1. These PSB are short and more or less at 45° from the loading direction shows that they are related to the activation of the easiest crystallographic slip systems in the slip plane, as an e.g. [110]. The surface scan in Figure 6-12 revealed the average extrusion height of PSB are around $\sim 5\text{-}10\mu\text{m}$, while the surface between them is smooth. With the increasing number of fatigue cycles, it is assumed in the current work that more PSBs are formed within the primary grain. Even though significant amount of PSB are found on non-crack initiation regions, for most test cases PSBs are assumed to have possibly developed towards the end of lifetime. From the qualitative investigations, it is not evident that if the crack initiation activity is influenced by PSBs as the intrusion level (surface protrusions)

of PSB peaks are minimal. Moreover, the macro-failures are not observed from the PSB detected zones.

At substructure regions (mostly on softer β -Sn dominated regions), nucleation of micro-cracks at interface between the hard layer and soft matrix are found to exhibit a zigzag like pattern [14, 154] as seen in *Figure 6-11-c*. Void initiations and crack propagation thereafter followed the subgrains resulting in intergranular cracks, which is assumed as a dominant initiation mechanism for the higher temperature ($\geq 80^\circ\text{C}$) specimens. The polygon subgrains formation tends to deviate the fracture propagation on the cross section investigated which will also affect the crack propagation rate. In some cases, the secondary cracks are hindered by the rod like Ag_3Sn inter-metallic [14], coarsened during the solidification rate as seen in *Figure 6-11*.

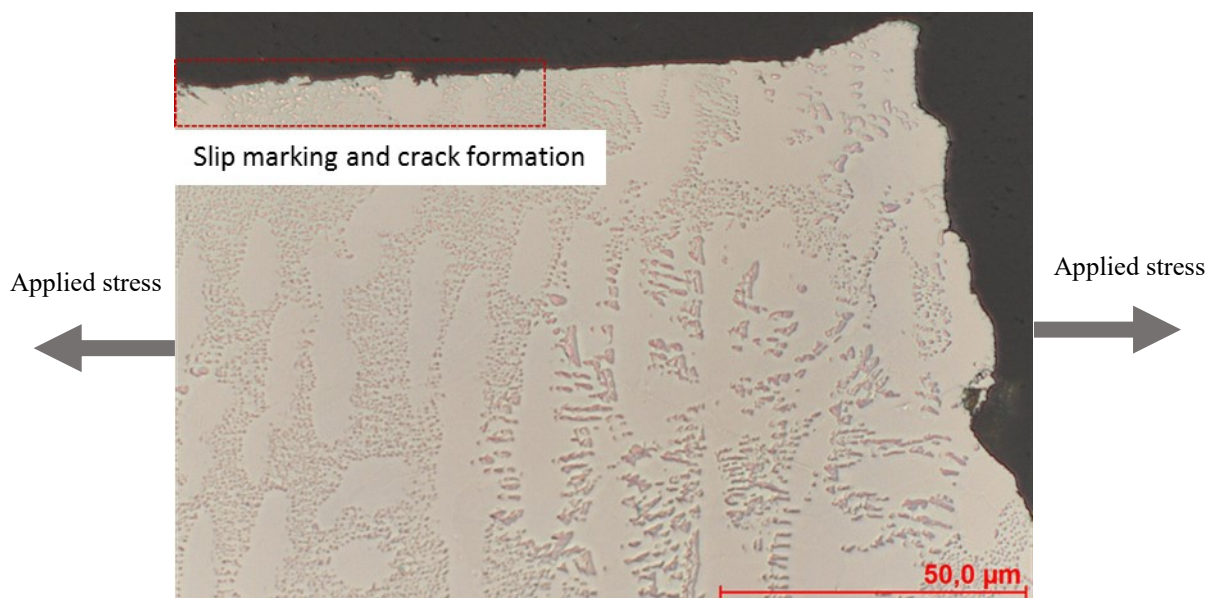


Figure 6-13: Microstructure of a 35°C and LS tested specimen, showing development of short parallel slip markings and secondary cracks on the stress concentration regions

A common feature of the elevated temperatures ($\geq 80^\circ\text{C}$) and the room temperature (35°C) crack nucleation is the formation of PSBs as also seen with the 35°C test specimens in *Figure 6-13*. Towards the end of fatigue life, secondary micro crack formations are based on PSB for both high and low temperature specimens. However, there are very less evidences of macro-cracks propagating from PSBs near the fracture surface for elevated temperature specimens. Therefore, for elevated temperatures ($\geq 80^\circ\text{C}$), cyclic creep and subgrain boundaries can be postulated to be a primary dominant mechanism, compared to PSBs for the initiation of macro cracks and failure.

For low temperature (35°C) specimens, stress concentration regions revealed microcracks formation on the soft β -Sn matrix as seen in *Figure 6-13*, also investigated in the work of Barry [8]. SEM investigations, which will be discussed in *Figure 6-15* also revealed that low temperature fatigue specimen showed crack initiation sites associated mainly in the stress concentration regions and PSB are observed on the local stress concentration regions [56, 169, 170]. A summarized overview of the entire phenomenon for room and elevated temperatures is tabulated in *Table 17*.

6.5 HIGH CYCLE FATIGUE FRACTURE SURFACE ANALYSIS

The macroscopic fracture surface of HCF test specimen is examined qualitatively with SEM in this section. It should be considered that the fracture surface is distinguished by two distinct process: crack initiation and crack growth of a dominant fatigue crack (apart from secondary cracks) followed by general plastic collapse or sometimes called as overstress failure. The analysis of the fracture surface features corresponding to the failure mode(s).

Principally, it is found that the fracture surfaces in the current work could be distinguished for various failure modes by investigating phenomenon like formation of persistent slip bands (PSB) [56, 169, 170], failure due to local stress concentration [8], secondary cracks, the formation of striations and finally formation of dimples (typically represents overstress regions). The phenomenon investigated in SEM for different test cases (mostly temperature influence) are shown in *Figure 6-14* to *Figure 6-18*.

Solder specimen under HCF unlike LCF shows very detailed striations usually on the crack initiation sites and the propagation sites [8]. Fundamentals explanation of the formation stages of the striation can be referred in Laird [171]. Another important feature in identifying the striations is to identify the crack propagation directions. The crack propagates in the direction perpendicular to the striation patterns as seen with higher magnification in *Figure 6-17*. The experiments tested under lower and higher stresses, could not yield a different fatigue mechanism, which can be seen the fatigue results (see *Figure 5-2*), strain amplitude comparison (see *Figure 5-3*), and also from the SEM studies in this section. Therefore, the discussion of the comparison between higher and lower stress specimens is not the primary focus in this section.

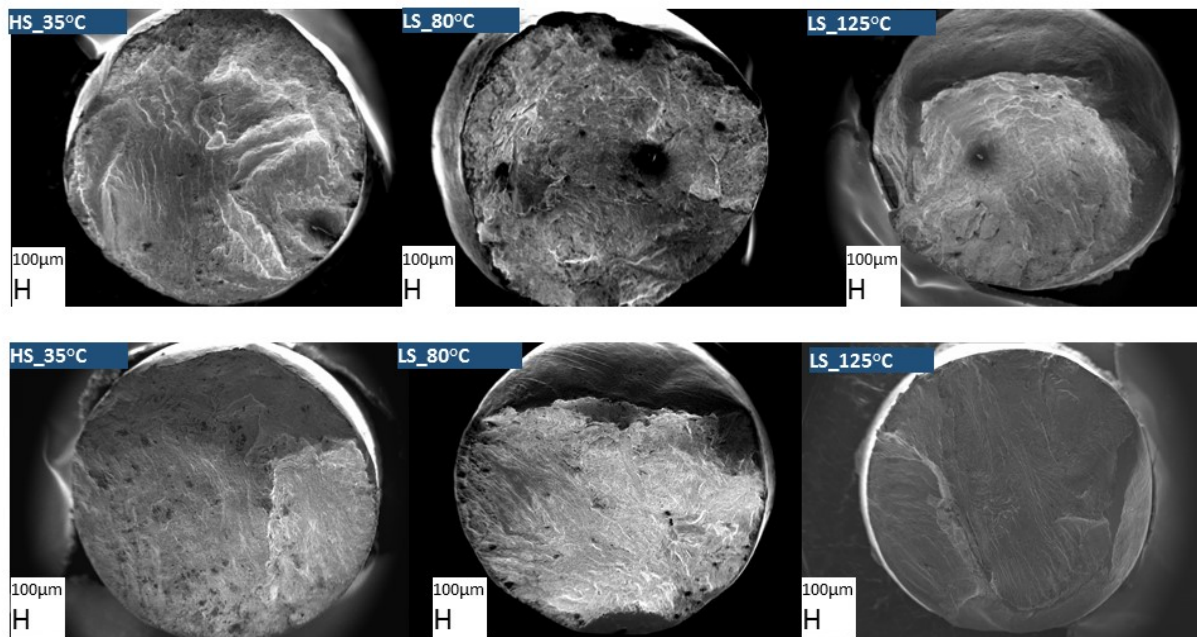


Figure 6-14: SEM of HCF fracture surface for temperatures (35°C, 80°C, 125°C) at relatively: (top row) $N_f \sim 10^5$ cycles (bottom row) $N_f \sim 10^7$ cycles

The effect of temperature is found to be one of the most important factor influencing the fracture in a solder specimen (S-N curve seen in *Figure 5-2*). Thereby, the primary aim of the analysis is to confirm the possible fundamental fracture mechanisms at higher and lower temperatures. Summarized results can be referred from the conclusion section in *Table 17*. Higher magnifications are used on the selected region to determine the different failure modes. As seen in *Figure 6-14*, the high temperature 125°C specimen compared to the 35°C not only facilitates

ductile failure mode (increased amount of plastic deformation) but also gives an indication of plastic strain concentration regimes at or near the vicinity of the fracture surface.

Once the overview of the specimen is analysed (see *Figure 6-14*), different zones are detected and analysed on the fracture surface to identify the crack initiation, propagation sites, and over-stress regions as visualised in overview fracture surfaces *Figure 6-15*, *Figure 6-17*, and *Figure 6-18*. For room temperature specimens at 35°C and LS, significant striation patterns on the crack initiation sites are observed. At the end of fatigue life, they undergo ductile fracture (overload fracture) characterized by a dimple structure over a small fracture surface area as seen in *Figure 6-15*. This is a very common phenomenon for plenty of metals and alloys [14]. PSBs are detected on the surface (Zone B) towards the necking region but not towards the crack initiation sites (Zone A). *Figure 6-16* gives a higher magnification of such ductile zones formed during end of fatigue experiments.

The cavities that comes from the inclusions of coarser precipitates (Ag_3Sn and Cu_6Sn_5) are enlarged and upon further yielding of the material the cavities are necked and sheared [14, 8]. To a first approximation, the depth of these dimples can be considered as a measure of the ductility [8]. The particles de-cohere from the $\beta-Sn$ matrix forming a micro void around each particle during the final crack stages. Continuing true stress results in the expansion of these microvoids and finally leads to macro void coalescence, giving raise to the complete final fracture close to fatigue life, N_f .

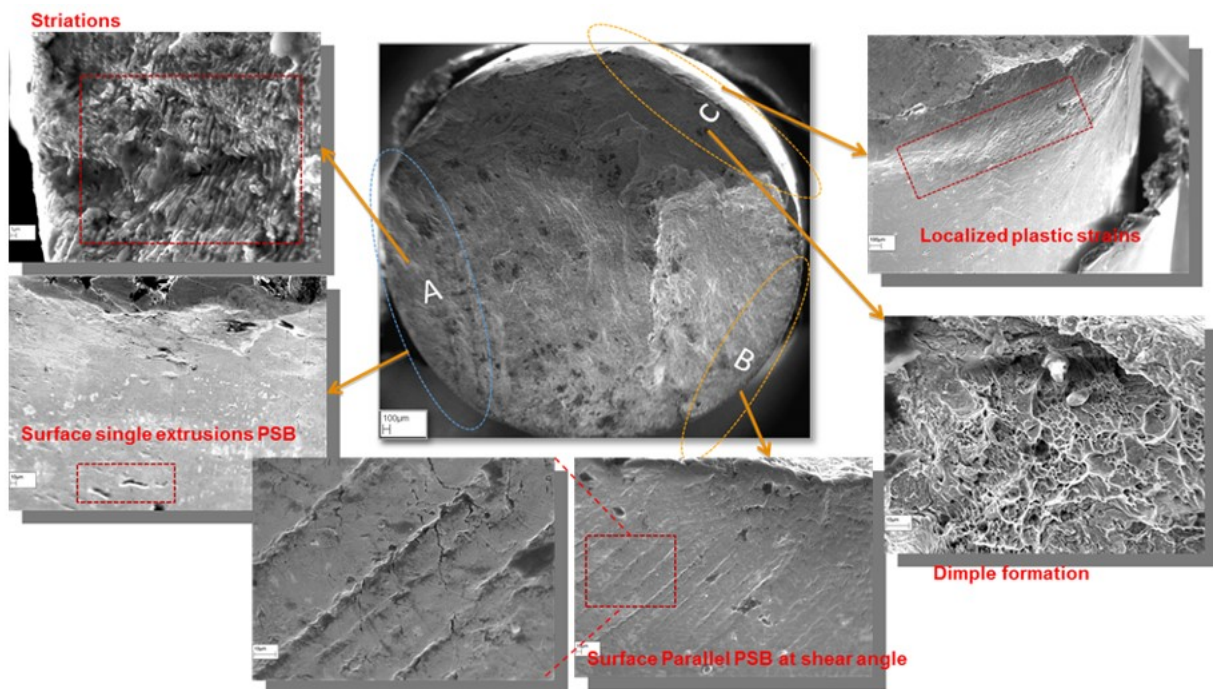


Figure 6-15: SE micrographs of a HCF specimen at 35°C, $N_f = 10^7$ and LS (zone A) high stress intensity striation region (zone B) PSB dominated on the surface, (zone C) micro-void coalescence with high local strain showing void initiating particles at the bottom of some dimples.

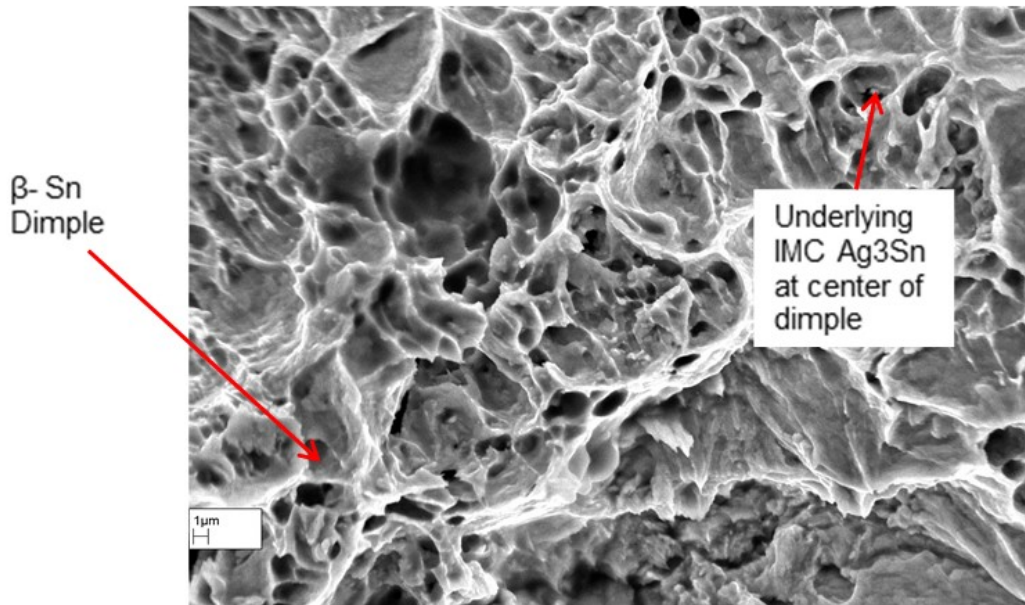


Figure 6-16: SE micrograph of a HCF specimen at 35°C and LS showing typical high stress intensity region of the fracture surface and dimples of solder with the underlying IMC layer revealed by voids developing in their centre

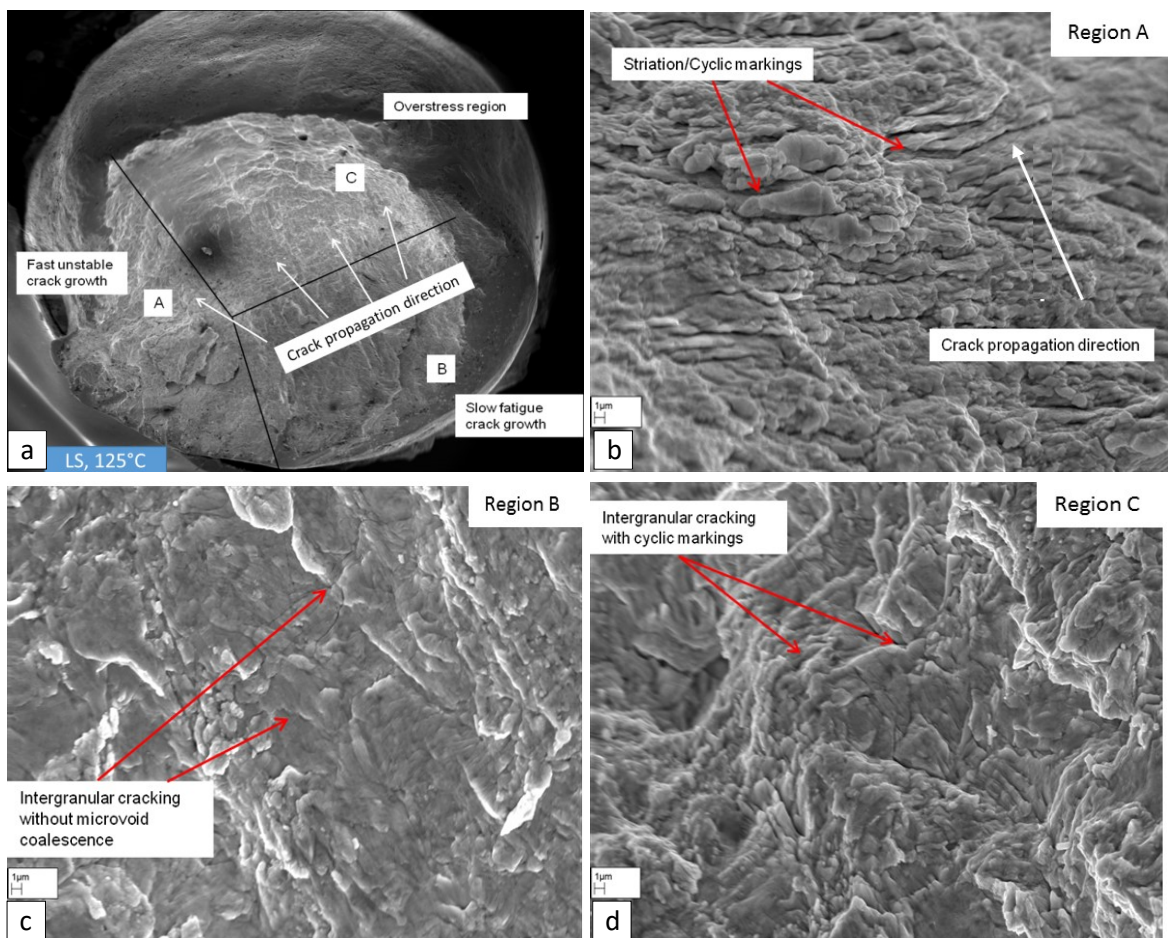


Figure 6-17: (a) SE micrograph of HCF specimen at 125°C, $N_f \sim 10^5$ and LS showing demarcations of probable stages of failure, (b) higher magnification on region A showing probable transition region and development of striations, (c) region B show probable slow fatigue crack growth zone with a 3-point morphology, (d) region C show cyclic marking along with intergranular cracking

High temperature fatigue specimens (125°C) are analysed with higher magnification as seen in *Figure 6-17-c and d*. Intergranular fracture is more prominent for high temperature specimens in comparison to low temperature specimens (*Figure 6-15*). Evidences are extracted out of the analysis and postulated to have intergranular failure, which are normally associated with high temperature experiments. However, no dimple like formations are found on the inter-granular failures as a mixed mode or as an individual mode for higher temperature specimens. None of the zone A, B, or C in *Figure 6-17* indicated any evidence of dimple zones. However, when stresses are intensified just before the fracture the intergranular cracking is found to be associated along with the striations as seen in *Figure 6-17*, which is also observed in the works [14, 154]. By analysing the striations in zone A, the direction of the crack propagation can be identified seen in *Figure 6-17*, which would probably give a hint of the crack initiation and propagation direction. Zone A, with high cyclic markings will indicate the crack initiation site and zone C which has secondary cracks in the form of intergranular cracks will indicate the end of the fatigue life zone. Since the striation seen in the zone B is not so intensified as C, the zone B acts as a propagation zone.

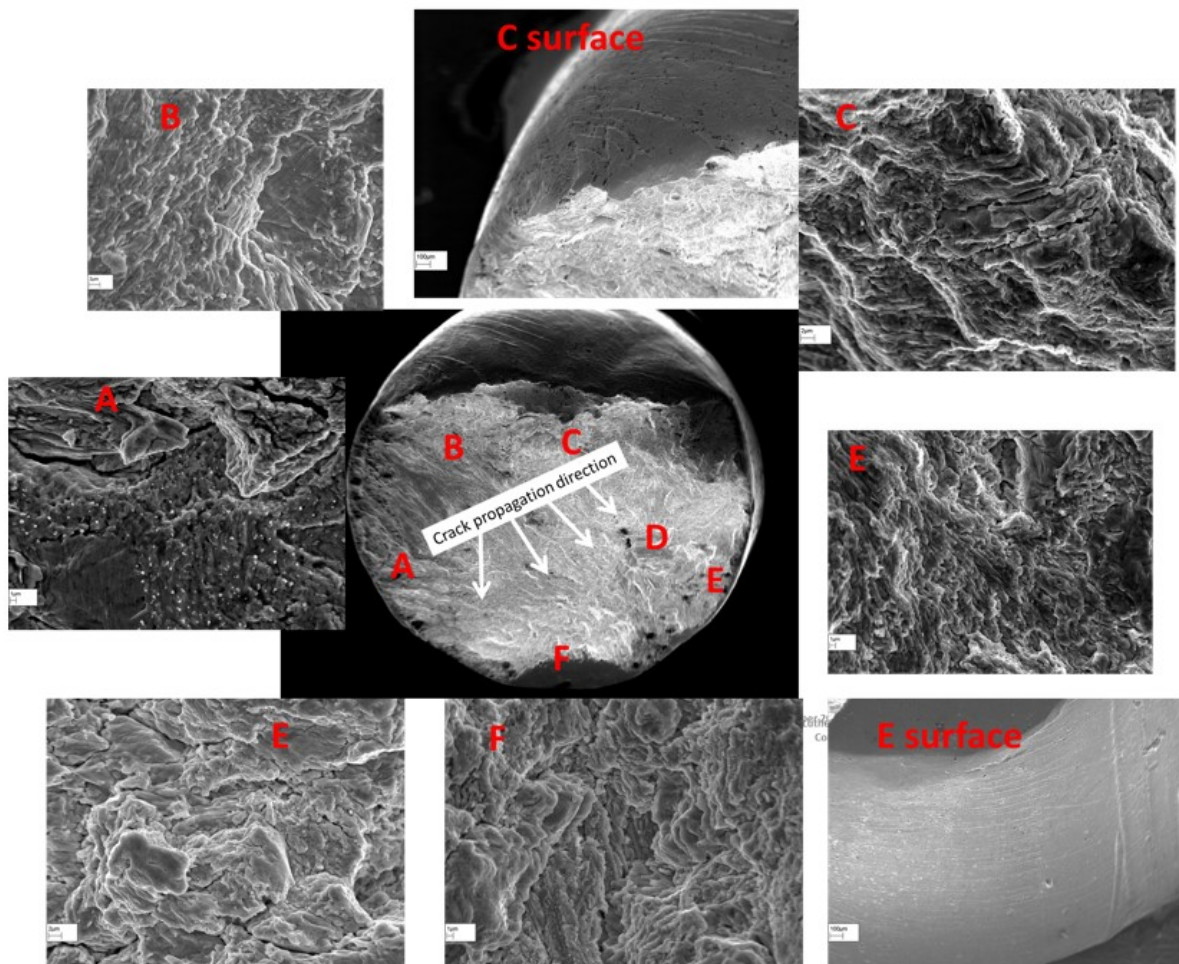


Figure 6-18: SE micrographs of HCF specimen at 80°C , $N_f \sim 10^7$ and LS (C, E, and F) high stress intensity striation region with secondary cracks and PSB (A, B) wavy striation patterns in the $\beta\text{-Sn}$ matrix (E and C) detected PSB formations

The same zone split analysis is also performed on higher lifetime ($N_f \sim 10^7$, 80°C, LS) experiments. In this case, six different zones are detected and analysed to find the crack initiation sites with overstress regions. Unlike low temperature observations, no dimple formations on the overstress regions are found which eventually makes the observations difficult. *Figure 6-18* reveals the six different zones with an overview of fractography in the middle graphics. Striation arrangement revealed on the Zone A and B hints at the crack propagation direction. Zone A shows the eutectic zones and the β -Sn matrix with the striation inflecting the β -Sn matrix.

Similar observations are also seen on zone B, which could mean that the crack initiation site is close to A and B. However, on the other zones (E, C and F), secondary cracks are observed, especially on the zone E, with the cracks reaching higher depth. This could from the zone that has inflected especially towards the end of fatigue life, N_f . In parallel, the surface of the specimens is also analysed to see any kind of PSB formation. The zone C and E showed indication of parallel slip markings, but is mostly seen on the necked regions. No significant amount of PSBs are observed again on the crack initiation sites.

6.6 CONCLUSIONS

For creep investigations, a qualitative microstructure analyses performed detailed in this chapter indicates the possible deformation mechanism(s), which supports the earlier theories postulated under discussion *section 4.5.3*. Various aspects from the microstructures of creep experiments in comparison with cast solder specimen gives evidences to explain the phenomenon and deformation mechanisms involved. Overall results reveals significant presence of subgrain boundaries irrespective of the stresses and temperatures applied. The investigation is performed in specific for low and high stress test specimens along with the various temperature variants. Key findings for SAC alloy under creep is summarized and discussed as follows:

- In either case of investigated necking and non-necking regions, subgrain formations is evident, which could indicate the possible substructure formation during the primary stage of the creep, when the strain hardening happened as known from literature [67]. For most of the micrographs that are investigated and irrespective of the applied stresses and temperature, a subgrain size intercept of $\lambda_{ss} \sim 10$ to 15 μm is statistically analysed. This is in line with the literature, [172, 36], that discusses the substructure formation, which directly controls the dislocation creep and acting as a potential resistance for material deformations at elevated temperatures.
- Subgrain formations is also detected on the elevated temperature HCF experiments in the LM micrograph and later confirmed by SE fractography. The substructures detected is assumed to have introduced additional mechanism like intergranular cracking as visualised in *Figure 6-9*.
- Primary grains (big grains) remains stable during the complete creep deformations with almost very less evidence of any possible grain boundary sliding. The primary grains did not contribute significantly to any intergranular macro cracks.
- The softer β -Sn matrix deformed in the presence of dislocation, are hindered by the subgrain boundaries (acting as sink [67]). The movement of dislocations in the eutectic regions can be a result of creep mechanisms like climb/glide and Orowan bowing. The analysis using EBSD, LM and EBCC performed in the work indicates subgrain formations. However, for a detailed analysis and further validation, it is encouraged to use TEM and other techniques.

- Presence of primary phase, Cu_6Sn_5 and Ag_3Sn particles is observed to resist defect movements, especially when located along the subgrain boundary. Evidence from the current chapter proves primary phases playing a key role in the local climb and Orowan mechanism for SAC alloys as postulated earlier under *section 4.3.1*.

For HCF investigations, crack initiation, crack propagation and fracture regions are investigated from fractography. This could explain the differences in performance of the solder alloy examined in this work for different test conditions discussed under *chapter 5*. Crack initiation sites in specific, provides information of the possible damage mechanisms involved for the fatigue in SAC alloy. The current chapter outlines the fatigue mechanisms and the theories postulated earlier under *section 5.2.2*. Some of the key finding of fractography analysis are concluded as follows:

- For the room temperature (35°C) fatigue specimens, ductile fracture is observed and characterized by a dimple structure over a small fracture surface area that are not normally seen for a high temperature tested specimens. The dimple structures are not detected on crack initiation sites, which could be a proof that crack initiation sites are associated with local stress concentration regions. For SAC387 alloy at room temperature, the hardened particles interact with the surrounding matrix to form dimple zones. Crack propagation in the primary grain is expected to be transgranular.
- For high temperature tested specimens, necking and PSB formations are observed on the same regions. Evidences of PSB formations are assumed to have only formed towards end of fatigue life and contributed minimal to any crack initiation sites. However, further investigations to stop experiments towards the end of lifetime and to analyse fracture surface is encouraged to prove the evidence of PSB. On contrast room temperature (35°C), specimens featured crack initiation sites on the stress concentration regimes. An overview of various test matrix and their corresponding mechanism for crack initiation sites is seen in *Table 17*.
- HCF specimens are analysed for possible crack propagation mechanisms like transgranular and intergranular cracking (see *Figure 2-10* for schematics). For both high and low temperature test specimens (see *Table 17*), transgranular cracks are evident on the primary grains. For high temperature specimens intergranular cracks are observed around the subgrains. The intergranular cracking is assumed as an evidence of subgrains controlling the crack propagation rate. PSBs had less significant influence on the crack initiation sites for low temperature. A summarised overview of subgrain and primary grains distinguished for intergranular and transgranular mode of failure is tabulated in *Table 17*.
- Ding *et al.* [173] investigated the crack propagation of *Sn-37Pb* solder, under ageing conditions. Ding *et al.* [173] found the cracks are promoted due to the transgranular rather than the intergranular cracking. This proof to support the nucleation at grain boundaries conditioned by the cyclic slip process is also investigated by Kim and Laird [174]. This is a possible indication of a transgranular fatigue crack on primary grains and intergranular cracks along subgrain boundaries, which was also discussed in the work of Shang *et al.* [14].
- One big notable difference between the microstructure of specimen before and after fatigue experiments at higher temperatures (80°C, 125°C) is the clear visualisation of

substructure development in individual grains visualised in *Figure 6-11*, just as the ones observed during creep experiments inducing the possible phenomenon of cyclic creep [57]. Firstly, the substructures are formed; and at later stages, nucleation of micro-racks at the interface between the eutectic region and soft matrix along with these substructure boundaries begins [67]. These cracks during final crack propagation revealed a zigzag like pattern along the substructure boundaries as seen in *Figure 6-11-c*. Crack growth thereby followed the subgrain boundary profile, resulting in inter-granular cracks (see schematics in *Figure 2-10-a*). This prove the polygon subgrains formation that tends to deviate the crack propagation rate. In some cases, these secondary cracks are hindered by the rod-like intermetallic as visualised in *Figure 6-11-c*.

Table 17: Summary of different mechanism involved in HCF testing for SAC alloy

HCF observed phenomenon [supporting literatures]	Room temperature (35°C)	Elevated temperatures (≥ 80°C)
Postulated crack initiation mechanism(s) [8, 174]	stress concentration dominated, PSBs	cyclic creep, sub-grain boundary, PSBs
Persistent slip bands (PSB) [56, 169, 170]	yes (less evidence from current work)	yes
Subgrain formation [154]	yes	yes
High necking towards the end of fatigue life [1, 8]	no	yes
Cyclic-creep [57]	no	yes
Intergranular cracks on subgrains, linked to subgrain formation [14, 154]	no	yes
Transgranular cracks on primary grains [8, 173]	yes	yes
Dimple formation around precipitates [14, 56]	yes	no
Crack propagation blocked by hardened phases [14, 56]	yes	yes

7 LIFE TIME PREDICTION UNDER VIBRATION AND THERMAL CONDITIONS

A generalised fatigue evaluation of SMT component solder joints using the generic bulk solder testing results and FE simulations is investigated in this chapter. The proposed methodology is validated by performing vibration experiments on two different SMT components (chip capacitors and transformers) soldered on single strap PCB subjected to sine swept loading at various temperatures. Local stresses calculated from the frequency response (introduced in *section 2.2.4*) on the solder joints will be used as damage parameters in predicting the lifetime. The material characterisation for the fatigue evaluation is carried out by conducting HCF experiments in uniaxial tensile specimens following FKM guidelines as studied in *chapter 5*. Influential fatigue factors such as temperature, stress gradient, R -ratio, roughness are also considered. Fatigue life of solder joints is determined and experimentally verified with that of the predicted fatigue life of solder joints results.

The second part of this chapter deals with the investigation of developing subroutines based on the new modified creep model in ANSYS studied in *section 4.3*. The subroutines will be verified using FE-models of ceramic capacitors under TMC loading.

7.1 GENERALISED METHOD OVERVIEW FOR VIBRATION PREDICTION

In order to save lengthy and extensive long-term testing of components/parts, a FE approach is investigated in the current chapter. The generalisation work involves fatigue specimen instead of testing SMT components to find the intrinsic material constants. The material constants can be used later for predicting lifetime of components/parts using FE analysis. The advantage being, whenever the component parameter or test condition changes it is still possible to predict the lifetime with FE calculations. In addition, it should be also possible to calculate the lifetime before the component is built during design phase.

This section focuses on the FE simulation validation aspects to predict the cycle to failure in a SMT solder joints under dynamic loading conditions.

The overall outline of the proposed validation technique is presented in *Figure 7-1*. Coupon level experiments (*1. Material specification on bulk solder specimen as in Figure 7-1*) are performed for determining material specification of solder fatigue specimen. HCF test results and material constants found from HCF solder specimen based on FKM guidelines is described in depth under *chapter 5*. Loading conditions like temperature enable one to study the possible deformation and fracture mechanism encountered in a solder joint under combined fatigue and temperature environments. Apart from temperature, other influential fatigue parameters like stress gradient, R -ratios, surface roughness are also considered in the HCF investigation.

Intrinsic solder material fatigue constants found/corrected are then used as an input material property in software, nCode Designlife™ (*4. Fatigue evaluation in Figure 7-1*). The nCode and ANSYS software finds the damage parameters and hotspot stress-strain field regions respectively. Both software are coupled to arrive at the ultimate lifetime prediction values. The dynamic response of the solder based on local stresses from the frequency response function (FRF) is used as the damage parameter in this study. By comparing, the local stresses from the SMT solder joint and bulk specimen, conventional damage accumulation theories can be applied to evaluate the remaining life [128].

To validate the approach of predicting the lifetime of SMT components, component level experiments (*2. Component testing on SMT in Figure 7-1*) are conducted for vibration loading. Component level vibration test on SMT gives a relationship between the local stresses on solder joint and the corresponding cycles to failure. The finite element model of the SMT and solder

joint (3. *FEA-component* in Figure 7-1) will be used in the 4. *Fatigue evaluation* and 2. *Component testing on SMT* to calculate the damage values and stress-strain responses respectively. Lastly, the predicted result of solder joint failure from *Fatigue evaluation* and *Component level experiments* on SMT will be compared to prove the hypothesis. A combination of experiment and simulation work followed in this work, enhances the result details and accuracy.

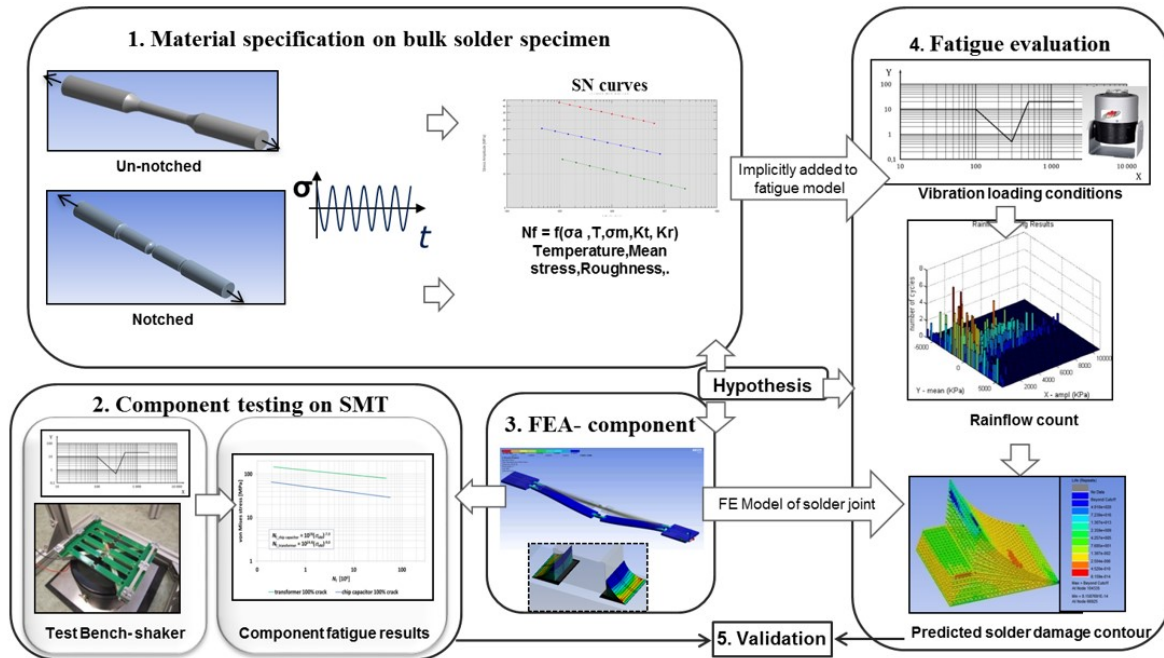


Figure 7-1: Local stress concept and overall take on the proposed methodology to assess the lifetime of solder joint under vibration loading

7.1.1 Experiment summary

Two different sets of experimental setups used in Figure 7-1 are summarized as follows:

1. Coupon level experiments (1. *Material specification on bulk specimen* in Figure 7-1)
2. Component level experiments (2. *Component testing on SMT* in Figure 7-1).

Coupon level experiments are done on the uniaxial-bulk solder specimens as explained earlier in section 3.4. All the results of this experiment can be referred in chapter 5, where a coupon level solder fatigue specimens is investigated under HCF fatigue environment.

Component level experiments are the vibration experiments done on SMT component level according to the test parameters as seen in Table 3. Test setup of the component SMT with solder joint details can be referred in Figure 3-11.

7.1.2 Finite element analysis - component level

For the sake of simplification to explain the FEA process, only chip capacitors are discussed detail in the current section. The experiments and FE validations are performed for both room and elevated temperatures. A FE analysis of the component with solder joint is investigated in this section (referred as *FEA- component* in Figure 7-1). A detailed solder joint geometry is captured and line-clamping boundary conditions are included.

Complete model of the one strap is modelled for better accuracy and only one strap is calculated for reducing computational time. Complete solder joint geometry is modelled based on the cross sections before the experiments with meniscus diameter of 0.25mm [17]. Material properties are implemented according to Meier *et al.* [61]. SAC solder, copper, ceramic, polymer

(for transformer), coil core (for transformer) uses elastic material models, and PCB is modelled with anisotropic elasticity properties. The PCB substrate is modelled with the corresponding material damping behaviour. *Figure 7-2* visualises the overall model of the strap and a closer look of the component solder joint with the detailed mesh elements.

Modal analysis is investigated firstly to calculate various modal frequencies (resonance). Later for extracting the FRF results, harmonic response analysis is done. To reproduce the vibration experiments at elevated temperatures, the chip capacitor PCB model is virtually heated around the component surrounding.

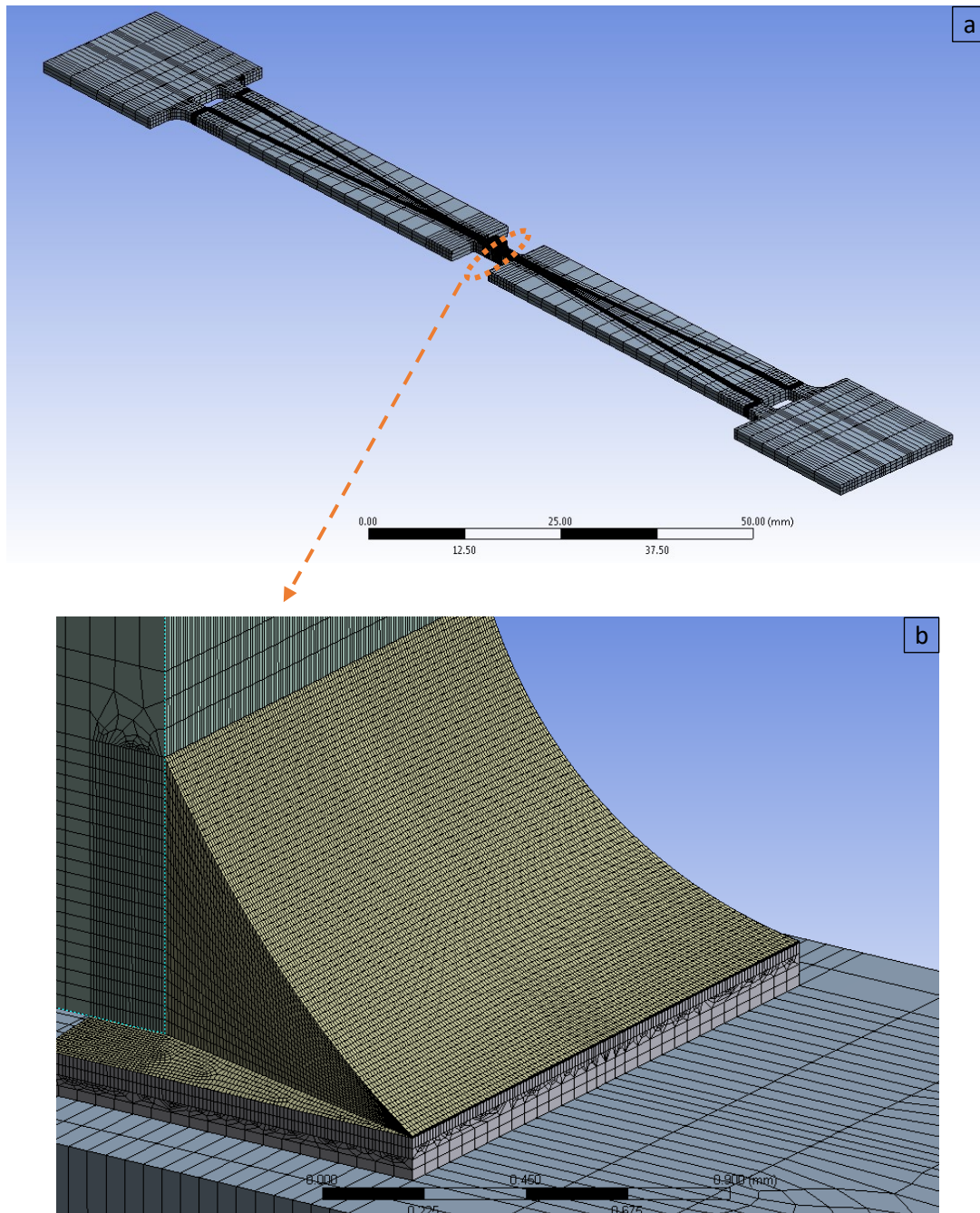


Figure 7-2: FEA model mesh (a) overall model of single PCB strap with component CC0805 (b) detailed view of the solder joint mesh

7.1.3 Mesh dependence

Apart from the methodology itself, the investigation encourages the right mesh settings and selecting the right material property for calibrating the FE results with the experimental observations. The mesh settings are important for the local stress methodology as the optimal quality of mesh metrics has to be adapted for taking the maximum local stress value of the element [175], especially on the surface elements, where the fatigue evaluation will be done. The smaller element size will reduce the discretisation error, but will increase the computation time. In this investigation, a compromise of the element quality is achieved by bringing the aspect ratio, parallel deviation, and maximum corner angle to the recommended settings [175]. A sample meshing is visualised in *Figure 7-2-b* with a better treatment of mesh sizing in the region of interest for fatigue evaluation.

Two different types of models based on hexahedron dominant meshing are analysed with coarse elements (*Type 1*) and fine elements (*Type 2*) on the solder joints. The total number of elements from the global system is increased by ~ 17 times. Local meshes are controlled on the solder joints and the elements are increased between the two types up to 26 times as seen in *Table 18*. Finally, a quality factor is computed for each element of a model (excluding line and point elements).

Table 18: Comparison of number of elements on coarse and fine meshing

	Type 1	Type 2
Total No of elements	55,424	956,412
No of Solder elements	25,584	687,792
Type	Quadratic hexahedron dominant	Quadratic hexahedron dominant

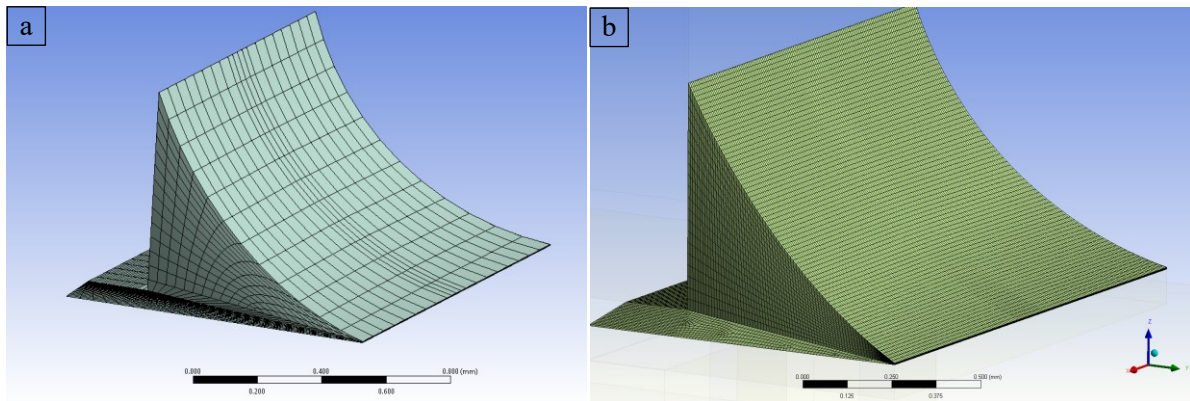


Figure 7-3: FE model of the solder joints showing the two different mesh density (a) type1 (b) type 2

The aspect ratio for a quadrilateral is the ratio of longest side to the shortest side of which the rectangle is most stretched. The best possible aspect ratio for a square is one. The aspect ratio is monitored during the quality check process. With the increase in the aspect ratio metrics, the elements get more stretched. The *type 1* elements had 44% of the solder joint elements above the aspect ratio. *Type 2* elements had reduced aspect ratio $\sim 8\%$ with fine meshing.

The parallel deviation of the quadrilateral is computed by finding the dot product of the unit vectors of the opposite edges. This metric is denoted by the angle ranging from 0 until 180° . The best possible deviation for a flat rectangle is 0° . Around 39% of the elements (considered as average quality) from coarse mesh type are reduced up to around 6% by increasing the mesh element density.

The final analysis is to find the maximum corner angle of the adjacent edges. The best possible maximum angle for a flat rectangle is 90° . The increase up to 180° shows the stretching of elements along the adjacent edges. The analysis on *type 1* showed that the surface elements on the meniscus of the solder joint where the crack is initiated had a higher adjacent edge angle above 150° , which is reduced below 150° using the *type 2* mesh. There are many different ways to increase the quality of mesh and the above-mentioned method is one such technique to find accurate lifetime prediction values. It is not within the focus of thesis to find alternate methods for a better mesh quality metric.

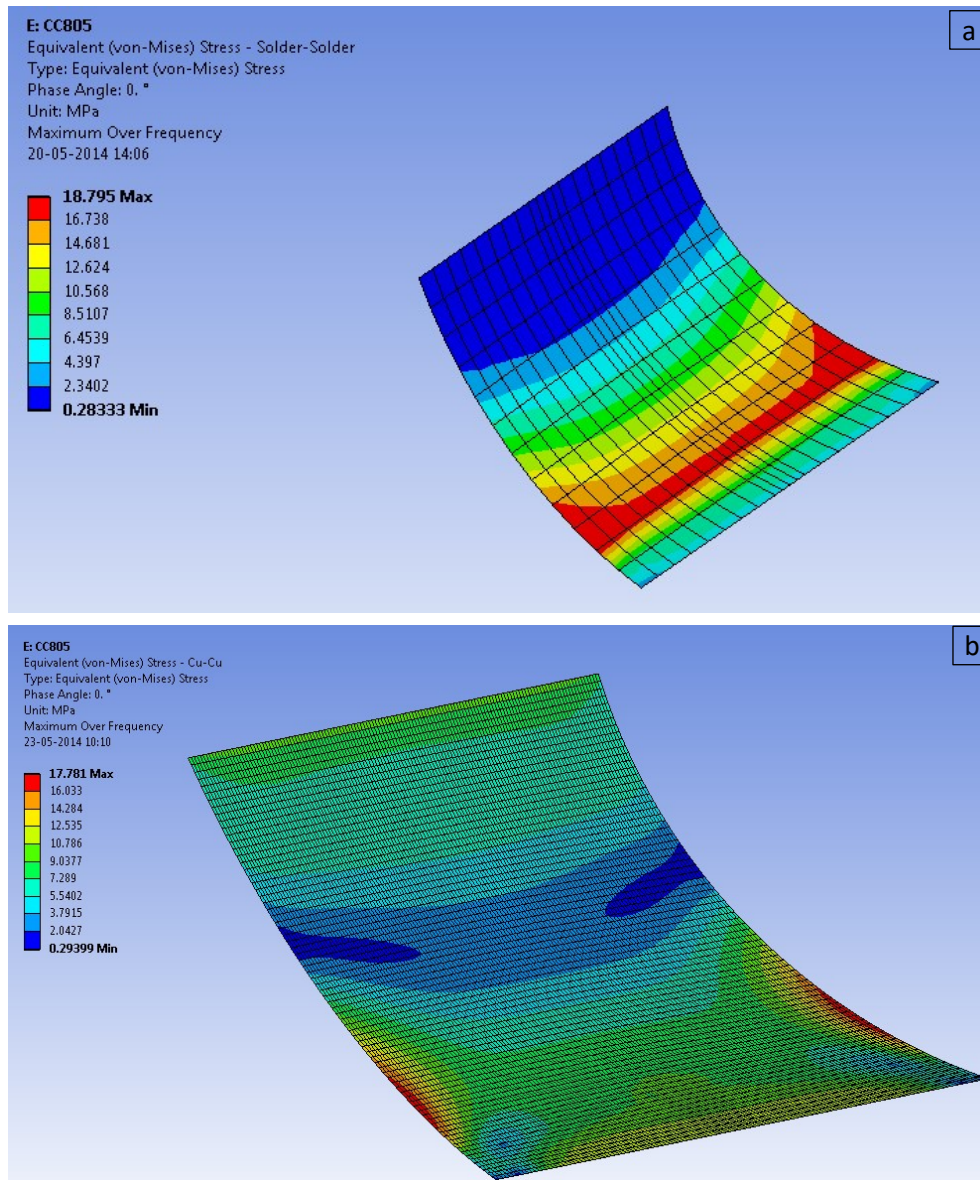


Figure 7-4: Example von Mises FEA results of surface elements for a harmonic unit excitation for mesh setting (a) type 1- coarse (b) type 2-fine

For a similar FE setting, the post processing analysis shows significantly different results as in Figure 7-4. Contour results of the von Mises stresses and the maximum element stresses had a 1MPa difference and at elevated temperatures, the difference is as high as ~ 3 MPa (resulting in relative error of 5-11% depending upon the temperature). The calculated stress difference is significant for SAC alloy, which is sensitive to stress tolerance while designing fatigue (see Figure 5-13). This analysis encourages proceeding the analysis with *type 2* fine mesh settings.

In case, the usage of *type I* settings are followed, this need separate evaluation techniques such as volume averaging of the elemental results, which induces slight deviation on the remaining calculated lifetime. It is also recommended to avoid the contact element and make the global model of the CC and transformers without the contact element, as various material properties are used for the global FE model. The substrate is modelled with damping behaviour and a detailed protocol followed during damping calculation is discussed in the next section.

7.1.4 Material damping properties of PCB

The fundamental support of the frequency transfer function (FRF) and the effect of damping on the dynamic response are investigated in this section. In this work, it is considered to control the dynamic response of the system by passive control method rather than with the active control methods [176]. The passive control involves modification of the stiffness, mass, and damping of the vibration system. Vibration in this case is dominated by the resonance of the PCB strap structure. Therefore, steps are taken to control the dynamic response of the system by altering the material damping of the PCB, to have a better correlation with the experimental strap deflection results.

The easiest way to find the right damping property and to make it fit appropriate to the experimental deformation response fit is to use meta-modelling techniques [177, 178]. The meta-modelling has been widely used for design optimization problem by building surrogate models for compute-intensive simulation models [179]. From the FE model of the PCB, surrogate models are constructed in the current work using response surface methodology and the Kriging method introduced by Krige in 1951 [180]. The Kriging method is selected over other methods like neural network, second order polynomial and non-parametric regression (packages available in ANSYS). Kriging method proved to predict better from the goodness of fit analysis with all the output variables.

There are lot of other variables available for the choices of optimization of the model in the current study. However, based on the initial analysis results and modelling process, two key factors are chosen to represent the damping response of the PCB. Material properties in the form of damping coefficient of the PCB- β_{pcb} (stiffness matrix) and the density of PCB (mass matrix) are selected that changes the dynamic response of the system.

The response of the system is tracked by finding the resonant frequency (f_0), maximum directional deformation of the PCB at f_0 , and maximum Von Mises stress on solder joint at f_0 by conducting the design of experiments (DoE).

DoE details are as follows:

DoE Type: Latin Hypercube Sampling design

Method: Central composite design (CCD)

Input Material variable:

- Material damping of PCB - β_{pcb}
- Density of PCB (Kg/m^3)

Load parameter:

- Acceleration Magnitude (mm/s^2)

Output response variable:

- Reported Frequency at Mode 1 - f_0
- Maximum directional deformation of PCB at f_0
- Max stress response on solder joint at f_0

The frequency of the PCB for DoE is set within the observed range from the experiments. For CC0805 component, the frequency range set is found between 250Hz to 300Hz according to the experimental input.

When meta-modelling is used to optimize the structure, the important factors are usually also the design variables. Here 15 design points for DoE including centre points are used in the design space on which the required responses of the PCB are computed. It is obvious that using more design points (different method) gives more information on the structural responses, and thus the estimation errors reduces when the number of design point increases. In practice, a compromise between the used computing time and required accuracy is followed. In order to determine the transfer function for fatigue analysis method, first a modal analysis for the PCB strap with line clamping is analysed. ANSYS 2014™ 15.0 version package is used for the complete analysis including the DoE runs.

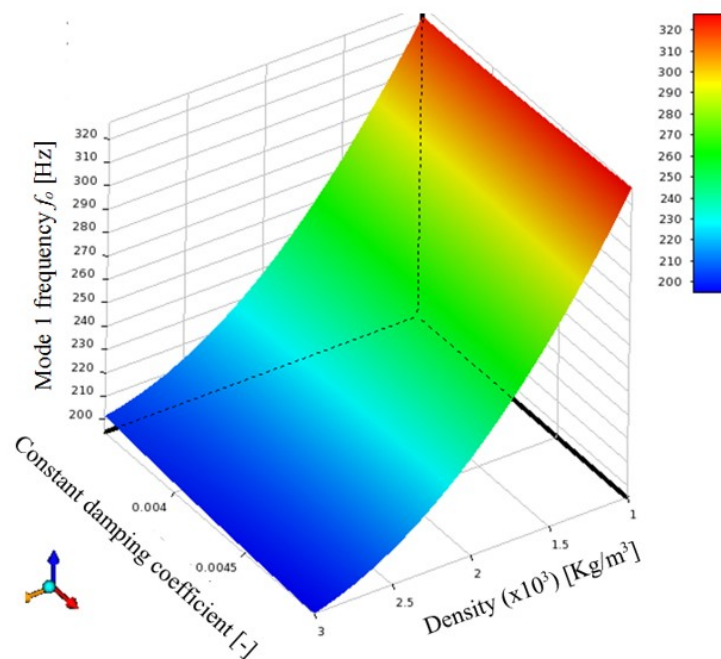


Figure 7-5: Surface response with an exemplary 3D contour plot showing the PCB response on the solder joint VM -stress for different damping and density values of the PCB

Table 19: Parameters and values changed to calibrate the FE model with experimental results

Output variables	Parameters changed-PCB (FE)	Parameter values-PCB (FE)	Obtained values (FE)	Experimental values
Target 1 st mode frequency [Hz] f_o	Density [Kg/m ³]	1595	265.5	265.85
Max PCB strap deflection [mm]	PCB damping coefficient	0.0036	0.94	0.94

One example of the DoE runs is shown in Figure 7-5. When plotted, the density and the damping coefficient of the PCB material against the frequency as in Figure 7-5, the fundamental frequency changes along with the PCB density. The desired frequency for the component chip capacitor that is 265Hz approximately is set by choosing the optimal density values. Similarly, the strap deflection values is also determined by understanding the right value needed for the

PCB damping and changing the acceleration value accordingly for the target span of the maximum deflection. The final chosen values for the density and coefficient to get the objective value of the experiments that is calibrated to the simulated results is tabulated in *Table 19*. Since the displacement of the PCB is monitored for the vibration testing using the sine wave, the maximum value of the PCB displacement and first natural frequency, f_o is used to compare with the simulated results (see *Figure 7-6* for more details).

7.1.5 Correlating PCB deflections (simulation vs. experiment)

The calibration of the component level experiments vs. simulation is done by comparing and fitting the deformation behaviour along the vertical axis (Z) as seen in *Figure 7-6*. The experimental displacement readings from the PCB strap is monitored as seen in *Figure 7-6-b* and the corresponding values from simulation are shown in *Figure 7-6-c*. *Figure 7-6-b* shows the exciting input sine wave [V] in the shaker and output response of maximum deflection tracked from the PCB [mm]. The correlation between the experimental and predicted strap deflection of one such vibration testing is shown in *Figure 7-6-c*.

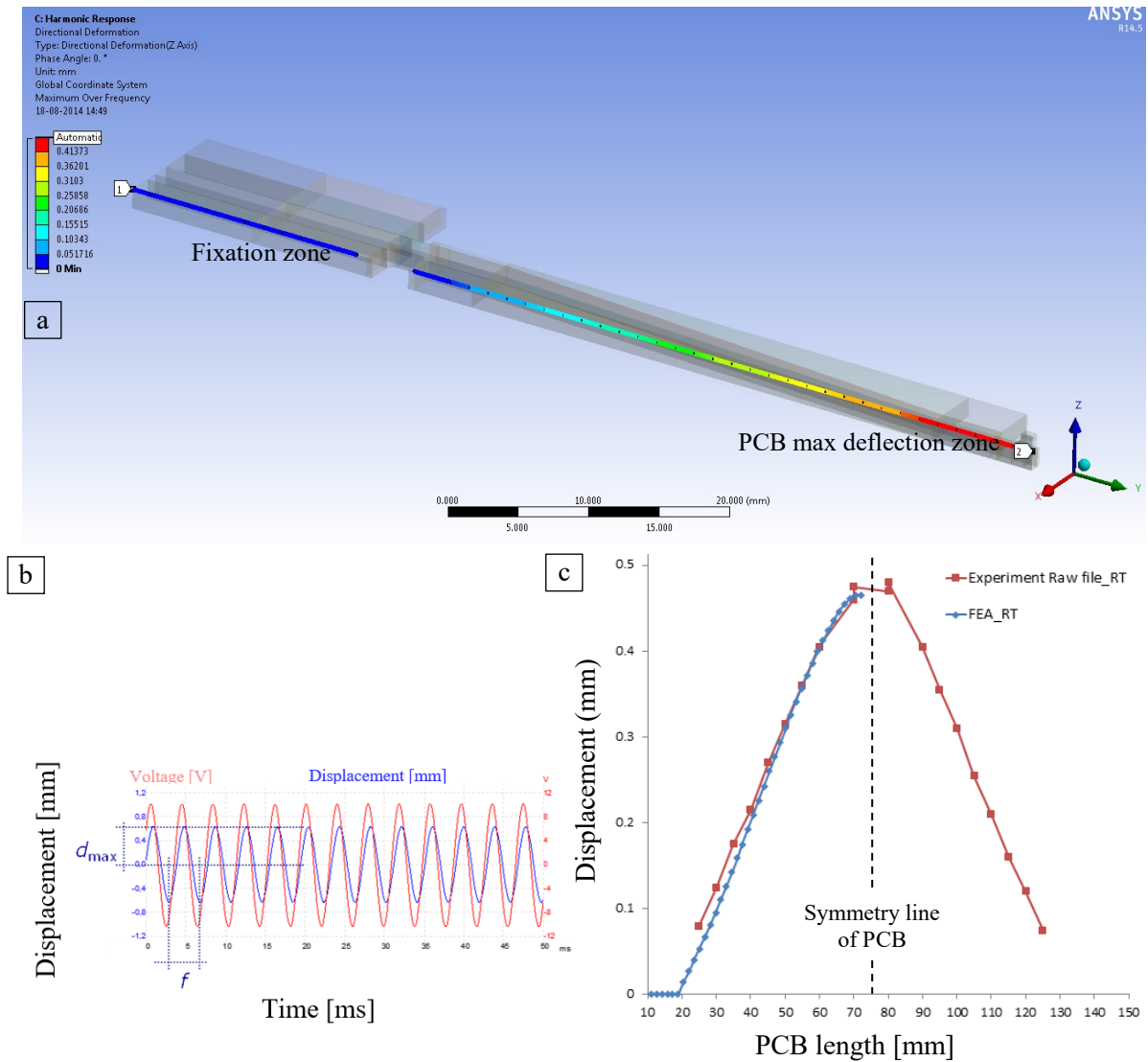


Figure 7-6: (a) Linearized FEA results of maximum Z-axis deformation from the PCB (b) 2-y axis showing measured displacement amplitude in blue and input voltage from the vibration experiment in red (c) comparison of the deformation behaviour of PCB from experiments to FE analysis with a symmetric model

The whole system with PCB is accelerated with dynamic loading to get the possible maximum PCB strap deflection between experimental ranges (~0.2 to 0.94 mm). For example, the acceleration required to get the PCB strap deflection of 0.2 mm is considered as the unit load in nCode Designlife™. This way, the loads for transformation on to the fatigue analysis can be correlated to the calibrated FE analysis of the strap deflection. The unit load transformation is now used in correspondence with the SN-property of the bulk solder results to route the fatigue analysis on solder joints.

7.3 RESULTS AND DISCUSSION

The results of SMT vibration experimental results and their validation with predicted values are discussed in this section.

Figure 7-8 visualises the SMT solder joint and the crack region of the chip capacitors (CC0805)/transformer (EHP16). As mentioned in *section 3.5* the failure criterion is any crack observed and quantified according to the length of each solder joint from cross sections. The crack length is observed to increase with strap deflection and higher vibration cycles.

For capacitor components, cracks normally initiates at the outer meniscus of the solder joint and propagates towards the substrate pad along an angle of 45°, visualised in *Figure 7-8-a*. This is the same hot-spot region where the predicted results showed the stress concentration regions (hot spots) as seen in *Figure 7-8-b*. *Figure 7-8-b* and *Figure 7-8-d* shows the predicted hotspot regions that is quantified by the failure region and its corresponding cycles to failure indicated in the legend. The predicted results using nCode Designlife™, shows the damage accumulated spots and the number of cycles to failure on the corresponding hot spot. In comparison to outer meniscus, the inner meniscus shows relatively lesser damage values.

Since the cross sectioning of all solder joints of a transformer is extensive, only four out of the eight joints are explored. The crack length in each solder joint is evaluated separately and classified. *Figure 7-8-c* shows the observed the crack propagation of the transformer loaded under vibration loading (HCF). Solder joints in the transformers shows grain refinement across the cyclic bended meniscus not just close to the crack. However, very fewer evidences are observed to have contributed to any crack initiation from the grain boundary of solder joint.

Unlike the chip capacitor experiments, transformer failure shows multiple cracks that are more or less simultaneously initiating at the outer or inner meniscus as visualised in *Figure 7-8-c*. It is observed that the cracks propagates through the solder, but do not penetrate the pad intermetallic components (IMC). Crack evaluation shows that crack length for the outermost meniscus revealed higher crack length. The predicted hot spot region of the transformer is seen in *Figure 7-8-d* and the outer meniscus region of the transformer shows the highest damage locations, as compared to the inner meniscus.

Before correlating with the simulation predictions of the overall fatigue results, a two-parameter Weibull analysis is performed to analyse the scatter on the fatigue results for ceramic capacitors and transformers (see *Figure 7-9*). The analysis is done for a constant life and the scatter of the stress results are observed with the help of the reference line of the Weibull plot. Constant life is the lifetime where 63.7% of the experiments fail, wherein the components are tested. Weibull shape is the parameter that is compared here, which gives an indication of the type of failure rate as visualised in *Figure 7-9*.

The Weibull shape is found to be ~1.204 for the ceramic components (CC0805), which is an indication of the decreasing failure rate with higher failure cycles for most of the constant life [162].

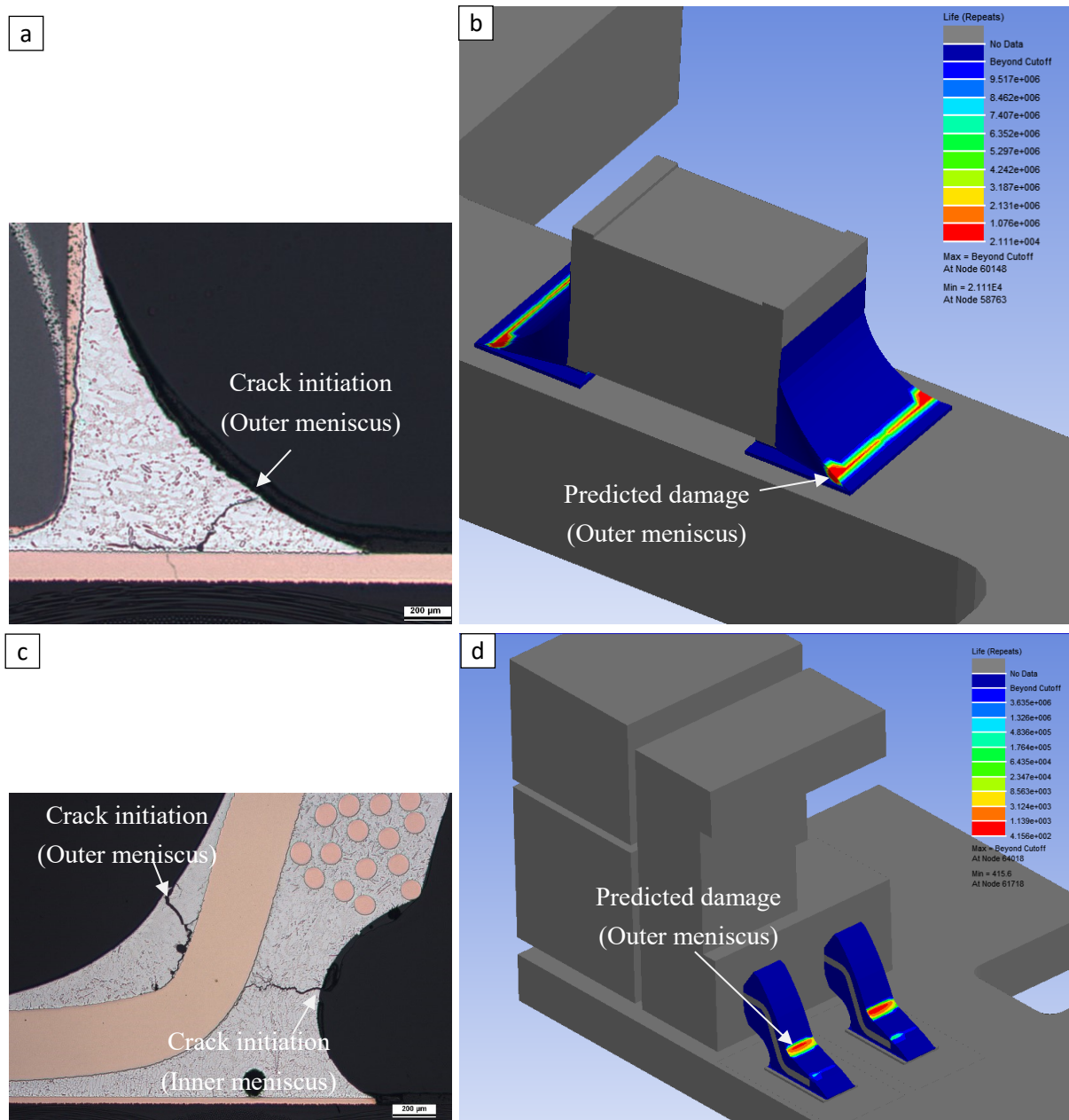


Figure 7-8: Convex geometric shape of the solder joint showing crack initiation for (a) ceramic capacitor experiment (b) predicted lifetime of capacitor (c) transformer experiment (d) predicted lifetime of transformer

For transformer, the Weibull shape is found to be less than one, ~ 0.903 , which is an indication of the failure rate drastically increasing with the increasing lifetime for most constant life as seen in *Figure 7-9*. This indicates the two SMT (chip capacitor and transformers) vibration experiments faced values below and above one for Weibull shape that has very different failure rates. This could be due to multiple joint fracture and sensitive stress values observed in the grain location of the transformer solder joint being tested.

Since a damage-initiation has to be predicted for long term assessment in this study, failure criterion is remarked as any form of crack length observed in the solder joint. Solder joints free of any cracks are excluded from the scatter points in *Figure 7-10*. The outer meniscus, which shows the hotspot regions (calculated as predicted lifetime *Figure 7-8*) are selected for the correlation, from both chip capacitors and transformers.

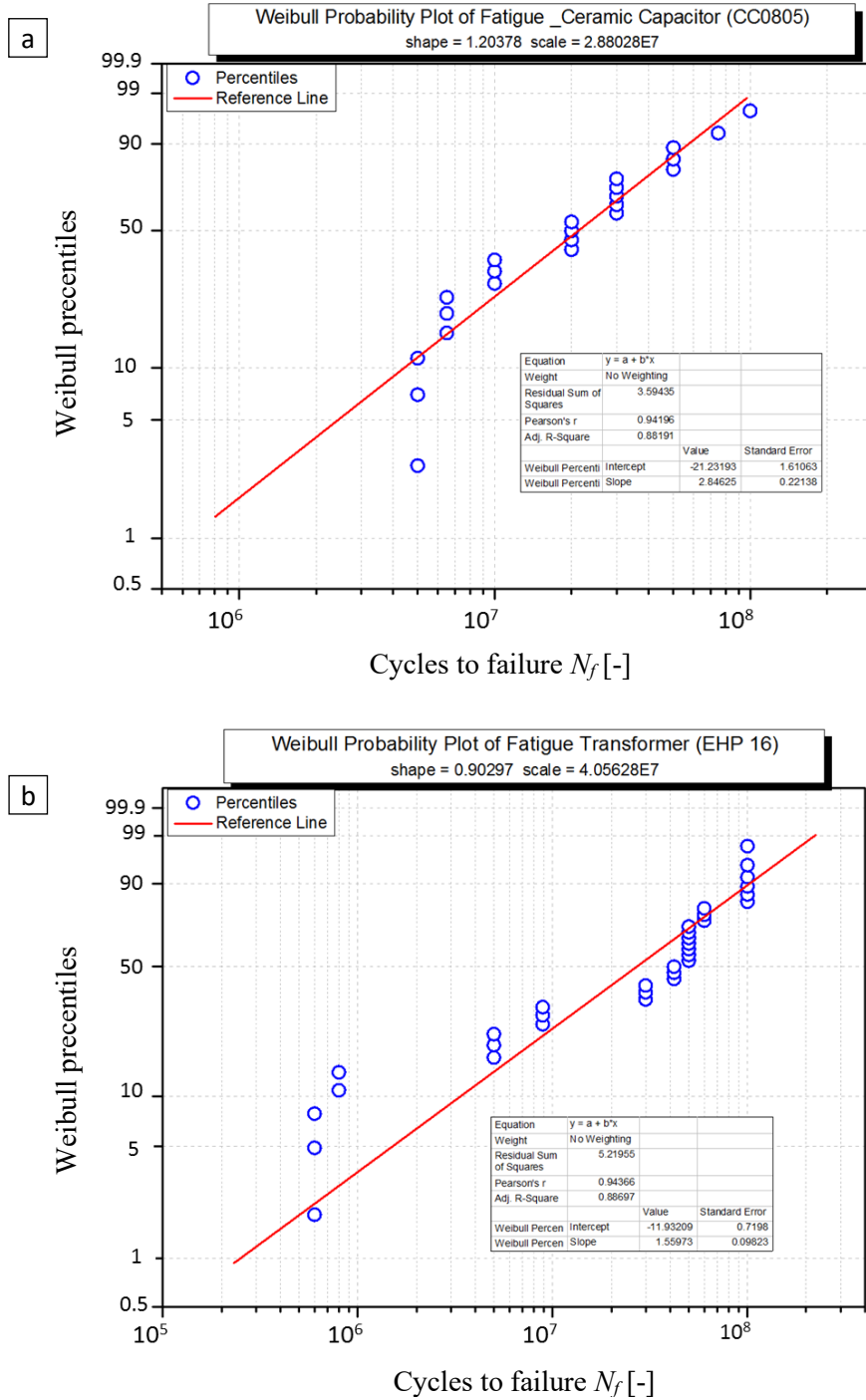


Figure 7-9: Weibull analysis with reference line of the experimental scatter points for (a) chip capacitor (b) transformer

With the help of the fatigue evaluation methodology as explained in section 7.2, it is possible to compare the predicted points from FE with that of experimental results as visualised in Figure 7-10. Using the FE models of solder joints, von Mises stress σ_{vm} data is calculated on the applied strap deflections for both component types at room temperature. Strap deflection has been varied within the experimental settings to establish a dependency of solder joint stresses on strap deflections. In other words, a reverse engineering is performed to determine the solder joint stresses for numerous strap deflections as seen in the experiments. It is observed for the

ceramic component, CC0805 the predicted line in *Figure 7-10-a*, acted not just as a threshold line for most experiments, in fact, the probable scatter slope is in good agreement with predicted line.

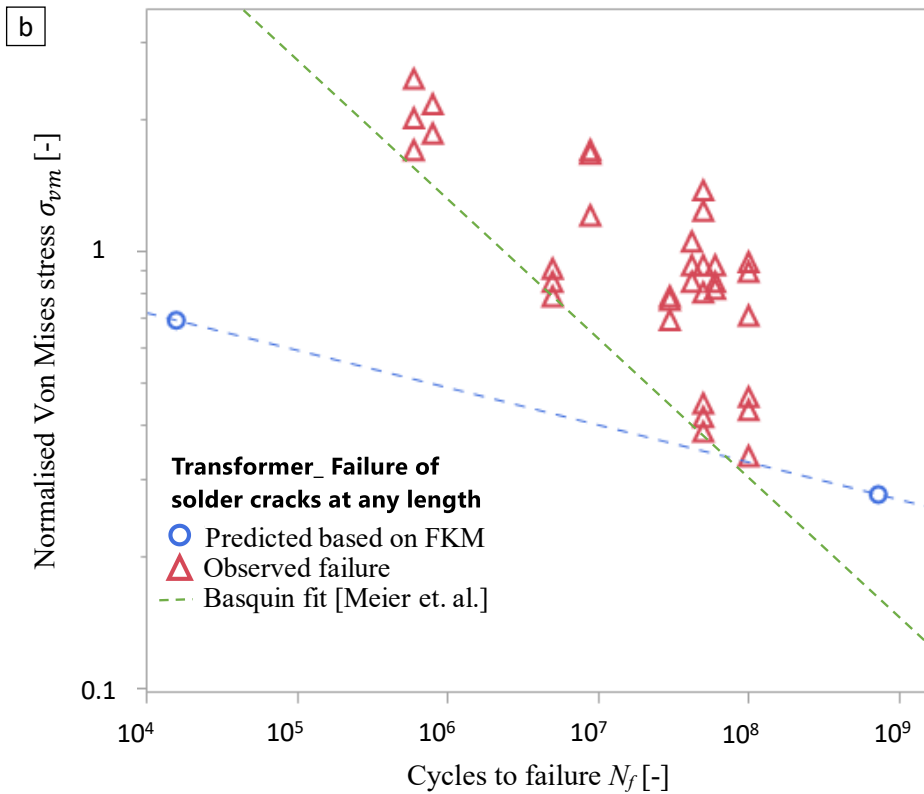
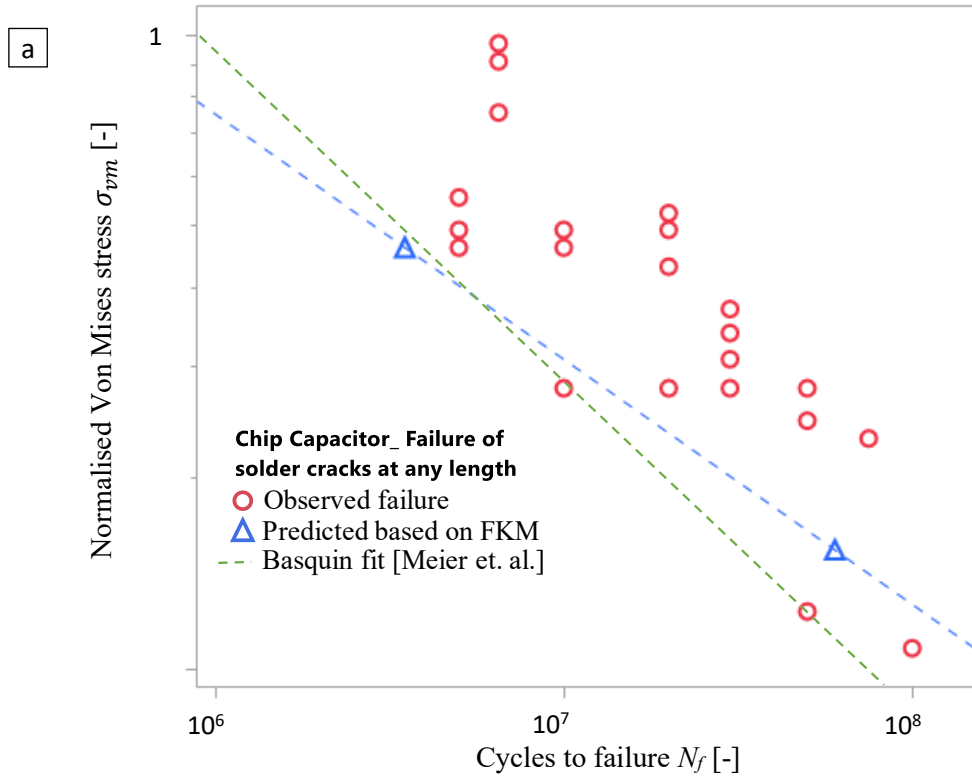


Figure 7-10: Fatigue scatter data from vibration experiment at room temperature vs. predicted threshold line for (a) chip capacitors (b) transformer

For transformer, correlations (see *Figure 7-10-b*) has a different accordance with predicted line. This is possibly due to the higher scatter results of transformers as investigated in Weibull analysis in *Figure 7-9-b*. Different crack length of transformer and multiple crack initiation locations (outer and inner meniscus) contributed higher for the scatter. Even though a design of solder performance can be assessed with such a methodology, accurate crack monitoring system is encouraged to prevent such scatter measurement for transformers.

The model is benchmarked with the state of art works of Meier *et al.* [61], which uses the Basquins fit to predict the lifetime of solder joints. In the work of Meier *et al.* [61], FE models of solder joints are used to calculate the applied strap deflections for both type of components. Strap deflections has been varied within the experimental settings to establish a dependency of solder joint stresses on strap deflections. Using a power law equation (or Basquins equation), a linear dependency is achieved between stress to failure (from FE model) and cycles to failure.

When compared with the work of Meier *et al.* [61], a comparable correlation is achieved for the chip capacitors (see *Figure 7-10-a*). The slope values of Baquins equation, b is found to be around 0.502 from the work of Meier and the predicted values based on FKM in the current work has a slope value, b of 0.401. This means, the predicted line according to this work using the FKM guideline based on S-N curves from bulk solder experiments had a better relevance to that of Basquins equation from Meier *et al.* [61].

When the same methodology is applied to the transformer (see *Figure 7-10-b*), the predicted values based on FKM guideline seems to differ from the work of Meier *et al.* [61]. The slope values of Baquins equation, b is found to be around 0.324 from the work of Meier and the predicted values based on FKM in the current work has a slope value, b of 0.085. The slope value clearly indicates a significantly different predicted lifetime values from both methodologies, where FKM model under predicts and the Basquin fit from Meier over predicts. The Basquins fit of Meier *et al.* [61] relatively deviated from the transformer fatigue results in comparison to a better fit proposed in this model using local stress approach of bulk specimen. It is also observed that the von Mises stress values of transformers from the work of Meier had higher values than the bulk strength of the solder.

Possible error source for the transformer predictions/experiments could be from the cracking at multiple solder joint locations (see *Figure 7-8*) of a single solder joint, and from different solder joints from the same transformer. Another error source could be from the predictive modelling of the transformer components. As concluded in *section 5.2.2* by introducing creep models for vibration loading could improve the predicted results, since it is found from earlier chapter that the creep fatigue interaction plays an important role during HCF especially at higher temperatures. Another possible error source could be the plasticity models that is required for the FE calculations of solder joints, as in this case only an elastic model is used. This is especially well observed in the LCF (10^4 - 10^6 cycles) region of the *Figure 7-10-b*, where the plastic deformation seems to be the dominant deformation mechanism for solder alloys. Other theories that are postulated to show this deviation could be possibly from the geometry, surface, metrology in measurements etc.

The predicted FKM lines proposed in the current work holds a good indication for chip capacitors. It could be a good threshold for transformers, however one has to understand the predicted values on FKM is based on the damage mechanics, so a potential damage is already observed on the predicted line, whereas the failure is observed in the later stages in the experiment. An online measurement system to detect crack is still believed to be key addition, which could further validate the proposed approach.

7.4 IMPLEMENTING NEW CREEP MODEL IN FEA

In this section, the creep model developed in *chapter 4.3* will be implemented in FE software to solve for complex geometries and boundary conditions (e.g. thermo-mechanical cycling). The current section is divided into three ways; the first section shows the adaptation of the developed creep model to the formulas used in the FE analysis, the second sections details on the subroutines written in ANSYS and the final section shows some of the benefits of the approach.

7.4.1 Mechanistic creep model into FE problems

The background behind the implementation of new creep laws in FE is introduced earlier in *section 2.1.7.4*. The mechanistic model developed in *Eqn. (4.13)* can be combined with the FE theories described in *section 2.1.7.4*. Unknown terms in *Eqn. (2.23)* are $\dot{\bar{\epsilon}}_{cr}$ and $\frac{\partial \dot{\bar{\epsilon}}_{cr}}{\partial \bar{\sigma}}$ are derived in this section by linking and expanding the new constitutive creep equation proposed as per *Eqn. (4.13)* [99].

The creep strain during the secondary stage is assumed for total strain here. This is because after a relatively short transient period the material creeps in such a manner that an approximate equilibrium exists for a long time and the long term behaviour of a structure can be analysed assuming stationary secondary stage creep process.

Eqn. (4.13) is restated again in assuming the secondary creep strain rate $\dot{\epsilon}_s$ and equivalent creep rate $\dot{\bar{\epsilon}}_{cr}$ along with treating equivalent stress, $\bar{\sigma}$ is the equivalent stresses which is due to the creep flow stress σ . Equivalent stresses, $\bar{\sigma}$ as well as equivalent strains, $\bar{\epsilon}$ are used in conjunction with the von Mises yield surface to define the von Mises equivalent stress as well as the incremental work per unit volume.

$$\dot{\bar{\epsilon}}_{cr} = C_1 \frac{E}{T} (\lambda_{ss})^{-n_1 p} \left[1 + C_2 \left(\frac{\bar{\sigma}}{E} \right)^{n_2} \exp \left(- \frac{(Q_c - Q_l) - (\alpha - \beta) \left(\frac{\bar{\sigma}}{E} \right)}{RT} \right) \right] \exp \left(- \frac{Q_l - \beta \left(\frac{\bar{\sigma}}{E} \right)}{RT} \right), \quad (7.1)$$

where E is the temperature dependent Young's modulus or E -modulus [MPa], T is the temperature [K]. Rest of the parameters from *Eqn. (7.1)* are tabulated in *Table 11*.

Now the incremental creep strain (In ANSYS referred as; *delcr*), is found out from *Eqn. (7.1)* as follows¹⁴:

$$\bar{\epsilon}_{cr} = \dot{\bar{\epsilon}}_{cr} \times \Delta t. \quad (7.2)$$

$$\dot{\bar{\epsilon}}_{cr} = C_1 \frac{E}{T} (\lambda_{ss})^{-n_1 p} \left[1 + C_2 \left(\frac{\bar{\sigma}}{E} \right)^{n_2} \exp \left(- \frac{(Q_c - Q_l) - (\alpha - \beta) \left(\frac{\bar{\sigma}}{E} \right)}{RT} \right) \right] \exp \left(- \frac{Q_l - \beta \left(\frac{\bar{\sigma}}{E} \right)}{RT} \right) \times \Delta t \quad (7.3)$$

Derivative of the incremental creep strain to effective stress (In ANSYS referred as, *dcrda* (1)) can be found from the product rule of partial differentiation.

¹⁴ Developed together with CADFEM GmbH, Munich, Germany. For complete derivation and further details, kindly refer to ANSYS documentations

$$\frac{\partial \Delta \bar{\varepsilon}_{cr}}{\partial \bar{\sigma}} = \Delta t \frac{\dot{\partial \varepsilon}_{cr}}{\partial \sigma}$$

$$\frac{\dot{\partial \varepsilon}_{cr}}{\partial \sigma} = C_4 C_2 \frac{E}{T} (\lambda_{ss})^{-n_1 p} \left[\frac{n_2}{E} \left(\frac{\bar{\sigma}}{E} \right)^{n_2 - 1} \exp \left(- \frac{(Q_c - Q_l) - (\alpha - \beta) \frac{\bar{\sigma}}{E}}{RT} \right) + \frac{(\alpha - \beta)}{ERT} \left(\frac{\bar{\sigma}}{E} \right)^{a - bT} * \exp \left(- \frac{(Q_c - Q_l) - (\alpha - \beta) \frac{\bar{\sigma}}{E}}{RT} \right) \right] \exp \left(- \frac{Q_l - \beta \frac{\bar{\sigma}}{E}}{RT} \right)$$

$$+ C_4 \frac{E}{T} (\lambda_{ss})^{-n_1 p} \frac{\beta}{ERT} \left[1 + C_2 \left(\frac{\bar{\sigma}}{E} \right)^{n_2} \exp \left(- \frac{(Q_c - Q_l) - (\alpha - \beta) \frac{\bar{\sigma}}{E}}{RT} \right) \right] \exp \left(- \frac{Q_l - \beta \frac{\bar{\sigma}}{E}}{RT} \right)$$

simplify:

$$\frac{\dot{\partial \varepsilon}_{cr}}{\partial \sigma} = C_4 C_2 \frac{E}{T} (\lambda_{ss})^{-n_1 p} \left(\frac{\bar{\sigma}}{E} \right)^{n_2} \exp \left(- \frac{Q_c - (\alpha - 2\beta) \frac{\bar{\sigma}}{E}}{RT} \right) * \left[\frac{n_2}{\sigma} + \frac{\alpha - \beta}{ERT} \right] + \frac{\dot{\varepsilon}_{cr}}{\varepsilon_{cr}} \frac{\beta}{ERT} \quad (7.4)$$

For strain hardening the derivative of incremental creep strain to creep strain [In ANSYS™ referred as *dcrda* (2)] [99]:

$$\frac{\partial \Delta \bar{\varepsilon}_{cr}}{\partial \bar{\varepsilon}_{cr}} = \Delta t \frac{\dot{\partial \varepsilon}_{cr}}{\partial \varepsilon_{cr}} = 0 \quad (7.5)$$

Eqns. (7.3), (7.4), and (7.5) will be also used for analytical computation and serve as a reference to calculate the proposed creep strain rate model for the numerical calculations. The subroutines are verified using a test case for numerical situation using single element in *Appendix III*.

7.4.2 Subroutine of the modified creep law in ANSYS

The potential unknown parameter found in Eqns. (7.3), (7.4), and (7.5) has to be converted into a high-level language in the form of FORTRAN codes before it can be used in ANSYS to perform the user subroutines¹⁵. The coding is divided into further section like defining primary functions, input arguments, input output arguments, output arguments, local variables, defining parameter types and finally calculating the incremental creep strain in Eqn. (7.3) along with incremental creep strain to effective stress and creep strain in Eqns. (7.3) and (7.5). The right input and output arguments defined in the beginning section are referred in writing the equations. The whole steps and the FORTRAN coding in a detailed way are shown in the *Appendix III*.

To verify the approach in global terms for the thesis, different types of validation works are done with tensile tests based on different loading condition and element types to validate the viscous relaxation of creep strain (few examples in *Appendix III.a*).

¹⁵ Developed together with CADFEM GmbH, Munich, Germany. For complete derivation and further details, kindly refer to ANSYS documentations

7.4.3 FEA with new subroutine using chip capacitors under TMC

The objective in this section is to investigate the advantages (not limitative) of using the developed physical model for numerical simulation. The modified creep model is implemented to the SMT solder joints that can capture the creep strain and relaxation effects on to the solder interconnect. This section describes the usage of the new creep law with an example geometry SMT in a chip capacitor (CC0805). The added feature of the modified law can be explored by changing the physical state variable subgrain size (λ_{ss}) and seeing the effects on the damage creep strains developed under thermal cycling. This is done to optimize for a better material solution or the other way around, to analyse the physical values and implemented onto numerical calculations.

A 3D-FEM model of the chip capacitor is developed in ANSYS15.0™ with the boundary condition, loading and material property as described in the *Table 20*. Quarter symmetry is used for the thermal cycling for better computational efficiency and accuracy.

Table 20: Test case and material description for testing the ANSYS subroutines using a CC0805 SMT in a thermal cyclic scenario

Material type	Material property	Loading
Solder	$E = E(T)$, User creep parameters 11 constant from Table 11, Poisson's ration $\nu = 0.3467$, Thermal expansion coefficient $\alpha = 2.51E5$ 1/K [1]	Thermo- mechanical cycling: sinus cycling $f(t) = 55.5$ (in °C) + $76.5 * \sin(360/1000 * time)$
PCB	Anisotropic elastic	
Copper connector	Isotropic Elastic	
Ceramic Al_2O_3	Isotropic Elastic	
Inter-Metallic phase	Isotropic Elastic	

The FE results and optimization results shown in this section from here onwards are subjected to distortion. Here only nominal and distorted values are shown in the graphics, as Continental Automotive GmbH owns the intellectual property rights of the results. Therefore, the results can be treated as a qualitative information for promotion of technological innovation and to the transfer and dissemination of technology.

The local axial creep strain and shear strain that is developed on the solder joint is used for quantitative comparative purpose. The maximum local axial creep strain and shear creep strain that is developed on the solder joint is traced for verification. The results of such an axial creep strain and shear creep strain from FE calculations are plotted in *Figure 7-11* (only nominal values).

The implementation of the creep model to predict final fatigue thermal cycles to failure (TMC) is not a primary focus of the study, as the primary objective here is to implement the new creep model onto FE programs. Another objective is to predict the local failure regions by analysing different component of creep strain for a thermos-mechanical cycling. Such type of predictive tools can be potentially integrated into device packages co-design practises in electronic industries.

Histograms of the six-different component creep strains are evaluated using the implemented creep model library. The calculation can explain the multiple failure location in a solder joint (*Figure 7-12*). Especially in ceramic components, solder joint failures are observed on multiple locations. In experiments, the crack propagation is observed on the standoff region of the solder joint between component and PCB substrate. This can be clearly seen from the calculated component shear creep strain (EPCRYZ) in *Figure 7-11* and *Figure 7-12*, which acts as a primary damage parameter for evaluation. The second parallel damage location being the meniscus side, where the crack developed on the standoff will induce the secondary crack on the meniscus due to the accumulated strain that is observed on the meniscus side.

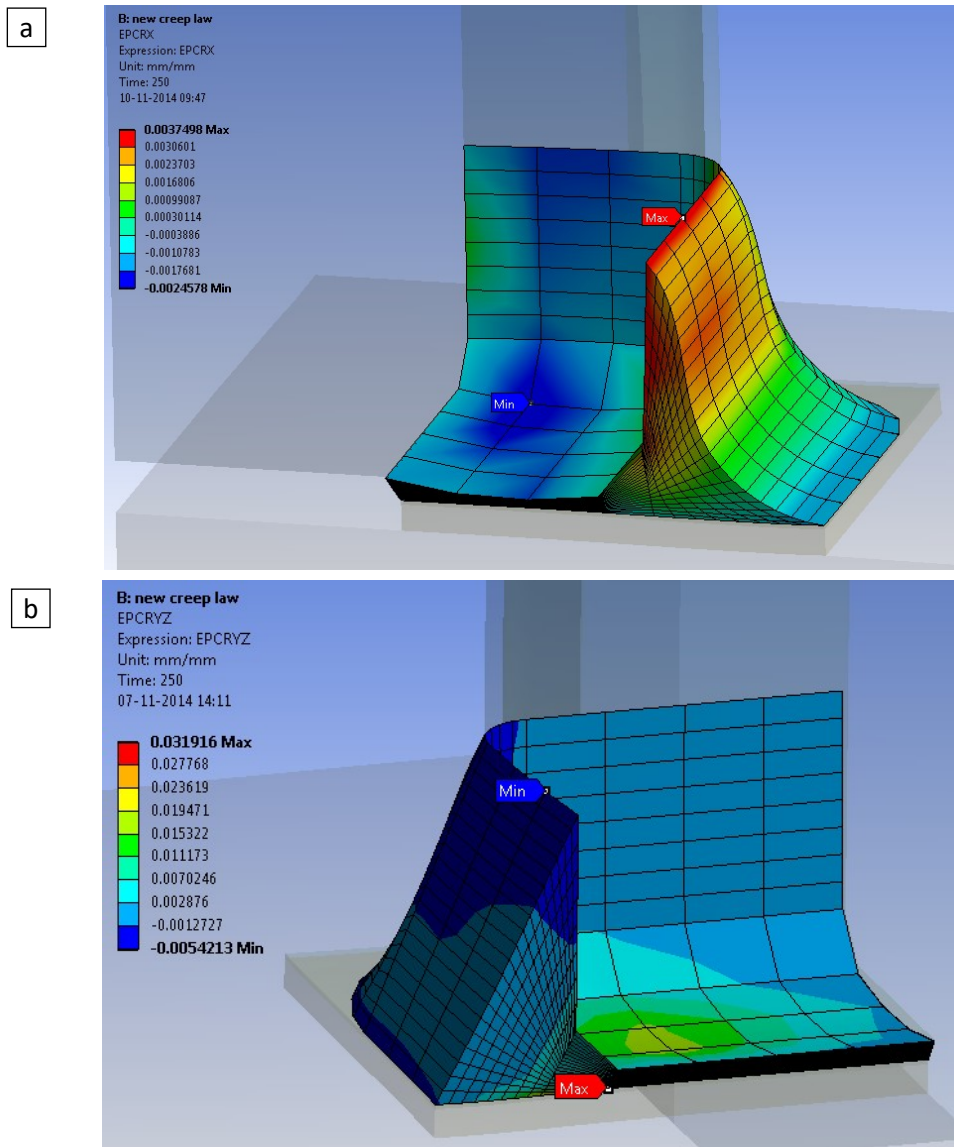


Figure 7-11: Contour creep strain plot (a) maximum axial creep strain developed on the meniscus of the solder joint (b) maximum shear strain developed on the standoff region of the interconnect causing the initiation of damage¹⁶

¹⁶ The FE results and optimization results shown in this picture are subjected to distortion. Only nominal and distorted values are shown in the graphics, as Continental Automotive GmbH owns the intellectual property rights of the results. Therefore, the results can be treated as a qualitative information for promotion of technological innovation and to the transfer and dissemination of technology.

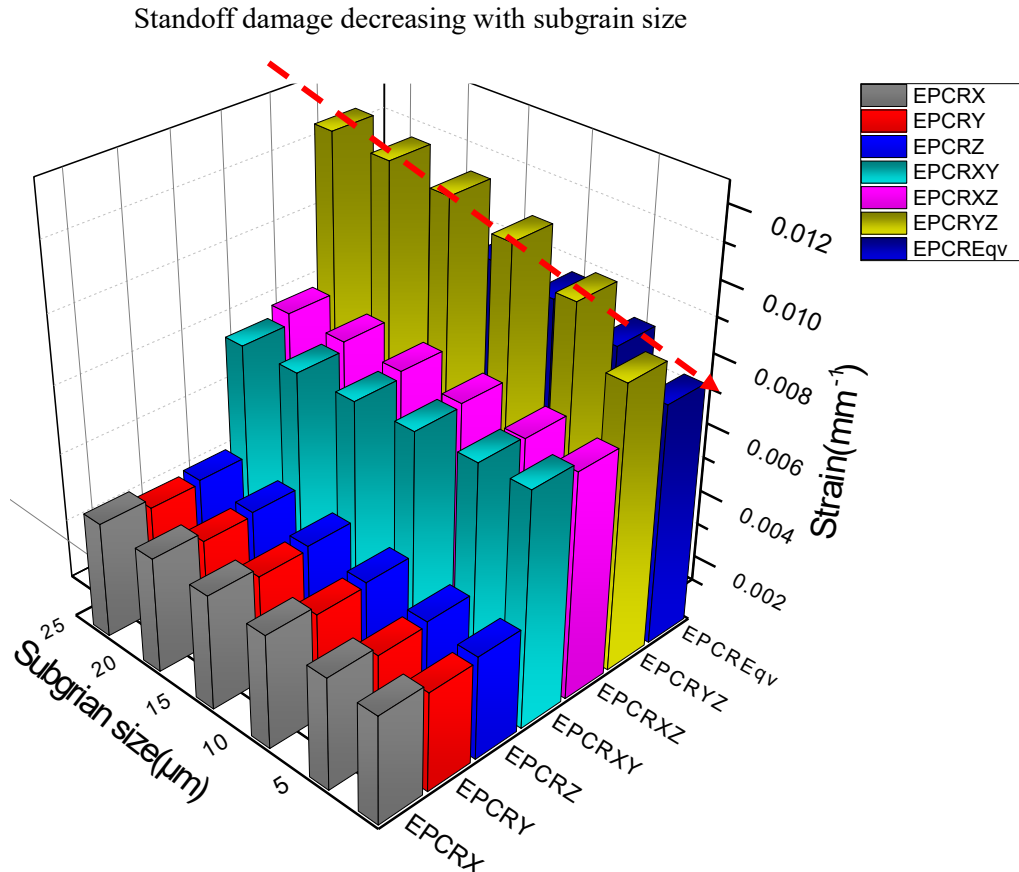


Figure 7-12: Creep strain behaviour of the six-component axis for different subgrain size ¹⁷

Another exemplary feature of using the model library is the ability to change its physical state variable (e.g. subgrain size, λ_{ss}) and see the effects on the damage parameters. For examples in Figure 7-12, the subgrain size value is changed between 0.5 up to 25 μm and the corresponding effect on the component-accumulated creep values are noted. The major damage on the standoff region of the solder is found to decrease effectively with the potential decrease of the subgrain size. The standoff region revealed, the effects compared higher to other axial or shear strain.

Using such features, it opens up discussion and possibilities for combining physical parameters in FEA solution or in other words, using micro modelling techniques to evaluate the stress-strain field. It is possible to establish a relationship between the damage parameter for the fatigue model and the corresponding micro-structural features. This enables one to get an optimized geometry/size that can be used for obtaining a very less damage parameter distribution on the solder joint or even to optimise material solution based on specific target applications. Further validation of these effects on microstructure and numerical simulation is encouraged.

¹⁷ The FE results and optimization results shown in this figure are subjected to distortion. Here only nominal and distorted values are shown in the figure, as Continental Automotive GmbH owns the intellectual property (IP) rights of the results. Therefore, the results can be treated as a qualitative information for promotion of technological innovation and also for the transfer and dissemination of technology.

7.5 CONCLUSION

- A simplified fatigue evaluation using the generic experiments based on tensile fatigue specimens is proposed as a potential solution to predict the lifetime of solder joints. Material characterisation is performed using fatigue models from the generic HCF bulk specimen experiments and explicitly combining with the influential parameters like roughness, stress gradients, mean stress correctivity, temperature so on.
- The FEA predicted lifetime values can be compared to that of the experiments performed with SMT components like chip capacitor and transformer under vibration experiments. It is found that the local stress fatigue evaluation methodology is in line with the experimental results, as the predicted line in both the experiments acted as a threshold line for the fatigue point to failure for the whole stress range. This approach can be used comprehensively for predicting the vibration performance of solder joints for different temperatures.
- For high temperature validation, the scatter of prediction is higher, and the reason could be from the linear material property and exclusion of the creep-fatigue interaction assumptions of solder joint for calculations. Further validation using this methodology is encouraged for higher temperature vibration testing.
- The predicted model based on this work is benchmarked (using slope values, b) with that of a Basquins equation from Meier *et al.* [61]. For chip capacitors, good correlation is observed for both the current work and the work of Meier *et al.* However, for transformer only a reasonable correlation is achieved. This can be explained due to the potential error sources from experiments and FE models. Further investigation to improve both models and experiments for transformers are encouraged.
- As concluded in *section 5.2.2* by introducing creep models for vibration could improve the predicted results, since it is found from earlier chapter, that the creep-fatigue interaction plays vital role during HCF at elevated temperatures. An introduction of creep or viscoplastic model can improve the stress prediction rather than using elastic models. Another improvement could be an online measurement system (*in-situ techniques*) to observe damages in solder joints.
- The material property for calibrating the FEA and experimental works are normally done with a trial and error (setting extreme boundary range) involves plenty of computational time. Here the calibration on the PCB for vibration experiments is completed by changing the density of the PCB, damping coefficient, which will induces the mass matrix and stiffness matrix during the calculation respectively. A meta-modelling technique of DoE is proposed using the Kriging method, as the quality of predicted values for finding the proper fundamental resonant frequency and maximum strap deflection of the PCB is highly possible with just a single finite element analysis methodology.
- In addition, the scatter from the vibration of the failed CC and transformer components are analysed using the Weibull analysis and found the probability of failure for the scatter points are quite high. This is analysed by comparing the Weibull shape for the vibration experiments, which can be seen in for both the ceramic capacitor, transformer vibration experiments. From the shape parameters, the failure rate of the transformer increased drastically with the increasing lifetime.

- The subroutine used in the thesis allows the users of the ANSYS™ to derivate customized creep model library developed in the thesis for structural related creep calculations in microelectronic packages. With the knowledge gained in material constitutive modelling and software programming, a detailed subroutine is coded (see *Appendix III*) and documented for the new creep model. To ensure the results (validation) the coded routine is tested with both single elements and multiple elements with various loading conditions (see *Appendix III-a*). In addition to the numerically calculated creep strain rate, separate routines are written to determine the creep rate analytically from the creep formulation. Further optimization of solder joint performance under TMC, and how to apply model to calculate lifetime in a TMC situation is not presented in this thesis, being subjected to IP rights.
- Physical features like substructure sizes, λ_{ss} and temperature dependent activation energy concepts of the new modified creep law is used in this chapter to optimise the damage parameters faced in a solder joint reliability assessment. This eventually open up discussion for a various ways to incorporate mechanistic models within FEA. It can be used as a potential feedback loop (which is not present conventionally) in designing the right creep resistant solder alloys for desired target microelectronic applications and industrial requirements.

8 SUMMARY & FURTHER RECOMMENDATIONS

The final chapter outlines the overall summary of the thesis, including the achievements, effectiveness, benefits, and further recommendations.

8.1 CREEP INVESTIGATIONS

- A new modified mechanistic creep model proposed in *chapter 4*, demonstrated a description of modelling creep deformation of SAC alloy with mechanistic dependence on microstructural features. *Chapter 4* reviews the results with well-established phenomenological models (Norton power law, Garafalo hyperbolic sine law and double power law) and addresses the limitations of using such phenomenological models for SAC alloys.
- The proposed mechanistic model is capable of estimating the material creep response based on the underlying mechanisms and microstructural features. This is achieved by investigating the type of mechanism undergone when the dislocations interacts with the hardened Ag_3Sn and Cu_6Sn_5 particles. Together with a microstructure analysis in *Chapter 6*, evidence of “Orowan climb mechanism” and “dislocation detachment mechanism from IMC particles”, along with the subgrain interaction is found to be the rate-controlling mechanism for SAC alloys.
- Physical state variables for e.g. substructure sizes and temperature dependent activation energies (Q_c, Q_l) are incorporated into the proposed mechanistic model, which is derived from a basic Arrhenius type equation.
- Industries can potentially use the wide scope of the mechanistic model, which establishes an underlying relationship between the damage parameter for the creep model and its microstructural salient features. One example of the value differentiators compared to the other phenomenological models is highlighted in *Figure 8-1*. The proposed creep model enhances and brings in new perspectives for the micro modelling for microelectronics industry.

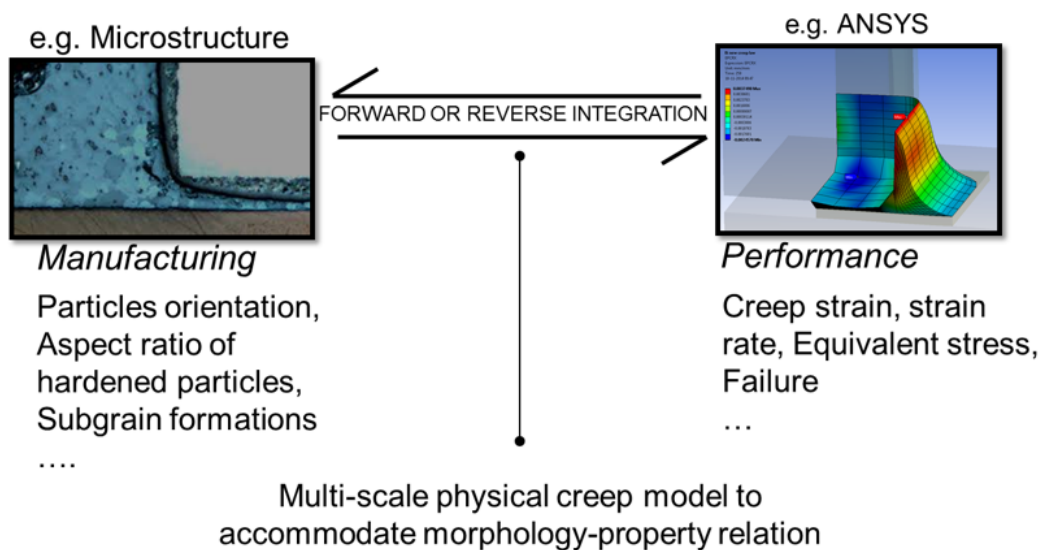


Figure 8-1: Connecting the bridge between microstructural and structural field of study using the proposed mechanistic creep model

- Holistically, with the help of the proposed model one can gain fundamental understanding of the underlying deformation mechanisms and quantitative insights into the effect of various driving forces and microstructural features on the overall creep response of the trending SAC solder alloys.
- In *section 7.4*, it is shown that the mechanistic models can also be used across the length scale of solder joints in FE libraries by coding and validating the subroutines. The subroutine used in the thesis (*Appendix III*) allows the FE users to use the customized creep model developed in the thesis for establishing a *structure-property* relationship in microelectronic packages. In other words, the designers and material developers in industries can work in tandem by doing a forward or reverse integration connecting the manufacturing and performance study on solder joints as depicted in *Figure 8-1*. This allows users to develop or optimize the performance of solder joints or to develop solder materials that withstand high temperature requirement in future.
- The FE subroutines and codes are documented in the current work, so that it can be referred and adopted for different customized creep models. To ensure the correct results, the subroutine is validated with both single elements and multiple elements (*Appendix III-a*) under different loading conditions including thermal cycling. In addition to a numerically calculated creep strain rate, separate routines are written to determine the creep rate analytically from the creep formulation.
- The influence of subgrains and recrystallization is a debated topic in the microelectronics reliability field, and sometime considered as the missing parameters in understanding the deformation of SAC solder alloys. This work is one such effort to provide the scientific community in understanding and modelling the salient features of subgrains, Orowan mechanisms etc.

Discussions under *section 4.5.3* showed that, similar to the subgrain development in bulk specimen observed in the current study literatures agrees on similar subgrain developments also the application of SMT solder joints, which proved the hypothesis as postulated earlier. The subgrain values from solder interconnects can be substituted to the new creep equation to get the potential dependency of a physical microstructural values on the creep behaviour on component level.

- Creep damage models for SAC alloys are investigated in the current work to find the best damage models. Very handful literatures are available for creep rupture models for SAC alloys. From the investigations between the two methods (based on stress and minimum strain rate as damage parameter) with the experimental fit, it is apparent that the empirical Monkman-Grant relationship, which is proposed 50 years back [97] (based on creep kinetics), revealed a better agreement than other creep damage model, with the experimental data of SAC alloys. The Monkman-Grant model exhibited a good fit with experimental results, when compared to other models like Manson-Haferd [93] and Larson-Miller [91].

8.2 HCF INVESTIGATIONS

- The HCF investigation in the current study collects the intrinsic material fatigue models of SAC alloy and addresses the challenges in a broader scope about the solder joint reliability assessment on SMT component solder joints. The HCF works presented in the current study represents certainly one of very few investigations to include a bulk specimen to characterize high cycle fatigue behaviour of solder alloys.
- The method proposed in this work is geometry and stress independent as compared to other published works [41, 125, 61]. Product designers and material developers can translate the approach to a wide range of applications (e.g. SMT solder joints) thereby reducing the extensive component or part testing. It is also possible to test solder specimen in the high-cycle fatigue regime without using complicated test equipment as demonstrated together with the results in *Chapter 5*.
- A comprehensive study (*Chapter 5*) of HCF behaviour showed the influential parameters could have a significant impact on the fatigue performance of solder alloys (see *Figure 5-13*). Certainly lifetime of the solder depends on multiple superimposed influential functions; $N_f = f(T, R, M, K_R)$, where T being the temperature influence [K], R is the surface roughness [μ], M is the mean stress sensitivity [-], K_R being the notch factor [-].
- The results in the present work do however contain phenomena, which are difficult to explain in a unified manner. Evidence collected indicates different cases of failure and deformation mechanism, and in some cases superimposed to each other. For example, the temperature effects seems to be a dominant factor and observed to be associated with microstructural transformations of material such as cyclic softening and subgrains formation (dislocation restructuring). This is a clear evidence of cyclic creep during HCF at elevated temperatures (even at 60 Hz); along with evidences from the local strain measurements from the specimens (see *Figure 5-3*).
- During the fatigue assessment of solder joints, it is often left to the judgement of engineers or designers, which induces most often errors to make inappropriate comparison with general material table [45]. The main questions that arises in industries during the process of fatigue evaluation process in solder joints are: type of stresses to be used?, introduce nonlinear material behaviour?, incorporating influential factors like surface roughness, stress gradient?, etc. To deal these open questions, FKM guideline [37] is adapted in the current work for the first time in microelectronics reliability field. The main evidence supporting the validity of FKM guideline for SMT solder joint reliability prediction is successfully validated and discussed in *Chapter 7*.
- Fatigue models along with the discussed corrections factors is transferred and used in the standalone-fatigue evaluation software such as nCode Designlife™. Coupled together with ANSYS™ the predicted values are compared and validated for the vibration experiments using chip capacitor and transformer components (see path diagram in *Figure 7-7* and validation results in *Figure 7-10*).
- Even though the influence of cyclic creep for high temperature specimens is evident, it is decided to use the elastic property for solder joint for the simplicity of calculation. In other words, stresses calculated from ANSYS are used to calculate the lifetime in

nCode and no creep strain values are transferred to include any potential damage accumulations due to creep interactions. Implementation of creep models for fatigue could possibly improve accuracy in lifetime prediction.

- The model based on local stress methodology and FKM is validated and benchmarked by comparing the with state of art works of Meier *et al.* [61], which uses the Basquins fit and FE analysis to predict the lifetime of solder joints.
- An in-depth study of fractography is performed in *Chapter 6*, to confirm the creep interactions at HCF and other phenomenon like effect of primary grains, transgranular vs. intergranular, influence of subgrains, crack initiation mechanisms etc. Both high and low temperature test matrix is considered to see the difference and the overall summary of various phenomenon are tabulated in *Table 17*.

8.3 FURTHER RECOMMENDATIONS

- Although the proposed mechanistic model is able to provide insights in the subgrain developments and formulations on the creep response of SAC alloy, the model still has certain simplifying assumptions and needs further refinement in future.
- Systematic correlations developed between dominant creep mechanism and the parameters, activation energy (Q), and stress exponent (n) are established in this thesis for SAC alloys, along with direct observations of microstructure at high homologous temperature. Due to the low melting point of SAC alloys, the thermally induced activation energy is considered the primary dependency factor for creep. Therefore, in the current work, activation energy dependency on stress is considered for the creep equation development. Future works for different materials is encouraged using stress exponent dependency on the temperature and by analysing systematically the difference between the solid solution β -Sn and SAC alloy separately.
- Physical features like substructure sizes and temperature dependent activation energy concepts of the new modified creep law can be directly used to optimise the damage parameters faced in a solder joint reliability assessment. This eventually can be used as a feedback loop in designing the right creep resistant solder alloys in future for desired target applications. Further validation of the effects on microstructure and numerical simulation results on SMT component solder joints are encouraged.
- The intrinsic solder property used for vibration analysis still uses elastic properties and the results validated for higher temperature vibration experiments showed deviations. Analysis with temperature dependent properties of solder alloys for vibration analysis is encouraged to optimize the method further. In addition, hint of the creep fatigue interaction has to be considered for accurate prediction models. The key focus of the thesis on material characterization, any further implementation of the proposed models to SMT component solder joints and validations are encouraged.
- Extensions of the present work would include a test matrix comprising creep and HCF on solder thus far included, at both elevated and sub-zero temperatures. Extending the work to low temperatures (e.g. -55 °C) would be of interest to all the high reliability

sectors; *i.e.* aerospace, military and automotive, since these could be encountered frequently. Another major area of interest is the effect of prior thermal ageing and/or cycling on the high-cycle fatigue of solders.

- Although the SEM, LM, EBSD, EBCC proved an adequate tool for the locating of cracks in broken fatigue specimens and subgrains, other possible techniques such as X-ray tomography and TEM would give a true different dimensional view of the internal cracking and subgrain formation. Additionally, the method used to obtain almost broken specimens is extremely laborious and would benefit from a degree of automation. An in-depth study of crystallographic orientation and defect effects near initiation areas is not in scope of the current work. Such study would provide more insight into the future works and for further scientific understanding.
- Length of crack is determined by taking cross section of solder joints and an accurate crack monitoring system is encouraged to prevent such scatter measurement for SMT components.
- Coupled load cases on thermo-mechanical (TMC) and vibration can be evaluated based on the local stress methodology. Especially the finding of creep interactions at 60Hz is crucial to incorporate creep during vibration prediction study, as it is seen to be damage parameters for HT test specimens.

REFERENCES

- [1] S. Weise, *Verformungs und Schädigungsverhalten metallischer Werkstoffe in Mikrodimensionen*, Dresden, 2008.
- [2] J. Cunningham, R. Valentin, C. Hillman and A. Dasgupta, "A demonstration of virtual qualification for the design of electronic hardware," in *IEEST*, Phoenix, 2001.
- [3] D. S. Steinber, *Vibration Analysis of electronic equipment*, Chicester: John Wiley & Sons, 1988.
- [4] K. Meier, M. Roellig, A. Schiessl and K. J. Wolter, "Lifetime prediction for Lead free solder joints under vibration," in *EUROSIME*, Linz, 2012.
- [5] F. X. Che, H. L. Pang, F. L. Wong and G. Lim, "Vibration fatigue test and analysis for flip chip solder joints," *Electronic packaging technology conference*, pp. 107-113, 2003.
- [6] J. M. Pitaressi and A. Akanda, "Random vibration response of a surface mount lead solder joint," *Proceedings of the ASME international electronics packaging conference*, 1993.
- [7] Y. B. Kim, N. Hiroshi and A. Masazumi, "Vibration fatigue reliability of BGA-IC package with Pb-free solder," *Electronic component technology conference*, pp. 891-897, 2003.
- [8] N. Barry, "Lead- free solders for high reliability applications: High cycle fatigue studies," Doctorate thesis submitted to 'The University of Birmingham', Birmingham, 2008.
- [9] N. T. King, *Solder joint technology- material, properties and reliability*, 2007: Springer, New York.
- [10] Continental Automotive GmbH, "Quick reference for iLTP and QPT," Innovation center for advanced electronics, Regensburg, 2015.
- [11] S. Mukherjee, M. Nuhi, A. Dasgupta and M. Modarres, "Creep constitutive models suitable for solder alloys in electronics assemblies," *Journal of electronic packaging*, vol. 138, no. September, 2016.
- [12] Y. Zhao, C. Basaran, A. Cartwright and T. Dischongh, "Thermomechanical behavior of micron scale solder joints under dynamic loads," *Mechanics of Materials*, vol. 32, pp. 161-173, 2000.
- [13] J. Betten, *Creep Mechanics*, Berlin: Springer, 2014.
- [14] J. K. Shang, Q. L. Zeng and L. Zhang, "Mechanical fatigue of Sn rich Pb free solder alloys," *Material Science-Mater Electron*, 2006.
- [15] J. H. Lee and H. Y. Jeong, "Fatigue life prediction of solder joints with consideration of frequency, temperature and cracking energy density," *International journal of fatigue*, vol. 61, pp. 264-270, 2014.
- [16] H. D. Solomon, "Effect of initial microstructure, frequency and temperature on the low cycle fatigue behaviour of the soldering alloys 96.5Sn-3.5Ag and 63Sn-37Pb," *Engineering failure analysis*, vol. 15, pp. 220-228, 2008.
- [17] Continental Automotive GmbH, "Database for package failure," Continental automotive pre-release, Regensburg, 2014.
- [18] L. A. Carapell and R. Hultgren, "The Ferromagnetic nature of Beta phase in the copper manganese tin system," *Transaction of the American Institute of Mining*, vol. 147, pp. 232-242, 1942.
- [19] E. S. Hedges, *Tin and its alloys*, London: Edward Arnold Publishers limited, 1960.
- [20] C. J. Smithells, *Smithells metals reference book*, Oxford: Butterworth-Heinemann Ltd, 1992.

-
- [21] M. E. Loomans and M. E. Fine, "Tin- Silver-Copper Eutectic temperature and composition," *TMS metallurgical and material transaction*, vol. 31, 2003.
- [22] C. M. Miller, I. E. Anderson and J. F. Smith, "A viable tin lead solder substitute, Sn -Ag-Cu," *Journal of electronic materials*, vol. 23, no. 7, pp. 595-601, 1994.
- [23] W. M. Plumbridge, R. J. Matela and A. Westwater, *Structural integrity and reliability in electronics*, Dordrecht: Kluwer Academic Publishers, 2003.
- [24] K. S. Kim, S. H. Huh and K. Sugunuma, "Effects of fourth alloying additive on microstructures and tensile properties of SnAgCu alloy and joints with Cu," *Microelectronics reliability*, pp. 259-267, 2003.
- [25] I. Shohji and et.al, "Tensile properties of Sn-Ag based lead free solders and strain rate sensitivity," *Material Science and Engineering*, pp. 50-55, 2004.
- [26] S. Ganesan and M. Pecht, *Lead free electronics*, vol. CALCE EPSC Press, 2004.
- [27] G. Y. Li, "Effects of Sb addition on tensile strength of Sn-3.5Ag0.7Cu solder alloy and joint," *Thin solid films*, vol. 504, pp. 421-425, 2006.
- [28] H. McCormick, P. Snugovsky, C. Hamilton and Z. Baheri, "The great SAC debate, comparing the reliability of SAC305 and SAC405 solder in a variety of applications," in *Pan Pacific symposium*, 2007.
- [29] Q. K. Zhang, Q. S. Zhu, H. F. Zhou and Z. F. Zhang, "Fatigue fracture mechanism of Cu/Lead-free solders interfaces," *Material Science and Engineering*, vol. 527, pp. 1367-1376, 2010.
- [30] B. Wunderle and B. Michel, "Progress in reliability research in micro and nano region," *Microelectronics and reliability*, vol. 46, no. 9-11, 2006.
- [31] Choi, C; Dasgupta, A, "Fatigue of solder interconnects in microelectronic assemblies under vibration loading," in *International Colloquium on Mechanical Fatigue of Metals*, 2014.
- [32] M. Lalanne, P. Berthier and J. D. Hegopian, *Mechanical Vibrations for Engineers*, John Wiley and Sons, 1983.
- [33] H. W. Zhang, Y. Liu, J. Wang and F. L. Sun, "Effect of elevated temperature on PCB responses and solder interconnect reliability under vibration loading," *Microelectronics reliability*, 2015.
- [34] Y. Ding, R. Tian, X. Wang and Y. Tian, "Coupling effects of mechanical vibrations and thermal cycling on reliability of CCGA solder joints," *Microelectronics reliability*, 2015.
- [35] M. Nejadari, O. Wittler and B. Michel, "Investigation of the reliability of electronic components under combined loads (vibration, humidity, temperature)," in *Deutscher verband für Materialforschung und -prüfung, Arbeitskreis Zuverlässigkeit Mechatronischer und Adaptronischer Systeme*, Darmstadt, 2010.
- [36] O. D. Sherby, R. J. Klundt and A. K. Miller, *Metall Trans*, vol. 8E, p. 843, 1977.
- [37] E. Haibach, *FKM Guideline ' Analytical strength assessment of components in mechanical engineering'- 5th Edition*, Frankfurt: VDMA Verlag, 2003.
- [38] J. Roesler, H. Harder and M. Baeker, *Mechanical Behavior of Engineering Materials-Metals, Ceramics, Polymers and Composites*, Berlin: Springer, 2007.
- [39] W. Engelmaier, "Surface mount solder joint reliability: Issues, design, testing, production," *Workshop notes Engelmaier associates Inc*, 1995.
- [40] P. P. Milella, *Fatigue and corrosion in metals*, Italia: Springer, 2013.
- [41] J. H. Pang, F. X. Che and T. H. Low, "Vibration fatigue analysis for FCOB solder joints," in *IEEE*, Las Vegas, 2004.

- [42] S. Kocanda, "Fatigue failure of metals," *Sithoff and Noordhoff international publishers*, 1978.
- [43] O. Basquin, "The experimental law of endurance tests," *Proceedings of ASTM*, 1910.
- [44] J. Roesler, M. Baeker and H. Harders, *Mechanical behaviour of engineering materials*, Berlin Heidelberg: Springer-Verlag, 2007.
- [45] S. Kochelin, "FKM guideline: strength, limitations and experimental validation," *Procedia engineering*, vol. 133, pp. 309-319, 2015.
- [46] E. Siebel and M. Gaier, "The influence of surface roughness on the fatigue strength of steels and non-ferrous alloys," *Engineering Digest*, vol. 18, pp. 1715-1723, 1957.
- [47] R. W. Suhr, "The effect of surface roughness on HCF of low alloy steel," *Mechanical engineering publications*, pp. 69-86, 1986.
- [48] N. A. Alang, N. A. Razak and A. K. Miskam, "Effect of surface roughness on fatigue life of notched carbon steel," *International Journal of Engineering & Technology IJET-IJENS*, vol. 11, p. 160, 2011.
- [49] B. Bertsche, *Reliability in Automotive and Mechanical Engineering*, Stuttgart: Springer, 2008.
- [50] M. Matsuishi and T. Endo, "Fatigue of metals subjected to varying stress," *Japan society of mechanical engineering*, 1969.
- [51] W. Z. Gerber, *Bayer Archit Ing, Munich: Vre. 6, 101*, 1984.
- [52] J. Goodman, *Mechanics Applied to Engineering*, London: Longmann, 1899.
- [53] B. P. Haigh, "Experiments on the fatigue of brasses," *J. Inst. Me*, vol. 18, pp. 55-86, 1917.
- [54] C. R. Soderberg, "Fatigue of the safety and working stress," *Trans. Am. Soc. Mech*, vol. Eng. 52, 1939.
- [55] W. R. Jong, H. C. Tsai and H. T. Chang, "The effects of temperature cyclic loading on lead free solder joints of wafer level chip scale package by taguchi method," *Journal of electronic packaging*, vol. 130, no. 1, pp. 1-10, 2008.
- [56] Q. K. Zhang, Q. S. Qhu, H. F. Zhou and Z. F. Zhang, "Fatigue fracture mechanism of Cu/lead-free solder interfaces," *Material Science and Engineering*, vol. 527, pp. 1367-1376, 2010.
- [57] J. Q. Shang, Q. L. Zeng, L. Zhang and Q. S. Zhu, "Mechanical fatigue of Sn-rich Pb-free solder alloys," *Journal of material science: Mater electron*, 2006.
- [58] R. Metasch, R. C. Boreto, M. Roellig and S. Wiese, "Primary and tertiary creep properties of eutectic SnAg_{3.8}Cu_{0.7} in bulk specimens," in *EuroSim*, 2009.
- [59] M. Nozaki, M. Sakane, M. Tsukada and H. Nishimura, "Creep fatigue life evaluation for SnAg solder," *ASME journal of engineering materials technology*, vol. 128, no. 2, pp. 142-1450, 2006.
- [60] M. Nozaki, M. Sakane and Y. Tsukada, "Notch effect on LCF of SnAg solder," *ASME journal of engineering material technology*, vol. 130, no. 1, pp. 1-7, 2008.
- [61] K. Meier, M. Roellig, G. Lautenschlaeger, A. Schiessl and K. J. Wolter, "Lifetime assessment for bipolar components under vibration and temperature loading," in *Thermal, Mechanical and Multi-Physics Simulation and Experiments in Microelectronics and Microsystems (EuroSimE)*, Wroclaw, 2013.
- [62] D. Radaj and M. Vormwald, *Ermüdungsfestigkeit*, Berlin-Heidelberg: Springer, 2007.
- [63] R. Agamennone, W. Blum, C. Gupta and J. K. Chakravartty, "Evolution of microstructure and deformation resistance in creep of tempered martensitic steels," *Acta materialia*, vol. 54, pp. 3003-3014, 2006.

- [64] K. Naumenko and H. Altenback, Modeling of creep for structural analysis, Berlin-Heidelberg: Springer, 2007.
- [65] J. Pelleg, Mechanical Properties of Materials, Dordrecht: Springer Science, 2013.
- [66] M. McLean, "On the threshold stress for dislocation creep in particle strengthened alloys," *Acta Metal*, vol. 33, pp. 545-56, 1985.
- [67] E. M. Kassner, Fundamentals of creep in metals and alloys, Amsterdam: Elsevier, 2009.
- [68] H. Ma, "Constitutive models of creep for lead-free solders," *Journal of material science*, vol. 44, pp. 3841-3851, 2009.
- [69] Z. G. Chen, Y. W. Shi and J. W. Morris, "The creep behavior of Sn-Ag eutectic solder joints," *Journal of Electronic material*, vol. 33, no. 9, pp. 964-971, 2004.
- [70] S. Wiese and K. J. Wolter, "Microstructure and creep behavior of eutectic SnAg and SnAgCu solders," *Microelectronics reliability*, vol. 44, pp. 1923-1931, 2004.
- [71] X. Li and Z. Wang, "Thermo-fatigue life prediction methodologies for SAC solder joints in flip chip assemblies," *Journal of mechanical strength*, vol. 28, no. 6, pp. 893-898, 2006.
- [72] R. Dudek, H. Walter, R. Doering and B. Michel, "Thermal fatigue modelling for SnAgCu and SnPb solder joints," *Thermal mechanical simulation and experiments in microelectronics and microsystems*, pp. 557-564, 2004.
- [73] A. Schubert, R. Dudek, H. Walter, E. Jung and H. Reichl, "Reliability assessment of lead free solder interconnects," in *8th International symposium on advanced packaging materials*, 2002.
- [74] M. F. Ashby and J. H. Frost, Deformation- mechanism maps, the plasticity and creep of metals and ceramics, New York: Pergamon Press, 1982.
- [75] X. Q. Shi, Z. P. Wang, W. Zhou, H. L. Pang and Q. J. Yang, "A new constitutive model for eutectic solder alloy," *Journal Of electronic packaging*, vol. 124, pp. 85-90, 2002.
- [76] J. W. Morris and Z. Mei, "Effects of cooling rate on mechanical properties of near eutectic Tin solder joints," *Journal of electronic materials*, pp. 599-608, 1991.
- [77] J. P. Raineri, F. S. Lauten and D. H. Avery, "Plastic constraints of large aspect ratio solder joint," *Journal of electronic material*, vol. 24, pp. 1419-23, 2004.
- [78] D. Frear, D. Grivas and J. Morris, "A microstructural study of thermal fatigue failure on SnPb solder joints," *Journal of electronic materials*, pp. 8-92, 1990.
- [79] Blum, W., "Creep of crystalline materials: experimental basis, mechanisms and models," *Materials science and engineering-ELSEVIER*, vol. A319, no. 321, pp. 8-15, 2001.
- [80] M. Kerr and N. Chawla, "Creep deformation behavior of Sn3.5Ag solder couple at small length scales," *Acta materialia*, vol. 52, pp. 4527-4535, 2004.
- [81] E. Orowan, in *Symposium on internal stresses in: metal and alloys*, London, 1948.
- [82] F. Ochoa, J. J. Williams and N. Chawla, "Effects of cooling rate on the microstructure and tensile behavior of Sn3.5Ag solder," *Journal of electronic materials*, vol. 33, no. 12, pp. 1596-1607, 2004.
- [83] B. Ilshner and R. Singer, *Werkstoffwissenschaften und Fertigungstechnik: Eigenschaften, Vorgang, Technologien*, Springer, 2001.
- [84] B. Bergman and R. Langenberg, "The stress/creep rate behavior of precipitation hardened alloys," *Metal science*, pp. 20-28, 1976.

-
- [85] W. Blum and W. Reppich, Creep behavior of crystalline solids, Swanse UK: Pineridge Press, 1985.
- [86] A. H. Clauer and N. Hansen, "High Temperature Strength of Oxide Dispersion Strengthened Aluminium," *Acta Metall. Mater*, vol. 32, no. 2, pp. 269-278, 1984.
- [87] J. Peterseim and G. Sauthoff, "The effect of fine precipitate particles on the creep behaviour of ferritic model steels," *Steel Res*, vol. 57, no. 19, 1986.
- [88] S. Terashima, K. Takahama, M. Nozaki and M. Tanaka, "Recrystallization of Sn grains due to thermal strain in Sn-1.2Ag-0.5Cu-0.05Ni solder," *Material transactions*, vol. 45, no. 4, pp. 1383-1390, 2004.
- [89] S. S. Manson, J. C. Freche and C. R. Ensign, "Fatigue crack propagation," *American Society of testing and materials*, pp. 384-412, 1067.
- [90] S. S. Manson and W. F. Brown, "Time temperature stress relaxations for the correlation and extrapolation of stress rupture data," *Proc ASTM*, vol. 53, pp. 693-791, 1953.
- [91] F. R. Larson and E. J. Miller, "Time-temperature relationship for rupture and creep stress," *Trans. ASME*, vol. 74, pp. 765-775, 1952.
- [92] L. Zhang, Z. G. Wang and J. K. Shang, "Creep Rupture of SN-Ag-Cu Pb free solder alloy," *Key Engineering Materials*, Vols. 345-346, pp. 585-588, 2007.
- [93] S. S. Manson and A. M. Haferd, "A linear time-temperature relation for extrapolation of creep and stress rupture data," *NACA TN*, p. 2890, 1953.
- [94] D. C. Dunand, B. Q. Han and A. M. Jansen, "Monkman- Grant analysis of creep fracture in dispersion strengthened and particulate reinforced aluminum," *Metallurgical and materials transaction*, vol. 30, no. A, pp. 829-832, 1999.
- [95] S. S. Manson and M. H. Hirshberg, "Fatigue an interdisciplinary approach," in *Proceeding of 10th Sagamore Army materials*, 1964.
- [96] S. S. Manson and C. R. Ensign, *ASME journal of material and technology*, vol. 101, p. 317, 1979.
- [97] C. F. Monkman and N. J. Grant, "An empirical relationship between creep rupture life and minimum creep rate in creep rupture test," in *Presented at the Fifty-ninth Annual Meeting*, Philadelphia, 1956.
- [98] R. Batra, "Elements of continuum mechanics," *Reston VA AIAA*.
- [99] ANSYS Inc, "ANSYS® Programmer's Reference: II. Guide to User-Programmable Features," 2014.
- [100] H. Mavoori, "Creep, stress relaxation and plastic deformation of SnAg and Sn-Zn eutectic solders," *Journal of electronic mater*, vol. 26, pp. 753-90, 1997.
- [101] W. R. Neu, "Thermomechanical behavior of 96Sn-4Ag and cast tin alloy," *Journal of Electronic package*, vol. 23, pp. 238-46, 2001.
- [102] N. Wade, "Effects of Cu, Ag and Sb on the creep rupture strength of lead free solder alloys," *Electronic mater*, vol. 30, pp. 1228-31, 2001.
- [103] A. Schubert, H. Walter and B. Michel, "Material mechanics and reliability issues of lead free solder interconnects," in *2nd ESIME conference*, 2001.
- [104] R. Darveaux and K. Banerji, "Constitutive relations for tin-based solder joints," in *42nd Electronic components and technology conference*, 1992.

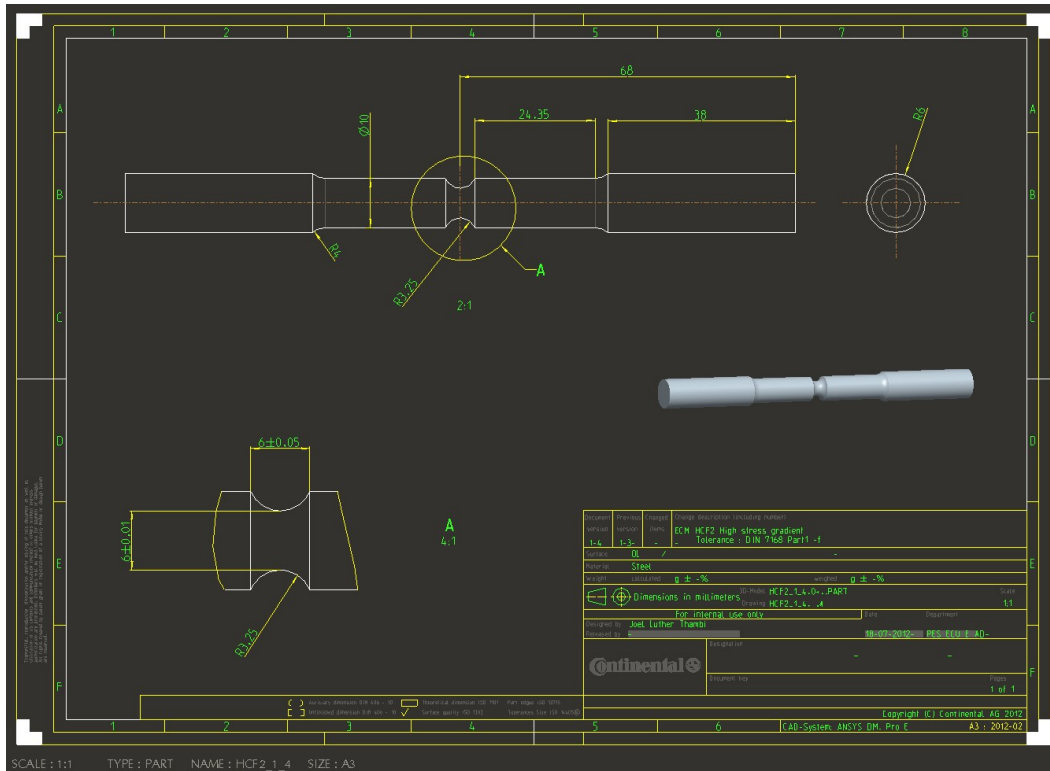
- [105] G. Cuddalorepatta, M. Williams and A. Dasgupta, "Viscoplastic creep response and microstructure of as-fabricated microscale SAC solder interconnects," *Journal of electronic matter*, vol. 39, no. 10, pp. 2292-2309, 2010.
- [106] I. Dutta, C. Park and S. Choi, "Impression creep characterization of rapidly cooled SAC solders," *Material science engineering*, vol. 379, no. 1-2, pp. 401-410, 2004.
- [107] J. Gong, C. Liu and P. Conway, "Modeling of Ag₃Sn coarsening and its effects on creep of Sn-Ag eutectics," *Material science and engineering*, vol. 427, pp. 60-68, 2006.
- [108] N. Chawla and R. S. Sindhu, "Microstructure based modeling of deformation of Sn rich Pb free solder alloys," *Journal of Materials Science: Materials in Electronics*, vol. 18, no. 1-3, pp. 175-189, 2006.
- [109] J. Rosler and E. Arzt, "A new model based creep equation for dispersion strengthened materials," *Acta Metallurgica et Materialia*, vol. 38, no. 4, pp. 671-683, 1990.
- [110] IPC, "Guidelines for accelerated reliability testing of surface mount attachments," *Institute of interconnecting and packaging electronics*, vol. SM, p. 195, 1992.
- [111] W. W. Lee, L. T. Nguyen and G. S. Selvaduray, "Solder joint fatigue models; review and applicability to chip scale packages," *Microelectronics reliability*, vol. 40, no. 2000, pp. 231-234, 2000.
- [112] A. Syed, "Accumulated creep strain and energy density based thermal fatigue life prediction models for SnAgCu solder joints," in *ECTC conference*, 2004.
- [113] J. H. Pang and D. Y. Chong, "Flip chip on board solder joint reliability analysis using 2-D and 3-D FEA models," vol. 24, no. 2, p. 499, 2001.
- [114] K. Knecht and F. L.R., "Constitutive relations of Tin based solder joints," *IEEE CHMT-A*, pp. 153-158, 1990.
- [115] C. Basaran, C. S. Desai and T. Kundu, "Thermomechanical FEA of problems in electronic packaging using the distributed state concept Part I: Theory and formulation," *Journal of electronic packaging*, vol. 120, no. 3, pp. 41-47, 1998.
- [116] Z. Qian and S. Liu, "On the life prediction and accelerated testing of solder joints. In: Thermo-Mechanical Characterization of Evolving Packaging Materials and Structures," *ASME International Mechanical Engineering Congress and Exposition*, vol. 24, pp. 1-11, 1998.
- [117] J. Zhao, Y. Miyashita and Y. Mutoh, "Fatigue crack growth behavior of 96.5Sn-3.5Ag lead-free solder," *International Journal of Fatigue*, vol. 23, pp. 723-731, 2001.
- [118] C. Basaran and R. Chandaroy, "Mechanics of Pb40/Sn60 near-eutectic solder alloys subjected to vibrations," *Applied Mathematical Modelling*, vol. 22, pp. 601-627, 1998.
- [119] C. Kanchanomai, W. Limtrakarn and Y. Mutoh, "Fatigue crack growth behavior in Sn-Pb eutectic solder/copper joint under mode I loading," *Mechanics of Materials*, vol. 37, pp. 1166-1174, 2005.
- [120] X. Liu, V. K. Sooklal, M. A. Verges and M. C. Larson, "Experimental study and life prediction on high cycle vibration fatigue in BGA package," *Microelectronics reliability*, vol. 46, pp. 1128-1138, 2006.
- [121] B. Farahmand, *Fatigue and Fracture Mechanics of High Risk Parts*, New York: Chapman & Hill, 1997.
- [122] F. A. Stam and E. Davitt, "Effects of thermomechanical cycling on lead and lead-free (SnPb and SnAgCu) surface mount solder joints," *Microelectronics Reliability*, vol. 41, pp. 1815-1822, 2001.

- [123] D. B. Baker, A. Dasgupta and M. G. Pecht, "PWB solder joint life calculation under thermal and vibration loading," *J.IES*, vol. 1, pp. 17-25, 1992.
- [124] D. B. Baker, Y. S. Chen and A. Dasgupta, "Estimating the vibration fatigue life of quad leaded surface mount components," *Journal of electronic package*, vol. 115, pp. 195-200, 1993.
- [125] T. E. Wong, F. W. Palmieri and B. A. Reed, "Durability/Reliability of BGA solder joints under vibration environment," *Electronic component and technology conference*, pp. 1083-1088, 2000.
- [126] F. X. Che and J. H. Pang, "Vibration reliability test and finite element analysis for flip chip solder joints," *Microelectronics reliability*, vol. 49, pp. 754-760, 2009.
- [127] S. Lampmann, *ASM Handbook of fatigue and fracture*, vol. 19, ASM International, 1996.
- [128] J. Mentley, "HBM Designlife theory," 2012.
- [129] ASTM, "Standard test methods for conducting creep, creep-rupture, and stress-rupture tests on metallic materials E139-11," in *ASTM International*, West Conshohocken, PA, Beuth Verlag, 2011.
- [130] L. B. Tuckerman and C. S. Aitchison, "Design of specimens for short-time fatigue tests," *Technologic papers of the bureau of standards*, vol. 19, p. 47, 1924.
- [131] ASTM, "Standard practice for conducting force controlled constant amplitude axial fatigue tests of metallic materials," in *ASTM International*, West Conshohocken, PA, Beuth Verlag, 2011.
- [132] M. Roellig, M. Meier, A. Schiessl and R. Metasch, "High and Low cycle fatigue experiments on solder joints for long term reliability of Automotive electronics".
- [133] J. W. Kim and S. B. Jung, "Design of solder joint structure for flip chip package with an optimized shear test method," *Journal of electronic materials*, vol. 36, no. 6, pp. 690-696, 2007.
- [134] F. X. Chen and J. W. Pang, "Thermal Fatigue analysis for PBGA package with SN3.8Ag0.7Cu solder joints," *Electronic packaging technology conference*, pp. 787-792, 2004.
- [135] H. T. Ma, "Constitutive creep models for Lead-free solders," *Journal of material science*, vol. 14, no. 44, pp. 3841-3851, 2009.
- [136] Y. D. Han, H. Y. Jing and S. M. L. Nai, "A new creep model for SAC Lead free composite solders: Incorporating back stress," *Electronic packaging technology conference -IEEE*, vol. 10, pp. 689-695, 2008.
- [137] X. Qi, H. R. Ghorbani and J. Spelt, "Thermal fatigue of SnPb and SAC resistor joints: analysis of stress strain as a function of cyclic parameters," *IEEE transaction of Advanced packaging*, vol. 29, no. 4, pp. 690-700, 2006.
- [138] R. Dwayne, "Transient and steady state creep in a SAC lead free solder alloy: experiment and modeling," PhD disertation, Toronto, 2009.
- [139] G. S. Zhang, H. Y. Jing and L. Y. Xu, "Creep behavior of eutectic 80Au/Sn solder alloy," *Journal of alloy and compounds*, vol. 476, no. 1-2, pp. 138-141, 2009.
- [140] B. Z. Hong, "Finite element modelling of Thermal Fatigue and damage of Solder joints in a Ceramic Ball Grid Array Package," *Journal of Electronic Material*, vol. 26, no. 7, 1997.
- [141] J. Lau and W. Daushker, "Effects of ramp-time on the thermal fatigue life of SnAgCu lead free solder joints," *Electronic components and technology conference*, pp. 1292-1298, 2005.
- [142] J. H. Lau, S. H. Pan and C. Chang, "Creep analysis of wafer level chip scale package with 96.5Sn3.5Ag and 100In lead free solder joints and microvia build up," *Journal of Electronic Package*, vol. 124, no. 2, pp. 69-76, 2002.

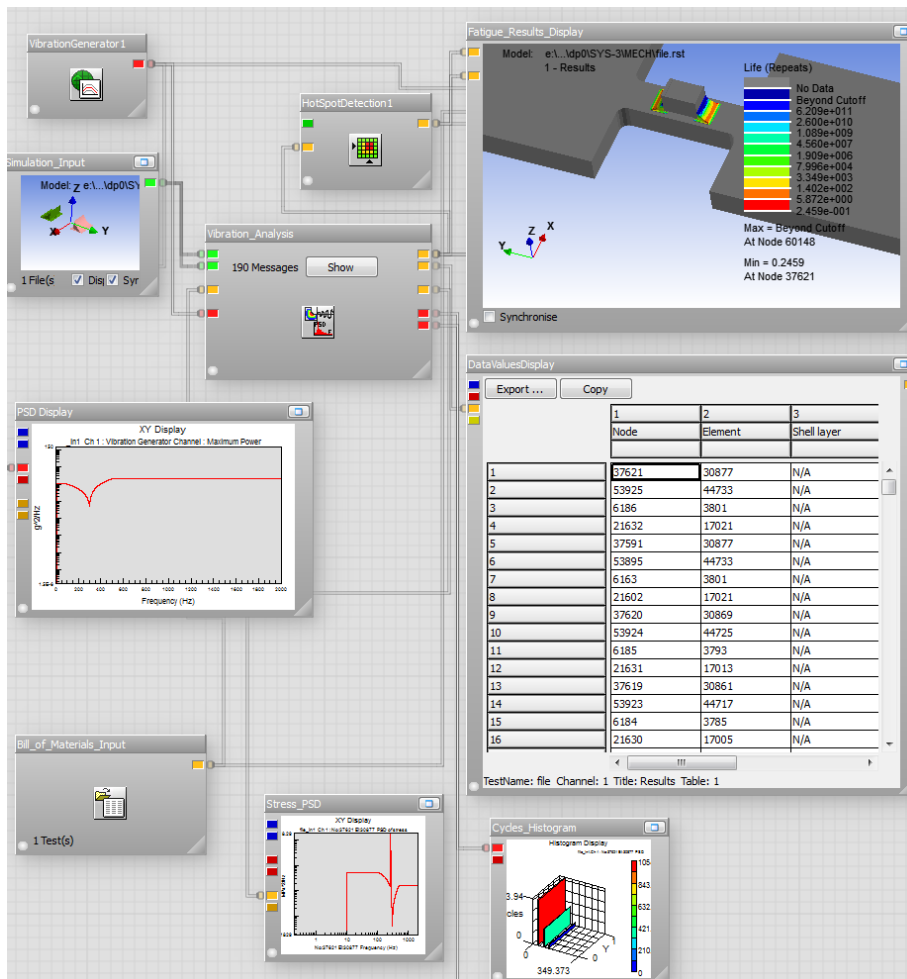
- [143] L. Zhang, S. B. Xue, L. L. Gao and Y. Chen, "Creep behavior of SnAgCu solder with rare earth Ce doping," *Transaction of nonferrous metals*, vol. 18, no. 6, pp. 753-778, 2009.
- [144] J. W. Kim and S. B. Jung, "Reexamination of the solder ball shear test for evaluation of the mechanical joint strength," *International Journal of Solids and Structures*, vol. 43, pp. 1928-1945, 2006.
- [145] R. Darveaux, K. Banerji, A. Mawer and G. Dody, "Reliability of Plastic Ball Grid Array Assembly," *Ball Grid Array Technology*, J. Lau Editor, McGraw-Hill, Inc., 1995.
- [146] J. H. Lau and Y. H. Pao, *Solder Joint Reliability of BGA, CSP, Flip Chip, and Fine Pitch SMT Assemblies*, New York: McGraw-Hill, 1997.
- [147] S. H. Suh, J. B. Cohen and J. Weertman, "X-ray diffraction study of subgrain misorientation during high temperature creep of Tin single crystals," *Metallurgical transactions A*, vol. 14A, pp. 117-126, 1983.
- [148] U. F. Kocks, A. S. Argon and M. F. Ashby, "Thermodynamics and kinetics of slip progress in material science," *Pergamon press, New York*.
- [149] G. M. Pharr, "Some observations on the relation between dislocation substructure and power law breakdown," *Scripta Metall*, vol. 15, pp. 713-717, 1981.
- [150] Q. Xiao, W. D. Armstrong and L. Nguyen, "Anomalously high tensile creep rates from thin cast Sn_{3.9}Ag_{0.6}Cu lead-free solder," *Journal of electronic materials*, vol. 34, no. 7, pp. 1065-1075, 2005.
- [151] E. G. Dieter, *Mechanical Metallurgy - 3rd Edition*, New York: McGraw Hill, 1986.
- [152] D. Hardwick, C. M. Sellars and W. J. Tegart, "Structural changes during the deformation of copper, aluminium and nickel at high temperatures and high strain rates," *J. Inst. Met*, vol. 90, p. 21, 1961.
- [153] D. McLean and M. H. Farmer, "The relation during creep between grain-boundary sliding, sub-crystal size, and extension," *J Inst Met*, 1957.
- [154] C. Kanchanomai, Y. Miyashita, Y. Mutoh and S. L. Mannan, "Influence of frequency on LCF behaviour of Pb-free solder 96.5Sn-3.5Ag," *Material science and engineering*, vol. 345, pp. 90-98, 2003.
- [155] H. Chen, H. Jing and M. Li, "Localized recrystallization induced by subgrain rotation in SAC BGA solder interconnects during thermal cycling," *Journal of electronic materials*, vol. 40, no. 12, 2011.
- [156] C. Kanchanomai, Y. Miyashita and Y. Mutoh, "Low cycle fatigue behavior and mechanisms of a eutectic Sn-Pb," *International journal of fatigue*, vol. 24, pp. 671-683, 2002.
- [157] S. Wiese, M. Mueller and K. L. Wolter, "The twinning phenomenon in SAC solder balls," *Electronic component and technology conference*, pp. 1027-1033, 2009.
- [158] T. R. Bieler, H. Jiang, L. P. Lehman, E. J. Kirkpatrick and B. Nandagopal, "Influence of Sn Grain size and orientation on the thermomechanical response and reliability of Pb-free solder joints," *IEEE transaction for component packaging technology*, vol. 32, no. 370, 2008.
- [159] Q. Zhou, B. Zhou, T. Lee and T. Bieler, "Microstructural evolution of SAC305 solder joints in wafer level chip-scale packaging (WLCSP) with continuous and interrupted accelerated thermal cycling," *Journal of electronic materials*, vol. 45, no. 6, pp. 3013-3024, 2016.
- [160] N. A. Fleck, C. S. Shin and R. A. Smith, "Fatigue crack growth under compression loading," *Engineering fracture mechanics*, vol. 21, pp. 173-185, 1985.

- [161] R. W. Hertzberg, Deformation and fracture mechanics of engineering materials, New York: John Wiley, 1996.
- [162] J. Roesler, M. Baeker and H. Harders, Mechanical behaviour of engineering materials, Berlin Heidelberg: Springer-Verlag, 2007.
- [163] Y. Chen, Y. Jin and R. Kang, "Coupling damage and reliability modeling for creep and fatigue of solder joints," *Microelectronics Reliability*, vol. 75, pp. 233-238, 2017.
- [164] R. Agamenonne, W. Blum and C. Gupta, "Evolution of microstructure and deformation resistance in creep of tempered martensitic steels," *Acta Materialia*, vol. 54, pp. 3003-3014, 2006.
- [165] S. K. Seo, S. K. Kang, D. Y. Shih and H. M. Lee, "An investigation of microstructure and microhardness of Sn-Cu and Sn-Ag solders as functions of alloy composition and cooling rate," *Journal of electronic materials*, vol. 38, no. 2, pp. 257-265, 2009.
- [166] B. Philippi, K. Matoy, J. Zechner, C. Kirchlechner and G. Dehm, "Fracture toughness of intermetallic Cu₆Sn₅ in lead-free solder microelectronics," *Scripta materialia*, vol. 123, pp. 38-41, 2016.
- [167] P. Gay and A. Kelly, "X-ray study of polycrystalline metals deformed by rolling," *Acta crystallographica*, vol. 6, pp. 172-179, 1953.
- [168] D. Hardwick, C. M. Sellars and W. J. Tegart, "The occurrence of recrystallization during the high temperature creep," *Journal of institute of metals*, vol. 90, pp. 21-29, 1961.
- [169] M. A. Matin, "Microstructure evolution and thermomechanical fatigue of solder materials," TU Eindhoven library, Eindhoven, Netherlands, 2005.
- [170] Q. Zhang, "Investigation on microstructure and mechanical properties of Cu/Pb free solder interfaces," *Springer theses*, vol. 143, p. 115, 2016.
- [171] C. Laird, "Fatigue crack propagation," *ASTM STP*, vol. 415, p. 131, 1967.
- [172] O. D. Sherby, C. M. Young and S. L. Robinson, *Acta Metalla*, vol. 23, p. 633, 1975.
- [173] Y. Ding, "In-situ observation microfracture behavior ahead of the crack tip in 63Sn37Pb solder alloy," *Metallurgical and materials transactions*, vol. 37, no. 3, pp. 1017-1025, 2006.
- [174] W. H. Kim and C. Laird, "The local X-ray investigation of C-Fe-Cr-Mo alloys after friction tests and after oxidation," *ACTA MET*, p. 777, 1978.
- [175] R. Harwood, "Documentation, ANSYS 15.1.," ANSYS Inc, 2014.
- [176] C. Cai, Zheng, M. S. Khan and K. C. Hung, "Modeling of material damping properties in ANSYS," *ANSYS Conf*, vol. 197, 2002.
- [177] N. Cressie, Statistics for spatial data, New York: Wiley, 1993.
- [178] O. Heinonen, "Optimal design of stiffened plate using metamodeling techniques," *Journal of structural mechanics*, vol. 44, no. 3, pp. 218-230, 2011.
- [179] Z. Liang and K. K. Choi, "A metamodeling method using dynamic Kriging and sequential sampling," *American institute of aeronautics and astronautics*.
- [180] D. Krige, "A statistical approach to some basic mine valuation problems on the witwatersrand," *Journal of chemical metallurgical and mining engineering society of South Africa*, vol. 52, no. 6, pp. 119-139, 1951.
- [181] M. Leonard, Fundamental of vibrations, Long Grove, IL: Waveland Pr Inc. 1 edition, 2010.
- [182] P. Jean, "SnAgCu properties and creep data," *National Institute of Standards and Technology*.

-
- [183] K. Meier, M. Roellig, R. Metasch and A. Schiessl, "Lifetime assessment for bipolar components under vibration and temperature loading," in *Thermal, mechanical and multi-physics simulation and experiments in microelectronics and microsystems (EuroSimE)*, Wroclaw, 2013.
- [184] M. L. Huang, C. M. Wu, J. K. Lai and Y. C. Chan, "Microstructural evolution of lead free solder alloy prepared by mechanical alloying during thermal shock and aging," *Journal of electronic materials*, vol. 29, pp. 1021-1361, 2000.
- [185] Q. Zhang, A. Dasgupta and P. Haswell, "Viscoplastic constitutive properties and energy-partitioning model of lead-free Sn3.9Ag0.6Cu solder alloy," *Proceeding of the 53rd electronic components and technology conference*, pp. 1862-1868, 2003.
- [186] J. P. Clech, Review and analysis of lead-free materials properties, NIST, Available at: <http://www.metallurgy.nist.gov/solder/clech/>.
- [187] J. H. Lau, J. H. Pang, N. C. Lee and L. Xu, "Material properties and intermetallic compounds of Sn 3 wt% Ag 0.5 wt% Cu 0.019 wt% Ce (SACC)," In: *The proceedings of 57th electronic components and technology conference (ECTC07)*, pp. 211-218, 2007.
- [188] P. T. Vianco, "Fatigue and creep of lead-free solder alloys: fundamental properties," *ASM International*, pp. 67-106, 2006.



II. FATIGUE VIBRATION PATH PLOT: nCODE DESIGNLIFE™ 10.0



III. SUBROUTINE FOR THE NEW MODIFIED CREEP LAW IN ANSYS

```

Language: FORTRAN; Compiler: Intel FORTRAN 12.1
*deck, usercreep      parallel user gal
  SUBROUTINE usercreep (impflg, ldstep, isubst, matId , elemId,
    &kDInPt, kLayer, kSecPt, nstatv, nprop,
    &prop , time , dtime , temp , dtemp ,
    &toffst, Ustatev, creqv , pres , seqv ,
    &delcr , dcrda)
c*****
c    *** primary function ***
c      Define creep laws when creep table options are
c      TB,CREEP with TBOPT=100.
c      Implementation of usercreep subroutine for diffusion controlled
creep
c      CON-14-CON-002 /on demand on Continental Automotive GmbH/
c
c      Creep equation is
c      dotcreq := C4 *E/T*lambda_ss^(-n1*p)
c                * (1+C2*(seqv/E)^(n2)*exp(-(Qc-Ql-(alpha-
beta)*(seqv/E)))/(RT))
c                *exp(-(Ql-beta*(seqv/E))/(RT))
c
c      seqv is equivalent effective stress (Von Mises stress)
c      creqv is equivalent effective creep strain
c      T is the temperature
c      E is the Young's modulus (isotropic material)
c
c      Eleven Material constants (11):
c      Qc activation energy for core creep [kJ/mol]
c      Ql activation energy for lattice creep [kJ/mol]
c      alpha constant alpha (ansatz for diffusion coefficient
of core creep) [-]
c      beta constant beta (ansatz for diffusion coefficient of
lattice creep) [-]
c      n1 constant n1 (in power exponent for lambda_ss) [-]
c      n2 constant n2 (in power exponent for seqv/E) [-]
c      R Boltzmann's ideal gas constant [kJ/(mol*K)]
c      lambda_ss averaged subgrane size [micro m]
c      C4 material constant [micrps m/s]
c      C2 material constant [1/s]
c      p exponent for lambda_ss [-]
c
c
c
c
c*****
c
c      input arguments
c      =====
c      impflg (in ,sc ,i) Explicit/implicit integration
c                          flag (currently not used)
c      ldstep (in ,sc ,i) Current load step
c      isubst (in ,sc ,i) Current sub step
c      matId (in ,sc ,i) number of material index
c      elemId (in ,sc ,i) Element number
c      kDInPt (in ,sc ,i) Material integration point
c      kLayer (in ,sc ,i) Layer number
c      kSecPt (in ,sc ,i) Section point
c      nstatv (in ,sc ,i) Number of state variables
c      nprop (in ,sc ,i) size of mat properties array

```

```

c
c      prop      (dp ,ar(*) ,i)      mat properties array
c                                         This array is passed all the
creep
c                                         constants defined by command
c                                         TBDATA associated with TB, CREEP
c                                         (do not use prop(13), as it is
used
c                                         elsewhere)
c                                         at temperature temp.
c      time      Current time
c      dtime     Current time increment
c      temp      Current temperature
c      dtemp     Current temperature increment
c      toffst   (dp, sc, i)         temperature offset from absolute
zero
c      seqv     (dp ,sc , i)         equivalent effective stress
c      creqv    (dp ,sc , i)         equivalent effective creep strain
c      pres     (dp ,sc , i)         hydrostatic pressure stress, -
(Sxx+Syy+Szz)/3
c
c      input output arguments      input desc      / output desc
c      =====
c      Ustatev (dp,ar(*) , i/o)    user defined iinternal state var-
iables at
c                                         time 't' / 't+dt'.
c                                         This array will be passed in con-
taining the
c                                         values of these variables at
start of the
c                                         time increment. They must be up-
dated in this
c                                         subroutine to their values at the
end of
c                                         time increment, if any of these
internal
c                                         state variables are associated
with the
c                                         creep behavior.
c
c      output arguments
c      =====
c      delcr    (dp ,sc , o)         incremental creep strain
c      dcrda    (dp,ar(*) , o)       output array
c                                         dcrda(1) - derivative of incre-
mental creep
c                                         strain to effective
stress
c                                         dcrda(2) - derivative of incre-
mental creep
c                                         strain to creep strain
c
c      local variables
c      =====
c      Qc,Ql,alpha,beta (dp, sc, 1)  temporary variables as creep
constants
c      n1,n2,R,lambdas (dp, sc, 1)   temporary variables as
creep constants
c      C4,C2,p      (dp, sc, 1)      temporary variables as creep
constants

```

```

c      E      (dp, sc, 1)      temporary variable: Young's
modulus
c      t      (dp ,sc, 1)      temporary variable: absolute
temperature
c      con1,con2,a1,sE (dp ,sc, 1)      temporary variables
c      RT, exp1, exp2 (dp ,sc, 1)      temporary variables
c      power, ERT (dp ,sc, 1)      temporary variables
c      bracket (dp ,sc, 1)      temporary variables
c      numerator1 (dp ,sc, 1)      temporary variables
c      numerator2 (dp ,sc, 1)      temporary variables
c
c*****
c
c --- parameters
c
#include "impcom.inc"
c
c      DOUBLE PRECISION ZERO
c      PARAMETER      (ZERO = 0.0d0)
c      DOUBLE PRECISION ONE
c      PARAMETER      (ONE = 1.0d0)
c
c --- argument list
c
c      INTEGER      ldstep, isubst, matId , elemId,
&kDInPt, kLayer, kSecPt, nstatv,
&impflg, nprop
c      DOUBLE PRECISION dtime , time , temp , dtemp , tofst,
&creqv , seqv , pres
c      DOUBLE PRECISION prop(*), dcrda(*), Ustatev(nstatv)
c
c --- local variables
c
c      DOUBLE PRECISION Qc,Q1,alpha,beta,a,b,R,lambda_ss,C1,C2,p,
&E, con1 ,con2, delcr , t,
&a1, sE, RT, exp1, exp2, power, ERT, bracket,
&numerator1, numerator2
c
c*****
c
c *** skip when stress and creep strain are all zero
c      if (seqv.LE.ZERO.AND.creqv.LE.ZERO) GO TO 990
c *** add temperature offset
c      t = temp + tofst
c *** determine Young's modulus
c      CALL propel (elemID,matID,1,temp,E)
c *** creep material constants
c      Qc = prop(1)
c      Q1 = prop(2)
c      alpha = prop(3)
c      beta = prop(4)
c      n1 = prop(5)
c      n2 = prop(6)
c      R = prop(7)
c      lambda_SS = prop(8)
c      C1 = prop(9)
c      C2 = prop(10)
c      p = prop(11)
c
c *** user need to make sure if "Qc-Q1-(alpha-beta)*sE" has nonzero value,
temperature should be also nonzero.

```

```

c *** user need to make sure if "Q1-alpha*sE" has nonzero value, tempera-
ture should be also nonzero.
  sE = seqv/E
  RT = R*t
  numerator1=Qc-Q1-(alpha-beta)*sE
  numerator2=Q1-beta*sE
c *** conditions proof
  con1 = ZERO
  con2 = ZERO
  if(numerator1.ne.ZERO .and. RT.gt.ZERO) con1 = numerator1/RT
  if(numerator2.ne.ZERO .and. RT.gt.ZERO) con2 = numerator2/RT
c *** calculate incremental creep strain
c   delcr := dotcreq * dtime
  if (creqv .le. TINY) creqv = sqrt(TINY)
  delcr = ZERO
  IF (C1.gt.ZERO) then
c ***
c   incremental creep strain
c ***
          a1 = C4*E/t*lambda_ss**(-n1*p)
          exp1 = exp(-con1)
          exp2 = exp(-con2)
          power = n2
c ***
          delcr = a1*(ONE+C2*sE**power*exp1)*exp2*dtime

          ENDIF
c ***
c *** derivative of incremental creep strain to effective stress
c ***
  ERT = E*RT
  bracket = power/seqv+(alpha-beta)/(ERT)
  dcrda(1)=C2*a1*sE**power*bracket*exp1*exp2*dtime
  &+ beta*delcr/ERT
c ***
c *** derivative of incremental creep strain to effective creep strain
c ***
  dcrda(2)=ZERO
c ***
990 continue
  return
  end

```

III.a. Verification Examples

Example 1: One Element $T = \text{const}$

1.1. Overview

Analysis Type(s): Static Analysis with USERCREEP (ANTYPE = 0)

Element Type(s): 3-D Structural Solid Elements (SOLID185)

Input Listing: EX1_UserCreep_Tconst.inp

1.2. Test Case

A cube, meshed by one element, is loaded by an axial displacement at room temperature. The viscous relaxation is calculated over the defined time period. The numerically calculated creep strain rate is compared to the strain rate, determined analytically from the creep law formulation.

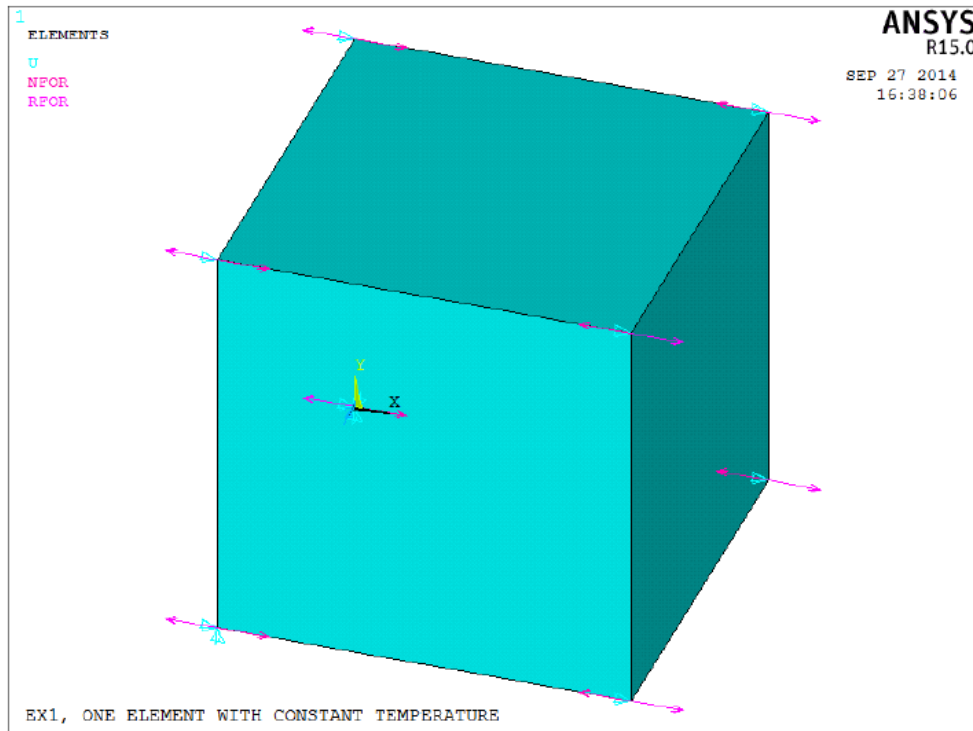


Figure 1: FE Model

Material Properties (Isotropic) Young's modulus $E = E(T)$, USERCREEP parameters: 11 constants (Table 11), Poisson's ratio: = 0.3467 Thermal Expansion Coefficient: = $2.51 \times 10^{-5} \text{ 1/K}$

$V = 100^3 \text{ mm}^3$ Displacement: $ux = 1 \text{ mm}$

Temperature: $T = 22^\circ\text{C}$ (const)

1.3 Results

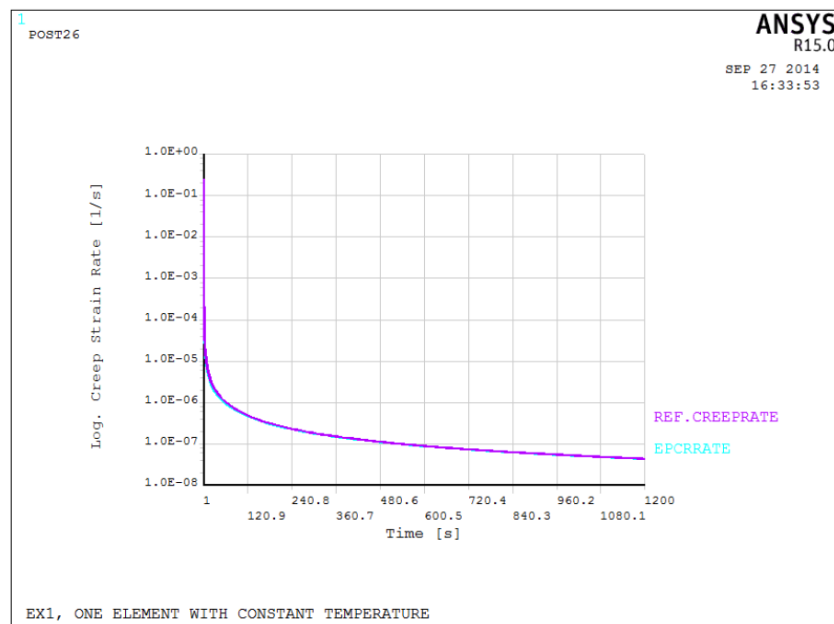


Figure 2: Comparison between numerically calculated creep strain rate (from USERCREEP) and a reference solution

Note: The reference creep strain rate in all examples is calculated by the creep law ansatz, substituting the Young's modulus and stress, determined for each time point in /POST26.

Example 2: Multiple elements with bulk specimen geometry, $T = T(t)$

2.1. Overview

Analysis Type(s): Static Analysis with USERCREEP (ANTYPE = 0)

Element Type(s): 3-D Structural Solid Elements (SOLID186)

WB Project: EX4_UserCreep_Multiple_Tsinus_V150.wbpz

2.2. Test Case

A quarter of test sample with a circular cross section is applied to initial tensile stress. The temperature is given as a sinus function of the time. The creep strain rate, calculated by the USERCREEP subroutine, is compared to a reference solution.

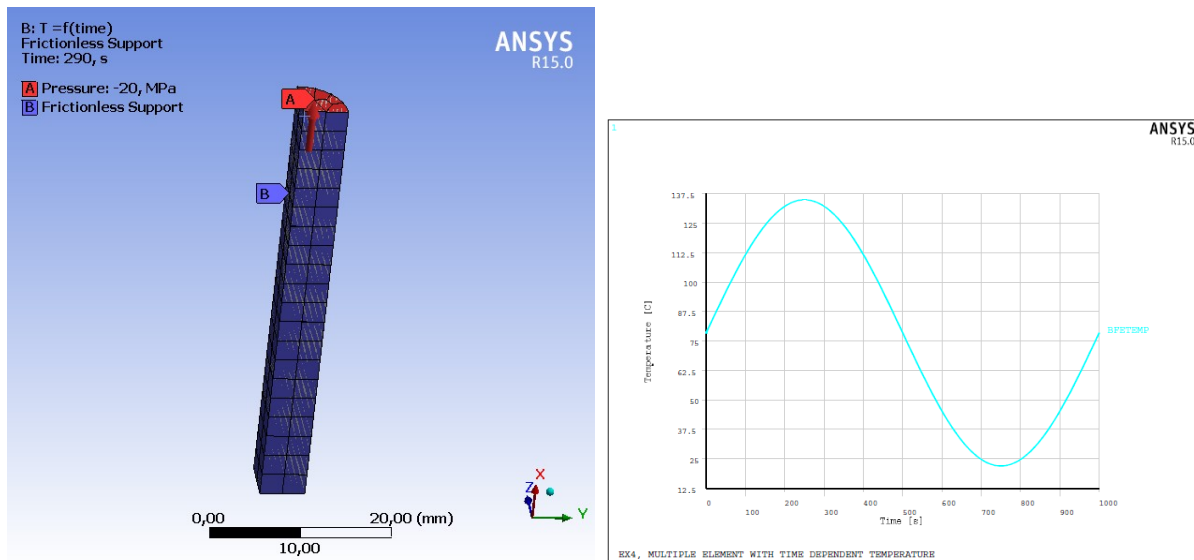


Figure 1: (a) FE Model (b) Load temperature vs time

Young's modulus: $E = E(T)$, $R = 5$ mm, $L = 50$ mm, USERCREEP parameters: 11 constants (Table 11), Thermal Expansion Coefficient: $= 2,51 \cdot 10^{-5}$ 1/K

Pressure: $p = -20$ MPa, Temperature: $T = T(t)$

Poisson's ratio: $\nu = 0.3467$

2.3. Results

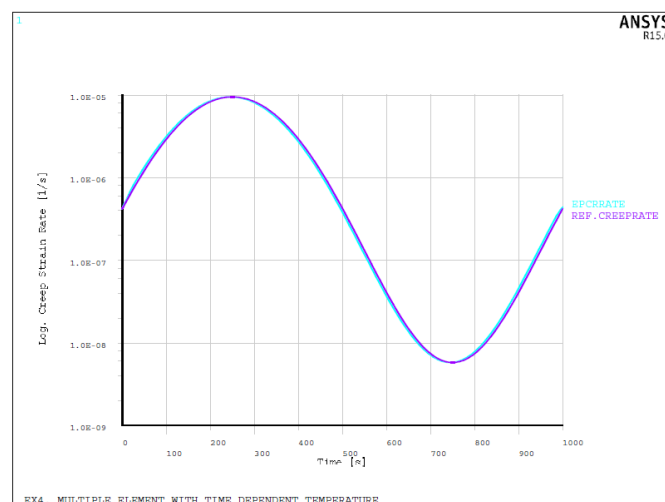
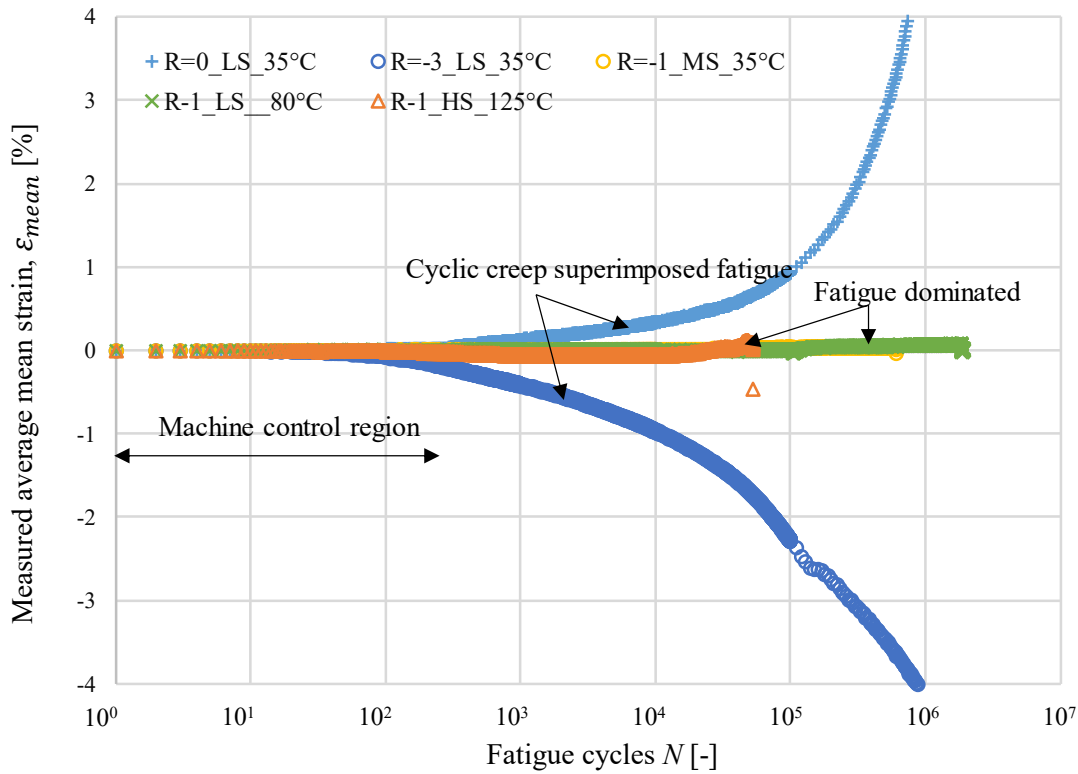
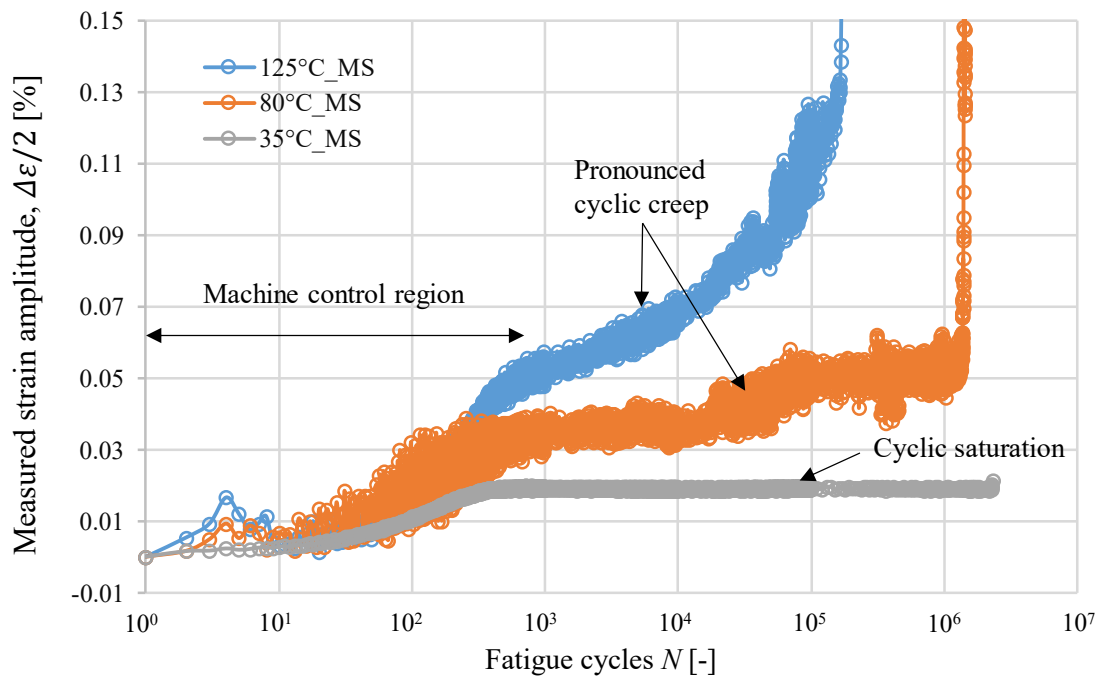


Figure 2: Comparison between numerically calculated creep strain rate (from USERCREEP) and a reference solution

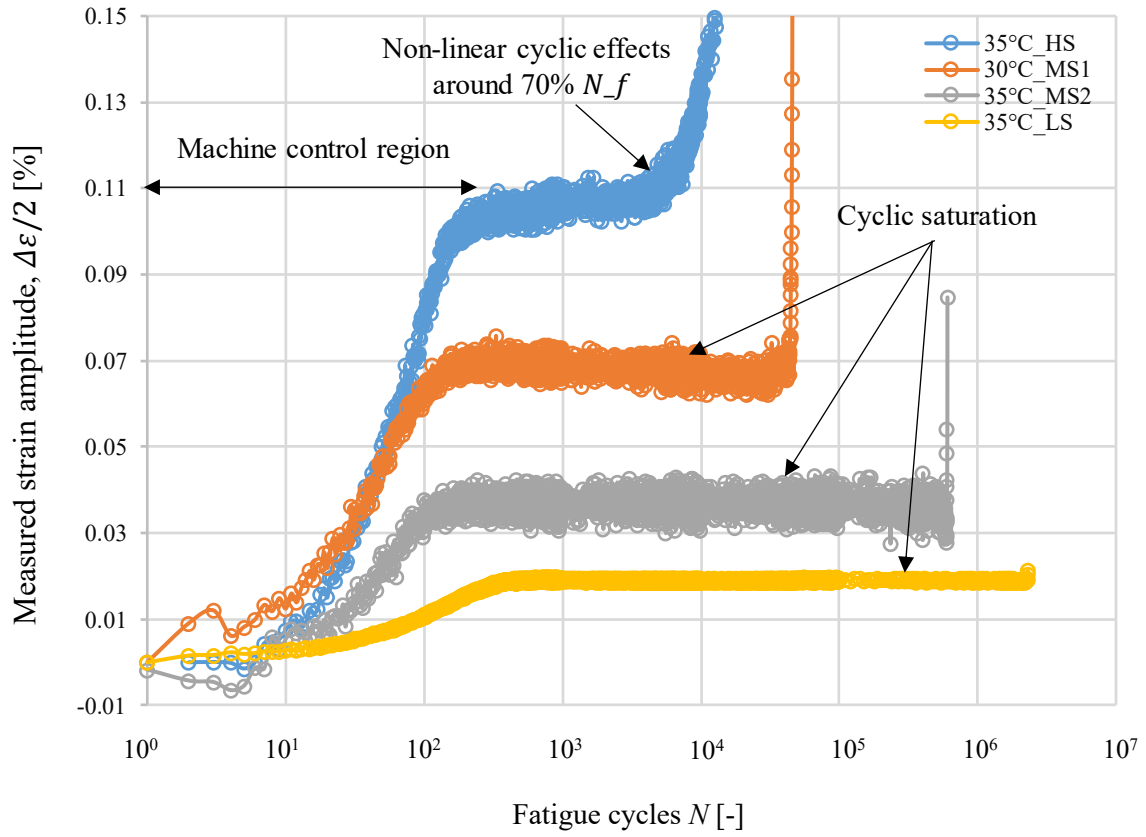
IV. FATIGUE MEASURED STRAIN PROGRESSION (WITH MACHINE CONTROL REGION)



Average mean strain progression (see Eqn. (3.3) of the solder specimen over lifetime for different load cases, temperatures and stresses- high stress (HS), medium stress (MS), low stress (LS)



Cyclic true strain amplitude measured, $\Delta\varepsilon/2$ as per Eqn.(3.3) vs. cycles for solder alloys subjected to completely reversed load at $R = -1$ for different temperatures, at medium stress (MS)



Strain amplitude measured $\Delta\epsilon/2$, as per Eqn.(3.3) vs. cycles subjected to $R=-1$ at 35°C, Low stress- LS, Medium stress-MS and High stress HS

NOMENCLATURE

Variable	Units	Description
$\dot{\bar{\epsilon}}_{cr}$	s^{-1}	Equivalent creep strain rate
$\overline{G_\sigma}$	mm^{-1}	Normalised stress gradient
$\dot{\epsilon}_s$	$1/s$	Secondary creep strain rate
$\bar{\epsilon}$	-	Equivalent creep strain
$\bar{\sigma}$	MPa	Equivalent stress
σ_b	MPa	Back stress for Orowan mechanism
A	μm^{-1}	Material constant for solder alloy (surface roughness)
a_g	-	Material constant for solder alloy (stress gradient)
b	-	Fatigue strength exponent
B	MPa	Material constant for solder alloy (surface roughness)
b_g	MPa	Material constant for solder alloy (stress gradient)
b_v	nm	Burgers vector
C	-	Material coefficients
d	μm	Diameter of hardened particles
E	MPa	Young's modulus
f	%	Volume fraction
f_0	Hz	First modal frequency (natural frequency)
f_c	Hz	Cyclic frequency
G	MPa	Shear modulus
K_R		Roughness factor
K_r	-	Intensity of attraction between the particles and dislocation
K_t	-	Stress concentration factor
L	μm	Average separation of intermetallic particles
M	-	Taylor factor
M_1, M_2, M_3, M_4	-	Mean stress correctivity FKM
n	-	Stress exponent
N	-	Number of cycles
N_f	-	Cycle to failure
N_v	μm	Number of particles per unit volume
n_σ	-	Stress gradient correction factor
p	-	Substructure exponent
Q	kJ/mol	Activation energy

Q_c	kJ/mol	Core diffusion activation energy
Q_l	kJ/mol	Lattice diffusion activation energy
R	-	Cyclic R- ratio (fatigue study)
r	μm	Mean radius of precipitates
R	$kJ/mol.K$	Universal gas constant (creep study)
R_a	μm	Average surface roughness
β_{pcb}	-	Material damping of PCB
T	K	Absolute temperature
T_d	N	Dislocation line tension
t_f	h	Time to failure
T_p	s	Time period
α_{CTE}	ppm	Coefficient of thermal expansion
ε	-	Strain
ε_s	-	Secondary creep strain
ε_t	-	Transient strain
λ	μm	Interparticle spacing
λ_{ss}	μm	Subgrain intercept size
σ	MPa	Stress
σ_a	MPa	Stress amplitude
σ_m	MPa	Mean stress
σ_{max}	MPa	Maximum stress
σ_{min}	MPa	Minimum stress
σ_{th}	MPa	Threshold stress
σ_{UTS}	MPa	Ultimate tensile strength of material
γ		Proportionality factor for creep implementation
ATC	-	Accelerated thermal cycling
BSE	-	Back scatter electron
DoE	-	Design of experiments
EBCC	-	Electron backscatter channelling contrast
EBS	-	Electron backscatter diffraction
EDX	-	Energy dispersive X-ray spectroscopy
FEA	-	Finite element analysis
FRF	-	Frequency response function
IMC	-	Inter-metallic components
LCF/HCF	-	Low cycle fatigue/high cycle fatigue
LM	-	Light microscopy
LS/MS/HS	-	Low stress/medium stress/high stress
PSB	-	Persistent slip bands

PSD	-	Power spectral density
SAC	-	<i>SnAgCu</i> alloy
SEM	-	Scanning electron microscopy
SMT	-	Surface mount technology
SN	-	Stress life curve
TEM	-	Transmission electron microscopy
TMC/TC	-	Thermo-mechanical cycling/thermal cycling
XRD	-	X-ray diffraction

LIST OF FIGURES

Figure 1-1: Product development cost split up for an electronic based OEM's [2].....	2
Figure 2-1: Cross section of SMT components showing (a) transformer EHP16-solder joints with lead frame (b) chip capacitor CC0805-without lead-frame – (Source: Engine control unit cross sections- Continental Automotive GmbH [17]).....	7
Figure 2-2: Changes in the IMC coarsening at automotive field temperature over aging time at a) 0hr b) 500hr c) 1000hr	9
Figure 2-3: Microstructure of a typical SMT component solder joint depicting eutectic region consisting of second phase hardened particles in a β -Sn matrix	10
Figure 2-4: SEM-mapping of cross-section visualising different elements in SMT component (ceramic capacitors) used in this study	10
Figure 2-5: SEM line scan of a SMT component (ceramic capacitor) solder joint used in this study..	11
Figure 2-6: (a) Schematics of SMT showing various stages, marked in alphabets, encountered during thermomechanical cycling (b) corresponding stages of a TMC depicting temperature measured from various sample points in a SMT [17]	12
Figure 2-7: Characterizing maximum and minimum cycle with sinusoidal waveform, (a) compression/tension loading (b) tension/tension loading [38]	14
Figure 2-8: Stress controlled cycling resulting in softening and hardening, Millela [40].....	15
Figure 2-9: Time distribution in terms of cycles $N_{i,j}$ ($i = 1, 2, 3, 4$) of the four fatigue phases:(1) cyclic hardening or softening: (2) slips with mechanical small cracks, MSC formation (3) macro crack formation(4) growth of macro crack to failure, at four selected stress amplitude S_j , Millela [40]	16
Figure 2-10: Schematics depicting the event progression after crack initiation by means (a) intergranular fraction from the micro voids [39]- for e.g. in fine grain alloys (b) transgranular crack from persistent slip bands (PSB) [40].....	17
Figure 2-11: Different load types with varying means stresses (a) fully reversed cycle the mean stress is zero and $R = -1$, (b) fluctuating symmetric load from origin to tension $R = 0$, (c) fluctuating load from tension to compression dominant $R = -3$	20
Figure 2-12: Haigh fatigue strength schematics used for mean stress corrections [40].....	20
Figure 2-13: Stress concentration surfaces formed from the buoyant force provided by the molten solder surface tension on solder joint– (a) transformer, (b) ceramic capacitor [Source: Continental Automotive GmbH]	21
Figure 2-14: (a) Schematics of strain vs. time creep curve showing the typical three stages of creep and an instantaneous elongation on application of load (b) corresponding strain rate vs. time plot, Pelleg [65], (c) creep-rate vs. applied stress- Norton plot, showing change in stress exponents [66]	23
Figure 2-15: Dislocation motion under two-stress regimes (a) low stress region -glide assisted climb (b) high stress region -Orowan bowing mechanism [83]	25
Figure 2-16: Creep behaviour of precipitate strengthened materials and pure matrix materials (only schematics), Kassner [67]	26
Figure 2-17: Subgrain detected from SEM, revealing subgrain formation along the β -Sn matrix in SAC 387 alloy.....	27
Figure 2-18: Schematic illustration to explain the subgrain and intergranular- crack behaviour in a SMT solder joint [88].....	28
Figure 2-19: Schematic diagram of Manson-Haferd parameter.....	29
Figure 2-20: Summary of consolidating the fatigue analysis for vibration load using FRF local stresses with the implicit material parameters for fatigue models from the HCF experiments on SAC specimen, nCode [128]	38
Figure 3-1: 3D- CAD model of the creep solder specimen with special shoulder design, detailed dimension in Appendix I.....	40
Figure 3-2: 3D-CAD model of the fatigue specimens (a) notched specimen with higher stress concentration value $K_t > 1$ and (b) unnotched specimen with K_t value ~ 1 , detailed dimension in Appendix I	41
Figure 3-3: (a) CAD model of the die cast for the solder creep specimen (b) manufacturing mould cast setup showing resistors controlling the temperature in the aluminium die cast	42

Figure 3-4: (a) Manufactured creep specimen taken out from the aluminium dies (b) notched and unnotched solder specimen for fatigue testing, detailed dimension, detailed dimension in Appendix I.....	43
Figure 3-5: Cross-polarized optical micrograph of the cast solder specimens showing the primary grain orientations of (a) fatigue (b) creep specimens.....	44
Figure 3-6: X-ray inspection for cast quality and void detection on random lots (a) creep (b) fatigue	44
Figure 3-7 : (a) Universal test equipment for uniaxial creep and dynamic fatigue experiments (b) magnified view of the clamping wedges installed to the specimen and attached extensometer ..	46
Figure 3-8: Time independent derivation steps at low medium stress (MS) showing (a) creep strain, ϵ vs. time (b) creep strain rate, $\dot{\epsilon}$ vs. time (c) time independent diagram, $\dot{\epsilon}$ vs. ϵ	48
Figure 3-9: Time independent derivation steps at lower stresses (LS) showing (a) creep strain, ϵ vs. time with smoothening function (b) time independent diagram, $\dot{\epsilon}$ vs. ϵ	49
Figure 3-10: (a) Experimental setup and schematics of vibration experiment setup on the PCB strap with SMT, including vibration shaker and optical data-acquisition measurement systems (b) closer view of component placed on the PCB straps.....	50
Figure 3-11: (a) PCB strap design for vibration experiments on SMT ceramic components integrated on a shaker table setup (b) top view of the ceramic capacitor placed on the middle of the straps for achieving highest deformation (c) cross section of failure observed	51
Figure 4-1: Strain ϵ vs. strain rate $\dot{\epsilon}$ plot at low stress (LS), medium stress (MS) up to high stress (HS) for some test parameters (a) 35°C (b) 80°C (c)125°C	55
Figure 4-2: Norton power law fit over experimental creep strain results at different temperatures, with normalised fit parameters.....	57
Figure 4-3: Hyperbolic sine fit over experimental creep strain results at different temperatures, with normalised fit parameters.....	58
Figure 4-4: Power law fit over experimental creep strain rate results at different temperature, with normalised fit parameters.....	59
Figure 4-5: SEM micrographs showing microstructure of SAC alloy with the intermetallics (Ag_3Sn and Cu_6Sn_5) and the β -Sn matrix	62
Figure 4-6: Distribution of Ag_3Sn intermetallic precipitates analysed from pre-experimental samples.....	63
Figure 4-7: Threshold stress line (dotted) calculated as per Eqn. (4.3) - values from Table 9, plotted at various temperatures to differentiate the low stress (LS) and high stress (HS) regime	64
Figure 4-8: (a) Stress exponents of LSR and HSR showing steady relationship with temperature (b) stress exponents plotted versus σ/RT	66
Figure 4-9: Iso-stress lines plotted for creep strain versus reciprocal of temperature to determine activation energy Q	67
Figure 4-10: Activation energy, Q plotted against the normalised stress for high temperature range and low temperature range.....	67
Figure 4-11: EBSD investigations of the substructure formation on a creep specimen from the necking region revealing subgrain orientations	70
Figure 4-12: (a) EBCC image showing subgrain between dendrites on the non-necking region (b) EBCC, EBSD measurements of subgrain size measured from random samples.....	71
Figure 4-13: Creep strain- rate obtained from the experimental results (a) with new modified creep model incorporated subgrain size as in Eqn. (4.13), (b) without subgrain dependency as in Eqn. (4.12).....	73
Figure 4-14: Predicted vs. actual creep strain rate for the best-fit creep model that has subgrain dependency on applied stress as in Eqn. (4.13)	74
Figure 4-15: Manson-Brown model correlating creep rupture life versus different temperatures and stresses	76
Figure 4-16: Manson-Haferd plot of $\log \sigma$ versus P_{MH} (normalised coordinates) for SAC alloy, dotted line represents the predicted model Eqn. (2.16).....	76
Figure 4-17: Monkman – Grant model for SnAgCu alloy correlating creep rupture against minimum strain rate: dotted line represents predicted model in Eqn. (2.17).....	77
Figure 4-18: Comparison of proposed subgrain based model with other phenomenological models for SAC solder alloys at 125°C	78

Figure 4-19: Inverse pole figure of BGA solder joint cross section after thermal cycling revealing subgrain formation during a multiaxial stress state on the stress concentration region and intergranular crack along the grain, Terashima [88].....	80
Figure 4-20: SMT subgrain formation after thermal cycling visualised by (a) cross polarized image (b) EBSD orientation map (c) grain boundary map, and (d) non-recrystallized region of SAC solder interconnects after thermal cycling [155]	81
Figure 5-1: Average mean strain progression- Eqn. (3.3) of the solder specimen over lifetime for different load cases, temperatures and stresses- high stress (HS), medium stress (MS), low stress (LS)	85
Figure 5-2: Normalised nominal stress amplitude vs. fatigue life (S-N) for different temperatures at 60 Hz, R=-1: symbols represent measured points and dotted line shows the fit based on Basquin Eqn. (2.5).....	86
Figure 5-3: Cyclic true strain amplitude measured, $\Delta\epsilon/2$ as per Eqn.(3.3) vs. cycles for solder alloys subjected to completely reversed load at R = -1 for different temperatures, at medium stress (MS).....	87
Figure 5-4: Normalised nominal stress amplitude vs. fatigue life (S-N), for different stress ratios subjected to fatigue loading at 35°C and 60 Hz: symbols represent measured points and dotted line corresponds to the fit based on Basquin Eqn. (2.5).....	88
Figure 5-5: Strain amplitude measured $\Delta\epsilon/2$, as per Eqn.(3.3) vs. cycles subjected to R= -1 at 35°C, Low stress- LS, Medium stress-MS and High stress HS	89
Figure 5-6: 3D- matrix scatter of the two parametric damage property of SAC387 solder under mean stress and normalised stress amplitude	90
Figure 5-7: Haigh fatigue diagram of SAC 387 alloy at 1E8 cycles to failure designed based on FKM guideline at 35°C.....	91
Figure 5-8: Determination of the normalised stress gradient, (a) stress- contour plot of the cross section from the notched solder specimen (b) corresponding linearized values of the von-Mises stresses	92
Figure 5-9: S-N curve for notched and unnotched specimens to investigate stress gradient effects: symbols represent measured points and dotted line corresponds to the fit based on Basquin Eqn. (2.5).....	93
Figure 5-10: (a) Laser scan contour plot of the surface roughness on a ceramic component solder joint, (b) line map of the corresponding measurement of the Rz measured over the profile of the solder joint	95
Figure 5-11: Rz measured over the profile of the solder specimen (as grinded) performed using laser scan showing peak profile values.....	96
Figure 5-12: S-N curve, impact of surface roughness on the fatigue property of the solder alloy at 35°C, R= -1, 60 Hz: symbols represent measured points and dotted line corresponds to the fit based on Basquin Eqn. (2.5)	96
Figure 5-13: Summarized S-N diagram of SAC387 for various fatigue factors: symbols represent measured points and dotted line corresponds to the fit based on Basquin Eqn. (2.5).....	97
Figure 6-1: (a) Qualitative comparisons of a cast solder specimen and a non-aged solder joint at two different magnifications (b) XRD analysis on cast solder to confirm the phase constituents.....	102
Figure 6-2: EDX- spot analysis on the β -Sn-rich region to identifying alloying elements for (a) casted solder, (b) solder joint	103
Figure 6-3: EDX/SEM mapping of the element distribution in a cast solder specimen, visualising the distributions alloying constituents in β -Sn matrix and dendrites.	104
Figure 6-4: Hardness measurement, HV 0.01 (10g) on cast solder, solder joint and the IMC phases that is developed between the Cu pad and solder joint	105
Figure 6-5: (a) Fractured creep specimens showing interesting regions analysed for cross section studies (b) optical LM of the creep specimens at 35°C, 80°C, and 125°C tested at lower stress	106
Figure 6-6: EBCC pictures showing subgrain polygon formation in β -Sn crystal during primary creep stage, non-necking regions for (a)medium stress, 35°C, (b) medium stress, 125°C.....	107
Figure 6-7: Inverse pole figures revealing substructure formations and recrystallized grains with low angle orientation detected from necking region at MS and 80°C	108

Figure 6-8: SEM picture of the fracture surface at LS and 80°C (a) showing the overview of the fracture surface with high necking (b) at higher magnification with view of the dimple formation.....	110
Figure 6-9: SEM micrograph at constant lower stresses (LS) at (a) 80°C (b) 125°C showing the dimple like formations (c) (d) corresponding higher magnification around the strain concentrations regions illustrating the different grain boundary wedges with cleavage (subgrain formation)	111
Figure 6-10: Cross polarized LM pictures of cross section showing the transgranular cracks on the primary grain at LS for (a) 35°C (b) 80°C (c) 125°C	112
Figure 6-11: Microstructure of a non-necking region, LS and 125°C tested specimen showing (a) development of short parallel slip markings at an angle of 45° (b) nucleation hindered by the Ag ₃ Sn precipitate (c) subgrain formations and crack growth in a zigzag pattern along subgrain boundaries	113
Figure 6-12: Surface scan of the specimen tested at LS and 125°C showing the wavy slip markings (PSB) (b) corresponding intrusion values over line scan.....	114
Figure 6-13: Microstructure of a 35°C and LS tested specimen, showing development of short parallel slip markings and secondary cracks on the stress concentration regions.....	115
Figure 6-14: SEM of HCF fracture surface for temperatures (35°C, 80°C, 125°C) at relatively: (top row) N _f ~ 10 ⁵ cycles (bottom row) N _f ~ 10 ⁷ cycles	116
Figure 6-15: SE micrographs of a HCF specimen at 35°C, N _f = 10 ⁷ and LS (zone A) high stress intensity striation region (zone B) PSB dominated on the surface, (zone C) micro-void coalescence with high local strain showing void initiating particles at the bottom of some dimples.	117
Figure 6-16: SE micrograph of a HCF specimen at 35°C and LS showing typical high stress intensity region of the fracture surface and dimples of solder with the underlying IMC layer revealed by voids developing in their centre	118
Figure 6-17: (a) SE micrograph of HCF specimen at 125°C, N _f ~10 ⁵ and LS showing demarcations of probable stages of failure, (b) higher magnification on region A showing probable transition region and development of striations, (c) region B show probable slow fatigue crack growth zone with a 3-point morphology, (d) region C show cyclic marking along with intergranular cracking.....	118
Figure 6-18: SE micrographs of HCF specimen at 80°C, N _f ~ 10 ⁷ and LS (C, E, and F) high stress intensity striation region with secondary cracks and PSB (A ,B) wavy striation patterns in the β-Sn matrix (E and C) detected PSB formations.....	119
Figure 7-1: Local stress concept and overall take on the proposed methodology to assess the lifetime of solder joint under vibration loading	124
Figure 7-2: FEA model mesh (a) overall model of single PCB strap with component CC0805 (b) detailed view of the solder joint mesh	125
Figure 7-3: FE model of the solder joints showing the two different mesh density (a) type1 (b) type 2	126
Figure 7-4: Example von Mises FEA results of surface elements for a harmonic unit excitation for mesh setting (a) type 1- coarse (b) type 2-fine	127
Figure 7-5: Surface response with an exemplary 3D contour plot showing the PCB response on the solder joint VM -stress for different damping and density values of the PCB	129
Figure 7-6: (a) Linearized FEA results of maximum Z-axis deformation from the PCB (b) 2-y axis showing measured displacement amplitude in blue and input voltage from the vibration experiment in red (c) comparison of the deformation behaviour of PCB from experiments to FE analysis with a symmetric model.....	130
Figure 7-7: Flow path to arrive at stresses and predicted lifetime values of SMT components	131
Figure 7-8: Convex geometric shape of the solder joint showing crack initiation for (a) ceramic capacitor experiment (b) predicted lifetime of capacitor (c) transformer experiment (d) predicted lifetime of transformer.....	133
Figure 7-9: Weibull analysis with reference line of the experimental scatter points for (a) chip capacitor (b) transformer	134
Figure 7-10: Fatigue scatter data from vibration experiment at room temperature vs. predicted threshold line for (a) chip capacitors (b) transformer	135
Figure 7-11: Contour creep strain plot (a) maximum axial creep strain developed on the meniscus of the solder joint (b) maximum shear strain developed on the standoff region of the interconnect causing the initiation of damage	140

Figure 7-12: Creep strain behaviour of the six-component axis for different subgrain size 141
Figure 8-1: Connecting the bridge between microstructural and structural field of study using the
proposed mechanistic creep model 144

LIST OF TABLES

Table 1: Alloy composition of the SAC alloy (all compositions in weight %)	40
Table 2: Test matrix for the solder material mechanical characterization	46
Table 3: Parameters for vibration experiment testing on ceramic capacitors and transformer	52
Table 4 : Parameters of the Norton power law fit out of experimental optimization	57
Table 5 : Parameters of the hyperbolic Garafalo law fit out of experimental optimization	57
Table 6 : Parameters of the double power law fit out of experimental optimization	58
Table 7: Values of the coefficients in Eqn. (4.1) for different Sn- based alloys from various research works	60
Table 8: Calculated parameters from the volume fraction Eqn. (2.14), inter-particle spacing Eqn. (4.2), and Orowan stress Eqn. (2.26)	63
Table 9: Calculated back stress from the Eqn. (4.3)	64
Table 10: Summarized value of activation energy related parameters (intercept and slope in Figure 4-10) with respect to the temperature	68
Table 11: Summarized values of creep model with and without subgrain size dependency	75
Table 12: Tabulated fatigue parameters of the Basquin Eqn. (2.5) for different temperatures (log-log scaling)	86
Table 13: Tabulated fatigue parameters of the Basquin equation Eqn. (2.5) for different R-ratios (log-log scaling)	88
Table 14: Mean stress corrective description and their corresponding values for SAC387 alloy	91
Table 15: Values of the normalised stress gradient in Eqn. (2.9) and their corresponding correction factors	94
Table 16: Tabulated fatigue parameters of the Basquin equation Eqn. (2.5) for different roughness cases (log-log scaling)	97
Table 17: Summary of different mechanism involved in HCF testing for SAC alloy	122
Table 18: Comparison of number of elements on coarse and fine meshing	126
Table 19: Parameters and values changed to calibrate the FE model with experimental results	129
Table 20: Test case and material description for testing the ANSYS subroutines using a CC0805 SMT in a thermal cyclic scenario	139

LIST OF PUBLICATIONS

1. J. Thambi, A. Schiessl, M. Waltz, K-D. Lang, U. Tetzlaff “Modified constitutive creep law with micro-mechanical modelling of *Pb*-free solder alloys”- ASME Journal of electronic package: 2016
2. J. Thambi, U. Tetzlaff, A. Schiessl, K-D. Lang, M. Waltz, “High cycle fatigue behavior and generalized fatigue model development of *Pb*-free solder alloys based on local-stress approach”- Elsevier Microelectronics Reliability: 2016
3. J. Thambi, U. Tetzlaff, A. Schiessl, K-D. Lang, M. Waltz, “Lifetime evaluations of *Pb*-free solder joints under vibration load by means of generalised local-stress approach”- Elsevier Microelectronics Reliability: 2018

CONFERENCES

1. J. Thambi, “Lifetime prediction of surface mounted devices soldered on printed circuit board under multiple environment using FEA”- Continental Automotive GmbH, conference of simulation platforms, 2013, Regensburg, Germany
2. J. Thambi, “Reliability assessment of *Pb*-free solder joint based on creep and HCF studies” Material Science workshop, June 9-10, 2016, THI, Ingolstadt, Germany